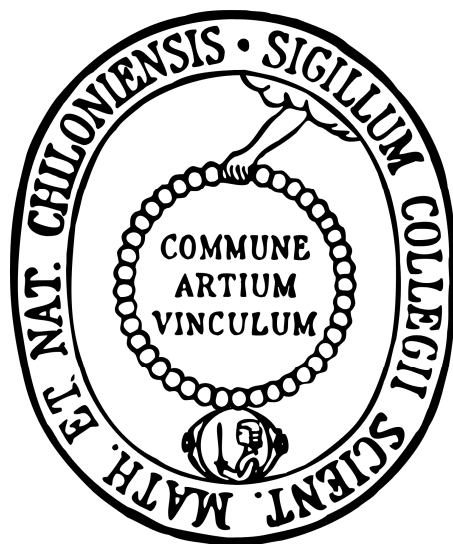


High-Throughput Investigation of Inorganic-Organic Hybrid Materials: Metal Phosphonatobenzenesulfonates and Ni- based MOFs with Paddle-Wheel Building Units

Cumulative Dissertation

in fulfillment of the requirements for the degree *Dr. rer. nat.* :

of the Faculty of Mathematics and Natural Sciences
at Christian-Albrechts-University zu Kiel



submitted by

Palanikumar Maniam, Dipl.-Ing. (FH)

Kiel, Germany, 2011

Affidavit

I declare that the work presented here was performed by me independently, apart from the scientific guidance of my doctoral advisor and only using the devices, resources and media mentioned in the thesis. The doctoral thesis is solely submitted to the Christian-Albrechts-Universität zu Kiel.

Palanikumar Maniam

Kiel, June 2011.

First examiner: Prof. Dr. Norbert Stock

Second examiner: Prof. Dr. Wolfgang Bensch

Date of the oral examination : 29.07.2011

Approved for publication on : 29.07.2011

Signed: Prof. Dr. Lutz Kipp, Dean

Zusammenfassung

Der Schwerpunkt dieser Doktorarbeit ist die systematische Untersuchung der Bildung anorganisch-organischer Hybridmaterialien mit verschiedenen Metallionen und polyfunktionellen organischen Linkern. Die Synthese und Charakterisierung der Materialien wurden unter solvothermalen Bedingungen mit Hilfe von Hochdurchsatz (HT)-Methoden durchgeführt. Die HT-Methoden umfassen die Parallelisierung der einzelnen Reaktionen in Miniatur-Teflon[®] Reaktoren und die anschließende Charakterisierung der kristallinen Produkte mittels automatisierter HT-XRPD Analyse. Diese Methoden ermöglichen die schnelle Untersuchung der Einflüsse von Edukt-Zusammensetzungen und Prozessparametern auf die Kristallbildung.

Im ersten Teil dieser Dissertation wurde das Reaktionssystem $M^{2+} / H_2O_3PC_6H_4SO_3H / NaOH / H_2O$ ($M = Ni, Mg, Cu, Zn, Co, Fe, Mn, Sn, Cd, Sr, Pb$ and Ba) erforscht. Die Auswertung des Metallion-Screenings ergab sechs Metall-4-phosphonatobenzolsulfonate mit Cu^{2+} , Sn^{2+} and Pb^{2+} -Ionen. Weitere detaillierte Untersuchungen bei denen das molare Verhältnis Metallsalzen : Linker : NaOH untersucht wurde, half bei der Bestimmung der spezifischen Phasenbildungsbereiche jeder Verbindung. Unterschiedliche M-O Polyeder und M-O-M Cluster wurden in den Kristallstrukturen beobachtet, die zur Bildung von 2D oder 3D M-O-Netzwerken geführt haben, insbesondere in den Kupfer-basierten Verbindungen. Ein Misch-Linker Cu-Phosphonatosulfonat wurde auch mit 4,4'-Bipyridin als Co-Ligand erhalten, das eine reversible Strukturumwandlung unter De-/Rehydratisierung aufweist. Die Charakterisierung der Metallphosphonatosulfonate wurde mittels Röntgenpulver- und Einkristallröntgenbeugung, Magnetsuszeptibilitätsmessungen, thermogravimetrischer Analyse (TGA), energiedispersiver Röntgenspektroskopie (EDX), CHNS Elementaranalyse, Infrarotspektroskopie (IR) und Rasterelektronmikroskopie (REM) durchgeführt.

Der zweite Teil dieser Arbeit befasst sich mit der Entdeckung und Charakterisierung poröser Nickel(II)-basierter metall-organischer Gerüstverbindungen mit Schaufelrad-Baueinheiten. Die Schaufelrad-Dimere bestehen aus Ni^{2+} -Ionen, die von vier äquatorialen $R(COO)^-$ Gruppen und zwei axialen Liganden umgeben sind. Das Reaktionssystem $Ni^{2+} / R(COOH)_3 / \text{Additiv} / \text{Lösungsmittel}$, mit $R = C_6H_3, 1,3,5-(C_6H_4)_3C_6H_3$, wurde systematisch durch Screening von Nickelsalzen, organischen Basen und Lösungsmitteln bei verschiedenen Reaktionstemperaturen untersucht. Zwei nickelbasierte Verbindungen mit Schaufelrad-Einheiten wurden mit 1,3,5-Benzoltricarbonsäure (H_3BTC) and 4,4',4''-Benzol-1,3,5-triyl-trisbenzoesäure (H_3BTB) erhalten. Zusätzlich wurden zwei Pseudopolymorphe mit der Gerüstzusammensetzung $[Ni_2(BDC)_2(DABCO)]$ ($H_2BDC = \text{Terephthalsäure}$, $DABCO = 1,4\text{-diazabicyclo}[2.2.2]\text{oktan}$) entdeckt. Die Optimierung der Reaktionsbedingungen führte zu einphasigen Produkten. Dazu wurde der Einfluss der Heizmethode (konventionelle vs. Mikrowellen-unterstützte Synthese), die DABCO-Menge, das Rühren, die

Gesamtkonzentration und die Reaktionstemperaturen untersucht. Nach der Optimierung der Synthese, konnten alle vier Nickel(II)-Verbindungen, die Schaufelrad-Baueinheiten enthalten, in größeren Mengen hergestellt und ausführlich mittels Sorptionsmessung, IR-Spektroskopie, Elementaranalyse, REM und thermogravimetrischer Analyse charakterisiert werden.

Abstract

The focus of this Ph.D. work is to systematically investigate the formation of inorganic-organic hybrid materials with different metal ions and polyfunctional organic linkers. The synthesis and characterization of the materials were performed under solvothermal conditions employing high-throughput (HT) methods. The HT methods incorporate the parallelization of individual reactions in miniaturized Teflon[®] reactors and the subsequent characterization of the crystalline products via automated HT-XRPD analysis. The HT methods have enabled the rapid study of the influences of compositional and process parameters on the formation fields and helped to optimize the synthesis conditions.

In the first part of the thesis, the reaction system $M^{2+} / H_2O_3PC_6H_4SO_3H / NaOH / H_2O$ was investigated (M = Ni, Mg, Cu, Zn, Co, Fe, Mn, Sn, Cd, Sr, Pb and Ba). The evaluation of the metal-ion screening yielded six metal 4-phosphonatobenzenesulfonates with Cu^{2+} , Sn^{2+} and Pb^{2+} ions. Further detailed investigation of the molar ratio metal salt : linker : NaOH has helped to pinpoint the specific formation fields of each compound. Various M-O-M polyhedra and clusters are observed in the crystal structures which lead to 2D or 3D networks, especially in copper-based structures. A mixed-linker copper phosphonosulfonate was also obtained with the auxiliary ligand 4,4'-bipyridine which exhibits an interesting reversible structural transition upon de-/rehydration. The characterization of the metal phosphonosulfonates was performed with X-ray powder and single crystal X-ray diffraction, magnetic susceptibility measurements, thermogravimetric (TG) analysis, energy-dispersive X-ray (EDX) and CHNS elemental analysis, infrared (IR) spectroscopy and scanning electron microscopy (SEM).

The second part of the thesis deals with the discovery and characterization of porous nickel(II) based metal-organic frameworks containing paddle-wheel building units. The dimeric paddle-wheel units are comprised of Ni^{2+} ions that are coordinated by four equatorial $R(COO)^-$ groups and two axial terminal ligands. The reaction system $Ni^{2+} / R(COOH)_3 / additive / solvent$, with $R = C_6H_3, 1,3,5-(C_6H_4)_3C_6H_3$, was systematically investigated through screening of nickel salts, organic bases and solvents at various reaction temperatures. Two nickel(II) based compounds with paddle-wheel units were obtained with 1,3,5-benzenetricarboxylic (H_3BTC) and 4,4',4''-benzene-1,3,5-triyl-tris-benzoic acid (H_3BTB). In addition, two pseudo-polymorphs with the framework composition $[Ni_2(BDC)_2(DABCO)]$ ($H_2BDC =$ terephthalic acid, $DABCO = 1,4$ -diazabicyclo[2.2.2]octane) were discovered. For the phase selective synthesis, the influence of conventional vs. microwave-assisted heating, DABCO amount, stirring, overall concentration and reaction temperature was examined in detail. After the optimization of synthesis conditions, the scale-up of all four nickel(II) paddle-wheel compounds was accomplished and all the compounds were characterized via sorption experiments, IR spectroscopy, elemental analysis, SEM measurements and TG analysis.

To my dearest parents and my loving fiancée, Begoña.

*Ideas normally contain three stages:
1) It's nonsense – stop wasting my time
2) It's possible, not worth trying
3) I told you it was a good idea!*

Arthur C. Clarke (1917-2008)

Acknowledgements

I always wanted to be a chemist. Although I did my undergraduate studies in the field of engineering, now I did get the chance to be a chemist. For that, I thank my doctoral advisor, Prof. Dr. Norbert Stock. Through his engaging scientific discussions, I have managed to grasp vast amounts of knowledge in the field of chemistry which I gratefully appreciate and will certainly be helpful for my future undertakings.

The efforts taken by Dr. Andreas Sonnauer to mentor me during the initial stages of my PhD work will not be easily forgotten. I thank him sincerely for investing his precious time in assisting me whenever I needed some help and foremost, for his friendship.

I am also thankful to Prof. Dr. Wolfgang Bensch and Prof. Dr. Christian Näther for their extensive advice on magnetic and single crystal measurements. This work was also made possible with the support of Tim Ahnfeldt, with whom I spent a lot of time arguing about numerous scientific and non-scientific subjects. I also express my gratitude to Antje Reher and Mark Feyand for lending their expertise in sorption experiments and Rietveld refinements, respectively.

I also owe a great deal of gratitude to Adam Wutkowski and Beatrix Seidlhofer for the thermogravimetric measurements and to Henning Lühmann as well as Maren Rasmussen for the magnetic susceptibility experiments. Many thanks as well to Uschi Cornelissen and Stephanie Pehlke for conducting IR- and elemental analyses. I am also deeply obliged to thank Inke Jess for all the troubles she took in selecting single crystals and conducting countless X-ray diffraction measurements.

The co-operation with the group of Prof. Dr. Michael Fröba at the University of Hamburg is also greatly appreciated. I am very grateful for the support given by Britta Bahn throughout the duration of my stay. The encouragement given by her and all the past and present members of Stock group has made my life as a PhD student in Kiel enjoyable.

Last but not least, I thank my loving parents and my dearest Begoña for all the motivation and guidance through all the good and bad times.

Table of contents

1	Introduction	1
2	Characterization methods	6
3	Experimental section	15
4	Cumulative section	24
4.1	From metal phosphonates to metal phosphonosulfonates	24
4.2	High-throughput synthesis of metal phosphonates	38
4.3	Inorganic-organic hybrid materials based on 4-phosphonobenzenesulfonic acid (H ₂ O ₃ P-C ₆ H ₄ -SO ₃ H)	45
4.3.1	Systematic Hydrothermal Investigation of Metal Phosphonatobenzenesulfonates by High-Throughput Methods	47
4.3.2	A three-dimensional tin(II) phosphonatobenzenesulfonate with Sn ₄ O ₁₂ clusters	56
4.3.3	Synthesis and characterization of the mixed-linker copper(II) coordination polymer [Cu(HO ₃ PC ₆ H ₄ SO ₃)(C ₁₀ N ₂ H ₈)]·H ₂ O	62
4.4	Polycarboxylate based MOFs	70
4.4.1	Isorecticular chemistry	72
4.4.2	Porous nickel-based MOFs with paddle-wheel building units	73
4.4.3	Investigation of Porous Ni-Based Metal Organic Frameworks Containing Paddle-Wheel Type Inorganic Building Units via High-Throughput Methods	84
4.4.4	Poly[(μ ₃ -benzene-1,3,5-tricarboxylato-κ ³ O ¹ :O ³ :O ⁵)(μ ₂ -2-methylimidazolato-κ ² N:N')tris(2-methylimidazole-κN)dizinc(II)]	98
5	Conclusion	102
6	Outlook	109
7	Appendix	111
8	List of publications / Contribution to conferences	185

1 Introduction

Extended framework materials built of organic ligands (or linkers) coordinated to metal ions or clusters can be categorized as coordination polymers. In this class of hybrid materials, different types of structural properties are observed, such as amorphous and crystalline.^[1,2] These amorphous or crystalline coordination polymers can also either be non-porous or porous. Those porous coordination polymers (PCPs) are also known as metal-organic frameworks (MOFs).^[3,4] Through infinite interconnection of bridging organic ligands coordinated to metal ions, the typical well ordered, crystalline assembly of three-dimensional structures of MOFs or PCPs is accomplished. The research of these porous substances evolved from the field of zeolites which are based on aluminosilicates.^[5] For years, zeolites have established a firm foothold in the chemical industry due to their important applications, mostly as ion exchangers, petrochemical catalysts and gas adsorbers. Zeolites are mainly constructed of tetrahedral MO_4 ($M = Al$ or Si) units and in MOF structures, whole molecules act now as modular building units. MOFs share many similarities to zeolites that include the synthesis procedure, permanent porosity and crystallinity. Although MOFs are thermally and chemically less stable than zeolites, they offer a higher surface area^[6] and most importantly, more chemical diversity through the usage of different metal ions or organic ligands.^[7,8] This advantage can be exploited to synthesize structures with desired properties by using a “*modular building principle*”.^[9] Diverse linkers with varying dimensions and functional groups can be utilized during the synthesis and thus, manipulating the pore size and attributes of the resulting MOF such as hydrophobicity, hydrophilicity, acidity etc. Among the functional groups of the linkers reported are for example, carboxylic-, phosphonic- and sulfonic acids, amines as well as thiols.^[10] Most of the well investigated MOFs are based on polycarboxylates, for example HKUST-1, MOF-5, MIL-53 and MIL-100.^[11,12,13,14] These compounds have been successfully scaled-up and tested for many potential applications such as gas storage, gas separation, catalysis, drug delivery, sensing and light-emitters.^[15,16,17]

Coordination polymers with phosphonate-based linkers have been shown to exhibit high thermal and chemical stabilities compared to many of the carboxylate counterparts. These remarkable properties are mostly due to various deprotonation levels and a higher number of bonding sites. But these factors also render the structural prediction of the compounds much more difficult. Nevertheless, most metal phosphonates obtained are made of layered structures which make them a good candidate for intercalation studies.^[18] Some of the methods used to generate open-framework phosphonates are for example, partial replacement of the phosphonates groups with non-pillaring phosphates,^[19] employment of

large, sterically hindering organic ligands which prefer non-layered arrangements^[20] as well as using mixed-ligand system where the other non-phosphonate ligand will disrupt the usual layered motif.^[21] Early works on metal phosphonates have focused on zirconium(IV) based compounds,^[22, 23] but recent developments have shown the usage of nearly all types of metal ions.^[24, 25] By using aluminium, titanium and nickel ions with N,N'-piperazinebismethylene-phosphonic acid, porous non-layered metal phosphonates were obtained.^[26, 27] Recent studies have reported the potential applications of metal phosphonates in the area of ion-exchange,^[18] flame retardant,^[28] anti-corrosion,^[29] proton conductor,^[30] catalysts^[31] and sensors^[32].

The number of studies on metal sulfonates is less profound compared to metal carboxylates and phosphonates. Although crystalline products are obtained, the coordination of sulfonate groups is relatively weak^[33] which can lead to dynamic single crystal to single crystal transformations.^[34, 35] The structures are mostly not robust enough to be permanently porous. Similar to metal phosphonates, a high percentage of the metal sulfonates reported are layered and/or dense structures.^[36] Cote and co-workers have systematically studied the spacing effect of arene groups in silver(I) monosulfonates whereby three types of layered structures were obtained.^[37] Their study has shown that the π - π interactions between aryl groups influence the coordination modes of silver ions and $-\text{SO}_3^-$ groups. The work of Shimizu and co-workers on silver(I) sulfonate MOFs comprised of pillared-layered and other three-dimensional frameworks are one of the first reports about open-framework metal sulfonates.^[38]

In order to combine the high thermal stability of metal phosphonates and the dynamic structure properties of sulfonates, the idea of employing a linker with both phosphonic and sulfonic acid comes into consideration. This topic is slowly gaining interest in the scientific community where Clearfield and co-workers first documented in 1987 a partially substituted phenylsulfonate derivate of zirconium phosphonate, which was obtained by subsequent sulfonation of $\text{Zr}(\text{HPO}_3)(\text{O}_3\text{PC}_6\text{H}_5)$ with fuming sulfuric acid.^[39] Lately, reports of direct use of phosphonosulfonic linkers to synthesize metal phosphonate-sulfonates have emerged. Mao and co-workers have worked with a rigid 3-phosphonobenzenesulfonic acid linkers in combination with various M^{2+} as well as M^{3+} ions that mostly generated compounds with polynuclear clusters incorporating auxiliary amine ligands.^[40, 41, 42, 43, 44]

The vast number of metal phosphonate structures and the various synthesis methods demonstrate the immense abundance of metal phosphonates. Although various studies have been performed by many groups, it is hard to compare and correlate the results with each

other since different synthesis conditions (i.e. solvent, reaction time, reaction temperature, reactor size and material, etc.) have been employed. Unfortunately, only few systematic studies have been reported that investigate the role of chemical and process parameters. This would be of substantial interest in order to learn more about reaction trends and to “comprehend” the chemistry of metal phosphonates. Nevertheless, explorative investigations require a lot of time and effort and therefore, a method involving parallelized and miniaturized synthesis as well as automated sample characterization would be of great advantage. A methodology has been applied over the last decade, the so-called high-throughput (HT) methods that allow the systematic investigation of complex synthesis fields and thus the elucidation of reaction trends. By employing high-throughput (HT) methods, our group has synthesized several new metal phosphonosulfonates utilizing a flexible phosphonoalkyl-sulfonic acid linkers.^[45] The system in our group is designed for solvothermal syntheses up to 200 °C and enables us to carry out 24 or 48 reactions simultaneously. A recent development includes the implementation of a temperature gradient reactor system which allows the parallel investigation of various reaction temperatures up to 100 °C.^[46]

This thesis focuses on the hydrothermal synthesis of new metal phosphonosulfonates using a new linker, 4-phosphonobenzenesulfonic acid, via HT-methods and the subsequent elaborate characterization of the new compounds. Systematic investigations encompass the HT screening of process and compositional reaction parameters in order to obtain a clearer view on reaction and structural trends. The work is also extended to the usage of auxiliary amine ligands in order to obtain new structural motifs. As most HT investigations concentrate only on hydrothermal synthesis, the second part of this work deals with HT solvothermal synthesis using organic solvents such as dimethylformamide (DMF). The reaction system Ni^{2+} / carboxylic acid linker / base / DMF was chosen for these studies in order to investigate the feasibility of synthesizing MOFs containing paddle-wheel building units. Prior to the characterization of all compounds, a detailed systematic HT study of reaction parameters needs to be conducted to reveal the respective formation fields and thus, help to optimize the synthesis procedures. The optimal synthesis conditions are important for the scale-up synthesis to obtain a sufficient amount of the compounds for the elaborate characterization.

References

- [1] F. Bonaccorsi, P. Albonico, R. Pappa, T. P. Lockhart, *Int. J. Polym. Mater.* **1992**, *18*, 165-177.
- [2] G. Becker, O. Mundt, H. Standelmann, *Z. Anorg. Allg. Chem.* **1990**, *580*, 139-150.
- [3] S. Subramanian, M. J. Zaworotko, *Angew. Chem. Int. Ed. Engl.* **1995**, *34*, 2127-2129; *Angew. Chem.* **1995**, *107*, 2295-2297.
- [4] O. M. Yaghi, G. Li, H. Li, *Nature*, **1995**, *378*, 703-706.
- [5] A. K. Cheetham, G. Férey, T. Loiseau, *Angew. Chem Int. Ed.* **1999**, *38*, 3268-3292; *Angew. Chem.* **1999**, *111*, 3466-3492.
- [6] M. E. Davis, R. F. Lobo, *Chem. Mater.* **1992**, *4*, 756-768.
- [7] H. Furukawa, N. Ko, Y. B. Go, N. Aratani, S. B. Choi, E. Choi, A. Ö. Yazaydin, R. Q. Snurr, M. O'Keeffe, J. Kim, O. M. Yaghi, *Science*, **2010**, *329*, 424-428.
- [8] S. Kitagawa, R. Kitaura, S.-I. Noro, *Angew. Chem Int. Ed.* **2004**, *43*, 2334-2375; *Angew. Chem.* **2004**, *116*, 2388-2430.
- [9] M. Eddaoudi, D. B. Moler, H. Li, B. Chen, T. M. Reineke, M. O'Keeffe, O. M. Yaghi, *Acc. Chem. Res.* **2001**, *34*, 319-330.
- [10] J. L. C. Rowsell, O. M. Yaghi, *Microporous Mesoporous Mater.* **2004**, *73*, 3-14.
- [11] S. S.-Y. Chui, S. M.-F. Lo, J. P. H. Charmant, A. Guy Orpen, I. D. Williams, *Science*, **1999**, *283*, 1148-1150.
- [12] H. Li, M. Eddaoudi, M. O'Keeffe, O. M. Yaghi, *Nature*, **1999**, *402*, 276-279.
- [13] C. Serre, F. Millange, C. Thouvenot, M. Noguès, G. Marsolier, D. Louër, G. Férey, *J. Am. Chem. Soc.* **2002**, *124*, 13519-13526.
- [14] C. Serre, C. Mellot-Draznieks, F. Millange, S. Surblé, J. Dutour, I. Margiolaki, *Angew. Chem. Int. Ed.* **2004**, *43*, 6296-6301; *Angew. Chem.* **2004**, *116*, 6456-6461.
- [15] U. Mueller, M. Schubert, F. Teich, H. Puetter, K. Schierle-Arndt and J. Pastré, *J. Mater. Chem.* **2006**, *16*, 626-636.
- [16] A. U. Czaja, N. Trukhan, U. Müller, *Chem. Soc. Rev.* **2009**, *38*, 1284-1293.
- [17] S. T. Meek, J. A. Greathouse, M. D. Allendorf, *Adv. Mater.* **2011**, *23*, 249-267.
- [18] R. C. Wang, Y. P. Zhang, H. L. Hu, R. R. Frausto, A. Clearfield, *Chem. Mater.* **1992**, *4*, 864-871.
- [19] M. B. Dines, R. E. Cooksey, P. C. Griffith, R. H. Lane, *Inorg. Chem.* **1983**, *22*, 1003-1004.
- [20] G. Alberti, U. Constantino, F. Marmottini, R. Vivani, P. Zappelli, *Angew. Chem. Int. Ed. Engl.* **1993**, *32*, 1357-1359; *Angew. Chem.* **1993**, *105*, 1396-1398.
- [21] J. Zhu, X. Bu, P. Feng, G. D. Stucky, *J. Am. Chem. Soc.* **2000**, *122*, 11563-11564.
- [22] G. Alberti, U. Costantino, S. Allulli, N. Tomassini, *J. Inorg. Nucl. Chem.* **1987**, *40*, 1113-1117.
- [23] Y. P. Zhang, A. Clearfield, *Inorg. Chem.* **1992**, *31*, 2821-2826.
- [24] A. Clearfield, *Prog. Inorg. Chem.* **1998**, *47*, 371-510.
- [25] J. G. Mao, *Coord. Chem. Rev.* **2007**, *251*, 1493-1520.
- [26] C. Serre, J. A. Groves, P. Lightfoot, A. M. Z. Slawin, P. A. Wright, N. Stock, T. Bein, M. Haouas, F. Taulelle, G. Férey, *Chem. Mater.* **2006**, *18*, 1451-1457.

- [27] S. R. Miller, G. M. Pearce, P. A. Wright, F. Bonino, S. Chavan, S. Bordiga, I. Margiolaki, N. Guillou, G. Ferey, S. Bourrelly, P. L. Llewellyn, *J. Am. Chem. Soc.* **2008**, *130*, 15967-15981.
- [28] S. V. Levchik, R. Mazor, A. Ben-Zvi, WO/2011/028351, **2011**.
- [29] K. D. Demadis, S. D. Katarachia, M. Koutmos, *Inorg. Chem. Commun.* **2005**, *8*, 254-258.
- [30] G. Alberti, F. Cherubini, R. Palombari, *Sensors Actuators*, **1995**, *B24*, 270-272.
- [31] K. P. Reis, V. K. Joshi, M. E. Thompson, *J. Catal.* **1996**, *161*, 62-67.
- [32] L. C. Brousseau, K. Aoki, H. C. Yang, T. E. Mallouk, *Interfacial Design and Chemical Sensing*, **1994**, *561*, 60-70.
- [33] A. P. Côté, G. K. H. Shimizu, *Coord. Chem. Rev.* **2003**, *245*, 49-64.
- [34] B. D. Chandler, G. D. Enright, S. Pawsey, J. A. Ripmeester, D. T. Cramb and G. K. H. Shimizu, *Nat. Mater.* **2008**, *7*, 229-235.
- [35] M. P. Suh, Y. E. Cheon, *Aust. J. Chem.* **2006**, *59*, 605-612.
- [36] G. Smith, B. A. Cloutt, D. E. Lynch, K. A. Byriel, C. H. L. Kennard, *Inorg. Chem.* **1998**, *37*, 3236-3242.
- [37] A. P. Côté, G. K. H. Shimizu, *Inorg. Chem.* **2004**, *43*, 6663-6673.
- [38] D. J. Hoffart, S. A. Dalrymple, G. K. H. Shimizu, *Inorg. Chem.* **2005**, *44*, 8868-8875.
- [39] C. Y. Yang, A. Clearfield, *React. Polym.* **1987**, *5*, 13-21.
- [40] Z. Y. Du, H. B. Xu, J. G. Mao, *Inorg. Chem.* **2006**, *45*, 6424-6430.
- [41] Z. Y. Du, H. B. Xu, J. G. Mao, *Inorg. Chem.* **2006**, *45*, 9780-9788.
- [42] Z. Y. Du, X. L. Li, Q. Y. Li, J. G. Mao, *Cryst. Growth. Des.* **2007**, *7*, 1501-1507.
- [43] Z. Y. Du, H. B. Xu, X. L. Li, J. G. Mao, *Eur. J. Inorg. Chem.* **2007**, 4520-4529.
- [44] Z. Y. Du, A. V. Prosvirin, J. G. Mao, *Inorg. Chem.* **2007**, *46*, 9884-9894.
- [45] A. Sonnauer, Ph.D. Thesis: *Systematic Investigation of Inorganic-Organic Hybrid Compounds Based on Polyfunctional Phosphonic Acids Using High-Throughput Methods*, **2008**, Christian-Albrechts-Universität zu Kiel, Germany.
- [46] S. Bauer, N. Stock, *Angew. Chem Int. Ed.* **2007**, *46*, 6857-6860; *Angew. Chem.* **2007**, *119*, 6981-6984.

2 Characterization methods

The characterization of the compounds synthesized in this thesis work was conducted using the methods listed below:

- X-ray diffraction on single crystals and microcrystalline powder
- Mid-infrared spectroscopy
- Thermogravimetric and differential thermal analysis
- Quantitative elemental analysis (C,H,N,S)
- Semi-quantitative elemental analysis (EDX)
- Scanning electron microscopy measurements (SEM)
- Magnetic susceptibility measurements (AC-/DC-field)
- Volumetric gas/vapor sorption measurement

The most essential characterization method in this work is X-ray diffraction which is used to determine the crystal structures and therefore, the principles behind the methods will be described in more detail in the following sections. The information about all other methods and the respective device types are tabulated in the Table 2.1.

Table 2.1 Summary of the characterization methods and the respective instrumental details.

Methods	Device type /Manufacturer	Remarks
Single crystal X-ray diffraction	STOE IPDS I	Mo-K α ($\lambda = 0.71073 \text{ \AA}$)
	STOE IPDS II	Mo-K α ($\lambda = 0.71073 \text{ \AA}$)
	Bruker-Nonius APEX II	Mo-K α ($\lambda = 0.71073 \text{ \AA}$), FR591 rotating anode
X-ray diffraction	STOE Stadi P combi	Transmission geometry, Cu-K α_1 ($\lambda = 1.5406 \text{ \AA}$), linear PSD detector, opening angle 6° , xy- 48 sample stage
	STOE Stadi P	Transmission geometry, Cu-K α_1 ($\lambda = 1.5406 \text{ \AA}$), linear PSD detector, opening angle 6° ,
MIR	ATI Matheson Genesis	KBr-Matrix, $400\text{-}4000 \text{ cm}^{-1}$,
	Bruker ALPHA ATR	$375\text{-}4000 \text{ cm}^{-1}$
TG-DTA	Netzsch STA-409CD	Air-/N $_2$ -atmosphere, 75 ml/min
Elemental analysis	Eurovektor Euro EA	C,H,N,S-analysis, He-carrier gas, combustion in O $_2$ at 1010 °C, detection via thermal conductivity detector
ESEM/EDX	Phillips ESEM XL 30	Scanning electron microscope with EDAX detector
	JEOL JSM-6500F	
Susceptometer	Lake Shore Cryomatic 7000	ZFC, AC- & DC-mode
Gas-/vapor sorption	BEL JAPAN INC. Belsorp $_{\text{max}}$	Sorption of N $_2$, Ar at 77 K, CO $_2$, H $_2$ O at 298 K
	Quantachrome Autosorb 1-C	Sorption of H $_2$ at 77 K

2.1 X-ray diffraction

The Nobel Prize winning discovery of X-rays by Wilhelm Röntgen in 1895 has given scientists a priceless gift in determining atomic and molecular crystal structures. He found that an electrically heated tungsten filament emits electrons that strike a metal target or anode which then releases X-rays. Most commonly used metal anodes are copper and molybdenum with K α -radiation wavelengths of 1.5418 and 0.7107 Å, respectively. The pure K α_1 -radiation is usually obtained by using a monochromator which reflects the beam from a lattice plane. The interatomic spacings in the order of 1 Å in the well ordered array of atoms or molecules of crystalline solids is in the same order of magnitude with the wavelength of the X-ray radiation. Therefore, this enables the sample crystals to act as a three-dimensional diffraction grating. The constructive interference of the diffracted beams results in a pattern

which is dependent of the atomic positions in the crystal. The relationship between the periodic lattice plane spacings (d_{hkl}) and the scattering angle (θ_{hkl}) is given by the Bragg's equation (E1).

$$n \cdot \lambda = 2 \cdot d_{hkl} \cdot \sin \theta_{hkl} \quad (\text{E1})$$

In the single crystal and powder diffractometry, the wavelength (λ) of the X-ray beam is pre-given and the scattering angle (θ) of the observed reflection is measured. Thus, the spacing between crystal lattice planes (d) can be calculated.

2.2 X-ray powder diffraction (XRPD)

A sample of finely ground crystalline powder is comprised of crystallites, which are randomly oriented to each other. During a XRPD measurement, the X-rays are diffracted from the planes of crystallites that lie at the correct angles to fulfil the Bragg equation.^[1] The angles and the intensity of the diffracted beams are plotted as intensity (I) against 2θ . This data then can be used to assign the correct hkl index to each reflection; a procedure known as "XRPD pattern indexing". Once the cell parameters of a certain crystal structure have been determined, the data can be compared to the existing structures in the database to identify unknown materials and also to check for phase purity as well as isomorphous structures. The relevant databases employed for this work are the inorganic structure databank (ICSD)^[2] and the organic as well as metal-organic database (CSD).^[3] Indexing a powder diffraction belonging to low symmetry crystal structure can be complicated sometimes due to the increased number of reflections and the resulting overlap of reflections. One solution is to index the XRPD patterns with different algorithms which may help to find the correct cell parameters (Table 2.2). The preliminary cell parameters can be then further refined, for example with the WinXPOW program. The systematic absence of certain reflections can be used to narrow down the possible space groups.

X-ray powder diffraction can also be applied to observe phase transformations of a crystalline substance. Temperature sensitive structural changes of a material can be tracked down by performing *in situ* XRPD measurements at various temperatures.

2.3 Structure determination via single crystal diffraction

X-ray diffraction on single crystals with suitable size enables the precise determination of not only the cell dimensions and space group, but also the atomic coordinates. Nevertheless, the structure determination via single crystal X-ray diffraction is not always a straightforward process. Several factors have to be considered during a crystal structure analysis.

Scattering factor: The X-ray scattering strength depends on the number of electrons an atom has. The effectiveness of an atom to scatter X-rays is called scattering factor (f_0) and this factor also depends on the Bragg angle (θ) and the radiation wavelength (λ).

Structure factor: The sum of the waves scattered by all atoms in the unit cell, in the direction of the hkl reflection is the structure factor (F_{hkl}). The F_{hkl} factor is calculated from atomic positions and scattering factors.^[1] It can be expressed for j atoms in a unit cell as:

$$F_{hkl} = \sum_j f_j e^{2\pi i(hx_j + ky_j + lz_j)} \quad (\text{E2})$$

whereby f_j is the scattering factor of the j -th atom and x_j, y_j, z_j are its fractional coordinates. To reflect the periodic nature of the wave, such series can be described in term of sines and cosines with the **Fourier series**. For a crystal with a center of symmetry and n unique atoms in the asymmetric unit, the equation E2 can be simplified to:

$$F_{hkl} = 2 \sum_n f_n \cos 2\pi \cdot (hx_n + ky_n + lz_n) \quad (\text{E3})$$

The distribution of electron density ($\rho_{x,y,z}$) within a crystal with unit cell volume (V) can be described as a three-dimensional Fourier series:

$$\rho(x, y, z) = \frac{1}{V} \sum_{hkl} F_{hkl} e^{-2\pi i(hx + ky + lz)} \quad (\text{E4})$$

The electron density is the **Fourier transform** of the structure factors which basically means if the structure factors are known, the electron density distribution in the cell can be calculated leading to the determination of the atomic positions. The structure factor (F_{hkl}) is related to the measured intensity of the hkl reflections (I_{hkl}) with the following expression:

$$|F_{hkl}| \propto \sqrt{I_{hkl}} \quad (\text{E5})$$

A routine correction procedure has to be applied to the measured intensities. This procedure includes the Lorentz correction (L) relating to the data collection geometry mode, polarization correction (p) due to partially polarized X-ray beam upon reflection and an absorption correction (A), mostly for crystal structures with heavy atoms.

From the geometry of the X-ray diffraction, the dimension of the unit cell can be obtained via the indexing routine. With the help of the XPREP program (Table 2.2), the lattice centering and the presence of symmetry elements in the crystal structure can be determined from the systematic absences of certain reflections. However, the *phase* information is lost from reflection intensities as only the absolute value of the observed structure factors (F_o) can be derived from the measured reflection intensities (see E5). The phase angle (α_{hkl}) is unknown which leads to the so-called *phase problem*.

Structure solution: The *phase-problem* can be solved using a set of trial phases for the structure factors. One method is the *Patterson* method which needs the presence of at least one heavy atom in the unit cell, thus becoming very valuable in solving inorganic crystal structures.^[4] By using the experimental F_{hkl}^2 values as Fourier coefficients, a Fourier synthesis can be calculated. With this method, instead of obtaining the electron density distribution of the effective atomic positions, the Patterson function computes the end points of the atomic distance vectors. However, most crystal structures can nowadays be solved completely using *direct methods* which do not rely on the presence of heavy atoms or anomalous scatterers.^[5] With this method, the probable phase values is calculated and thus, creating a electron density map of unit cell. The SHELXS program implements both Patterson and direct methods (Table 2.2).

Structure refinement: The coordinates of the atomic positions from the structure solution are only approximate values because thermal motion/vibrations of the atoms have not been taken into account. The thermal motion is strongly dependent of the temperature, atomic mass and the bond strengths. A structural refinement is needed to enable the electron density of each atom to behave as a sphere around the atomic center. The factor which describes such thermal motion in spherical form is called *isotropic displacement parameter* (B). In order to further refine the thermal motion parameters to reflect a more probable ellipsoid form, an *anisotropic displacement parameter* can be applied which has six adjustable parameters.

To refine all these parameters, a computed set of structure factors (F_c) is compared with the absolute values of the observed factors (F_o) with a mathematical *least square* method. By

minimizing the sum of all the squared structure factor difference (E6), the parameters are varied to obtain the final optimal crystal structure. The weighting factor (w) provides the weight for each difference (Δ) as the standard deviation (σ) of strong reflections differs from the weak ones.^[6]

$$\sum_{hkl} w\Delta = \sum_{hkl} w \left(|F_o| - |F_c| \right)^2 = \text{minimum}, \quad w = 1/\sigma^2 \quad (\text{E6})$$

A typical crystal structure refinement requires the fulfillment of several criteria. The foremost criterion is the sensible bond distances between correctly assigned atoms. Secondly, the correctness and the precision of the structure refinement can be judged via several quality factors.

Figure of merits: The residual factors or R-factors are calculated to measure the discrepancy between the observed and calculated structure factors. For the conformity of symmetry equivalent reflections n , the internal R-factor (R_{int}) is used (E7). The deviation between the observed and calculated structure amplitudes is given by the conventional R-factor (R_1).^[7]

$$R_{int} = \frac{\sum_{i=1}^n \left| F_o^2 - \overline{F_o^2} \right|}{\sum_{i=1}^n F_o^2} \quad (\text{E7})$$

n : Nr. of reflections, $\overline{F_o^2}$: averaged square derived from symmetry equivalent reflections

$$R_1 = \frac{\sum_{hkl} \left| |F_o| - |F_c| \right|}{\sum_{hkl} |F_o|} \quad (\text{E8}) \quad wR_2 = \sqrt{\frac{\sum_{hkl} w (F_o^2 - F_c^2)^2}{\sum_{hkl} w (F_o^2)^2}} \quad (\text{E9})$$

To considering the weighting of each reflection, a weighted residual factor wR_2 is also calculated during the refinement routine of SHELXL and is directly minimized (E9). The R_1 and wR_2 factors are given for reflections with $F_o > n\sigma(F_o)$ ($n = 1, 2, 3, \dots$) or all reflections and in general, the lower the R -value, the better the structure refinement. The level of conformity between the structural parameters and the reflections is expressed as “Goodness of fit” (GoF), of which the value should be close to 1 for a correct and properly weighted structure refinement (E10).

$$GoF = \sqrt{\frac{\sum_{i=1}^n (F_o^2 - F_c^2)^2}{m-n}}, \quad m: \text{Nr. of independent reflections}, n: \text{Nr. of refined parameters} \quad (\text{E10})$$

2.4 Structure determination via X-ray powder diffraction

Not all crystal structures can be solved by single crystal X-ray diffraction due to the unavailability of suitable single crystals. Nevertheless, crystal structures can be routinely refined from powder diffraction data. Two requirements need to be fulfilled for this purpose; an already known structure model and good quality powder diffraction data. However, with the current advancement of computing technology, the starting structure model can also be determined directly from powder diffraction data. For example, the EXPO2009 program utilizes the same *direct methods* applied in single crystal structure solution as well as a combination with the *simulated annealing* (SA) optimization (Table 2.2).^[18] The SA approach randomly moves a given trial molecular fragment in the unit cell, adjusting its position, orientation and conformation in order to find a global optimum and thus giving the final molecule positions.

A major obstacle in structure determination from powder diffraction is the loss of spatial information as it is only a '*compressed*' one-dimensional plot of the reflections against scattering angle which leads to an overlap of the reflections. Once a structure model is obtained, either by structure solution or using an isostructural cell, the crystal structure refinement is carried out using *Rietveld methods*.^[8] This method analyzes not only the reflection positions and the intensities, but also the whole XRPD pattern. Prior to the introduction of the structural information for Rietveld refinement, the XRPD pattern can be decomposed into individual reflections and the unit cell parameters can be refined employing the structure independent *Le Bail* or *Pawley methods*.^[9,10,11] For the Rietveld refinement, the profile fitting of reflections is performed with for example Pseudo-Voigt or Pearson VII profile functions.^[6] Structural parameters such as cell parameters, atomic coordinates, site occupancy and thermal factors are also gradually refined until an optimal fit is obtained. The parameters such as background, texture correction and profile type can also be simultaneously refined. The atomic coordinate refinement can be kept to chemically sensible positions through the introduction of distance and angle restraints. The assessment of the structure refinement is conducted by judging at the R-factors, the difference plot of the two patterns and most importantly, sensible bond lengths. The commonly reported R-factors are the profile (R_p), weighted profile (R_{wp}) and Bragg (R_{Bragg}) factors (E11-13). The refinement of crystal structures from powder data in this work are performed using the TOPAS-Academic program (Table 2.2).

$$R_p = \frac{\sum_i |y_{io} - y_{ic}|}{\sum_i y_{io}} \quad (\text{E11})$$

$$R_{wp} = \sqrt{\frac{\sum_i w_i (y_{io} - y_{ic})^2}{\sum_i w_i y_{io}^2}} \quad (\text{E12})$$

y_{io}, y_{ic} : observed and calculated intensities at the i^{th} step, w_i : weighting factor

$$R_{\text{Bragg}} = \frac{\sum_i |I_o - I_c|}{\sum_i I_o} \quad (\text{E13})$$

I_o : observed intensity, I_c : calculated intensity,

Table 2.2 Summary of the software utilized for single crystal structure determination as well as structure solution and Rietveld refinement of crystal structures from X-ray powder diffraction (XRPD) data.

Tasks	Software	Remarks
Data collection	STOE X-Area ^[12]	Single crystal data collection
	STOE WinXPOW ^[13]	XRPD data collection
Data reduction	XPREP ^[14]	Data preparation & reciprocal space exploration
	STOE X-RED ^[15]	Data reduction for absorption correction
Structure solution	SHELXS ^[16]	Structure solution using direct or Patterson method
	STOE X-Step32 ^[15]	Single crystal structure software package
	SIR2008 ^[17]	Single crystal structure software package
	EXPO2009 ^[18] FOX ^[19]	Structure solution from X-ray powder data <i>Ab-initio</i> structure determination from powder data
Structure refinement	SHELXL ^[16]	Single crystal structure refinement
Absorption correction	STOE X-SHAPE ^[15]	Numerical absorption correction
Symmetry/space group check, handling disordered solvent contribution, CIF-publication check	PLATON ^[20]	Multi-purpose crystallographic tool
Crystal structure graphics	DIAMOND ^[21]	Visualization and graphical editing of crystal structures
Rietveld refinement	TOPAS-Academic ^[22]	Multi-purpose crystal structure determination package
X-ray powder pattern indexing	STOE WinXPOW	Indexing using TREOR ^[24] , ITO ^[25] and DICVOL ^[26] algorithms
	TOPAS-Academic ^[23]	Iterative singular value decomposition method
Structure modeling	EXPO2009	N-TREOR algorithm
	Materials Studio ^[27]	Geometry optimization of unit cell contents
Structure simulation	PowderCell ^[28]	Simulation of isomorphic subgroups
CIF editing	Encifer ^[29]	Verification of CIF files prior to database submission

References

-
- [1] L. E. Smart, E. A. Moore, *Solid state chemistry: an introduction*, **2005**, Taylor & Francis Group, Florida, USA.
- [2] A. Belsky, M. Hellenbrandt, V. L. Karen, P. Luksch, *Acta Cryst.* **2002**, *B58*, 364–369; http://www.fiz-karlsruhe.de/icsd_content.html.
- [3] F. H. Allen, *Acta Cryst.* **2002**, *B58*, 380–388; <http://www.ccdc.cam.ac.uk/index.php>
- [4] A. L. Patterson, *Phys. Rev.* **1934**, *46*, 372–376.
- [5] H. Hauptman, J. Karle, *Phys. Rev.* **1950**, *77*, 491–499.
- [6] W. Massa, *Kristallstrukturbestimmung*, **2007**, B. G. Teubner Verlag, Wiesbaden, Germany.
- [7] H. Krischner, *Einführung in die Röntgenfeinstrukturanalyse*, **1974**, Friedr. Vieweg & Sohn Verlag, Braunschweig, Germany.
- [8] H. M. Rietveld, *J. Appl. Cryst.* **1969**, *2*, 65–71.
- [9] A. Le Bail, H. Duroy, J. L. Fourquet, *Mat. Res. Bull.* **1988**, *23*, 447–452.
- [10] G. S. Pawley, *J. Appl. Cryst.* **1981**, *14*, 357–361.
- [11] H. Toraya, *The Rigaku Journal*, **1989**, *6*, 28–34.
- [12] X-Area version 1.44, **2008**, Stoe & Cie GmbH, Darmstadt, Germany.
- [13] WinXPOW version 2.11, **2005**, Stoe & Cie GmbH, Darmstadt, Germany.
- [14] XPREP version 5.1, **1997**, Bruker Analytical X-ray Systems, Madison, Wisconsin, USA.
- [15] X-RED version 1.19, X-SHAPE version 1.06, X-Step32 version 1.05b, **1999**, Stoe & Cie GmbH, Darmstadt, Germany.
- [16] G. M. Sheldrick, *Acta Cryst.* **2008**, *A64*, 112–122.
- [17] M. C. Burla, R. Caliendo, M. Camalli, B. Carrozzini, G. L. Cascarano, L. De Caro, C. Giacovazzo, G. Polidori, D. Siliqi, R. Spagna, *J. Appl. Cryst.* **2007**, *40*, 609–613.
- [18] A. Altomare, M. Camalli, C. Cuocci, C. Giacovazzo, A. Moliterni, R. Rizzi, *J. Appl. Cryst.* **2009**, *42*, 1197–1202.
- [19] V. Favre-Nicolin, R. Cerny, *J. Appl. Cryst.* **2002**, *35*, 734–743.
- [20] A. L. Spek, *J. Appl. Cryst.* **2003**, *36*, 7–13.
- [21] W. T. Pennington, *J. Appl. Cryst.* **1999**, *32*, 1028–1029.
- [22] A. A. Coelho, *TOPAS-Academic* version 4.1, **2007**, Coelho Software, Brisbane, Australia.
- [23] A. A. Coelho, *J. Appl. Cryst.* **2000**, *33*, 899–908.
- [24] P. E. Werner, L. Eriksson, M. Westdahl, *J. Appl. Cryst.* **1985**, *18*, 367–370.
- [25] J. W. Visser, *J. Appl. Cryst.* **1969**, *2*, 89.
- [26] A. Boultif, D. Louer, *J. Appl. Cryst.* **2004**, *37*, 724–731.
- [27] *Materials Studio* version 5.0, **2009**, Accelrys Inc. San Diego, CA, USA.
- [28] G. Nolze, W. Kraus, *Powder Diffr.* **1998**, *13*, 256–259.
- [29] F. H. Allen, O. Johnson, G. P. Shields, B. R. Smith, M. Towler, *J. Appl. Cryst.* **2004**, *37*, 335–338.

3 Experimental section

In this chapter the basic concepts behind the solvothermal synthesis of coordination polymers using conventional and microwave-assisted heating are explained. In the second section, the high-throughput method workflow will also be described in detail. The sections 3.2, 3.3 and 3.4 in this chapter will be published in the book “*Metal phosphonate chemistry: From Synthesis to Applications*” edited by A. Clearfield, K. Demadis in the chapter: “*High Throughput Methods for the Systematic Investigation of Metal Phosphonate Synthesis Fields*” written by me and Prof. Dr. Norbert Stock. These sections are reproduced with permission of The Royal Society of Chemistry (2012), Cambridge, United Kingdom.

3.1 Solvothermal synthesis

The origins of solvothermal process can be traced back to 19th century, where the formation of geological minerals has been investigated.^[1] One of the most important industrial application of this method is the synthesis of quartz and GaPO₄, which have piezoelectric properties. Other solvothermally synthesized materials include gemstones, magnetic pigments of CrO₂ and porous materials such as zeolites.

Solvothermal method for the synthesis of solid state materials is a type of high pressure solvent method in addition to high pressure gas and direct hydrostatic pressure methods.^[2,3] Solvothermal methods normally involve heating of reactants with the solvent inside a sealed vessel. The sealed vessel is typically a stainless steel autoclave with Teflon-lining to withstand the high pressure, temperature and possible corrosion of reactor materials. The definition of a solvothermal synthesis also states that the ‘synthesis temperature must be higher than the boiling point of the respective solvent’.^[4] Although the term solvothermal is valid for both aqueous and non-aqueous solutions, the term is used commonly for non-aqueous syntheses, for example with dimethylformamide (DMF) as solvent. The term hydrothermal is for aqueous solutions, for which the synthesis temperatures between 100 ° and 1000 °C is common. The autogenous pressure generated in the autoclaves can reach up to 150 bar.^[5] The main parameters controlling solvothermal reactions are chemical and thermodynamical parameters. The chemical nature of the solvent such as polarity and molecular size can decide the composition of the final product. Thermodynamical factors which affect solvothermal processes are temperature and pressure as well as reaction time. At very high temperature and pressure conditions, the dielectric constant, viscosity and density of the solvent decrease and thus, the solubility of organic compounds in the solvent is increased and thus rendering the reaction mixture more homogeneous as well as enhancing the crystal growth process. Compared to conventional solid state synthesis,

solvothermal reactions need much milder conditions due to sufficient reactant diffusion at lower temperatures and pressures. Reaction time also governs the final product formation, for example in the synthesis of Sb(III)Sb(V)O_4 crystals in ethylenediamine solvent, reaction time of one day prefers Sb(III)Sb(V)O_4 but after three days, metallic Sb particles are formed.^[6]

3.2 High-throughput technology

A convenient and efficient tool for investigations in the field of materials science is the high-throughput (HT) technology. The pharmaceutical industry has long embraced this method to conduct screening tests for drug discovery and drug design in order to reduce time and costs required in their research and development phase.^[7] The two important and relevant terms used in the literature are “combinatorial” and “high-throughput”. In combinatorial chemistry “a combinatorial process is used to prepare sets of compounds from sets of building blocks”.^[8] This approach is used in medicinal chemistry where a number of components are combined in a single pot reaction process to produce a mixture of compounds. On the other hand, the term high-throughput synthesis encompasses reactor arrays with individual miniaturized reaction vessels. For each reaction vessel an individual point in parameter space (defined by temperature, composition, pressure, etc.) can be investigated. Thus a diverse data library can be set up that allows the accelerated discovery as well as the optimization of new materials.^[9] By looking closely at high-throughput methods, the words automation, parallelization and miniaturization come into play, meaning that tasks will be rapidly and/or simultaneously performed and that small amounts of material are needed.^[10] The number of experiments to be performed increases dramatically in a multi-parameter system. Each molar ratio of starting materials can lead to a new product. For example, a solvothermal reaction of reactants A and B, whereby the molar fraction A : B is varied in 0.1 steps (0.1 to 0.9) leads to nine individual reactions. However, with the inclusion of a new reactant C and varying the molar fractions A : B : C in 0.1 steps (in the range of 0.1 – 0.9, sum of molar fractions of A + B + C = 1) already gives 36 reactions and 0.05 steps will then necessitate 171 individual reactions (calculated using E14-15).

$$n = \frac{(1-2x)}{x}, x = \text{step increments, i.e. } 0.05, 0.1 \text{ etc.} \quad (\text{E14})$$

$$\sum_{i=1}^n i = \frac{n}{2} \cdot (n+1) = \text{sum of individual reactions.} \quad (\text{E15})$$

Practically, conventional methods are not applicable for this large number of reactions but utilizing HT reactors this study can be performed in a day. Hence the HT methodology is an

efficient tool for finding new compounds, discovering reaction trends and optimizing synthesis conditions. Nonetheless, the goal of a high-throughput study is not to conduct as many reactions as possible, but rather to focus on relevant parameters in order to gain the maximum information of a certain experiment. Therefore, a well-thought-out design of experiments is needed since “A poorly designed experiment will give bad information with unprecedented speed and in outstanding quantity”.^[11]

3.3 High-throughput methods for solvothermal syntheses

Heterogeneous catalyst impregnation process, sol-gel and solvothermal synthesis are among the most important solvent-based processes, where HT-methods have been applied.^[12,13] Employing HT-solvothermal syntheses, i.e. reactions in enclosed containers at temperatures above the boiling point of the solvent and autogenous pressures, many new compounds such as zeolites, metal-phosphates, -carboxylates and -imidazoles have been discovered.^[14, 15, 16, 17] The harsh temperature and pressure conditions in solvothermal syntheses require the usage of durable and corrosion resistant materials as well as autoclaves. Most often Teflon[®]-lined steel autoclaves are used and maximum temperatures of around 200 °C and thereby, accomplishing autogenous pressure. While single reactors are commercially available and also easy to build, only few research groups have been able to construct multiclaves containing 24, 48 or even 100 miniaturized reaction chambers. One example of such a multiclave is shown in Figure 3.1. The multiclaves are comprised of miniaturized Teflon[®]-liners inserted into a 96-well-plate-based stainless steel block.^[14,18,19]



Figure 3.1 Stainless steel HT-multiclaves with 48- and 24-Teflon[®]-lined reaction chambers (120 mm x 80 mm) employed by the group of Stock.

3.4 High-throughput methodology

A typical high-throughput workflow is shown in Figure 3.2.^[20] It begins with the design of the experiments (Step 1). This could be done manually or with computer software depending on the complexity of the experiment. The next step is the preparation of the reaction mixtures (Step 2 & 3), which will be facilitated by an automated dosing station. It should be able to deliver precise amounts of powder or liquid in the mg- and μL -range into the designated reaction chambers. One fine example of a fully automated system employing a central robotic arm was described by Moliner *et al.* that handles liquid dosing, solid weighting, stirring and solvent evaporation.^[21] A more practical, semi-automated approach was described by Bein and Stock. These groups use tools based on the 96-well-plate-format for synthesis, characterization and storage of materials (Figure 3.2).^[22] The synthesis in 24 or 48 multiclaves (Step 4) is carried out in an oven with defined temperature program. Product isolation by filtration is done in a custom made filtration apparatus (Figure 3.3) and the subsequent automated characterization (Step 5 & 6) of the products is typically done by X-ray powder diffraction (XRPD) in a period of ~ 3 min per sample (Figure 3.4).^[23] The evaluation of these XRPD data (Step 7) can get complicated due to textural problems, preferred orientation of the crystalline product or the presence of phase mixtures. New methods have been discussed recently to identify phase mixtures from XRPD data.^[24]

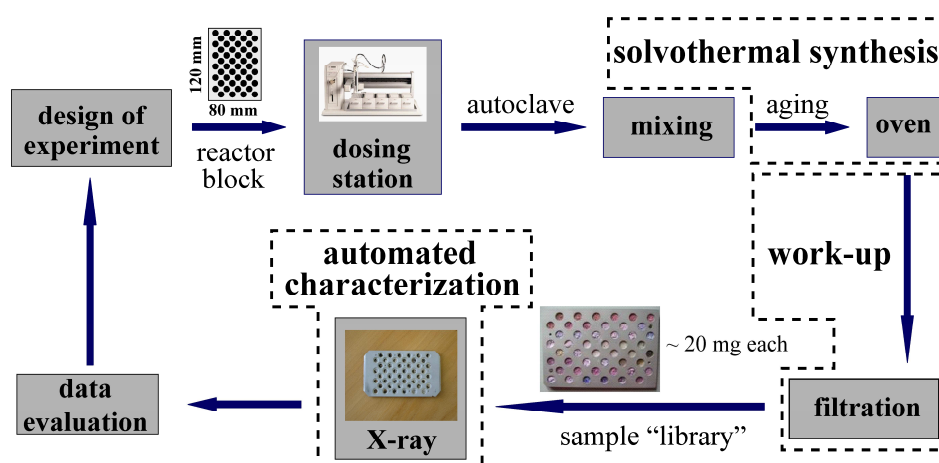


Figure 3.2 A typical HT workflow scheme for the synthesis and characterization of reactions under solvothermal conditions.^[20]

Most of the HT-investigations of metal phosphonates involve the study of three component systems usually a metal salt, the phosphonic acid ligand and the base ($M : H_xL : B$). Ternary plots, so-called crystallization diagrams are used to locate the molar composition of the reaction mixtures employed and to summarize the results of the investigation. Thus formation

fields of each individual compound can be determined. There are various approaches to the systematic investigation of such chemical systems, which is based on the results from previous investigations and literature data. Very often the molar ratio $M : H_xL$ has only a minor influence on the product formation while the acid/base content (pH) is the decisive factor in determining the product formation.

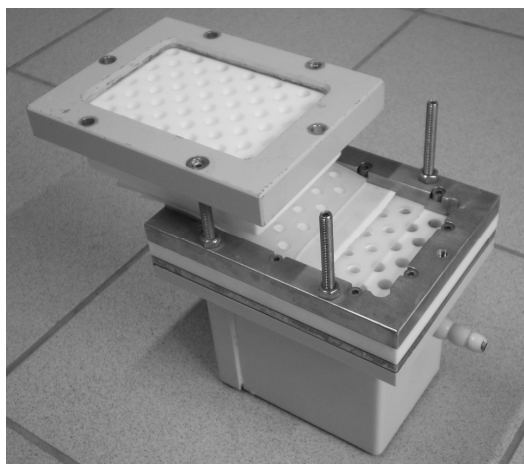


Figure 3.3 The assembly of the customized 48 sample HT filter unit used in the Stock group from top to bottom: lid, PTFE filter block, rubber gasket, filter paper, rubber gasket and reservoir for waste solvent. The whole block is fastened using four wing nuts on top of the lid. The filter block is connected to a vacuum line to achieve maximum filtration.

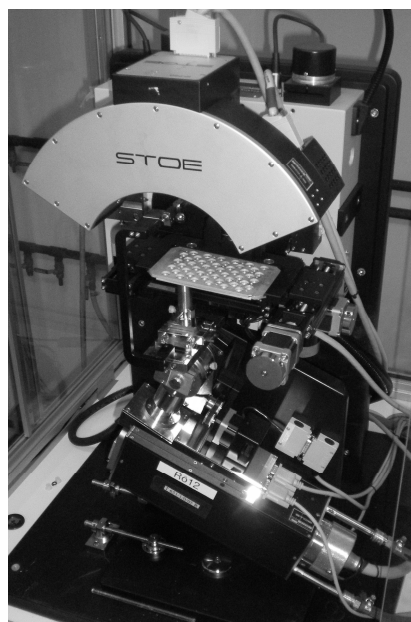


Figure 3.4 High-throughput (HT) X-ray powder diffractometer in transmission mode equipped with an automated 48 sample holder grid and curved image plate position sensitive detector (IPPSD). The measurement ranges are $2-50^\circ$ (2θ) and 3-15 min (time).

3.5 Microwave-assisted heating

The most commonly applied heating method in the solvothermal synthesis of metal-organic compound is conventional heating which is basically conducted in thermal ovens. The heat is generated from the heating elements is transferred to the surroundings via natural and/or forced air convection. Compared to such energy intensive conventional heating processes, a microwave-assisted (MW) heating method requires much less energy input.^[25] In order to MW heating to function, at least one component of the reaction mixture must absorb microwave radiation. In solvothermal synthesis, almost all the radiation is absorbed by the polar solvent medium. The solvents themselves can be classified into high (ethanol, dimethylsulfoxide), medium (water, DMF, acetic acid) or low radiation absorber (CHCl_3 , THF, toluene) depending on their so-called loss tangent ($\tan \delta$). $\tan \delta$ is the quotient of ϵ''/ϵ' , where ϵ'' is the dielectric loss (electromagnetic radiation heat conversion efficiency) and ϵ' is the dielectric constant (polarizability of molecules by electric field).^[26] There are two main effects behind microwave-assisted heating, namely the thermal (kinetic) effect and the non-thermal microwave effects. The thermal effects are caused by the *dipolar polarization* and *ionic conduction*.^[27] For the first case, the realignment of solvent molecule dipoles to the oscillating electric field and the molecular friction as well as collisions due to these movements generate heat which is also called dielectric heating. The other mechanism, *ionic conduction*, is caused by the oscillation of ionic particles in the solvent owing to the interaction with the electric field. Thus, the resulting collisions produce heat energy higher than dipolar polarization effect. The non-thermal microwave effects cannot be explained easily and are considered to be a on-going debate in the scientific community with many works being currently reported.^[28,29]

Recent developments have shown that microwave-assisted heating in solvothermal syntheses is slowly gaining ground mainly due to shorter reaction times. Other advantages of MW heating include phase selectivity, homogeneity in crystal morphology and high yields.^[30] Microwave based heating was first applied for the hydrothermal reactions of fine powdered metal oxides^[31], ceramic powders^[32], metal phosphates^[33] and zeolites^[34]. The first case of MW synthesis of metal-organic compound was reported by Liao *et al.* in 2001 whereby the compounds contain phosphorus- and nitrogen-based organic ligands.^[35] The report of metal cyclohexylphosphonates by Murugavel *et al.* in 2005 was one of the earliest record of metal phosphonate synthesized hydrothermally with MW heating.^[36] Gradually, MW based synthesis was also used to obtain porous metal-organic frameworks. Masel and co-worker reproduced IRMOF-1, -2 and -3, a zinc dicarboxylate based porous metal-organic frameworks^[37], with MW heating.^[38] Most importantly, they observed that all the crystals have

almost the same dimensions and the sizes can be regulated by varying the overall reaction mixture concentration. Nevertheless, the sizes of the single crystals yielded by microwave-assisted heating are too small for single crystal X-ray structure determination purposes. For this goal, the conventional heating stills offer the best solution yet. Khan *et al.* has observed with their work on HKUST-1^[39] synthesis that the MW radiation plays a bigger role in the nucleation step than the crystal growth.^[40] The group of Jung *et al.* has studied the influences of MW heating on phase selectivity with nickel glutarates and chromium benzenedicarboxylates.^[41,42] Their investigations have demonstrated that kinetically favored phases can be synthesized selectively with the help of MW heating.

Until now, microwave-assisted heating in combination with high-throughput (HT) methods have been implemented for the synthesis of organic compounds.^[43] In those investigations, the Synthos 3000 HT microwave unit from Anton Paar GmbH was frequently used where 24 glass vials can be placed in a silicon carbide (SiC) plate for the synthesis. A detailed study on the heating mechanism of SiC plate via internal temperature and thermoimaging measurements showed that only during the initial heating phase, both indirect heat transfer (*passive heating*) and direct microwave heating (*dielectric heating*) are involved. However, during the constant temperature regulation ramp, the major heating is contributed only by *passive heating* from SiC plate.^[44] The HT Synthos 3000 MW system with 24 sample SiC plate from Anton Paar is used in this work for the synthesis of nickel MOFs (Figure 3.5).

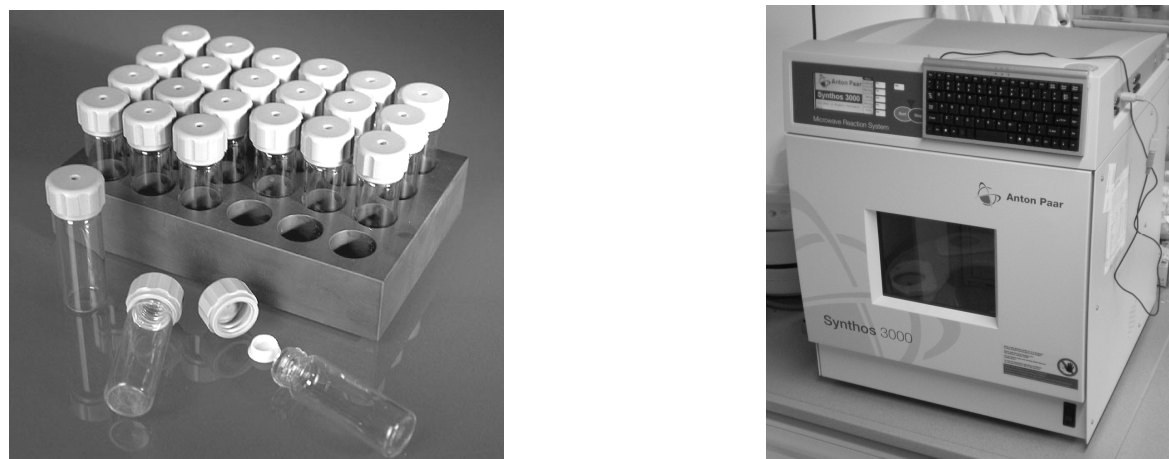


Figure 3.5 Borosilicate glass vials with lip type PTFE seals placed into 24 sample SiC plate (left). Synthos 3000 high-throughput microwave unit with 4 X 24 rotor and 1400 MW maximum power output (right).

References

- [1] H. de Sénarmont, *Ann. Chim. Phys.* **1851**, 32, 129-175.
- [2] H. Huppertz, *Z. Kristallogr.* **2004**, 219, 330-338.
- [3] T. C. Gibb, A. J. Herod, D. C. Munro, N. H. Peng, *J. Mater. Chem.* **1994**, 4, 1451-1455.
- [4] G. Demazeau, *J. Mater. Sci.* **2008**, 43, 2104-2114.
- [5] A. Rabenau, *Angew. Chem. Int. Ed. Engl.* **1985**, 24, 1026-1040; *Angew. Chem.* **1985**, 97, 1017-1032.
- [6] T. Ji, M. Tang, L. Guo, X. Qi, Q. Yang, H. Xu, *Solid State Commun.* **2005**, 133, 765-769.
- [7] D. L. Coffen, J. E. A. Luithle, *Handbook of Combinatorial Chemistry*, ed. K. C. Nicolaou, R. Hanco, W. Hartwig, **2002**, Wiley-VCH, Weinheim, Germany, p.10.
- [8] D. Maclean, J. J. Baldwin, V. T. Ivanov, Y. Kato, A. Shaw, P. Schneider, E. M. Gordon, *Pure Appl. Chem.* **1999**, 71, 2349-2365.
- [9] W. F. Maier, K. Stöwe, S. Sieg, *Angew. Chem. Int. Ed.* **2007**, 46, 6016-6067; *Angew. Chem.* **2007**, 119, 6122-6179.
- [10] N. Stock, *Microporous Mesoporous Mater.* **2010**, 129, 287-295.
- [11] J. N. Cawse, *Experimental Design for Combinatorial and High Throughput Materials Development*, ed. J. N. Cawse, **2003**, John Wiley & Sons, New York, USA.
- [12] U. Rodemerck, D. Wolf, O. V. Buyevskaya, P. Claus, S. Senkan, M. Baerns, *Chem. Eng. J.* **2001**, 82, 3-11.
- [13] K. Choi, D. Gardner, N. Hilbrandt, T. Bein, *Angew. Chem. Int. Ed.* **1999**, 38, 2891-2894; *Angew. Chem.* **1999**, 111, 3070-3073.
- [14] D. E. Akporiaye, I. M. Dahl, A. Karlsson, R. Wendelbo, *Angew. Chem. Int. Ed.* **1998**, 37, 609-611; *Angew. Chem.* **1998**, 110, 629-631.
- [15] Y. Song, J. Yu, G. Li, Y. Li, Y. Wang, R. Xu, *Chem. Commun.* **2002**, 1720-1721.
- [16] S. Bauer, C. Serre, T. Devic, P. Horjacadá, J. Marrot, G. Férey, N. Stock, *Inorg. Chem.* **2008**, 47, 7568-7576.
- [17] R. Banerjee, A. Phan, B. Wang, C. Knobler, H. Furukawa, M. O'Keeffe, O. M. Yaghi, *Science*, **2008**, 319, 939-943.
- [18] J. Klein, C. W. Lehmann, H.-W. Schmidt, W. F. Maier, *Angew. Chem. Int. Ed.* **1998**, 37, 3369-3372; *Angew. Chem.* **1998**, 110, 3557-3561.
- [19] N. Stock, T. Bein, *Solid State Sci.* **2003**, 5, 1207-1210.
- [20] S. Bauer, N. Stock, *Chem. Unserer Zeit*, **2007**, 41, 390-398.
- [21] M. Moliner, J. M. Serra, A. Corma, E. Argente, S. Valero, V. Botti, *Microporous Mesoporous Mater.* **2005**, 78, 73-81.
- [22] N. Stock, T. Bein, *Angew. Chem. Int. Ed.* **2004**, 43, 749-752; *Angew. Chem.* **2004**, 116, 767-770.
- [23] STOE Stadi P Combi X-Ray Powder Diffractometer, STOE & Cie GmbH, Darmstadt, Germany.
- [24] L. A. Baumes, M. Moliner, M. Nicoloyannis, A. Corma, *CrystEngComm.* **2008**, 10, 1321-1324.
- [25] K. Y. Choi, G. Tompsett, W. C. Conner, *Green Chem.* **2008**, 10, 1313-1317.

- [26] A. C. Metaxas, R. J. Meredith, *Industrial Microwave Heating*, **1983**, Peter Perigrinus Ltd., London, England.
- [27] C. O. Kappe, A. Stadler, *Microwaves in Organic and Medicinal Chemistry*, **2005**, Wiley-VCH, Weinheim, Germany.
- [28] M. A. Herrero, J. M. Kremsner, C. O. Kappe, *J. Org. Chem.* **2008**, *73*, 37-47.
- [29] A. de la Hoz, Á. Díaz-Ortiz, A. Moreno, *Chem. Soc. Rev.* **2005**, *34*, 164-178.
- [30] J. Klinowski, F. A. Almeida Paz, P. Silva, J. Rocha, *Dalton Trans.* **2011**, *40*, 321-330.
- [31] S. Komarneni, R. Roy, Q. H. Li, *Mater. Res. Bull.* **1992**, *27*, 1393-1405.
- [32] S. Komarneni, Q. Li, K. M. Stefansson, R. Roy, *J. Mater. Res.* **1993**, *8*, 3176-3183.
- [33] S. Komarneni, Q. H. Li, R. Roy, *J. Mater. Chem.* **1994**, *4*, 1903-1906.
- [34] X. Querol, A. Alastuey, A. Lopezsoler, F. Plana, J. M. Andres, R. Juan, P. Ferrer, C. R. Ruiz, *Environmental Sci. Technol.* **1997**, *31*, 2527-2533.
- [35] J. H. Liao, P. L. Chen, C. C. Hsu, *J. Phys. Chem. Solids*, **2001**, *62*, 1629-1642.
- [36] R. Murugavel, P. Davis, M. G. Walawalkar, *Z. Anorg. Allg. Chem.* **2005**, *631*, 2806-2811.
- [37] M. Eddaoudi, J. Kim, N. Rosi, D. Vodak, J. Wachter, M. O'Keeffe, O. M. Yaghi, *Science*, **2002**, *295*, 469-472.
- [38] Z. Ni, R. I. Masel, *J. Am. Chem. Soc.* **2006**, *128*, 12394-12395.
- [39] S. S.-Y. Chui, S. M.-F. Lo, J. P. H. Charmant, A. Guy Orpen, I. D. Williams, *Science*, **1999**, *283*, 1148-1150.
- [40] N. A. Khan, E. Haque, S. H. Jhung, *Phys. Chem. Chem. Phys.* **2010**, *12*, 2625-2631.
- [41] S. H. Jhung, J. H. Lee, P. M. Forster, G. Férey, A. K. Cheetham, J. S. Chang, *Chem.–Eur. J.* **2006**, *12*, 7899-7905.
- [42] N. A. Khan, S. H. Jhung, *Cryst. Growth. Des.* **2010**, *10*, 1860-1865.
- [43] M. Treu, T. Karner, R. Kousek, H. Berger, M. Mayer, D. B. McConnell, A. Stadler, *J. Comb. Chem.* **2008**, *10*, 863-868.
- [44] M. Damm, C. O. Kappe, *Mol. Diversity*, **2009**, *13*, 529-543.

4 Cumulative section

The following sections give an overview of the class of inorganic-organic hybrid materials investigated for this thesis. In the following sections 4.1-4.2, a list of known metal phosphonosulfonates in the literature is given in order to gather information on the synthesis methods, structural diversity and trends of this type of materials. In the section 4.4 in this chapter, a short overview on porous metal-organic frameworks is presented and the importance of paddle-wheel based structures is discussed.

4.1 From metal phosphonates to metal phosphonosulfonates

The interest on metal phosphonosulfonates originates from the research of metal diphosphonates and therefore, the field of metal phosphonates must be discussed first. Phosphonic acid linkers are employed with various metal ions via hydrothermal synthesis to obtain crystalline structures with different structural features. One of the reasons behind the structural diversity is due to the increased number of coordinating atoms compared to amines and carboxylate ligands. The high acidity of phosphonic acid also contributes to the formation of extensive hydrogen bonds and thus, increasing the number of structural possibilities. One of the pioneers in the metal phosphonate chemistry is the group of Clearfield.^[1] They started with the investigation of metal phosphates and gradually expanded their work to metal phosphonates by mostly working with tetravalent metal ions to create inorganic-organic hybrid materials. By using pillaring diphosphonic acid linkers, porous materials can be obtained. The porous metal phosphonates with layered and three-dimensional structural motifs possess acid sites that can be used for catalytic and proton conducting purposes.^[2] In addition, the layered structures also provide the basis for intercalation investigations whereby the interlayer distances are increased via the insertion of amines.^[3] The structures of most metal phosphonates can be generalized into some basic types. The oxygen atoms from single phosphonate group bond with different metal ions leading to inorganic $-(M-O-P-O-M)-$ layers and thus forcing the organic groups to orient themselves into pillared arrangement. No porosity is achieved due to the narrow lamellar packing in the self-assembled pillared arrangement.^[4] One of the several methods to induce accessible channels in the metal phosphonates is the use of small coordinating ions such as phosphate. In this case, an alternating phosphonate/phosphate configuration in the inorganic layer forms gaps due to the now periodically absent organic groups in the pillaring region.^[3,5] Another way to induce porosity is by employing different metal ions other than M^{4+} which can lead to other coordination geometries and thus lead to new crystal structures. Metal ions with lone electron pairs such as Sn^{2+} , Sb^{3+} and Pb^{2+} led to frameworks with narrow voids, for

example in the structures of $[\text{Sn}_4(\text{O}_3\text{PCH}_2\text{CH}_2\text{CO}_2)_2(\text{C}_2\text{O}_4)]$, $[\text{Sb}_2\text{O}(\text{O}_3\text{PCH}_2\text{PO}_3)]$ and $[\text{Pb}_3(\text{O}_2\text{CCH}_2\text{CH}_2\text{PO}_3)_2]$ [6,7,8] Open-framework structures were obtained with Ni^{2+} , Cu^{2+} and Zn^{2+} [9,10,11].

Using polyfunctionalized phosphonic acids, different connectivities in metal phosphonates can be expected compared to using only polyphosphonic acid linkers. Examples of other functional groups that complement phosphonic acid are hydroxyl, amines and carboxylic acid. Isorecticular hydroxy functionalized metal phosphonates $[\text{M}(\text{O}_3\text{PCH}_2\text{OH})]$ with divalent Zn, Co, Cu and Mn ions highlight the possibility of obtaining highly symmetrical metal phosphonate structures with cylindrical channels.^[12] Similar cylindrical channels were also observed in with $[\text{Zn}(\text{O}_3\text{PC}_2\text{H}_4\text{NH}_2)]$ that incorporates an amino functionalized phosphonate linker.^[13] Lin and co-workers have employed 4-pyridinephosphonic acid as linker and the resulting open-framework structure of $[\text{Cu}_2(\text{NC}_5\text{H}_4\text{PO}_3)_2] \cdot 2\text{H}_2\text{O}$ has four-fold coordination to metal ions resembling square planar coordination geometry.^[14] The earliest report of metal carboxyphosphonate was in 1985 whereby the structure of $[\text{Cu}_3(\text{O}_2\text{C}_3\text{H}_4\text{PO}_3)_2(\text{H}_2\text{O})] \cdot 6\text{H}_2\text{O}$ was obtained which exhibits one-dimensional channels.^[15] Using a trifunctional linker, glyphosate ($\text{HO}_2\text{CCH}_2\text{NHCH}_2\text{PO}_3\text{H}_2$), an extensively hydrogen-bonded layered Ca^{2+} -based structure was synthesized.^[16] Our group has intensively worked within the area of carboxyphosphonates and obtained diverse structures with the help of high-throughput (HT) methods. HT hydrothermal synthesis delivered a series of zinc(II) (phosphonomethyl)-benzoates of which the formation field of each compound was determined to be dependent on the pH values and the overall concentration.^[17] Further investigations with a tripodal linker, 5-phosphonobenzene-1,3-dicarboxylic acid resulted in four different crystal structures with varying coordination modes mainly due to different deprotonation states of the linker.^[18] HT reaction temperature screening of 4-(bis(phosphonomethyl)aminomethyl)benzoic acid with Cd^{2+} ions generated seven different phases whose formations are strongly regulated by pH and reaction temperatures.^[19]

Although several metal phosphonates with void channels were synthesized, none of them has any effective microporosity. Hence, the discovery of adsorptive molecules accessible structures was a huge challenge. A breakthrough was reported by Alberti's group in 1993 where a zirconium-based mixed phosphonate-phosphite $\text{Zr}(\text{HPO}_3)_{1.33}(\text{O}_3\text{P}-\text{Me}_2\text{H}_2\text{C}_6-\text{C}_6\text{H}_2\text{Me}_2-\text{PO}_3)_{0.33}$ compound was obtained and nitrogen sorption experiment has confirmed the microporosity.^[20] Nevertheless, only a structure model was reported due to insufficient long range order in the crystal structure. Maeda and his group in 1997 discovered aluminium methylphosphonates but the microporosity is quite low compared to other known microporous materials.^[21] Higher specific surface areas of up to $400 \text{ m}^2/\text{g}$ were gained with a

series of aluminium 4,4'-biphenylphosphonates^[22] and the continued work with Al³⁺ ions and a flexible linker, *N,N'*-piperazinebismethylphosphonic acid yielded a microporous compound (MIL-91).^[23] The MIL-91 structure with well defined one-dimensional pores was not only obtained with Al³⁺, but also with Ti⁴⁺ ions. Remarkably, a completely different microporous structure [M₂(H₂O)₂-(O₃PCH₂-NC₄H₈N-CH₂PO₃)]·5.4H₂O with larger (> 7 Å) one-dimensional hexagonal pores is obtained by using the same linker and divalent ions, M = Fe²⁺, Ni²⁺, Co²⁺.^[24] In order to get a similar structure near to the mesoporous region (~ 20 Å), isorecticular synthesis was utilized by employing an extended linker, *N,N'*-4,4'-bipiperidinebis(methylenephosphonic acid) with Ni²⁺ and Co²⁺ ions.^[25]

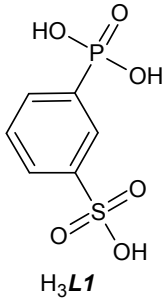
Polyfunctionalized phosphonic acid linkers have until now shown a great deal of structural diversity mainly due to the different functional groups. Another type of polyfunctional linker which has been less intensively investigated contains phosphonic and sulfonic acid groups. Sulfonate groups are considered to be weaker coordinating ligand compared to phosphonate groups.^[26] Often phosphonate groups define the coordination modes in the M-O clusters in the compound while the sulfonate ions are just involved in hydrogen bondings.^[27] The difference in coordinating strengths may also be explained by the lower negative charge of R-SO₃⁻ compared to R-PO₃²⁻. The initial research momentum in the field of metal phosphonosulfonates was also dampened due to difficulties in obtaining pure-phase phosphonosulfonic acid linkers. Post-synthetic sulfonation treatment of metal phenylmonophosphonate in fuming SO₃ yielded zirconium phosphonatobenzenesulfonate which was poorly crystalline and intricate to characterize.^[28] An alternative effort was taken by Squarrito *et al.* by using a pre-sulfonated phosphonic acid directly for the synthesis.^[29] The structure determination of the resulting single crystals of [Ni(NH₃)₂(H₂O)₄]₃⁻(O₃SC₆FH₃CH₂PO₃)₂·4H₂O showed that the Ni²⁺ ions are coordinated by water and NH₃ molecules but not by the linker. In a another study with 5-phosphonobenzene-1,3-disulfonic acid, various barium salts were isolated of which the phosphonate ions were partially deprotonated and these groups played a influential role in proton conductivity.^[30] Although no coordination of sulfonate groups to metal ions is observed, these studies laid the foundation for the subsequent studies.

4.1.1 Metal 3-Phosphonatobenzenesulfonates

Sulfonation of phenylphosphonic acid leads to the formation of the rigid linker, 3-phosphonobenzenesulfonic acid (H₃L1)^[31] and Mao *et al.* begun their work on a series of new metal phosphonates. New compounds were synthesized on the basis of Zn²⁺, Ln³⁺ (lanthanoid), Cd²⁺, Mn²⁺, Cu²⁺, Pb²⁺, Y³⁺ ions and mostly, in the presence of amine ligands

such as 1,10-phenanthroline (*phen*) and 4,4'-bipyridine (*bipy*) (Table 4.1). The use of the chelating and large *phen* ligand restricts the coordination possibilities and thus, most of the compounds incorporating *phen* ligands are comprised of isolated polynuclear clusters. Three-dimensional (3D) networks are generated with the use of only H₃L1 acid or in combination with *bipy* as the co-ligand. Interestingly, some of the 3D structures have narrow channels occupied by water molecules, however no porosity measurement was reported. In the following sections, the structural details of selected compounds based on H₃L1 are discussed.

Table 4.1 List of metal 3-phosphonatobenzenesulfonates. *phen* = 1,10-phenanthroline, *bipy* = 4,4'-bipyridine, * = formation of 3D network via extensive hydrogen bonding.

Linker	Compound	Network type / nuclearity	Lit.
 H ₃ L1	[Zn(<i>phen</i>) ₃] ₂ [Zn ₄ (L1) ₄ (<i>phen</i>) ₄]·20H ₂ O	0D / ZnN ₆ , Zn ₂ N ₄ O ₅	32
	[Zn ₆ (L1) ₄ (<i>phen</i>) ₈]·11H ₂ O	0D / ZnN ₄ O, Zn ₂ N ₄ O ₅	
	[Zn ₆ (L1) ₄ (<i>bipy</i>) ₆ (H ₂ O) ₄]·18H ₂ O	3D / ZnN ₃ O ₃ , ZnN ₂ O ₂ , ZnNO ₃	
	[La ₂ (L1) ₂ (<i>phen</i>) ₄ (H ₂ O)]·4.5H ₂ O	1D / LaN ₄ O ₄ , La ₂ N ₆ O ₈	33
	[Ln ₂ (L1) ₂ (<i>phen</i>) ₂ (H ₂ O) ₅]·3H ₂ O, Ln = Nd, Eu, Er.	0D / LnN ₂ O ₆ , LnN ₄ O ₁₀	
	[Cd ₄ (L1) ₂ (<i>phen</i>) ₆ (Cl) ₂ (H ₂ O) ₂]·14H ₂ O	0D * / Cd ₄ Cl ₂ N ₁₂ O ₆	34
	[Cd ₆ (L1) ₄ (<i>phen</i>) ₈]·14H ₂ O	0D * / Cd ₆ N ₁₆ O ₁₂	
	[Cd ₃ (L1) ₂ (<i>bipy</i>) ₃ (H ₂ O) ₆]·4H ₂ O	3D / CdN ₂ O ₄ , Cd ₂ N ₄ O ₆	
	[Mn ₂ (HL1) ₂ (<i>phen</i>) ₄][Mn ₂ (HL1) ₂ (<i>phen</i>) ₄ (H ₂ O)] ₂ ·6H ₂ O	0D * / MnN ₄ O ₂	35
	[Mn ₄ (L1) ₂ (<i>phen</i>) ₈ (H ₂ O) ₂][ClO ₄] ₂ ·3H ₂ O	0D * / MnN ₄ O ₂	
[Mn(<i>phen</i>)(H ₂ O) ₄] ₂ [Mn ₄ (L1) ₄ (<i>phen</i>) ₄]·10H ₂ O	0D * / Mn ₄ N ₈ O ₁₀ , MnN ₂ O ₄		
[Mn ₆ (L1) ₄ (<i>phen</i>) ₈ (H ₂ O) ₂]·4H ₂ O	0D * / Mn ₄ N ₈ O ₁₀ , MnN ₄ O ₂		
[Mn ₆ (L1) ₄ (<i>phen</i>) ₈ (H ₂ O) ₂]·24H ₂ O	0D * / MnN ₄ O ₂ , Mn ₂ N ₄ O ₅		
[Mn ₆ (L1) ₄ (<i>phen</i>) ₆ (H ₂ O) ₄]·5H ₂ O	1D * / MnN ₂ O ₄ , Mn ₄ N ₈ O ₁₀		
[Cu(HL1)(<i>bipy</i>)(H ₂ O)]	2D * / CuN ₂ O ₃	36	
[Pb ₃ (L1) ₂ (H ₂ O) ₂]·4H ₂ O	3D / Pb ₃ O ₁₂	37	
[Pb(HL1)(<i>phen</i>)]·H ₂ O	2D * / Pb ₂ N ₄ O ₆		
[Pb ₆ (L1) ₄ (<i>phen</i>) ₈]·3H ₂ O	0D / Pb ₆ N ₁₆ O ₁₂		
[Pb ₆ (L1) ₄ (<i>phen</i>) ₁₀]·2H ₂ O	0D / Pb ₆ N ₂₀ O ₁₂		
[Pb ₆ (L1) ₄ (<i>bipy</i>)(H ₂ O) ₂]·2H ₂ O	3D / (Pb ₃ NO ₁₄) _∞ chain		
[Cu(HL1)(<i>phen</i>)]·0.5H ₂ O	1D / CuN ₂ O ₃	38	
[Y(L1)(<i>phen</i>)(H ₂ O) ₂]·2H ₂ O	1D * / YN ₂ O ₅		

0D-network: Synthesis of metal phosphonosulfonates with *phen* as the co-ligand often generates isolated -M-O/N-M- clusters and a good example of this type of structure is observed for $[\text{Nd}_2(\mathbf{L1})_2(\text{phen})_2(\text{H}_2\text{O})_5] \cdot 3\text{H}_2\text{O}$ ^[33] (Table 4.1). Lanthanoid ions, in this case, Nd^{3+} ions are eight-coordinated by N-atoms from the chelating *phen* ligand and O-atoms from the phosphonate groups as well as ligating water molecules (Figure 4.1). The sulfonate groups do not coordinate to the metal ions but instead they are only involved in hydrogen bonding with water molecules.

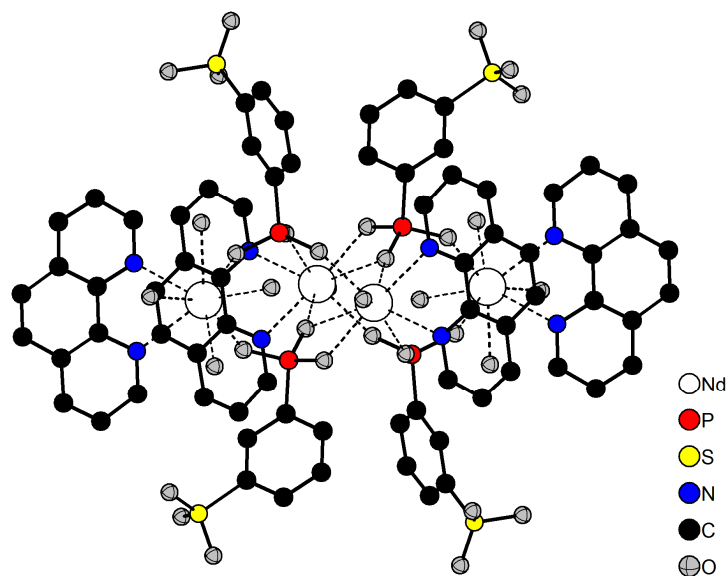


Figure 4.1 Tetranuclear cluster is observed in $[\text{Nd}_2(\mathbf{L1})_2(\text{phen})_2(\text{H}_2\text{O})_5] \cdot 3\text{H}_2\text{O}$. ^[33] Sulfonate groups do not coordinate to metal ions and point away from the cluster. The clusters are interconnected via hydrogen bonding between the sulfonate ions to ligating water molecules of other clusters. Coordinative bonds are marked by broken lines.

1D-network: The usage of *phen* co-ligand has also produced one-dimensional chains by the interconnection of mononuclear MnN_2O_4 and tetranuclear $\text{Mn}_4\text{N}_8\text{O}_{10}$ clusters via sulfonate groups in the compound $[\text{Mn}_6(\mathbf{L1})_4(\text{phen})_6(\text{H}_2\text{O})_4] \cdot 5\text{H}_2\text{O}$. ^[35] All phosphonate oxygen atoms coordinate to Mn^{2+} ions but only one oxygen atom of the sulfonate group participates in the coordination and the remaining oxygen atoms form hydrogen bonds with water molecules (Figure 4.2). This shows that *phen* co-ligands still restrict the coordination of the sulfonate groups similar to the 0D-network of $[\text{Nd}_2(\mathbf{L1})_2(\text{phen})_2(\text{H}_2\text{O})_5] \cdot 3\text{H}_2\text{O}$ in Figure 4.1.

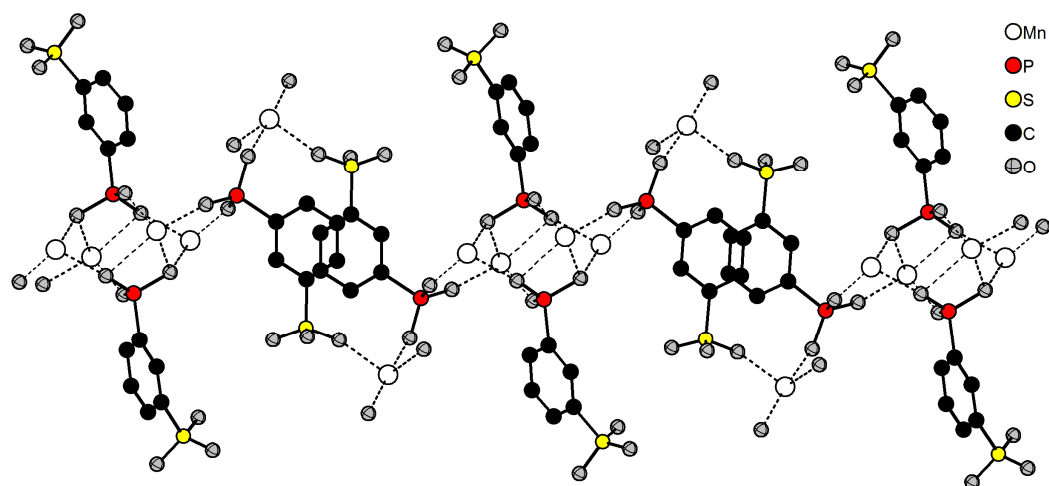


Figure 4.2 1D chain network observed in the crystal structure of $[\text{Mn}_6(\text{L1})_4(\text{phen})_6(\text{H}_2\text{O})_4] \cdot 5\text{H}_2\text{O}$.^[35] The chelating *phen* co-ligands are left out for clarity and the coordinative bonds are marked by broken lines.

2D-network: Only one compound with a layered structure was reported in the literature containing the $\text{H}_3\text{L1}$ linker and *phen* as the co-ligand.^[37] In $\text{Pb}(\text{HL1})(\text{phen}) \cdot \text{H}_2\text{O}$, Pb^{2+} ions are sixfold coordinated to form a distorted pentagonal pyramid and the lone pair of electrons plays also an important role in the formation of 1D chains of $\text{Pb}_2\text{N}_4\text{O}_6$ clusters interconnected by the phosphonate groups. These chains are further linked to other each other by the $(\text{HL1})^{2-}$ linkers (Figure 4.3). The weaker coordination of the oxygen atoms from the sulfonate groups can be observed by comparing the Pb-O bond lengths. The Pb-O bond involving the SO_3^- groups exhibits a bond length of 2.819(6) Å while the phosphonate based Pb-O bonds are shorter, between 2.550(5) and 2.727(4) Å.

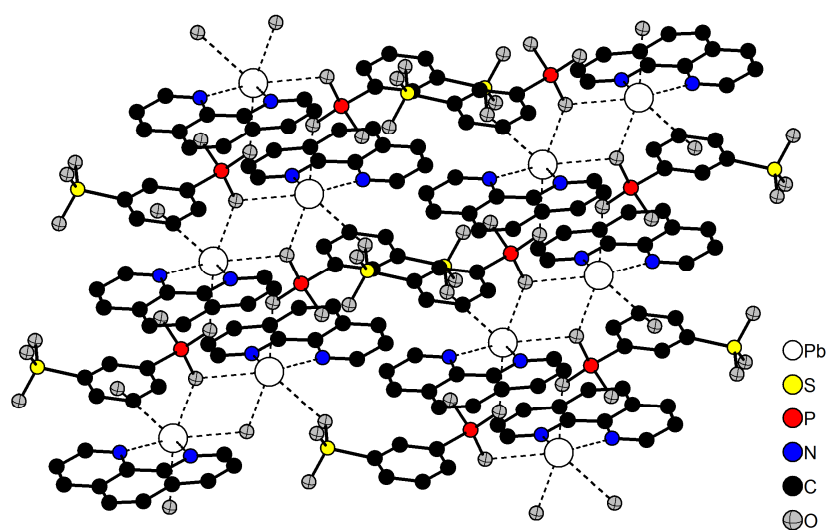


Figure 4.3 $\text{Pb}_2\text{N}_4\text{O}_6$ clusters and $(\text{HL1})^{2-}$ ions are interconnected to form a layered network in $\text{Pb}(\text{HL1})(\text{phen}) \cdot \text{H}_2\text{O}$. The coordinative Pb-O/N bonds are marked by broken lines.

3D-network: So far H_3L1 linkers only lead to three-dimensional frameworks when the *phen* co-ligand is not employed. A good example of such structure is observed for $[Pb_3(L1)_2(H_2O)_2] \cdot 4H_2O$.^[37] It is built of Pb_3O_{12} clusters which are cross-linked to each other by $(L1)^{3-}$ ions to construct a three-dimensional network (Figure 4.4). The completely deprotonated $(L1)^{3-}$ ion coordinates to Pb^{2+} ions as a μ_8 -linker and interestingly, this time all O-atoms from the sulfonate and the phosphonate groups coordinate to metal ions. Narrow voids occupied by H_2O molecules are observed and a total solvent accessible space of about 24 % of the unit cell was calculated, but no water sorption experiment was reported. The Pb-O bonds originating from sulfonate groups vary between 2.659(5) and 2.797(5) Å and are considerably longer than the Pb-O bonds stemming from phosphonate groups which lie in the range of 2.362(5) to 2.592(4) Å. $[Zn_6(L1)_4(bipy)_6(H_2O)_4] \cdot 18H_2O$ and $[Cd_3(L1)_2(bipy)_3(H_2O)_6] \cdot 4H_2O$ also exhibit 3D networks.^[32,34] In all these compounds with 3D-network, the O-atoms from the sulfonate groups do not coordinate to the metal ions (Table 4.1).

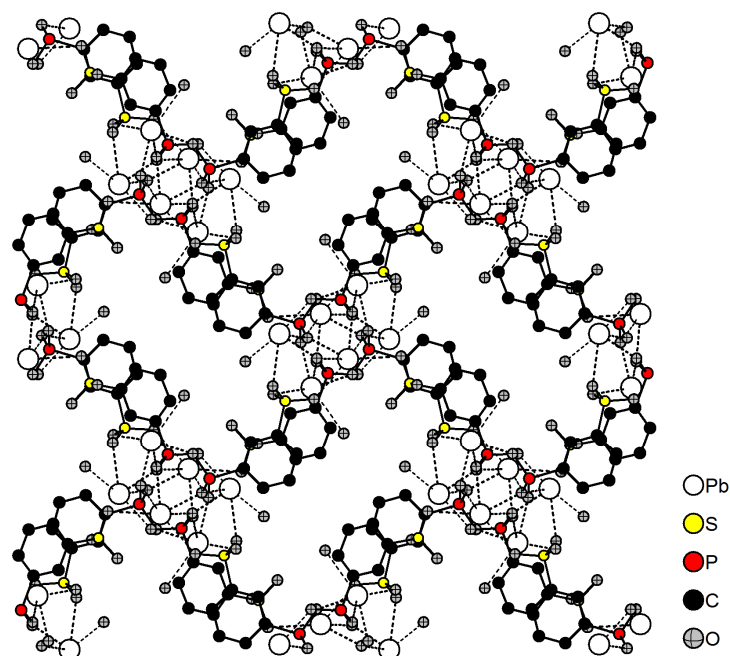


Figure 4.4 A section of the $[Pb_3(L1)_2(H_2O)_2] \cdot 4H_2O$ crystal structure along the *a*-axis.^[37] Non-coordinating water molecules and H-atoms are omitted for clarity. The coordinative Pb-O bonds are marked by broken lines.

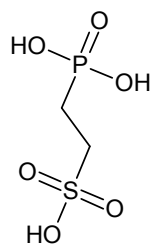
In general, it can be concluded that the presence of co-ligands especially *phen* severely restrict the formation of multidimensional networks. Most crystal structures with 3-phosphonobenzenesulfonic acid as linker generated metal clusters and the sulfonate groups do not take part in the metal coordination, but instead, only contribute to weak hydrogen bonding with water molecules. In the structures without 1,10-phenanthroline co-ligands, no chelating effect is observed and therefore, the assembly of 2D and 3D networks is promoted (Table 4.1).

4.1.2 Metal Phosphonatoalkylsulfonates

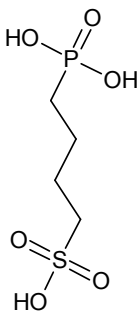
Our group has worked intensively with metal phosphonosulfonates in the recent years. Two types of linkers with alkyl groups were synthesized for the investigation of metal phosphonatoalkylsulfonates; 2-phosphonoethanesulfonic (H_3L2) and 4-phosphonobutane-1-sulfonic (H_3L3) acid (Table 4.2). The H_3L2 and H_3L3 linkers were synthesized using a previously reported procedure involving a two-step nucleophilic substitution of 1,2-dibromoethane and 1,4-dibromobutane respectively, with triethylphosphite and sodium sulfite.^[39] Such flexible linkers can theoretically produce diverse new structures depending on the conformation of the alkyl groups. In his Ph.D thesis work with H_3L2 and H_3L3 linkers, A. Sonnauer has employed various trivalent lanthanoid ions, Ba^{2+} , Sr^{2+} and Cu^{2+} ions without using co-ligands.^[40] Most importantly, high-throughput methods were applied to study the formation fields of each compound systematically. His thesis also concerns the investigation of the influences of the ionic charge and radii as well as the sulfonate group connectivities on the crystal structure network types. In the following sections, the structural details of selected studies based on H_3L2 and H_3L3 linker are discussed.

Table 4.2 List of metal phosphonatoalkylsulfonates. * = formation of 3D network via extensive hydrogen bonding. Sum formulas without square brackets indicate that the crystal structure of the compound have not been determined.

Linker	Compound	Network type / nuclearity	Lit.
	$[Ln(L2)(H_2O)]$, Ln = La, Ce, Pr, Nd, Sm, Eu, Gd, Tb, Dy	3D / $(LnO_8)_\infty$ chain	41
	$[Ca(HL2)(H_2O)_2]$	2D * / $(CaO_7)_\infty$ chain	
	$[Sr(HL2)]$	3D / $(SrO_8)_\infty$ chain	42
	$[Ba_2(HL2)_2]$	3D / $(Ba_2O_{14})_\infty$ layer	
	$[Ba(HL2)]$	3D / $(BaO_8)_\infty$ chain	43
	$[Cu_2(L2)(OH)(H_2O)_2] \cdot 3H_2O$	2D * / $(CuO_6)_\infty$ chain	44
	$[Er_2(L2)(OH)_3(H_2O)] \cdot H_2O$	2D * / $(ErO_8)_\infty$ layer	45
	$[Ln(L2)]$, Ln = Ho, Er, Tm, Yb, Lu, Y	3D / LnO_6	46
	$[Cu_2(L2)(OH)(H_2O)] \cdot H_2O$	3D / $(CuO_6)_\infty$ chain	
	$[Cu_{2.5}(L2)(OH)_2]$	3D / $(CuO_6)_\infty$ layer	
	$Cu_{1.5}(L2)(H_2O)_2$	-	47
	$NaCu(L2)(H_2O)_3$	-	
	$[Cu_{1.5}(L2)(H_2O)]$	2D * / Cu_3O_{12}	
	$[Sr_3(L2)_2(H_2O)_2]$	3D / $(SrO_8)_\infty$ layer	48



H_3L2

 <p>H₃L₃</p>	[Cu _{1.5} (L ₃)(H ₂ O)]·1.15H ₂ O	2D * / Cu ₃ O ₁₂	49
	[Cu _{2.5} (L ₃)(OH) ₂]	3D / (CuO ₆) _∞ layer	
	[Ln(L ₃)(H ₂ O)], Ln = La, Ce, Pr, Nd, Sm, Eu, Gd	3D / (LnO ₈) _∞ chain	50

Lanthanoid Phosphonatoethanesulfonate

In the synthesis involving trivalent lanthanoid rare earth metal (including Y³⁺ ion) and 2-phosphonoethanesulfonic acid (H₃L₂), two series of isotypic structures were obtained. The general formula of [Ln(L₂)(H₂O)]^[41] was obtained with La, Ce, Pr, Nd, Sm, Eu, Gd, Tb, Dy and a different compound, [Ln(L₂)]^[46] was observed with Ho, Er, Tm, Yb, Lu, Y. In [Ln(L₂)(H₂O)], the Ln³⁺ ions are eightfold coordinated by the oxygen atoms to form distorted square antiprismatic LnO₈ polyhedra while in [Ln(L₂)] the Ln³⁺ ions are sixfold coordinated. Although all O-atoms of the phosphonate groups coordinatively bind to Ln³⁺ ions, only two sulfonate oxygen atoms participate in the metal coordination in [Ln(L₂)(H₂O)]. In [Ln(L₂)], all O-atoms of the PO₃²⁻ and SO₃⁻ groups coordinate to metal ions (Figure 4.5).

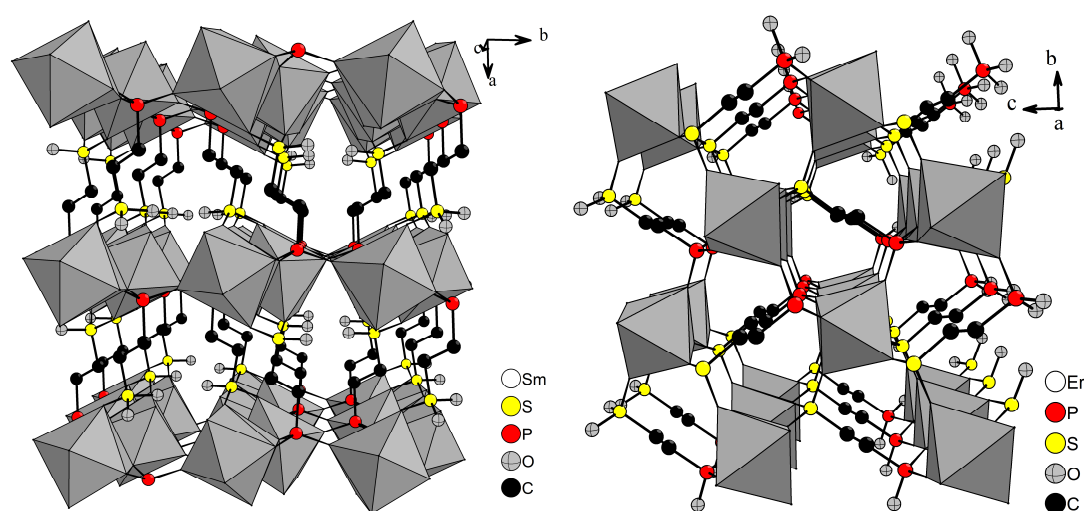


Figure 4.5 A section of [Ln(L₂)(H₂O)] (*left*) and [Ln(L₂)] (*right*) crystal structures. The edge-sharing polyhedra in [Ln(L₂)(H₂O)] lead to chains along the *c*-axis which then interconnected by sulfonate and phosphonate groups to form layers parallel to *bc*-plane. The layers are cross-linked to each other through the $-C_2H_4-$ group to build a 3D network. In [Ln(L₂)], the phosphonate and sulfonate groups interconnect the LnO₆ into a 3D-network. Hydrogen atoms are excluded for clarity.

An analysis of the lattice parameters of the isotypic lanthanoid compound $[\text{Ln}(\mathbf{L2})(\text{H}_2\text{O})]$ series has shown a substantial linear decrease of the c -lattice parameter from La^{3+} to Dy^{3+} which corresponds to the direction of the edge-sharing LaO_8 polyhedra chain and is in accordance with the 'lanthanoid contraction'.^[51]

Copper Phosphonatoethanesulfonate^[44,47]

The system $\text{Cu}(\text{NO}_3)_2/\text{H}_2\text{O}_3\text{PC}_2\text{H}_4\text{SO}_3\text{H}/\text{NaOH}/\text{H}_2\text{O}$ was systematically investigated at reaction temperatures from 90° to 190°C . The high-throughput study enabled the discovery of six new copper compounds and the crystal structures of four compounds were determined. Trimeric clusters (0D), zig-zag chains (1D) and layers (2D) containing Cu-O-Cu connectivities are observed in these structures. In $[\text{Cu}_2(\mathbf{L2})(\text{OH})(\text{H}_2\text{O})]\cdot\text{H}_2\text{O}$, zig-zag chains of edge-sharing CuO_6 octahedra are connected to layers by the phosphonate and sulfonate groups (Figure 4.6 *top-left*).

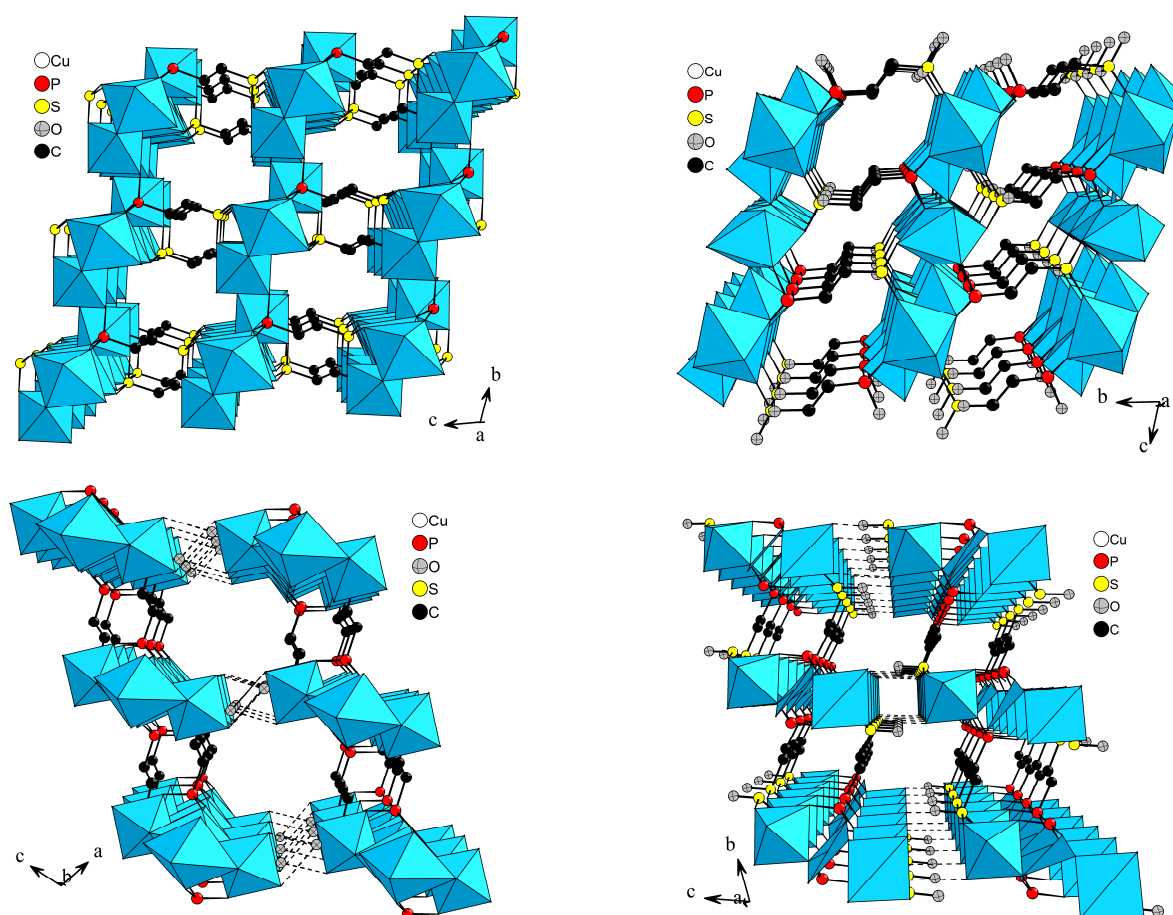


Figure 4.6 Crystal structure sections of $[\text{Cu}_2(\mathbf{L2})(\text{OH})(\text{H}_2\text{O})]\cdot\text{H}_2\text{O}$ (*top-left*), $[\text{Cu}_{2.5}(\mathbf{L2})(\text{OH})_2]$ (*top-right*), $[\text{Cu}_2(\mathbf{L2})(\text{OH})(\text{H}_2\text{O})_2]\cdot 3\text{H}_2\text{O}$ (*bottom-left*) and $[\text{Cu}_{1.5}(\mathbf{L2})(\text{H}_2\text{O})]$ (*bottom-right*). Zig-zag Cu-O-Cu chains are observed in all compounds except for $[\text{Cu}_{1.5}(\mathbf{L2})(\text{H}_2\text{O})]$. Hydrogen atoms are omitted for clarity. Broken lines indicate hydrogen bonds.

A similar zig-zag chain are also observed for $[\text{Cu}_{2.5}(\mathbf{L2})(\text{OH})_2]$ (Figure 4.6 *top-right*). The connection of another 1D chain of face-sharing CuO_6 octahedra to the zig-zag chain via corner-sharing forms Cu-O-Cu layers. The interconnection of layers in both structures is achieved by the $-\text{C}_2\text{H}_4-$ groups of phosphonoethanesulfonate linkers leading to three dimensional frameworks. Compound $[\text{Cu}_2(\mathbf{L2})(\text{OH})(\text{H}_2\text{O})_2] \cdot 3\text{H}_2\text{O}$ (Figure 4.6 *bottom-left*) also consists of 1D zigzag chains which form layers with the $\mathbf{L2}$ linker ions. Meanwhile, $[\text{Cu}_{1.5}(\mathbf{L2})(\text{H}_2\text{O})]$ has layers that are built of trimeric Cu_3O_{12} clusters interconnected to each other via $\mathbf{L2}$ linkers (Figure 4.6 *bottom-right*). These layers in $[\text{Cu}_2(\mathbf{L2})(\text{OH})(\text{H}_2\text{O})_2] \cdot 3\text{H}_2\text{O}$ and $[\text{Cu}_{1.5}(\mathbf{L2})(\text{H}_2\text{O})]$ are interlinked via weak hydrogen bonds.

A common feature shared by all copper phosphonatoethanesulfonates is that they tend to form multidimensional networks. The influence of using co-ligands remains to be seen as of now no co-ligand was employed in the investigations. The sulfonate group has again demonstrated its function as a weak ligand because in all compounds, only two oxygen atoms from the group coordinate to the copper ion with the exception of $[\text{Cu}_2(\mathbf{L2})(\text{OH})(\text{H}_2\text{O})] \cdot \text{H}_2\text{O}$. The Cu-O bonds stemming from sulfonate groups are also longer compared to the Cu-O bonds coming from phosphonate groups.

Copper Phosphonatobutanesulfonate^[49]

The continued work with an extended linker, $\text{H}_2\text{O}_3\text{PC}_4\text{H}_8\text{SO}_3\text{H}$ ($\mathbf{H}_3\mathbf{L3}$) and Cu^{2+} ions yielded two structures. The first compound, $[\text{Cu}_{1.5}(\mathbf{L3})(\text{H}_2\text{O})] \cdot 1.15\text{H}_2\text{O}$ has a 2D framework, formed through the interconnection of edge-sharing Cu_3O_{12} clusters by the butyl groups (Figure 4.7 *left*). The layers are held together by extensive hydrogen bondings. This compound can be considered to be isorecticular with the previously mentioned ethyl group containing $[\text{Cu}_{1.5}(\mathbf{L2})(\text{H}_2\text{O})]$ which also has trimeric Cu_3O_{12} clusters. However, the compound $[\text{Cu}_{1.5}(\mathbf{L3})(\text{H}_2\text{O})] \cdot 1.15\text{H}_2\text{O}$ can accommodate uncoordinated water molecules between the layers in the structure due to enlarged spacing. The other $\mathbf{H}_3\mathbf{L3}$ based compound, $[\text{Cu}_{2.5}(\mathbf{L3})(\text{OH})_2]$ is comprised of 3D network that is built of Cu-O-Cu layers linked to each other by the pillaring butyl groups (Figure 4.7 *right*). The Cu-O-Cu layers in $[\text{Cu}_{2.5}(\mathbf{L3})(\text{OH})_2]$ are composed of corner-, edge- and face-sharing CuO_6 polyhedra which are similar to the layers in the phosphonoethylsulfonate containing $[\text{Cu}_{2.5}(\mathbf{L2})(\text{OH})_2]$. Both the compounds $[\text{Cu}_{2.5}(\mathbf{L3})(\text{OH})_2]$ with $-\text{C}_3\text{H}_6-$ group and $[\text{Cu}_{2.5}(\mathbf{L2})(\text{OH})_2]$ with $-\text{C}_2\text{H}_4-$ group are considered as isorecticular as they have the same framework topology and only differ in alkyl chain length. In all compounds, only two oxygen atoms of sulfonate groups participate in the coordination to Cu^{2+} ions. The uncoordinated oxygen atoms are involved in hydrogen bonds.

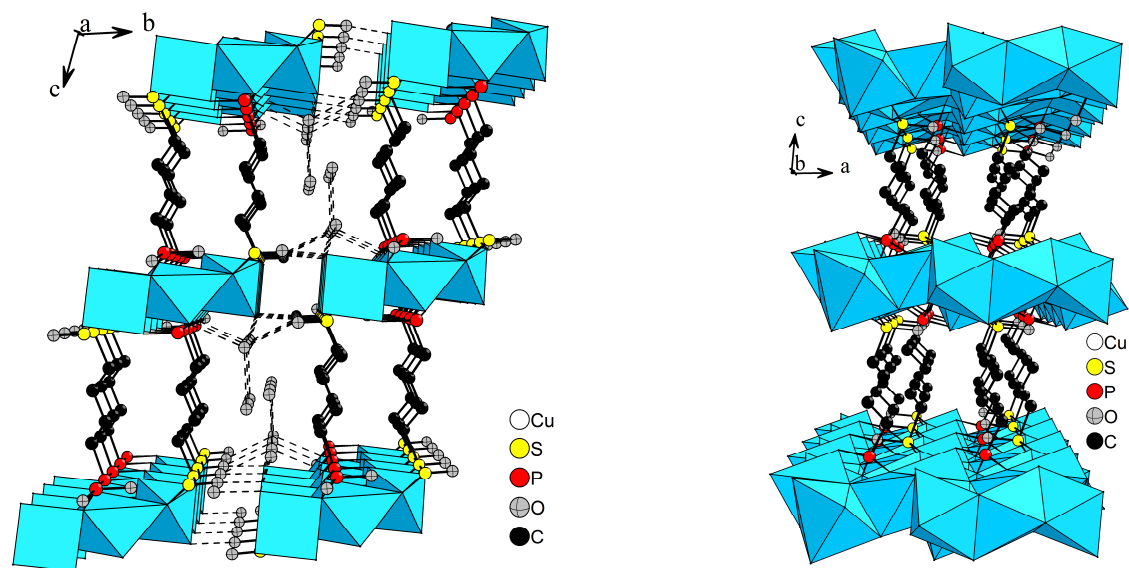


Figure 4.7 In the structure of $[\text{Cu}_{1.5}(\text{L3})(\text{H}_2\text{O})]\cdot 1.15\text{H}_2\text{O}$ (left), 2D layers are observed which are further bonded to each other via hydrogen bonding. In $[\text{Cu}_{2.5}(\text{L2})(\text{OH})_2]$, no hydrogen bonding is involved in the assembly of the three dimensional network (right).

References

- [1] A. Clearfield, *Current Opinion Solid State Mater. Sci.* **2002**, 6, 495-506.
- [2] A. Clearfield, Z. Wang, P. Bellinghausen, *J. Solid State Chem.* **2002**, 167, 376-385.
- [3] J. D. Wang, A. Clearfield, G. Z. Peng, *Mater. Chem. Phys.* **1993**, 35, 208-216.
- [4] M. E. Thompson, *Chem. Mater.* **1994**, 6, 1168-1175.
- [5] D. M. Poojary, B. L. Zhang, A. Clearfield, *Angew. Chem. Int. Ed. Engl.* **1994**, 33, 2324-2326; *Angew. Chem.* **1994**, 106, 2420-2422.
- [6] N. Stock, G. D. Stucky, A. K. Cheetham, *Chem. Commun.* **2000**, 2277-2278.
- [7] B. A. Adair, G. Diaz de Delgado, J. M. Delgado, A. K. Cheetham, *Solid State Sci.* **2000**, 2, 119-126.
- [8] S. Ayyappan, G. Diaz de Delgado, A. K. Cheetham, G. Férey, C. N. R. Rao, *J. Chem. Soc., Dalton. Trans.* **1999**, 2905-2907.
- [9] Q. Gao, N. Guillou, M. Nogues, A. K. Cheetham, G. Férey, *Chem. Mater.* **1999**, 11, 2937-2947.
- [10] J. Le Bideau, C. Payen, P. Palvadeau, B. Bujoli, *Inorg. Chem.* **1994**, 33, 4885-4890.
- [11] X. Xu, P. Wang, R. Hao, M. Gan, F. Sun, G. S. Zhu, *Solid State Sci.* **2009**, 11, 68-71.
- [12] G. B. Hix, A. Turner, B. M. Kariuki, M. Tremayne, E. J. MacLean, *J. Mater. Chem.* **2002**, 12, 3220-3227.
- [13] S. Drumel, P. Janvier, D. Deniaud, B. Bujoli, *J. Chem. Soc., Chem. Commun.* **1995**, 1051-1052.
- [14] P. Ayyappan, O. R. Evans, B. M. Foxman, K. A. Wheeler, T. H. Warren, W. Lin, *Inorg. Chem.* **2001**, 40, 5954-5961.

- [15] A. Britel, J. C. Boivin, D. Thomas, M. Wozniak, *Acta Cryst.* **1985**, C41, 1609-1612.
- [16] P. H. Smith, K. N. Raymond, *Inorg. Chem.* **1988**, 27, 1056-1061.
- [17] N. Stock, T. Bein, *Angew. Chem. Int. Ed.* **2004**, 43, 749-752; *Angew. Chem.* **2004**, 116, 767-770.
- [18] S. Bauer, N. Stock, *J. Solid State Sci.* **2007**, 180, 3111-3120.
- [19] S. Bauer, N. Stock, *Angew. Chem. Int. Ed.* **2007**, 46, 6857-6860; *Angew. Chem.* **2007**, 119, 6981-6984.
- [20] G. Alberti, U. Costantino, F. Marmottini, R. Vivani, P. Zappelli, *Angew. Chem. Int. Ed.* **1993**, 32, 1357-1359; *Angew. Chem.* **1993**, 105, 1396-1398.
- [21] K. Maeda, Y. Kiyozumi, F. Mizukami, *J. Phys. Chem. B*, **1997**, 101, 4402-4412.
- [22] M. D. Gomez-Alcantara, A Cabeza, L. Moreno-Real, M. A. G. Aranda, A. Clearfield, *Microporous Mesoporous Mater.* **2006**, 88, 293-303.
- [23] C. Serre, J. A. Groves, P. Lightfoot, A. M. Z. Slawin, P. A. Wright, N. Stock, T. Bein, M. Haouas, F. Taulelle, G. Férey, *Chem. Mater.* **2006**, 18, 1451-1457.
- [24] J. A. Groves, S. R. Miller, S. J. Warrender, C. Mellot-Draznieks, P. Lightfoot, P. A. Wright, *Chem. Commun.* **2006**, 3305-3307.
- [25] M. T. Wharmby, J. P. S. Mowat, S. P. Thompson, P. A. Wright, *J. Am. Chem. Soc.* **2011**, 133, 1266-1269.
- [26] G. K. H. Shimizu, R. Vaidhyanathan, J. M. Taylor, *Chem. Soc. Rev.* **2009**, 38, 1430-1449.
- [27] E. J. Kosnic, E. L. McClymont, R. A. Hodder, P. J. Squattrito, *Inorg. Chim. Acta*, **1992**, 201, 143-151.
- [28] C. Y. Yang, A. Clearfield, *React. Polym., Ion Exch., Sorbents*, **1987**, 5, 13-21.
- [29] A. F. Benedetto, P. J. Squattrito, F. Adani, E. Montoneri, *Inorg. Chim. Acta*, **1997**, 260, 207-216.
- [30] F. Adani, M. Casciola, D. J. Jones, L. Massinelli, E. Montoneri, J. Rozière, R. Vivani, *J. Mater. Chem.* **1998**, 8, 961-964.
- [31] E. Montoneri, *Phosphorus, Sulphur Silicon Relat. Elem.* **1991**, 55, 201-204.
- [32] Z. Y. Du, H. B. Xu, J. G. Mao, *Inorg. Chem.* **2006**, 45, 6424-6430.
- [33] Z. Y. Du, H. B. Xu, J. G. Mao, *Inorg. Chem.* **2006**, 45, 9780-9788.
- [34] Z. Y. Du, X. L. Li, Q. Y. Liu, J. G. Mao, *Cryst. Growth. Des.* **2007**, 7, 1501-1507.
- [35] Z. Y. Du, A. V. Prosvirin, J. G. Mao, *Inorg. Chem.* **2007**, 46, 9884-9894.
- [36] Z. Y. Du, Y. R. Xie, H. R. Wen, *Acta Cryst.* **2007**, E63, m2766-m2767.
- [37] Z. Y. Du, H. B. Xu, X. L. Li, J. G. Mao, *Eur. J. Inorg. Chem.* **2007**, 4520-4529.
- [38] Z. Y. Du, J. J. Huang, Y. R. Xie, H. R. Wen, *J. Mol. Struct.* **2009**, 919, 112-116.
- [39] E. Montoneri, G. Ricca, *Phosphorus, Sulphur Silicon Relat. Elem.* **1991**, 55, 111-115.
- [40] A. Sonnauer, Ph.D. Thesis: *Systematic Investigation of Inorganic-Organic Hybrid Compounds Based on Polyfunctional Phosphonic Acids Using High-Throughput Methods*, **2008**, Christian-Albrechts-Universität zu Kiel, Germany.
- [41] A. Sonnauer, C. Näther, H. A. Höpfe, J. Senker, N. Stock, *Inorg. Chem.* **2007**, 46, 9968-9974.
- [42] Z. Y. Du, H. R. Wen, Y. R. Xie, *J. Mol. Struct.* **2008**, 891, 272-277.

- [43] A. Sonnauer, N. Stock, *J. Solid State Chem.* **2008**, *181*, 473-479.
- [44] A. Sonnauer, A. Lieb, N. Stock, *Acta Cryst.* **2008**, *E64*, m1417-m1418.
- [45] A. Sonnauer, N. Stock, *Acta Cryst.* **2008**, *E64*, m1433.
- [46] A. Sonnauer, N. Stock, *J. Solid State Chem.* **2008**, *181*, 3065-3070.
- [47] A. Sonnauer, N. Stock, *Eur. J. Inorg. Chem.* **2008**, 5038-5045.
- [48] A. Sonnauer, N. Stock, *Solid State Sci.* **2009**, *11*, 358-363.
- [49] A. Sonnauer, M. Feyand, N. Stock, *Cryst. Growth Des.* **2009**, *9*, 586-592.
- [50] M. Feyand, C. Näther, A. Rothkirch, N. Stock, *Inorg. Chem.* **2010**, *49*, 11158-11163.
- [51] P. Pyykkö, *Chem. Rev.* **1988**, *88*, 563-594.

4.2 High-throughput synthesis of metal phosphonates

Portions of this section will be published in the book “*Metal phosphonate chemistry: From Synthesis to Applications*” edited by A. Clearfield, K. Demadis in the chapter: “*High Throughput Methods for the Systematic Investigation of Metal Phosphonate Synthesis Fields*” written by me and Prof. Dr. Norbert Stock. These sections are reproduced with permission of The Royal Society of Chemistry (2012), Cambridge, United Kingdom.

High-throughput methods have played a great role in generating numerous new metal phosphonates.^[1] These compounds are based on polyphosphonic acids $R-(PO_3H_2)_n$ ($n = 2-4$, $R =$ aryl or alkyl), phosphonocarboxylic acids $H_2O_3P-R-COOH$ or phosphonosulfonic acids $H_2O_3P-R-SO_3H$ (see Section 4.1). Most often compositional parameters and pH values of the reaction mixtures were investigated since these variables have the most influence on the product formation. The pH values are very important in the synthesis of metal phosphonates because they control the protonation levels and thus vary the coordination modes of the linker molecules. On the other hand, the effects of other important parameters such as concentrations, solvents, reaction temperatures, mode of heating (microwave vs. conventional oven), reaction time, and the cooling rates have been reported as well. The main goals for the application of HT methods are faster and more efficient ways towards the (a) discovery of new compounds, (b) discovery of reaction trends, (c) elucidation of synthesis-structure relationships, and (d) optimization of synthesis recipes or process conditions. Depending on the size/dimensionality of the parameter space under investigation, one can distinguish between discovery and focused arrays. Without any prior knowledge of a reaction system one has to screen many variables, normally compositional parameters. A set-up like this is called a discovery library. Once a new compound is discovered, the so-called focused libraries are set up, that screen only the relevant section of the parameter space close to the discovered composition.

In the following sections examples are given that focus on a certain parameter, i.e. concentration, metal salt, pH and temperature. In general these parameters cannot be investigated individually since they mutually affect each other. The following sections highlight examples that are most profoundly influenced by the respective parameter.

4.2.1 Dilution

Metal phosphonates discovered during the early stages of an HT investigation can be easily identified via X-ray powder diffraction measurement. However, the knowledge of the full crystal structure is fundamental to understand the synthesis-structure relationships.

Therefore, single crystals are needed for the structure elucidation via single crystal X-ray diffraction. The formation of single crystals depends on the nucleation and crystal growth rate, which can be influenced by the reaction temperature and time, the cooling rate and the solvent/solvent mixture employed. We have systematically investigated two approaches. The stepwise dilution of the reaction mixtures in the system $\text{Zn}^{2+} / \text{H}_8\text{L4} / \text{H}_2\text{O}$ ($\text{H}_8\text{L4} = (\text{H}_2\text{O}_3\text{PCH}_2)_2\text{N}-(\text{CH}_2)_4-\text{N}(\text{CH}_2\text{PO}_3\text{H}_2)_2$) generated crystals under high dilution that were suitable for the structure determination (Figure 4.8).^[2]

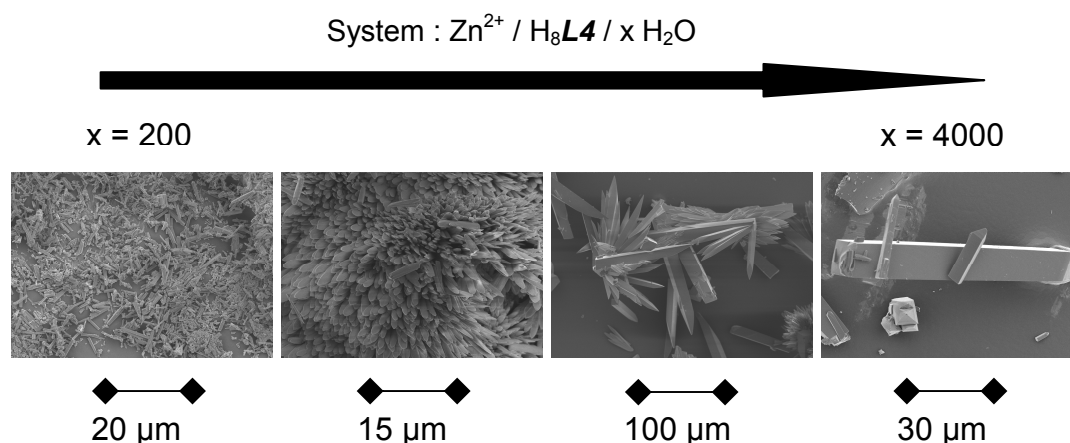


Figure 4.8 Crystal size growth of $[\text{Zn}(\text{H}_6\text{L4})]$ with increasing water content as evidenced by SEM micrographs. $\text{Zn}^{2+} / \text{H}_8\text{L4}$ molar ratios were fixed at 1 : 1.

On the other hand, the variation of the amount of water can also lead to the formation of a new compound.^[3] In this experiment, the mixtures $2.5 \text{Zn}^{2+} : 5 \text{H}_3\text{L5} : 1.5 \text{NaOH} : x \text{H}_2\text{O}$ ($\text{H}_3\text{L5} = p\text{-H}_2\text{O}_3\text{PCH}_2\text{-C}_6\text{H}_4\text{-COOH}$) with $400 \leq x \leq 5700$ were investigated. Two phases were obtained, $[\text{Zn}(\text{H}_2\text{L5})_2]$ at $400 \leq x < 4000$ and a previously unknown phase $[\text{Zn}(\text{H}_2\text{L5})_2(\text{H}_2\text{O})_4]$ at $x = 5700$; $x = 4000$ resulted in a mixture of both phases (Figure 4.9). Comparing the crystal structures of both compounds, it can be concluded that higher H_2O content tends to produce a new zinc phosphonate with inclusion of water as a ligand. The coordination environment of the zinc ions changed from tetrahedral in $[\text{Zn}(\text{H}_2\text{L5})_2]$ to octahedral in $[\text{Zn}(\text{H}_2\text{L5})_2(\text{H}_2\text{O})_4]$.

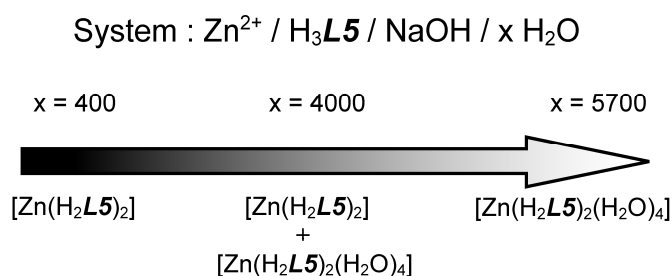


Figure 4.9 Investigation of the impact of water content in the compound $[\text{Zn}(\text{H}_2\text{L5})_2]$ leading to the discovery of a new phase. $\text{Zn}^{2+} : \text{H}_3\text{L5} : \text{NaOH}$ molar ratios were fixed at 2.5 : 5 : 1.5.

4.2.2 Metal-screening

To study the potential of a phosphonic acid for the formation of new metal phosphonates, different metal ions need to be screened. This is due to the properties of the metal ions, e.g. the charge, the ionic radius, the preferred coordination number, the presence of sterically active lone pairs of electrons. A metal ion screening was conducted in the system M^{2+} / H_8L4 ($H_8L4 = (H_2O_3PCH_2)_2N-(CH_2)_4-N(CH_2PO_3H_2)_2$) at four different molar ratios (1:1, 1:4, 4:1, 2:3) using twelve different divalent ions with ionic radii of 69 – 135 pm and two containing lone pairs of electrons. The set-up and the results of the study are presented in Figure 4.10 (left).^[2] Only one crystalline phase is obtained, $M^{II}(H_6L4)$. The XRPD analysis results showed that only metal ions with ionic radii between 69 and 100 pm and without lone pair of electrons were capable of forming crystalline compounds while bigger ions produce only X-ray amorphous products. This screening was followed by a more detailed investigation using focused arrays and varying the water content of the reaction mixtures, thus most of the new compounds could be isolated as single-crystalline products.

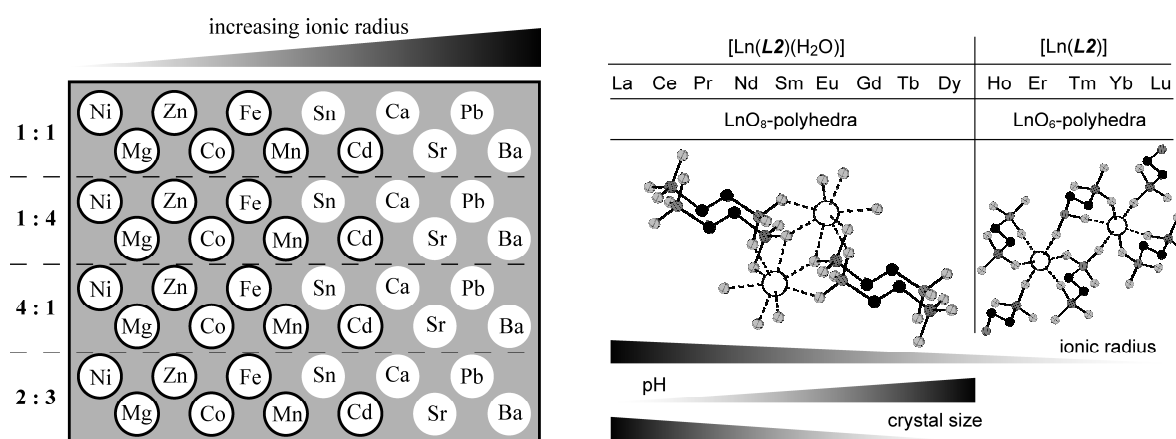


Figure 4.10 (left): Results from HT metal-screening experiment for the system M^{2+} / H_8L4 . Twelve different divalent metal ions (ionic radii range of 69 – 135 pm,^[4] Sn^{2+} ionic radii^[5]) were used. Outlined circles indicate crystalline products, normal circles is for X-ray amorphous products. (right): Results of HT metal screening experiment of the system $Ln^{3+} / H_3L2 / NaOH$. The correlation between ionic radius of lanthanoid ion and pH value with the crystal size were extracted. Zn : white, C : black, light gray : oxygen, dark gray : phosphorus/sulfur.

In another study, $H_2O_3P-C_2H_4-SO_3H$ acid (H_3L2) was investigated.^[6,7] Trivalent rare earth ions were screened and two new phases are observed. For larger ions (La-Dy) eightfold coordination and for Y and Ln = Ho – Lu sixfold coordination is observed. On the basis of SEM micrographs, a correlation of the crystal size with the pH and the ionic radius could be

drawn. Larger rare-earth ions lead under acidic conditions to larger crystals (Figure 4.10, right).

4.2.3 Counter-ion screening

The anions of the metal salts used in the synthesis can also have an influence on the formation of the products. They can, for example, influence the pH of the starting solution, be involved in the coordination to the metal ions during the reaction or in the final product, or they can take part in redox reactions. Thus depending on the counter-ions, new products or products of varying crystallinity were obtained.

In the system $\text{Co}^{2+} / \text{H}_5\text{L7} / \text{NaOH}$, four different cobalt(II) salts, namely CoCl_2 , $\text{Co}(\text{O}_2\text{CCH}_3)_2$, $\text{Co}(\text{NO}_3)_2$, and CoSO_4 , were used employing the same reaction conditions ($\text{H}_5\text{L7} = (\text{H}_2\text{O}_3\text{P}-\text{CH}_2)_2\text{N}-\text{CH}_2-\text{C}_6\text{H}_4-\text{COOH}$).^[8] Four new cobalt carboxyarylphosphonates were discovered. When using CoCl_2 or CoSO_4 only minor changes in the fields of formation were observed, due to changes in the pH of the starting solutions. Using $\text{Co}(\text{O}_2\text{CCH}_3)_2$ led only to one compound since its solutions are already slightly basic (Figure 4.11). In the case of $\text{Co}(\text{NO}_3)_2$ as the starting material, an *in situ* oxidation of $\text{H}_5\text{L7}$ is observed. The cleavage of the P-C bonds and the oxidation led to the new ligand containing a formamide group which is stabilized by complexation and the formation of the corresponding cobalt phosphonate.

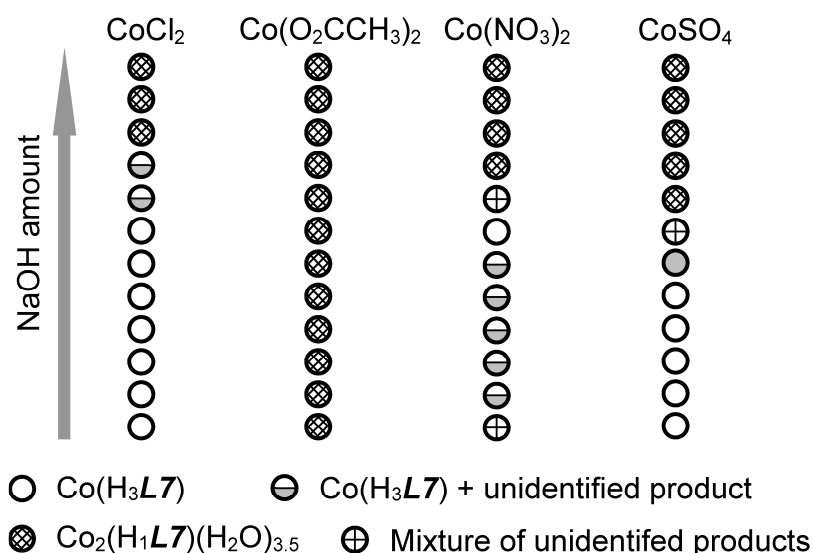


Figure 4.11 Results of HT counter-ion screening of the system $\text{Co}^{2+} / \text{H}_5\text{L7} / \text{NaOH}$ employing chloride, acetate, nitrate and sulfate salts. Results are based on XRPD data.

4.2.4 pH-screening

In the synthesis of metal phosphonates, the pH of the starting solution has in general the most profound influence on the product formation. Therefore this parameter is screened in most of the HT investigations. It is determined by the type of counter-ions and most importantly, by the amount of base added. The HT methodology is especially powerful in cases where an automated measurement of pH values is possible.^[2] This was demonstrated for the system $\text{Zn}^{2+} / \text{H}_3\text{L5} / \text{NaOH} / \text{H}_2\text{O}$ ($\text{H}_3\text{L5} = p\text{-H}_2\text{O}_3\text{PCH}_2\text{-C}_6\text{H}_4\text{-COOH}$). A discovery library was set up, keeping the water content constant and varying the molar ratios of the three starting materials according to Figure 4.12. The results are also presented in the same figure. Under basic conditions (pH > 9) the formation of ZnO is observed. In addition, three new phases and their crystal structures were obtained, $[\text{Zn}(\text{H}_2\text{L5})_2]$, $[\text{Zn}(\text{HL5})]$ and $[\text{Zn}_3(\text{L5})_2(\text{H}_2\text{O})_2] \cdot \text{H}_2\text{O}$. Automated pH measurements showed that a decrease in the H^+ concentration leads to higher condensed structures. While isolated columns are observed in $[\text{Zn}(\text{H}_2\text{L5})_2]$ (pH ~ 0 in region A), layers that are connected via hydrogen bonds are found in $[\text{Zn}(\text{HL5})]$ (pH ~ 1 in region B) and in $[\text{Zn}_3(\text{L5})_2(\text{H}_2\text{O})_2] \cdot \text{H}_2\text{O}$ a three-dimensional framework structure is observed (pH ~ 6 in region D).^[2]

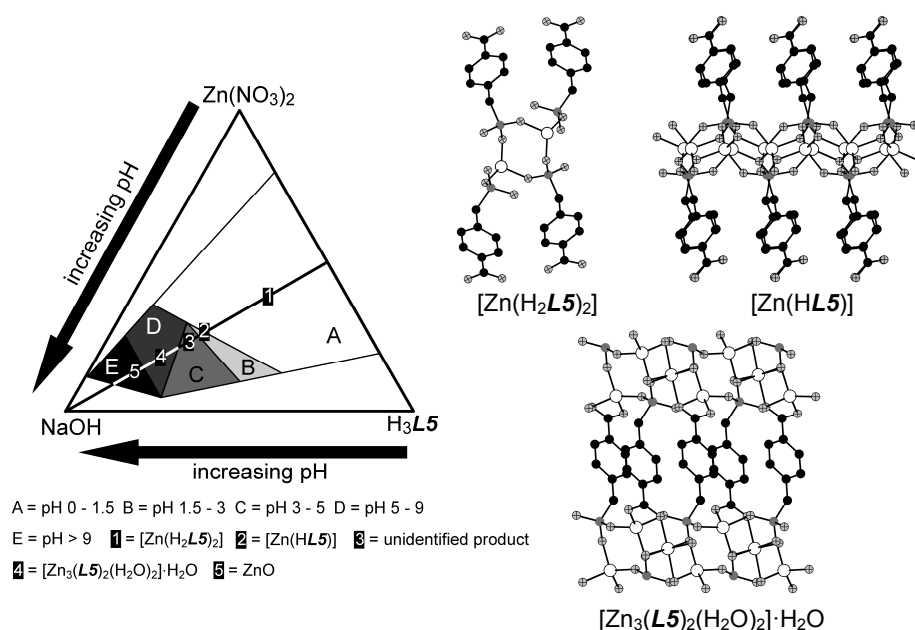


Figure 4.12 (left) Crystallization diagram of the phase obtained in the system $\text{Zn}(\text{NO}_3)_2 / \text{H}_3\text{L5} / \text{NaOH}$. Five different pH regions were classified whereby each region has a specific product formation. (right) Sections of crystal structures of compound 1, 2 and 4. Zn: white, C: black, P: dark gray, O: light gray.

4.2.5 Multi-parameter investigation – temperature screening

A breakthrough in high-throughput investigation of metal phosphonates is the study of the influence of the reaction temperature using a thermocycler which allows the setting of a temperature gradient. Up to now, this technology enables the simultaneous exploration of reaction temperatures up to 100 °C as well as compositional parameters. The molar ratios 1 Cd^{2+} : 1 $\text{H}_5\text{L7}$: x NaOH ($x = 0, 0.5, 1, 1.5, 2, 2.5$) were studied at 16 different temperatures (17 – 99.9 °C, Figure 4.13) ($\text{H}_5\text{L7} = (\text{H}_2\text{O}_3\text{PCH}_2)_2\text{N-CH}_2\text{-C}_6\text{H}_4\text{-COOH}$). Six new cadmium phosphonocarboxylates (A – F) were synthesized.^[9] In addition, reactions were performed using conventional reactors at temperatures up to 200 °C which led to pure-phase C as well as the discovery of phase G. In Figure 4.13 it is clearly observable that there are well defined formation fields for most of the phases, i.e. well defined pH and temperature ranges. A detailed structure – reaction temperature analysis reveal the following correlation: within a fixed molar ratio Cd^{2+} : $\text{H}_5\text{L7}$: NaOH higher reaction temperatures lead to a higher ratio Cd^{2+} : $\text{H}_{5-n}\text{L7}^{n-}$ (n depending on deprotonation) and a lower water content in the structures. Similar to the results of the previously mentioned copper(II) phosphonatoethanesulfonates, higher reaction temperatures lead to more condensed structures. In compound A (17 °C < T < 35 °C) and B (45 °C < T < 100 °C) isolated CdO_6 polyhedra are observed that are connected to chains and layers, respectively. Compound C has a similar layered structure but dinuclear Cd_2O_{10} clusters are observed. The structural composition – pH analysis reveals that the increase of the molar ratio NaOH : $\text{H}_5\text{L7}$ leads to a higher degree of ligand deprotonation and thus to compounds with higher molar ratios Cd^{2+} : $\text{H}_{5-n}\text{L7}^{n-}$, which in general is equivalent to more condensed structures.

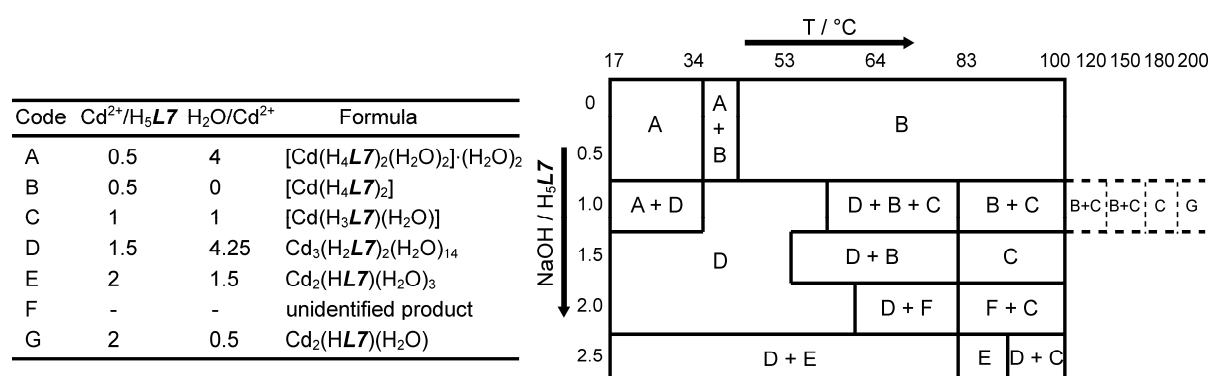


Figure 4.13 (left) Table summarizing the cadmium phosphonocarboxylates formed. Compounds A to F were discovered in the HT experiment in a thermocycler with temperature gradient. G was synthesized using conventional autoclave at 200 °C. (right) Schematic diagram illustrating the crystallization fields depending on reaction temperature and $\text{NaOH} / \text{H}_5\text{L7}$ molar ratio. Phases found above 100 °C were synthesized with conventional autoclaves.

References

- [1] S. Bauer, N. Stock, *Stud. Surf. Sci. Catal.* **2007**, *170*, 2015-2020.
- [2] N. Stock, T. Bein, *Angew. Chem. Int. Ed.* **2004**, *43*, 749-752; *Angew. Chem.* **2004**, *116*, 767-770.
- [3] N. Stock, private communications.
- [4] R. D. Shannon, *Acta Cryst.* **1976**, *A32*, 751-767.
- [5] L. H. Ahrens, *Geochim. Cosmochim. Acta*, **1952**, *2*, 155-169.
- [6] A. Sonnauer, C. Näther, H. A. Höpfe, J. Senker, N. Stock, *Inorg. Chem.* **2007**, *46*, 9968-9974.
- [7] A. Sonnauer, N. Stock, *J. Solid State Chem.* **2008**, *181*, 3065-3070.
- [8] S. Bauer, N. Stock, *Inorg. Chem.* **2005**, *44*, 5882-5889.
- [9] S. Bauer, N. Stock, *Angew. Chem Int. Ed.* **2007**, *46*, 6857-6860; *Angew. Chem.* **2007**, *119*, 6981-6984.

4.3 Inorganic-organic hybrid materials based on 4-phosphonobenzenesulfonic acid ($\text{H}_2\text{O}_3\text{P}-\text{C}_6\text{H}_4-\text{SO}_3\text{H}$)

The research of metal phosphonates has been mostly dependent on the commercial availability of phosphonic acid linker or the feasibility to synthesize the linker. Linkers based only on phosphonic acid groups are already very well established and numerous new metal phosphonates were reported. So far, the investigation of metal phosphonatosulfonates is limited to 3-phosphonobenzenesulfonic, 2-phosphonoethane-sulfonic and 4-phosphonobutanesulfonic acids. The organic synthesis of these linkers was conducted on the basis of post-sulfonation of the parent phosphonic acids. A new approach is necessary for the synthesis of a phosphonobenzenesulfonic acid with the functional groups in the *para*-positions. The electron withdrawing effect (*-I effect*) of the PO_3H_2 group forces the post-sulfonation to occur only in *meta*-position, resulting in 3-phosphonobenzene-sulfonic acid.^[1] A reverse approach was employed with the starting material, 4-bromobenzenesulfonyl chloride, which involves post-phosphonation of the sulfonate derivative that leads to 4-phosphonobenzenesulfonic acid.^[2] This difunctional linker is of much interest as it can potentially produce metal phosphonatosulfonates with pillared-layered structure which can be comprised of metal- $\text{O}_3\text{P}/-\text{O}_3\text{S}$ layers connected to each other by pillaring phenyl rings. A linker that shares many structural similarities with the 4-phosphonobenzenesulfonic acid is 1,4-phenylenebis(phosphonic acid). With this linker, several metal diphosphonates were synthesized with Cu^{2+} , Zn^{2+} , Ni^{2+} , Co^{2+} , Sn^{2+} , Sn^{4+} , UO_2^{2+} and V^{4+} ions.^[3-9] Their crystal structures were revealed to be mostly of pillared-layered architecture. In this work, the linker 4-phosphonobenzenesulfonic acid was synthesized and screened with various metal ions and in doing so, the structural network types can be compared to those of the typical pillared-layered form. Furthermore, the weakly coordinating sulfonate group is expected to provide different connectivities and also improved solubility in water.

References

-
- [1] E. Montoneri, G. Ricca, *Phosphorus, Sulphur Silicon Relat. Elem.* **1991**, *55*, 111-115.
 - [2] E. Montoneri, G. Viscardi, S. Bottigliengo, R. Gobetto, M. R. Chierotti, R. Buscaino, P. Quagliotto, *Chem. Mater.* **2007**, *19*, 2671-2678.
 - [3] D. M. Poojary, B. Zhang, P. Bellinghausen, A. Clearfield, *Inorg. Chem.* **1996**, *35*, 4942-4949.
 - [4] D. M. Poojary, B. Zhang, P. Bellinghausen, A. Clearfield, *Inorg. Chem.* **1996**, *35*, 5254-5263.
 - [5] D. K. Cao, S. Gao, L. M. Zheng, *J. Solid State. Chem.* **2004**, *177*, 2311-2315.
 - [6] A. Subbiah, N. Bhuvanesh, A. Clearfield, *J. Solid State Chem.* **2005**, *178*, 1321-1325.

- [7] S. Kirumakki, J. Huang, A. Subbiah, J. Yao, A. Rowland, B. Smith, A. Mukherjee, S. Samarajeewa, A. Clearfield, *J. Mater. Chem.* **2009**, *19*, 2593-2603.
- [8] P. O. Adelani, T. E. Albrecht-Schmitt, *Inorg. Chem.* **2009**, *48*, 2732-2734.
- [9] W. Ouellette, G. Wang, H. Liu, G. T. Yee, C. J. O'Connor, J. Zubieta, *Inorg. Chem.* **2009**, *48*, 953-963.

4.3.1 Systematic Hydrothermal Investigation of Metal Phosphonatobenzene-sulfonates by High-Throughput Methods

This is the pre-peer reviewed version of the above-mentioned article which has been published in its final form in "European Journal of Inorganic Chemistry": DOI: 10.1002/ejic.201000393. Copyright © 2010 WILEY-VCH Verlag GmbH & Co. KGaA, Weinheim. The supporting information of this article is placed in the Appendix section (Appendix 1).

The linker 4-phosphonobenzenesulfonic acid was prepared according to previously reported methods for the investigation of the system $M^{2+} / H_2O_3PC_6H_4SO_3H / NaOH / H_2O$. By employing 48 sample high-throughput (HT) reactors, the screening of metal ions (Ni^{2+} , Mg^{2+} , Cu^{2+} , Zn^{2+} , Co^{2+} , Fe^{2+} , Mn^{2+} , Sn^{2+} , Cd^{2+} , Sr^{2+} , Pb^{2+} and Ba^{2+}) was conducted and the XRPD evaluation of the products revealed that all metal ions, with exception of Co^{2+} , Fe^{2+} , Sr^{2+} and Ba^{2+} , have generated crystalline products. A subsequent metal ion screening was performed with the emphasis on the promising metal ions and varying NaOH amounts. Single crystals of good quality were extracted from the samples and the structures of four new metal phosphonatosulfonates were determined; $Pb_2[(O_3PC_6H_4SO_3)(OH)]$ (**1**), $Cu_{1.5}[(O_3PC_6H_4SO_3)(H_2O)]$ (**2**), $Cu_2[(O_3PC_6H_4SO_3)(OH)(H_2O)]$ (**4**) and $Cu_3[(O_3PC_6H_4SO_3)_2(H_2O)_2]$ (**5**). Further HT metal salt screening has helped to determine that $Pb(NO_3)_2$ as well as $CuCl_2 \cdot 2H_2O$ are the optimal salts. These results were taken into consideration in the investigation of the specific formation fields of each compound which is very important for the scale-up synthesis. Some of the compounds forms in a narrow formation field and others have a rather wide field of formation. Through the focused array experiment, a new compound $NaCu(O_3PC_5H_4SO_3)(H_2O)_3$ (**3**) was also discovered which tends to crystallize as a micro-crystalline powder. The composition of **3** was deduced from thermogravimetric as well as elemental analysis and the phase purity was verified by XRPD pattern indexing. The crystal structures of **1**, **2**, **4** and **5** were determined via single crystal X-ray diffraction. The crystal structure of **1** is built from 1D edge-sharing PbO_7/PbO_5 chains interconnected by phosphonate and sulfonates groups, thus forming layers cross-linked through pillaring phenyl rings to construct a three-dimensional framework. Similar pillared-layered arrangements were observed for **2** and **4** whereby the main difference between the compounds are the Cu-O-Cu connectivities. Compound **2** has isolated CuO_6 and Cu_2O_8 dimers while edge-sharing CuO_5 and CuO_6 octahedra lead to zigzag 1D chains in **4** and compound **5** is made of corner-sharing Cu_6O_{24} hexanuclear clusters. All oxygen atoms of the sulfonate groups in the 3D networks of **1**, **2** and **4** coordinate to metal ions. Only two oxygen atoms from sulfonate group in **5** participate in M-O coordination and the remaining oxygen atom acts as proton acceptor in hydrogen bonding.

Systematic Hydrothermal Investigation of Metal Phosphonatobenzenesulfonates via High-Throughput Methods

Palanikumar Maniam^[a], Christian Näther^[a] and Norbert Stock^{*[a]}

Keywords: Metal phosphonatosulfonates / Inorganic-organic hybrid compounds / High-throughput screening / Hydrothermal synthesis

A high-throughput (HT) investigation using the rigid bifunctional ligand 4-phosphonobenzenesulfonic acid, $\text{H}_2\text{O}_3\text{P-C}_6\text{H}_4\text{-SO}_3\text{H}$ (H_3L), generated five new phosphonatobenzenesulfonates with copper (II) or lead (II) ions. A comprehensive HT study comprising the screenings of different metal ions, metal salt types and the synthesis optimization were conducted whereby the influence of pH and molar ratios $\text{M}^{2+}/\text{H}_3\text{L}$ were investigated. The HT-study led to five new compounds $\text{Pb}_2[(\text{O}_3\text{P-C}_6\text{H}_4\text{-SO}_3)(\text{OH})]$ (**1**), $\text{Cu}_{1.5}[(\text{O}_3\text{P-C}_6\text{H}_4\text{-SO}_3)(\text{H}_2\text{O})]$ (**2**), $\text{NaCu}(\text{O}_3\text{P-C}_6\text{H}_4\text{-SO}_3)(\text{H}_2\text{O})_3$ (**3**), $\text{Cu}_2[(\text{O}_3\text{P-C}_6\text{H}_4\text{-SO}_3)(\text{OH})(\text{H}_2\text{O})]$ (**4**) and $\text{Cu}_3[(\text{O}_3\text{P-C}_6\text{H}_4\text{-SO}_3)_2(\text{H}_2\text{O})_2]$ (**5**).

Metal ion screening showed lead (II) and copper (II) to be suitable metal ions. The utilization of discovery and focused arrays allowed to determine the optimal formation fields of the respective compounds. The crystal structures were determined from single crystal X-ray diffraction and revealed the presence of various MO_x polyhedra that form clusters, chains or layers which are connected through the organic linker. IR spectra, thermogravimetric studies, magnetic susceptibility measurements and elemental analyses were conducted to further characterize the compounds **1**, **3**, **4** and **5**.

Introduction

The classes of inorganic-organic hybrid compounds range from amorphous nanocomposites such as self-assembled mesoporous materials to crystalline products.^[1] One intensively studied class of these compounds is the one of metal-organic frameworks (MOFs). These possess porous 3D networks and are therefore investigated for potential applications in gas storage, gas separation, catalysis and drug delivery.^[2,3] The organic building units that are mostly deployed in these materials are based on carboxylates (R-COO^-)^[4,5] and amines.^[6,7] On the other hand, sulfonate (R-SO_3^-) and phosphonate (R-PO_3^{2-}) based compounds have been less intensively investigated.^[8-14] This could be due to the more flexible coordination modes as well as the larger number of coordinating atoms which restricts structural diversity compared to the -COO^- counterpart. Thus for phosphonate based compounds mostly more dense layered materials are formed.^[15,16] Only a few porous phosphonate based materials are known to date, for example $\text{Ni-STA-12}^{[17]}$, $\text{Al}_2(\text{CH}_3\text{-PO}_3)_3\text{-H}_2\text{O}^{[18]}$ and $\text{Zr}(\text{O}_3\text{P-C}_6\text{H}_4\text{-PO}_3\text{H})^{[19]}$ and there are even less examples described for sulfonate-based porous compounds.^[20] Our research focuses on the use of organic linker molecules containing two or more different functional groups for the synthesis of inorganic-organic hybrid compounds. In addition to the number of functional groups, their geometry, coordination modes, as well as charge and

acidity have a strong influence on the formation of the final crystal structures.

Examples from our previous work encompass the use of linkers containing phosphonate and carboxylate groups,^[21,22] phosphonate and amine groups such as iminobis(methylphosphonate) units^[23] or iminobis(methylphosphonate) and carboxylate units.^[24,25] Linkers containing a phosphonic and a sulfonic acid group have only been recently investigated. By using the flexible linker molecules 2-phosphonoethane- and 4-phosphonobutanesulfonic acid, our group has explored the synthesis of several hybrid compounds with different Cu(II) ,^[26] Sr^{2+} ,^[27] Ba^{2+} ,^[28] and lanthanide ions.^[29,30] Rigid phosphonoarylsulfonic acids, i.e. 3-phosphonobenzenesulfonic were employed by Mao et al.^[31-35] 5-phosphono-1,3-disulfonic acid and 4-fluoro-3-sulfobenzylphosphonic acid by Montoneri et al.^[36,37], mostly in combination with amine linkers. The synthesis of most metal phosphonates is accomplished under hydrothermal conditions. Such reactions are often known to be strongly dependent on the process parameters, e.g. reaction time, temperature, heating rate, and the compositional parameters, e.g. molar composition of the starting materials, pH of the reaction mixture or concentration. An elegant way for the exploration of these complex systems can be accomplished using high-throughput (HT) methods.^[38-41] These allow a systematic and efficient investigation of large parameter spaces giving rise to the accelerated discovery of new compounds and optimization of synthesis parameters. Due to the large amounts of data, reaction and structural trends can be obtained. Investigations using new organic linker molecules are typically conducted using a two step approach. In order to get an overview about suitable metal/organic linker combinations that lead to crystalline hybrid compounds, discovery arrays are set up. In these reactions a wide variety of metal ions as well as compositional parameters, especially the influence of pH is

[a] Institut für Anorganische Chemie, Christian-Albrechts-Universität, Max-Eyth-Strasse 2, 24118 Kiel, Germany
Fax: +49-431-880-1775
E-mail: stock@ac.uni-kiel.de

Supporting information for this article is available on the WWW under <http://www.eurjic.org/> or from the author.

studied. Once new phases have been discovered, focused arrays are used, in which the synthesis parameters are only slightly varied in order to find the optimum synthesis conditions. Here we report, the synthesis and structural characterization of new copper(II)- and lead(II)-based compounds containing 4-phosphonobenzenesulfonic acid (H_3L) using our HT-methodology. Starting with metal screening discovery arrays, Pb^{2+} as well as Cu^{2+} ions were identified to form new crystalline hybrid compounds. The in-depth HT study of the systems $M^{2+}/H_3L/NaOH/H_2O$ ($M = Pb^{2+}, Cu^{2+}$) using discovery and focused arrays allowed to establish the fields of formation of the title compounds.

Results and Discussion

Metal Screening Investigation

A high-throughput screening of different divalent metal ions was initiated. For this discovery array a set of twelve M^{2+} ions was tested in a 48 HT-reactor system (V_{max} per reaction of 200 μL).^[38,42] To determine the influence of ionic radii,^[43] Ni^{2+} , Mg^{2+} , Cu^{2+} , Zn^{2+} , Co^{2+} , Fe^{2+} , Mn^{2+} , Sn^{2+} , Cd^{2+} , Sr^{2+} , Pb^{2+} and Ba^{2+} ions were chosen and were varied in the molar ratio range $M^{2+}:H_3L:NaOH:H_2O = 1.5-4:1:3:556$ (see Table S1). Molar ratios $M^{2+}:H_3L > 1$ were used since the reported metal phosphonosulfonate compounds have always high metal-to-linker ratios.^[26,35] All products were analyzed via high-throughput X-ray powder diffraction (XRPD). In this discovery array, only reactions with Ni^{2+} , Mg^{2+} , Cu^{2+} , Zn^{2+} , Mn^{2+} , Sn^{2+} , Cd^{2+} and Pb^{2+} resulted in the formation of crystalline products, while Co^{2+} , Fe^{2+} , Sr^{2+} and Ba^{2+} ions produced only X-ray amorphous substances (see Figure S1). By focusing the study only on the crystalline substances, a second metal ion screening test was conducted and the amount of added base was varied. In this second discovery array molar ratios $M^{2+}:H_3L:NaOH:H_2O = 3:1:0-5:556$ for $M^{2+} = Ni^{2+}, Mg^{2+}, Cu^{2+}, Zn^{2+}, Mn^{2+}, Sn^{2+}$ were used. For Cd^{2+} and Pb^{2+} molar ratios $M^{2+}:H_3L:NaOH:H_2O = 1.5:1:0-5:556$ and $4:1:0-5:556$, respectively, were chosen based on the results from the previous metal-screening investigations (see Table S2). The second discovery library yielded single crystalline compounds containing Pb^{2+} and Cu^{2+} ions. The other metal ions led to solids that were either X-ray amorphous or microcrystalline. Through comparison with literature data most of the crystalline compounds were identified as metal or metal hydroxides/oxides. Further investigations were focused on the use of Pb^{2+} and Cu^{2+} ions. Focused arrays were set-up in order to investigate these systems in more detail to establish their fields of formation.

High-Throughput Investigation of 1

To find the optimal precursor and to investigate the role of the counter ion, various lead salts were screened. In addition to $Pb(NO_3)_2$, $PbCl_2$, $Pb(NO_3)_2$, $PbSO_4$ and $Pb(CH_3COO)_2$ were also tested as starting materials. $Pb(NO_3)_2$ was established as the best metal salt as the other salts produce mixed phases comprised of $Pb_2[(O_3P-C_6H_4-SO_3)(OH)]$ (**1**), PbO and unreacted starting materials. To establish the optimal formation field of **1**, the molar ratio $Pb(NO_3)_2:H_3L:NaOH:H_2O$ was varied in a broad range. In this focused array, the molar ratio $Pb(NO_3)_2:H_3L$ was kept fixed at 1:2, 1:1, 2:1, 3:1 and 4:1 and the amount of NaOH was varied (see Table S3). The ternary diagram in Figure 1 shows the result of that HT set-up which

reveals the best molar ratios to be $Pb(NO_3)_2:H_3L:NaOH = 4:1:4-5$. At these compositions, **1** is obtained as a pure phase product. Based on these results scale-up of **1** was accomplished in a Teflon lined reactor with a volume of 2 mL and the product was used for IR, TG and elemental analysis.

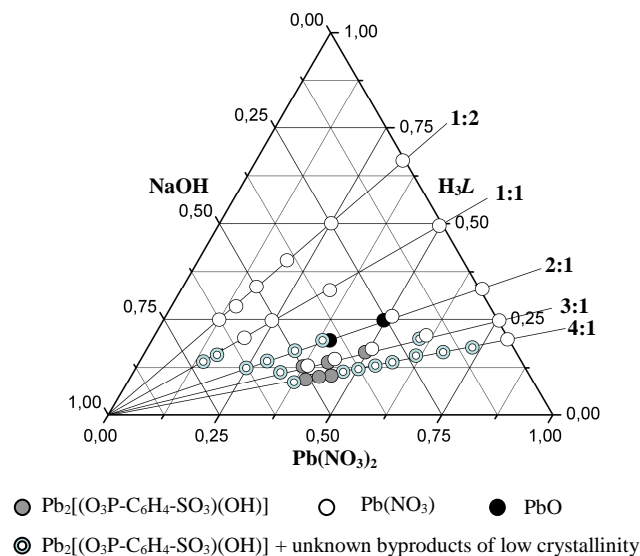


Figure 1. Crystallization diagram of the system $Pb(NO_3)_2:H_3L:NaOH:H_2O$ (**1**). Results are based on powder XRD measurements. Phase-mixtures are indicated by overlapping symbols with two or more colors. Each diagonal line represents the fixed molar ratios of $Pb(NO_3)_2:H_3L$.

High-Throughput Investigation of 2, 3, 4 and 5

A comprehensive HT-study was conducted to establish the formation fields of the copper compounds **2**, **3**, **4** and **5**. For that reason, the optimal starting copper(II) salt had to be determined and all possible areas in the ternary diagram had to be checked. HT-screening of various copper (II) salts comprising $Cu(NO_3)_2 \cdot 3H_2O$, $CuCl_2 \cdot 2H_2O$, $CuSO_4 \cdot 5H_2O$ and $Cu(CH_3COO)_2 \cdot H_2O$ was conducted with the molar ratios $Cu^{2+}:H_3L:NaOH = 1-4:1-4:1-4$. $Cu(CH_3COO)_2 \cdot H_2O$ salt tends to produce copper(I)oxide and $CuSO_4 \cdot 5H_2O$ exclusively led to X-ray amorphous substances. The results from the XRPD measurements showed that only $Cu(NO_3)_2 \cdot 3H_2O$ and $CuCl_2 \cdot 2H_2O$ produced the desired compounds. Since $Cu(NO_3)_2 \cdot 3H_2O$ produces mixed phase products, $CuCl_2 \cdot 2H_2O$ was established as the optimal starting material for further HT-studies. For the systematic investigation of the system $CuCl_2 \cdot 2H_2O / H_3L/NaOH$ two discovery arrays comprising 96 reactions were set up (see Figure 2). The ternary diagram showing the molar ratios employed as well as the results of the XRPD measurements is shown in Figure 2A. At molar ratios $H_3L:NaOH < 0.4$, CuO is formed (black circles in Figure 2A). Small amounts of NaOH, in combination with large amounts of H_3L and $CuCl_2$ led to clear solutions (white circles in Figure 2A). The three title compounds **3**, **4** and **5** only form at well defined molar ratio ranges, each in a small field of formation. Compound **2**, which was previously observed in the metal screening experiments, could not be reproduced in any following reaction. These results were used to set up focused arrays (Figure 2B and 2C). The compound $NaCu(O_3P-C_6H_4-SO_3)(H_2O)_3$ (**3**) was discovered in the focused arrays but could only be obtained as a microcrystalline product. Phase purity was demonstrated by elemental analysis as well as indexing of

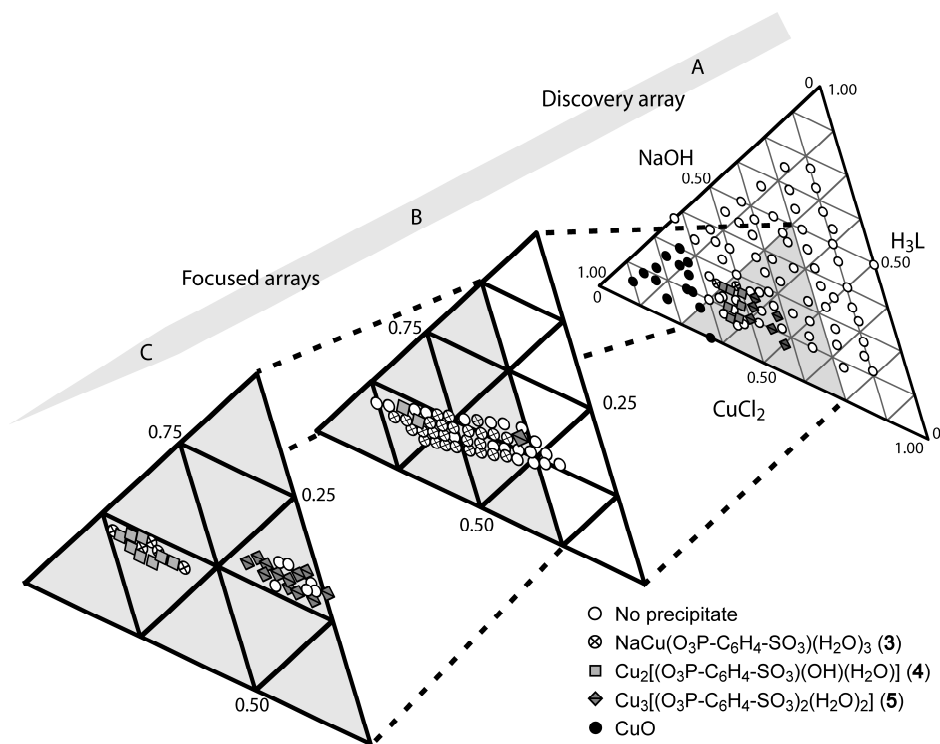


Figure 2. HT-investigation of copper(II) compounds starting with the two discovery arrays **A** (96 individual reactions). Middle: focused array **B** with 48 reactions indicates the approximate formation fields of compounds **3**, **4** and **5**. Focused array **C** with 48 reactions reveals the specific formation field of compounds **4** and **5**. Results are based on powder XRD patterns. Molar ratio values are normalized to 1.

the X-ray powder pattern. The first focused array (Figure 2B) indicated the preferred formation fields of compounds **3**, **4**, and **5**. Compound **3** is obtained in a wide molar ratio ranges $\text{CuCl}_2 \cdot 2\text{H}_2\text{O} : \text{H}_3\text{L} : \text{NaOH} = 3\text{-}3.5 : 1 : 3\text{-}5.3$. The second focused array (Figure 2C) was set up to get more precise information about the formation of **4** and **5**. Title compound **4** is formed in the molar ratio ranges $\text{CuCl}_2 \cdot 2\text{H}_2\text{O} : \text{H}_3\text{L} : \text{NaOH} = 2.8\text{-}3 : 1 : 4.8\text{-}4.9$ (pH ~ 5) and compound **5** at $2.9\text{-}3.2 : 1 : 2.6\text{-}2.9$ (pH ~ 4) respectively. To produce larger amounts of the substances, the HT reactors were used and the optimized reaction conditions were employed.

Crystal Structure Determination

The X-ray scattering factors of phosphorus and sulfur are very similar. Nevertheless, the distinction can be made by comparison of the P-O and S-O bond lengths. In $[\text{Pb}_3(\text{Z}_2)(\text{H}_2\text{O})_2] \cdot 4\text{H}_2\text{O}$ and $[\text{Pb}(\text{HZ})(\text{phen})]\text{H}_2\text{O}$ [$\text{Z} = (\text{O}_3\text{P}-\text{C}_6\text{H}_4-\text{SO}_3)^{3-}$, phen = 1,10-phenanthroline] P-O and S-O bond lengths in the range of 149.6(5)-157.8(5) pm and 144.3(9)-147.2(6) pm, respectively, were reported.^[35] The copper (II) phosphonatosulfonates, $\text{Cu}_2[(\text{O}_3\text{P}-\text{C}_2\text{H}_4-\text{SO}_3)(\text{OH})(\text{H}_2\text{O})](\text{H}_2\text{O})$ and $\text{Cu}_{2.5}(\text{O}_3\text{P}-\text{C}_2\text{H}_4-\text{SO}_3)(\text{OH})_2$ ranges from 151.9(3)-155.9(3) pm for P-O and 146.0(4)-147.2(3) pm for S-O.^[26] These values clearly show, that the S-O bond lengths are shorter than the P-O distances and thus, facilitate the identification of S and P atoms.

Crystal Structure of $\text{Pb}_2[(\text{O}_3\text{P}-\text{C}_6\text{H}_4-\text{SO}_3)(\text{OH})]$ (**1**)

The asymmetric unit of **1** is shown in Figure 3. The crystal structure was solved and refined in the triclinic space group $P\bar{1}$. The asymmetric unit contains two Pb^{2+} ions, one hydroxide ion O7-H7 and one $[\text{O}_3\text{P}-\text{C}_6\text{H}_4-\text{SO}_3]^{3-}$ ion with a positional disorder. Pb1 and Pb2 are seven- and fivefold coordinated, respectively,

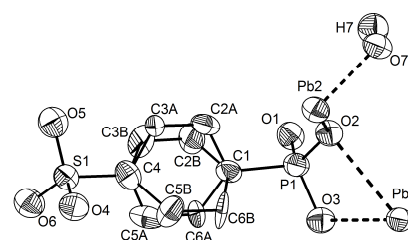


Figure 3. Asymmetric unit of **1**. Hydrogen atoms attached to C-atoms are not shown for clarity. Thermal ellipsoids are drawn at 50% probability.

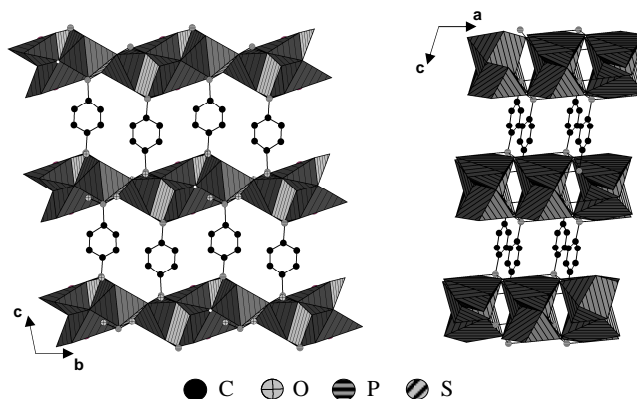


Figure 4. Left: infinite chains of edge-sharing $(\text{PbO}_7/\text{PbO}_5)$ -polyhedra along the b -axis in (**1**). Right: chains of PbO_x polyhedra are connected to each other via $-(\text{PO}_3)^{2-}$ and $-(\text{SO}_3)^-$ groups along the a -axis. Left and right: the layers are interconnected by the phenyl groups of the ligand molecules. The disordered phenyl rings and H-atoms were omitted for visual clarity.

and form a distorted pentagonal bipyramidal (PbO_7) and a distorted square pyramidal geometry (PbO_5 polyhedra). The Pb-O bond lengths are in the range of 225.3(12)-286.8(12) pm which are in agreement with literature data.^[35,44] Edge-sharing of the PbO_7 and PbO_5 polyhedra is observed which results in the formation of infinite zig-zag chains along the b -axis. These chains are connected to each other by the sulfonate and phosphonate groups along the a -axis. These layers are interconnected via the phenyl groups of the ligand to form a three-dimensional framework (see Figure 4).

Crystal Structure of $\text{Cu}_{1.5}[(\text{O}_3\text{P-C}_6\text{H}_4\text{-SO}_3)(\text{H}_2\text{O})]$ (2)

The Cu^{2+} ions in this structure have two types of coordination. One Cu^{2+} ion resides on a special position and is coordinated by four oxygen atoms from the ligand and two oxygen atoms from water molecules to form Jahn-Teller distorted CuO_6 polyhedra. The other Cu^{2+} ion is surrounded by five oxygen atoms with a square pyramidal geometry CuO_5 . These edge-sharing polyhedra form Cu_2O_8 clusters which are connected to the CuO_6 polyhedra through the phosphonate and sulfonate groups to form layers in the a,c -plane (Figure 5, compound 2, 2-D). The final three-dimensional assembly is achieved by the phenyl groups between the layers. Similar to compound 1, the phenyl groups is disordered along the C1/C4-axis.

Crystal Structure of $\text{Cu}_2[(\text{O}_3\text{P-C}_6\text{H}_4\text{-SO}_3)(\text{OH})(\text{H}_2\text{O})]$ (4)

The asymmetric unit is composed of two Cu^{2+} ions (Cu1, Cu2) and one 4-phosphonatobenzenesulfonate ion, as well as one water molecule and one hydroxide ion. Cu1 is surrounded by three oxygen atoms from the ligands and two hydroxide $\mu_3\text{-O}_7$ ions, thus forming a square pyramidal CuO_5 unit. Cu2 is

coordinated to four oxygen atoms from the ligand, one hydroxide oxygen atom and one water molecule which results in Jahn-Teller distorted CuO_6 polyhedra. Alternating edge-sharing CuO_5 and CuO_6 polyhedra form zig-zag chains along the b -axis (Figure 5, compound 4, 1-D). Phosphonate groups from the ligand link the chains along the c -axis to create a layered structure in the b,c -plane (Figure 5, compound 4, 2-D). The final dense three-dimensional framework is then completed by the phenyl groups of the ligand which link the layers along the a -axis (Figure 5, compound 4, 3-D).

Crystal Structure of $\text{Cu}_3[(\text{O}_3\text{P-C}_6\text{H}_4\text{-SO}_3)_2(\text{H}_2\text{O})_2]$ (5)

The asymmetric unit of 5 is comprised of three Cu^{2+} ions, two 4-phosphonatobenzenesulfonate ions and two water molecules. Cu1 is exclusively coordinated by four oxygen atoms from phosphonate groups and forms a square planar CuO_4 unit. Cu3 is connected to two sulfonate and phosphonate oxygen atoms each and one water molecule, thereby creating a square pyramidal geometry (CuO_5 polyhedra). For Cu2, Jahn-Teller distorted CuO_6 polyhedra are observed with three oxygen atoms from phosphonate groups, two from sulfonate groups and one from a water molecule. Corner-sharing, CuO_4 , CuO_5 and CuO_6 polyhedra build hexanuclear Cu_6O_{24} clusters (Figure 5, Compound 5, 1-D) which are connected through sulfonate and phosphonate groups along the a -axis to form a chain-like structure. These chains are connected to each other by the phenyl rings to form layers (Figure 5, compound 5, 2-D) which are held together exclusively by hydrogen bonding (Figure 5, compound 5, 3-D, hydrogen bond distances are given in Table S5 in the Supporting Information).

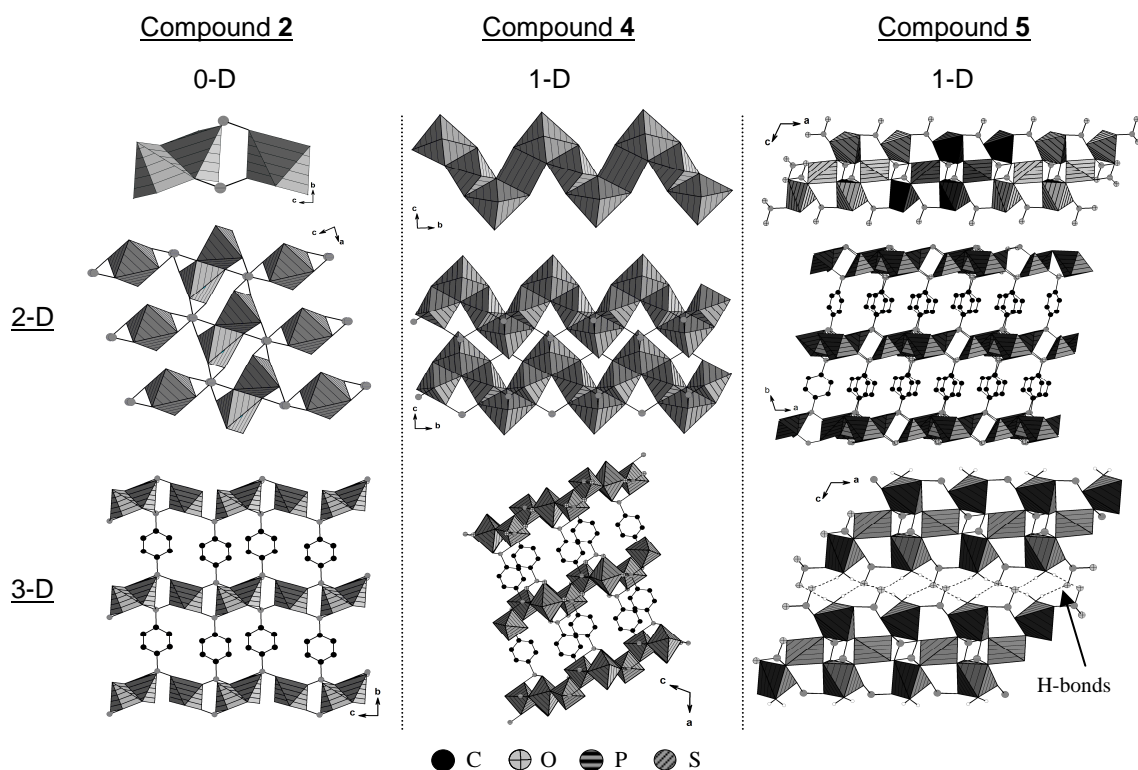


Figure 5. Crystal structure of compounds $\text{Cu}_{1.5}[(\text{O}_3\text{P-C}_6\text{H}_4\text{-SO}_3)(\text{H}_2\text{O})]$ (2), $\text{Cu}_2[(\text{O}_3\text{P-C}_6\text{H}_4\text{-SO}_3)(\text{OH})(\text{H}_2\text{O})]$ (4) and $\text{Cu}_3[(\text{O}_3\text{P-C}_6\text{H}_4\text{-SO}_3)_2(\text{H}_2\text{O})_2]$ (5) starting from the Cu-O building units as well as their connection by the phosphonate / sulfonate groups and the phenyl rings. For the sake of clarity, disordered phenyl rings and H-atoms from phenyl groups are omitted.

Table 1. Single crystal data for compounds $\text{Pb}_2[(\text{O}_3\text{P}-\text{C}_6\text{H}_4-\text{SO}_3)(\text{OH})]$ (**1**), $\text{Cu}_{1.5}[(\text{O}_3\text{P}-\text{C}_6\text{H}_4-\text{SO}_3)(\text{H}_2\text{O})]$ (**2**), $\text{Cu}_2[(\text{O}_3\text{P}-\text{C}_6\text{H}_4-\text{SO}_3)(\text{OH})(\text{H}_2\text{O})]$ (**4**) and $\text{Cu}_3[(\text{O}_3\text{P}-\text{C}_6\text{H}_4-\text{SO}_3)_2(\text{H}_2\text{O})_2]$ (**5**).

Parameter	1	2	4 ^[a]	5
Chemical formula	$\text{C}_6\text{H}_5\text{Pb}_2\text{O}_7\text{PS}$	$\text{C}_6\text{H}_6\text{Cu}_{1.5}\text{O}_7\text{PS}$	$\text{C}_6\text{H}_7\text{Cu}_2\text{O}_8\text{PS}$	$\text{C}_{12}\text{H}_{12}\text{Cu}_3\text{O}_{14}\text{P}_2\text{S}_2$
Crystal system	triclinic	triclinic	monoclinic	triclinic
Space group	$P\bar{1}$	$P\bar{1}$	$P2_1/n$	$P\bar{1}$
<i>a</i> [pm]	515.75(7)	484.70(5)	1160.33(9)	998.0(2)
<i>b</i> [pm]	1048.05(15)	994.49(11)	706.33(4)	1006.6(2)
<i>c</i> [pm]	1085.83(17)	995.76(11)	1397.17(10)	1137.7(2)
α [°]	96.502(12)	88.438(14)	90.00	96.63(3)
β [°]	95.217(12)	78.152(13)	110.630(8)	113.63(3)
γ [°]	94.515(11)	83.756(13)	90.00	101.82(3)
<i>V</i> [10 ⁶ pm ³]	578.38(15)	466.97(9)	1071.66(13)	999.7(3)
<i>Z</i>	2	2	4	2
Formula weight	666.51	348.45	397.25	696.90
Total number of data collected	8182	4645	7484	20336
Unique/obsd. data [$I > 2\sigma(I)$]	2458/1990	2233/1706	1861/1521	5794/3947
<i>R</i> (int.)	0.0748	0.0412	0.0479	0.0746
<i>R</i> 1, <i>wR</i> 2 [$I > 2\sigma(I)$]	0.0572/0.1057	0.0410/0.1008	0.0462/0.1212	0.0677/0.1227
<i>R</i> 1, <i>wR</i> 2 (all data)	0.0754/0.1122	0.0600/0.1097	0.0547/0.1310	0.1108/0.1375
GOF	1.144	1.040	1.024	1.065
Δe min./max. [$e \cdot \text{\AA}^{-3}$]	-2.322/1.769	-0.798/0.794	-0.998/1.188	-0.850/0.973

[a] Compound **4** is non-merohedrally twinned.

Characterization of Compound 3

Up to now, **3** could only be isolated as a microcrystalline powder. The indexing and refinement of the powder XRD pattern using the Louer's algorithm implemented in the STOE WinXPOW^[45] program results in a monoclinic unit cell with the lattice parameters $a = 2162.35(14)$ pm, $b = 875.27(7)$ pm, $c = 1282.68(7)$ pm, $\beta = 113.445(5)^\circ$ (the results of the refinement in Table S7). The composition of **3** was determined with the combined interpretation of thermogravimetric (TG), CHNS and Energy Dispersive X-ray (EDX) analyses data. Composition of **3** was then determined to be $\text{NaCu}(\text{O}_3\text{P}-\text{C}_6\text{H}_4-\text{SO}_3)(\text{H}_2\text{O})_3$. Atomic ratio via EDX measurement: Na/Cu/P/S = 1:1:1:1. Experimental amount of water in % (theoretical) = 11.6(12.3) (Figure S5).

IR-Spectroscopy

Compounds **1**, **3**, **4** and **5** were studied by IR spectroscopy (Figure S2). Their IR spectra exhibit broad bands in the region between 3600 and 3100 cm^{-1} , which are due to OH-stretching vibrations of the water molecules involved in weak hydrogen bonding. The weak band at 1630 ± 20 cm^{-1} is assigned to the deformation vibrations of water molecules. A sharp band seen at 3540 cm^{-1} for $\text{Cu}_2[(\text{O}_3\text{P}-\text{C}_6\text{H}_4-\text{SO}_3)(\text{OH})(\text{H}_2\text{O})]$ (**4**) is attributed to the hydroxyl group, however, a similar band was not seen for $\text{Pb}_2[(\text{O}_3\text{P}-\text{C}_6\text{H}_4-\text{SO}_3)(\text{OH})]$ (**1**) due to overlapping by intensive water bands. $\text{NaCu}(\text{O}_3\text{P}-\text{C}_6\text{H}_4-\text{SO}_3)(\text{H}_2\text{O})_3$ (**3**) shows in addition a broad band at 3031 cm^{-1} and comparison with literature values indicates that this could be due to OH-stretching vibrations forming strong hydrogen bonds.^[46,47,48] For all compounds the C-H stretching bands could not be seen due to overlap with the broad O-H bands, but all compounds exhibit a band in the region of 830 ± 10 cm^{-1} corresponding to the aromatic C-H out-of-plane deformation vibration. This band is typical for para substituted phenyl rings.^[49] The weak narrow band at 1386 ± 5 cm^{-1} which is found in all IR-spectra can be assigned to the P-C stretching vibration. Strong sharp bands in

the fingerprint region of 1250 – 900 cm^{-1} are assigned to symmetric and asymmetric stretching vibrations of CPO_3 and CSO_3 groups.^[50]

Thermal Properties

Thermogravimetric measurements confirmed the number of water molecules in the structures and provide insight in the decomposition temperatures of the compounds (Figure S5). The solid substances after the TGA analyses were characterized by powder XRD measurements. Compounds **3-5** exhibit the presence of water molecules. $\text{Pb}_2[(\text{O}_3\text{P}-\text{C}_6\text{H}_4-\text{SO}_3)(\text{OH})]$ (**1**) decomposes at about 500 °C to the final product, which is a mixture of $\text{Pb}_3(\text{PO}_4)_2$, PbO and PbSO_4 . The dehydration of compound **3** occurred in the temperature range of 30 – 150 °C. The water molecules are released in two steps (weight loss [%] calc./obsd = 14.4/13.0). Decomposition of the dehydrated phase is observed between 330 and 420 °C and as the final product crystalline $\text{Na}_3\text{Cu}_9(\text{PO}_4)_7$ was identified.^[51] The TGA curve of **4** is rather elaborate. The dehydration occurs up to 250 °C (weight loss [%] calc./obsd = 4.5/4.5, one water molecule per formula unit). The decomposition of the dehydrated phase is a multistep process and was not completed at the final temperature of 650 °C. These steps can not be assigned to defined decomposition products. CuO was identified as the only crystalline product by XRPD. The two coordinated water molecules in compound **5** are released from room temperature up to 150 °C. The resulting dehydrated structure is thermally stable up to 450 °C and decomposes into light blue coloured $\text{Cu}_3(\text{PO}_4)_2$ (weight loss [%] calc./obsd = 45.4/42.5).

Magnetic Properties

Based on EDX measurements, compound **3** was always contaminated with minor impurities of CuO, which were not detectable in the XRPD investigation. Only **4** and **5** were obtained as pure compounds and therefore investigated by magnetic susceptibility measurements. Figure S7 shows the results of the magnetic investigation in the temperature from 2-

300 K. For compound **4** the following plots are shown: χT plotted as a function of temperature (dc field) and frequency dependent ac-susceptibility (ac frequencies: 40, 400 and 4000 Hz, $T = 2 - 7$ K). For compound **5** the susceptibility χ , inverse susceptibility χ^{-1} and χT plotted as a function of temperature are shown. Compound **5** displays Curie-Weiss behaviour in the range between and 40-300 K. The Curie-Weiss equation $\chi = C/(T-\theta)$ was applied to fit the data (**5**: $C = 1.03 \text{ K cm}^3 \text{ mol}^{-1}$, $\theta_W = 1.52 \text{ K}$). The effective magnetic moment calculated from the fitted data is $1.7 \mu_B$ for **5**. This value compares well with the spin-only theoretical value for Cu^{2+} ($1.73 \mu_B$). Looking at the structure of **5** it appears that the primary magnetic motive is a trimer consisting of a square planar CuO_4 polyhedron μ -O connected to two square pyramidal CuO_5 polyhedra. Only weak coupling through the phosphonate groups takes place. Antiferromagnetic interactions are dominating at lower temperatures. For compound **4** at temperatures between 7 and 300 K, antiferromagnetic interactions were observed which switch to ferro/ferromagnetic interactions between 2.2 and 7 K in two steps and finally at 2.2 K antiferromagnetic interactions are found (inset Figure S7, top left). The ac measurements show an increase of the out-of-phase component at higher frequencies (Figure S7, top right). For **4** the spin-topology is more complex. Taking only the short Cu-O bond lengths into account a one-dimensional chain of square planar CuO_4 polyhedra is observed. Strong coupling takes place through the equal sided μ_3 -OH centred Cu_3 triangles which leads to spin frustration. Weaker coupling is only present through the phosphonate groups connecting neighbouring chains to layers and the organic part of the ligand connecting adjacent layers. The complex magnetic behaviour is probably further complicated by structural changes upon cooling. Thus further studies need to be performed to fully characterize this phenomenon.^[52]

Discussion

High-throughput metal ion and counter ion screening enabled the efficient search for optimal starting materials. From these results, $\text{Pb}(\text{NO}_3)_2$ and $\text{CuCl}_2 \cdot 2\text{H}_2\text{O}$ were selected for the discovery and focused arrays. Subsequent HT experiments led to the optimal synthesis conditions of the newly discovered compounds. These studies exemplify the multifaceted application of HT-investigation and shows that the methodology can also be used in the discovery of new metal phosphonosulfonates containing rigid organic linker molecules. The earliest report of the incorporation of 4-phosphonobenzenesulfonic acid was given by A. Clearfield et al., who obtained a zirconium sulfonophenylphosphonate by sulfonation of $\text{Zr}(\text{O}_3\text{P-C}_6\text{H}_5)_2$ with fuming sulfuric acid. However no detailed structural characterization of the compound was mentioned.^[19] The first structural analysis of this class of compounds by single crystal X-ray diffraction was done by Mao et al. by using 3-phosphonobenzenesulfonic acid in combination with co-ligands such as bipyridine or phenanthroline.^[31-35] These studies showed that 3-phosphonobenzenesulfonic acid is a versatile ligand that can adopt various coordination modes. Its use in combination with co-ligands lead mostly to structures containing isolated M-O clusters and the nature of the formed clusters is strongly affected by the amount and coordination nature of the co-ligand. The present study demonstrates that 4-phosphonobenzenesulfonic acid is also a versatile linker for the synthesis of metal phosphonosulfonates. This can already be seen in the absence of co-ligands. Thus, the compounds in this

work contain isolated mono-, di-, hexanuclear M-O clusters or infinite M-O chains which are, with the exception of **5**, connected by the 4-phosphonatobenzenesulfonate ions to form pillared layered structures. In comparison to our previous results using the flexible phosphonoalkylsulfonic acids some structural similarities of the Cu^{2+} containing compounds are observed. $\text{Cu}_2[(\text{O}_3\text{P-C}_6\text{H}_4\text{-SO}_3)(\text{OH})(\text{H}_2\text{O})]$ (**4**), synthesized under similar reaction conditions as $\text{Cu}_2[(\text{O}_3\text{P-C}_2\text{H}_4\text{-SO}_3)(\text{OH})(\text{H}_2\text{O})](\text{H}_2\text{O})$ ^[26] exhibits also infinite M-O-M zigzag chains of CuO_6 polyhedra which are further connected to a pillared layered structure. While the use of the alkyl linker leads to small pores that are filled with non-coordinating water molecules, the more bulky and rigid phenyl groups do not allow the incorporation of water molecules. These structural similarities are also reflected in the magnetic behaviour where switching from antiferromagnetic to ferro/ferromagnetic and again to antiferromagnetic interactions at very low temperatures are observed. Compound **5**, $\text{Cu}_3[(\text{O}_3\text{P-C}_6\text{H}_4\text{-SO}_3)_2(\text{H}_2\text{O})_2]$, is structurally related to the copper compounds with the $-\text{C}_2\text{H}_4-$ and the $-\text{C}_4\text{H}_8-$ containing linker molecules, i.e. $\text{Cu}_{1.5}[(\text{O}_3\text{P-C}_2\text{H}_4\text{-SO}_3)(\text{H}_2\text{O})]$ and $\text{Cu}_{1.5}[(\text{O}_3\text{P-C}_4\text{H}_8\text{-SO}_3)(\text{H}_2\text{O})] \cdot 1.15\text{H}_2\text{O}$, respectively. Although the clusters in these compounds are slightly different, Cu_6O_{24} cluster in **5** and Cu_3O_{12} cluster in the other two compounds, they are interconnected to layers by the phosphonosulfonate ions. These layers are only held together by hydrogen bonding interactions. Compound **1** is only the second example of co-ligand-free lead phosphonosulfonate. $[\text{Pb}_3(m\text{-O}_3\text{P-C}_6\text{H}_4\text{-SO}_3)_2(\text{H}_2\text{O})_2] \cdot 4\text{H}_2\text{O}$ contains 1D chains of Pb_3O_4 clusters which are further bridged by the phosphonosulfonate ligands.^[35] An open structure is formed with water molecules occupying the pores. The change of the position of the functional group from *meta* to *para* leads to drastic changes in the structure of **1**, although both compound were synthesized under very similar conditions. Thus we observe the formation of Pb-O zig-zag chains that are connected to pillared layered structure without any pores.

Conclusions

High-throughput investigation of $\text{M}^{2+}/\text{H}_3\text{L}/\text{NaOH}/\text{H}_2\text{O}$ yielded five new compounds $\text{Pb}_2[(\text{O}_3\text{P-C}_6\text{H}_4\text{-SO}_3)(\text{OH})]$ (**1**), $\text{Cu}_{1.5}[(\text{O}_3\text{P-C}_6\text{H}_4\text{-SO}_3)(\text{H}_2\text{O})]$ (**2**), $\text{NaCu}(\text{O}_3\text{P-C}_6\text{H}_4\text{-SO}_3)(\text{H}_2\text{O})_3$ (**3**), $\text{Cu}_2[(\text{O}_3\text{P-C}_6\text{H}_4\text{-SO}_3)(\text{OH})(\text{H}_2\text{O})]$ (**4**) and $\text{Cu}_3[(\text{O}_3\text{P-C}_6\text{H}_4\text{-SO}_3)_2(\text{H}_2\text{O})_2]$ (**5**) in the phosphonatoarylsulfonate family. Metal screening provided the information about suitable metal ions for the linker 4-phosphonobenzenesulfonic acid. Discovery and focused arrays were employed to find and exactly determine the formation field of the respective compounds. All compounds are observed in a small formation field within well defined molar ratio ranges. Each of the title compounds, with the exception of **2**, can be synthesized with high reproducibility and phase purity. In the structures of **2**, **4** and **5** different coordination modes of the ligand are observed and thereby multiple types of Cu-O connectivities are observed. These range from isolated CuO_6 polyhedra and $\text{Cu}_2\text{O}_8/\text{Cu}_6\text{O}_{24}$ cluster to zig-zag chains of edge sharing CuO_5 and CuO_6 polyhedra. These are connected by the phosphonate and sulfonate groups to form layers or a chain-like structure, which are further connected by the phenyl rings of the linker molecules. We have demonstrated that our high-throughput methodology can be employed with high efficiency for the detailed investigation of hydrothermal reaction systems ranging from metal screening experiments to the discovery of new compounds using discovery array as well as the optimization of synthesis conditions by employing focused arrays. Further experiments

with the rigid ligand 4-phosphonobenzenesulfonic acid are underway to investigate the influence of the rigid aryl group on the structural chemistry.

Experimental Section

Materials and Methods: 4-phosphonobenzenesulfonic acid (H_3L) was synthesized as previously described in three steps, starting from 4-bromobenzenesulfonylchloride, sodium ethanolate and triethylphosphite.^[53] All other reagents were of analytical grade (Aldrich and ABCR) and were used without further purification. High-throughput XRPD experiments were carried out in transmission mode using a STOE high-throughput powder diffractometer equipped with an image-plate position-sensitive detector (IPPSD). MIR spectra were recorded with an ATI Matheson Genesis spectrometer in the spectral range 4000-400 cm^{-1} using the KBr disc method. Thermogravimetric analyses were carried out in a nitrogen atmosphere (75 mL min^{-1} , 30-650 $^{\circ}C$, 4 $^{\circ}Cmin^{-1}$) using a NETZSCH STA 409 CD analyzer. CHNS analyses were performed with a Eurovektor EuroEA Elemental Analyzer. The semiquantitative elemental analyses were performed with a Phillips ESEM XL 30 hot cathode scanning electron microscope equipped with an energy-dispersive X-ray (EDX) EDAX analyzer for elemental analysis. Magnetic measurements for compounds **4** and **5** were performed with a Physical Property Measuring System (PPMS) from Quantum Design (9 T magnet), at 1 kOe and 10 kOe (DC-field) respectively in the temperature range from 2-300 K (ZFC).

High-Throughput Experiments: The reaction system $M^{2+}/H_3L/NaOH/H_2O$ was investigated using various molar ratios $M^{2+}:H_3L:NaOH$ (discovery and focused arrays) employing high-throughput methods (process and compositional parameters are listed in Tab. S1-S4 in the Supporting Information). Each HT experiment was performed under hydrothermal conditions in a custom-made stainless steel high-throughput reactor system containing 48 PTFE inserts each with a maximum volume of 300 μL .^[29] All reagents were manually dosed using aqueous solutions of the reactants (0.4 M to 1.2 M), with the exception of insoluble $Pb(NO_3)_2$ which was weighed in directly. The exact amounts of starting materials are given in the Table S1-S4. The evaluations of the HT experiments are based on XRPD measurements.

Synthesis of $Pb_2[(O_3P-C_6H_4-SO_3)(OH)]$ (1**):** In a typical HT experiment **1** was obtained by the following procedure ($Pb^{2+}:H_3L:NaOH = 4:1:4$). $Pb(NO_3)_2$ (26.5 mg, 0.08 mmol) was weighed in the PTFE insert and was mixed with aqueous solutions of H_3L (20 μL , 0.02 mmol), 1M NaOH (80 μL , 0.08 mmol) and 100 μL of deionized water. The mixture was heated at 150 $^{\circ}C$ for 48 h. The scale-up of **1** was accomplished using larger PTFE inserts with $V_{max} = 2500 \mu L$ employing $Pb(NO_3)_2$ (198.7 mg, 0.60 mmol), H_3L (200 μL , 0.15 mmol), 1M NaOH (600 μL , 0.60 mmol) and 700 μL of deionized water. The product (74 mg, 75% based on H_3L) contained fine white needles (SEM micrograph Figure S6) and was identified by PXRD diffraction (Figure S3) and elemental analysis. $Pb_2[(O_3P-C_6H_4-SO_3)(OH)]$ (**1**), $M = 666.51 \text{ g mol}^{-1}$: EDX measurement: atomic ratio P/S/Pb = 1:1:2; elemental analysis [%]: found C 10.5, H 0.5, S 4.6; calcd. C 10.8, H 0.8, S 4.8.

Synthesis of $NaCu(O_3P-C_6H_4-SO_3)(H_2O)_3$ (3**):** In a typical HT experiment **3** was obtained by the following procedure ($Cu^{2+}:H_3L:NaOH = 2.80:1:4.75$). Aqueous solutions of $CuCl_2$ (0.056 mmol, 56 μL), H_3L (0.02 mmol, 20 μL), NaOH (0.095 mmol, 95 μL) and H_2O (1.61 mmol, 29 μL) were mixed in a 300 μL reactor. The

mixture was heated at 150 $^{\circ}C$ for 48 h. The synthesis of compound **3** could not be scaled-up in glass or Teflon[®] reactors. Therefore, a larger amount of the pure phase product was collected from Teflon[®] reactors of a separate high-throughput experiment. The HT experiment contained 24 identical reaction mixtures with the same molar ratio $Cu^{2+}:H_3L:NaOH = 2.80:1:4.75$. The total product (72 mg, 40% based on H_3L) contained fine light blue powder and was identified by PXRD diffraction (Fig S3) and elemental analysis. $NaCu(O_3P-C_6H_4-SO_3)(H_2O)_3$ (**3**), $M = 375.72 \text{ g mol}^{-1}$: EDX measurement: atomic ratio P/S/Cu/Na = 1:1:1:1; elemental analysis [%]: found C 19.2, H 1.7, S 8.3; calcd. C 19.7, H 2.4, S 8.7.

Synthesis of $Cu_2[(O_3P-C_6H_4-SO_3)(OH)(H_2O)]$ (4**):** In a typical HT experiment **4** was obtained by the following procedure ($Cu^{2+}:H_3L:NaOH = 3.00:1:4.85$). Aqueous solutions of $CuCl_2$ (0.06 mmol, 60 μL), H_3L (0.02 mmol, 20 μL), NaOH (0.097 mmol, 97 μL) and H_2O (1.28 mmol, 23 μL) were mixed in a 300 μL reactor. The mixture was heated at 150 $^{\circ}C$ for 48 h. The synthesis of compound **4** could not be scaled-up in glass or Teflon[®] reactors. Therefore, a larger amount of the pure phase product was collected from Teflon[®] reactors of a separate high-throughput experiment. The HT experiment contained 24 identical reaction mixtures with the molar ratio $Cu^{2+}:H_3L:NaOH = 3.00:1:4.85$. The product (64 mg, 34% based on H_3L) contained thin green plates (SEM micrograph Figure S6) and was identified by PXRD diffraction (Figure S3) and elemental analysis. $Cu_2[(O_3P-C_6H_4-SO_3)(OH)(H_2O)]$ (**4**), $M = 397.25 \text{ g mol}^{-1}$: EDX measurement: atomic ratio P/S/Cu = 1:1:2; found C 16.6, H 1.6, S 7.7; calcd. C 18.1, H 1.8, S 8.1.

Synthesis of $Cu_3[(O_3P-C_6H_4-SO_3)_2(H_2O)_2]$ (5**):** In a typical HT experiment **5** was obtained by the following procedure ($Cu^{2+}:H_3L:NaOH = 3.20:1:2.75$). Aqueous solutions of $CuCl_2$ (0.064 mmol, 64 μL), H_3L (0.02 mmol, 20 μL), NaOH (0.055 mmol, 55 μL) and H_2O (3.39 mmol, 61 μL) were mixed in a 300 μL reactor and heated for 48 h at 150 $^{\circ}C$. The synthesis of compound **5** could not be scaled-up in glass or Teflon[®] reactors. Therefore, a larger amount of the pure phase product was collected from Teflon[®] reactors of a separate high-throughput experiment. The HT experiment contained 24 identical reaction mixtures with the same molar ratio $Cu^{2+}:H_3L:NaOH = 3.20:1:2.75$. The product (60 mg, 27% based on H_3L) contained thin blue needles (SEM micrograph Figure S6) and was identified by PXRD diffraction (Figure S3) and elemental analysis $Cu_3[(O_3P-C_6H_4-SO_3)_2(H_2O)_2]$ (**5**), $M = 696.90 \text{ g mol}^{-1}$: EDX measurement: atomic ratio P/S/Cu = 1:1:1.5; elemental analysis [%]: found C 19.8, H 1.6, S 8.5; calcd. C 20.7, H 1.7, S 9.2.

X-ray Crystallography: Suitable crystals of the compounds were carefully selected from the HT experiments using a polarizing microscope. Single-crystal X-ray diffraction for **1**, **2** and **4** were performed with a STOE IPDS-1 diffractometer equipped with a fine-focus sealed tube (Mo- K_{α} radiation, $\lambda = 71.073 \text{ pm}$). For data reduction and absorption correction the programs XRED and XSHAPE were used.^[54] Single crystal of **5** was measured with a Bruker-Nonius APEX II CCD equipped with a Bruker-Nonius FR591 rotating anode Mo- K_{α} radiation source. Absorption correction was done using SADABS software.^[55] The single crystal structures were solved by direct methods and refined using the program package SHELXTL.^[56] Crystals of compound **4** are non-merohedrally twinned. The reflections of both individuals were indexed separately using RECIPE and integration of the intensities was performed using TWIN.^[54] By this procedure, overlapping reflections are omitted. Experimental data and results of the structure determination of **1-5** are given in Table 1. Selected bond lengths are summarized in the Table S1.

CCDC entries 772438-772441 for compound **1**, **2**, **4** and **5** contain the supplementary crystallographic data for this paper. These data can be obtained free of charge from The Cambridge Crystallographic Data Centre via www.ccdc.cam.ac.uk/data/data_request/cif.

Supporting Information (see also the footnote on the first page of this article): Experimental powder patterns for **1**, **3**, **4** and **5** and simulated patterns for compounds **1**, **2**, **4** and **5**, IR-spectra, magnetic measurement plots for **4** and **5**, SEM images and TGA measurements are attached.

Acknowledgments

We gratefully appreciate the help of Professor Paul Kögerler (RWTH Aachen) and Professor Wolfgang Bensch (Uni. Kiel) for the discussions regarding the magnetic investigations. The authors thank Inke Jess and Alexandra Lieb for the acquisition of the single-crystal data, Adam Wutkowski for TG measurements, Henning Lühmann and Maren Rasmussen for magnetic measurements.

- [1] C. Sanchez, B. Julian, P. Belleville, M. Popall, *J. Mater. Chem.* **2005**, *15*, 3559-3592.
- [2] U. Müller, M. Schubert, F. Teich, H. Pütter, K. Schierle-Arndt, J. Pastré, *J. Mater. Chem.* **2006**, *16*, 626-636.
- [3] P. Horcajada, C. Serre, M. Vallet-Regí, M. Sebban, F. Taulelle, G. Férey, *Angew. Chem. Int. Ed.* **2006**, *45*, 5974-5978.
- [4] A. Sonnauer, F. Hoffmann, M. Froba, L. Kienle, V. Duppel, M. Thommes, C. Serre, G. Férey, N. Stock, *Angew. Chem. Int. Ed.* **2009**, *48*, 3791-3794.
- [5] H. Li, M. Eddaoudi, M. O'Keefe, O.M. Yaghi, *Nature*, **1999**, *402*, 276-279.
- [6] D.N. Dybtsev, H. Chun, K. Kim, *Angew. Chem.* **2004**, *116*, 5143-5146.
- [7] K.S. Park, Z. Ni, A.P. Cote, J.Y. Choi, R. Huang, F.J. Uribe-Romo, H.K. Chae, M. O'Keefe, O.M. Yaghi, *P. Natl. Acad. Sci USA*, **2006**, *103*, 10186-10191.
- [8] A. Clearfield, *Curr. Opin. Solid State Mater. Sci.* **2002**, *6*, 495-506.
- [9] D.M. Poojary, B. Zhang, P. Bellinghausen, A. Clearfield, *Inorg. Chem.*, **1996**, *35*, 5254-5263.
- [10] D.M. Poojary, B. Zhang, P. Bellinghausen, A. Clearfield, *Inorg. Chem.*, **1996**, *35*, 4942-4949.
- [11] D.K. Cao, S. Gao, L-M. Zheng, *J. Solid State Chem.*, **2004**, *177*, 2311-2315.
- [12] K. Maeda, *Micropor. Mesopor. Mater.* **2004**, *73*, 47-55.
- [13] R-G. Xiong, J. Zhang, Z-F. Chen, X-Z. You, C-M. Che, H-K. Fun, *J. Chem. Soc., Dalton Trans.* **2001**, 780-782.
- [14] G.B. Deacon, R. Harika, P.C. Junk, B.W. Skelton, A.H. White, *New J. Chem.* **2007**, *31*, 634-645.
- [15] G. K. H. Shimizu, R. Vaidhyanathan, J. M. Taylor, *Chem. Soc. Rev.* **2009**, *38*, 1430-1449.
- [16] S. Natarajan, P. Mahata, *Curr. Opin. Solid State Mater. Sci.* **2009**, *13*, 46-53.
- [17] S. Miller, G.M. Pearce, P.A. Wright, F. Bonino, S. Chavan, S. Bordiga, I. Margiolaki, N. Guillou, G. Férey, S. Bourrelly, P.L. Llewellyn, *J. Am. Chem. Soc.* **2008**, *130*, 15967-15981.
- [18] K. Maeda, Y. Kiyozumi, F. Mizukami, *Angew. Chem. Int. Ed.* **1994**, *33*, 2335-2337.
- [19] A. Clearfield, Z. Wang, P. Bellinghausen, *J. Solid State Chem.* **2002**, *167*, 376-385.
- [20] B.D. Chandler, D.T. Cramb, G.K.H. Shimizu, *J. Am. Chem. Soc.* **2006**, *128*, 10403-10412.
- [21] N. Stock, T. Bein, *J. Mater. Chem.* **2005**, *15*, 1384-1391.
- [22] C. Serre, N. Stock, T. Bein, G. Férey, *Inorg. Chem.* **2004**, *43*, 3159.
- [23] N. Stock, A. Stoll, T. Bein, *Micropor. Mesopor. Mater.* **2004**, *69*, 65-69.
- [24] S. Bauer, T. Bein, N. Stock, *J. Solid State Chem.* **2006**, *179*, 145-155.
- [25] S. Bauer, T. Bein, *Inorg. Chem.* **2005**, *44*, 5882-5899.
- [26] A. Sonnauer, N. Stock, *Eur. J. Inorg. Chem.* **2008**, 5038-5045.
- [27] A. Sonnauer, N. Stock, *Solid State Sci.* **2009**, *11*, 358-363.
- [28] A. Sonnauer, N. Stock, *J. Solid State Chem.* **2008**, *181*, 473-479.
- [29] A. Sonnauer, C. Näther, H. A. Hoppe, J. Senker, N. Stock, *Inorg. Chem.* **2007**, *46*, 9968-9974.
- [30] A. Sonnauer, N. Stock, *J. Solid State Chem.* **2008**, *181*, 3065-3070.
- [31] Z.-Y. Du, H.-B. Xu, J.-G. Mao, *Inorg. Chem.* **2006**, *45*, 9780-9788.
- [32] Z.-Y. Du, H.-B. Xu, J.-G. Mao, *Inorg. Chem.* **2006**, *45*, 6424-6430.
- [33] Z.-Y. Du, V. A. Prosvirin, J.-G. Mao, *Inorg. Chem.* **2007**, *46*, 9884-9894.
- [34] Z.-Y. Du, X.-L. Li, Q.-Y. Liu, J.-G. Mao, *Cryst. Growth Des.* **2007**, *7*, 1501-1507.
- [35] Z.-Y. Du, H.-B. Xu, X.-L. Li, J.-G. Mao, *Eur. J. Inorg. Chem.* **2007**, 4520-4529.
- [36] F. Adani, M. Casciola, D. J. Jones, L. Massinelli, E. Montoneri, J. Rozière, R. Viviani, *J. Mater. Chem.* **1998**, *8*, 961-964.
- [37] A. F. Benedetto, P. J. Squattrito, F. Adani, E. Montoneri, *Inorg. Chim. Acta.* **1997**, *260*, 207-216.
- [38] N. Stock, T. Bein, *Angew. Chem.* **2004**, *116*, 767-770.
- [39] N. Stock, *Micropor. Mesopor. Mater.* **2010**, *129*, 287-295.
- [40] S. Bauer, N. Stock, *Angew. Chem. Int. Ed.*, **2007**, *46*, 6857-6860.
- [41] S. Bauer, T. Bein, N. Stock, *Solid State Sci.*, **2008**, *10*, 837-846.
- [42] P. Forster, N. Stock, A.K. Cheetham, *Angew. Chem. Int. Ed.* **2005**, *44*, 7608-7611.
- [43] R.D. Shannon, *Acta Cryst.* **1976**, *A32*, 751-767.
- [44] N. Stock, *Solid State Sciences*, **2002**, *4*, 1089-1094.
- [45] *STOE WinXPOW version 2.11*, Stoe & Cie GmbH, Darmstadt, Germany, **2005**.
- [46] D. Hadzi, *J. Chem. Phys.* **1961**, *34*, 1445.
- [47] K. Okaniwa, H. Okamoto, T. Mitani, K. Toriumi, M. Yamashita, *J. Phys. Soc. Jap.* **1991**, *60*, 997-1004.
- [48] E. Libowitzky, *Monatsh. Chem.* **1999**, *130*, 1047-1059.
- [49] A. Stojiljkovic, D.H. Whiffen, *Spectrochim. Acta*, **1958**, *12*, 47-56.
- [50] *G. Socrates in Infrared and Raman Characteristic Group Frequencies*. John Wiley & Sons, Chichester, **2004**, 3rd. Edition.
- [51] A. Kolsi, *C. R. Seances Acad. Sci., Ser. C*, **1977**, *284*, 483-486.
- [52] S. Hatscher, H. Schilder, H. Lueken, W. Urland, *Pure. Appl. Chem.* **2005**, *77*, 497-511.
- [53] E. Montoneri, G. Viscardi, S. Bottigliengo, R. Gobetto, M.R. Chierotti, R. Buscaino, P. Quagliotto, *Chem. Mater.*, **2007**, *19*, 2671-2678.
- [54] *XRED version 1.19, XSHAPE version 1.06, RECIPE, TWIN*, Stoe & Cie GmbH, Darmstadt, Germany, **1999**.
- [55] G.M. Sheldrick, *SADABS version 2007/2*, Bruker AXS Inc., Madison, Wisconsin, USA.
- [56] G.M. Sheldrick, *SHELXL-PLUS Crystallographic System*, Siemens Analytical X-ray Instruments Inc., Madison, Wisconsin, **1992**.

4.3.2 A three-dimensional tin(II) phosphonatobenzenesulfonate with Sn₄O₁₂ clusters

This article has been published in its final form in “Acta Crystallographica Section C”: DOI: 10.1107/S0108270111005105. Copyright © 2011 International Union of Crystallography, Weinheim. The supporting information of this article is placed in the Appendix section (Appendix 2).

This article gives the structural description of the compound [Sn₂(O₃PC₆H₄SO₃)(OH)] which was obtained during the high-throughput metal ion screening experiments (see Section 4.3.1). Several attempts were carried out without any success to produce the pure-phase compound. The structure determination of the compound was performed via single crystal X-ray diffraction. The asymmetric unit of the structure consists of two crystallographic independent Sn²⁺ ions, one completely deprotonated (O₃PC₆H₄SO₃)³⁻ ion and one hydroxide ion. By considering the Sn-O bonds up to 2.726(3) Å, two types of polyhedra are exhibited, namely distorted seesaw-type SnO₄ and irregular square-pyramidal SnO₅. The orientation of the polyhedra is influenced by the sterically active lone pairs of electrons. Edge-sharing of these SnO₄ and SnO₅ polyhedra leads to Sn₄O₁₂ clusters. The clusters are cross-linked by phosphonate and sulfonate groups to form layers in the *ab*-plane. The layers are interconnected by the phenyl rings and thus, a three-dimensional pillared-layered assembly is observed. Narrow voids are present in the crystal structure where the sterically active lone pairs are positioned.

Acta Crystallographica Section C

**Crystal Structure
Communications**

ISSN 0108-2701

Editor: **Anthony Linden**

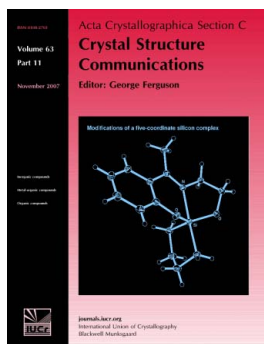
A three-dimensional tin(II) phosphonatobenzenesulfonate with Sn_4O_{12} clusters

Palanikumar Maniam and Norbert Stock*Acta Cryst.* (2011). **C67**, m73–m76

Copyright © International Union of Crystallography

Author(s) of this paper may load this reprint on their own web site or institutional repository provided that this cover page is retained. Reproduction of this article or its storage in electronic databases other than as specified above is not permitted without prior permission in writing from the IUCr.

For further information see <http://journals.iucr.org/services/authorrights.html>



Acta Crystallographica Section C: Crystal Structure Communications specializes in the rapid dissemination of high-quality studies of crystal and molecular structures of interest in fields such as chemistry, biochemistry, mineralogy, pharmacology, physics and materials science. The numerical and text descriptions of each structure are submitted to the journal electronically as a Crystallographic Information File (CIF) and are checked and typeset automatically prior to peer review. The journal is well known for its high standards of structural reliability and presentation. *Section C* publishes approximately 1000 structures per year; readers have access to an archive that includes high-quality structural data for over 10000 compounds.

Crystallography Journals **Online** is available from journals.iucr.org

A three-dimensional tin(II) phosphonato-benzenesulfonate with Sn_4O_{12} clusters

Palanikumar Maniam and Norbert Stock*

Institut für Anorganische Chemie, Christian-Albrechts-Universität zu Kiel,
Max-Eyth-Strasse 2, 24118 Kiel, Germany
Correspondence e-mail: stock@ac.uni-kiel.de

Received 27 January 2011

Accepted 10 February 2011

Online 16 February 2011

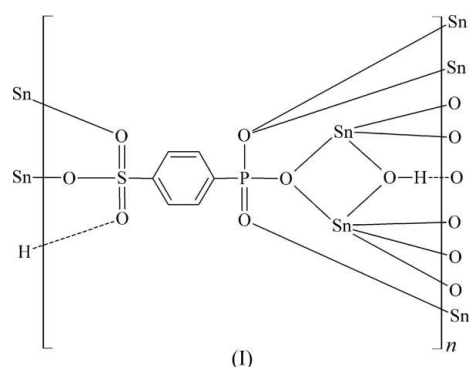
The hydrothermal reaction of $\text{SnCl}_2 \cdot 2\text{H}_2\text{O}$ with 4-phosphonobenzenesulfonic acid (H_3L) and sodium hydroxide has yielded the title compound, poly[μ -hydroxido- μ_7 -(4-phosphonato-benzenesulfonato)-ditin(II)], $[\text{Sn}_2(\text{C}_6\text{H}_4\text{O}_6\text{PS})(\text{OH})]_n$. The inorganic building unit is an Sn_4O_{12} cluster which is composed of edge-sharing SnO_4 and SnO_5 polyhedra. The clusters are interconnected *via* P and S atoms from the organic acid to form layers in the *ab* plane. These layers are linked to each other through pillaring benzene groups parallel to the *c* axis to form a three-dimensional structure.

Comment

The discovery of crystalline zirconium(IV) phosphates in 1964 sparked a surge of interest in the study of phosphate- and phosphonate-based inorganic–organic hybrid compounds (Clearfield *et al.*, 1964). This led to the class of crystalline zirconium(IV) phosphonates in 1978 (Alberti *et al.*, 1978). Originally, the scope of the research was focused on the synthesis of layered structures with metal(IV) ions and monophosphonic acids, but succeeding studies saw an expansion with the use of di- and trivalent metal ions and diphosphonic acids to generate new types of structures (Clearfield, 1998; Poojary *et al.*, 1996*a,b*). Subsequently, sulfonate groups were also incorporated in the metal phosphonates by post-synthetic sulfonation of the benzene rings (Yang *et al.*, 1987; Stein *et al.*, 1996). Some of these compounds were studied with respect to their proton-conducting abilities, which are relevant for polymer electrolyte membrane (PEM) fuel cells. Inorganic–organic hybrid compounds based on such polyfunctional acids have been reported to exhibit high proton conductivities (Adani *et al.*, 1998; Alberti *et al.*, 1992, 2003). The presence of strong acid sites also allows the application of such compounds for catalytic purposes (Alberti *et al.*, 1996).

Our research focuses on the use of organic linker molecules containing two or more different functional groups for the

synthesis of inorganic–organic hybrid compounds. In addition to the number of functional groups their geometry, coordination modes, charge and acidity have a strong influence on the formation of the final crystal structures (Maniam *et al.*, 2010). With the advent of phosphonoalkyl- and phosphonoarylsulfonic acids (Montoneri & Ricca, 1991*a,b*), many phosphonosulfonates with di- and trivalent metal ions were investigated (Sonnauer *et al.*, 2007, 2009; Sonnauer, Lieb & Stock, 2008; Sonnauer & Stock, 2008; Du *et al.*, 2006; Maniam *et al.*, 2010). By utilizing a new synthesis of phosphonoarylsulfonic acids, a rigid *para*-substituted 4-phosphonobenzenesulfonic acid (H_3L) was recently synthesized (Montoneri *et al.*, 2007). Employing this organic acid linker, we have synthesized five new compounds, namely $[\text{Pb}_2(\text{L})(\text{OH})]$, $[\text{Cu}_{1.5}(\text{L})(\text{H}_2\text{O})]$, $\text{NaCu}(\text{L})(\text{H}_2\text{O})_3$, $[\text{Cu}_2(\text{L})(\text{OH})(\text{H}_2\text{O})]$ and $[\text{Cu}_3(\text{L})_2(\text{H}_2\text{O})_2]$ (Maniam *et al.*, 2010).



In the present work, we describe the structure of a new Sn^{2+} -based phosphonatobenzenesulfonate, *viz.* poly[μ -hydroxido- μ_7 -(4-phosphonato-benzenesulfonato)-ditin(II)], (I), which crystallizes in the triclinic space group $P\bar{1}$. To the best of our knowledge, this compound is the first tin(II) phosphonosulfonate. As seen in Fig. 1, the asymmetric unit of (I) contains two Sn^{2+} ions, a fully deprotonated organic linker (L) and one hydroxide ion. The X-ray scattering factors of the P and S atoms are very similar, but they were successfully distinguished by comparing the S—O [1.460 (3)–1.469 (4) Å] and P—O [1.532 (3)–1.548 (3) Å] bond lengths. The fact that S—O bonds are generally shorter than P—O bonds has also been observed in other metal phosphonosulfonates (Du *et al.*, 2006; Sonnauer *et al.*, 2007, 2009; Sonnauer, Lieb & Stock, 2008;

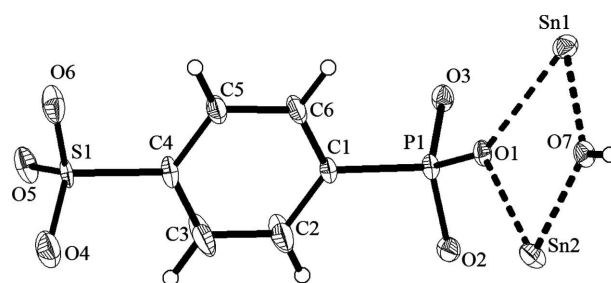
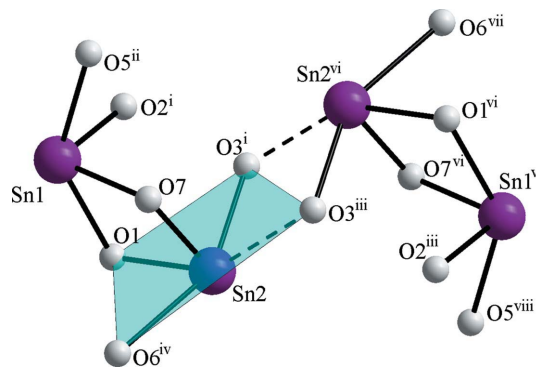


Figure 1
The asymmetric unit of (I), showing the atom-labelling scheme. Displacement ellipsoids are drawn at the 50% probability level and H atoms are shown as small spheres of arbitrary radii. Coordinative Sn—O bonds are marked as broken lines.

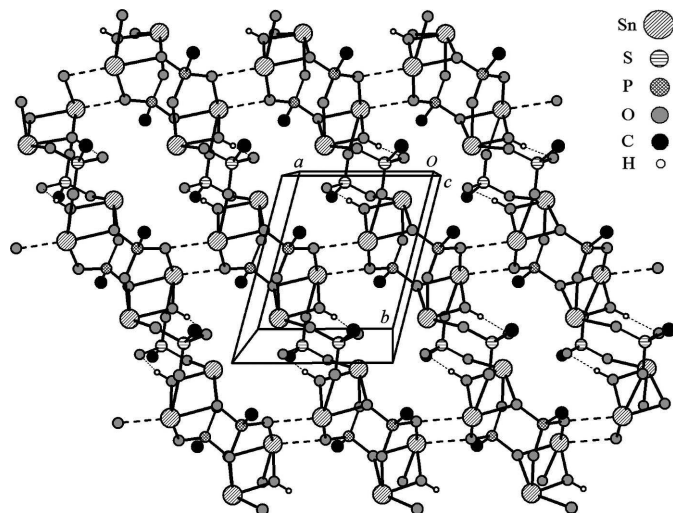

Figure 2

The coordination environment of the Sn1 and Sn2 atoms. Including only bond lengths $< 2.7 \text{ \AA}$, two distorted seesaw-type polyhedra are observed. Edge sharing leads to the formation of dimeric Sn_2O_6 clusters (solid lines). By considering the $\text{Sn2}-\text{O3}^{\text{iii}}$ bond of $2.726(3) \text{ \AA}$ (dashed line), one distorted seesaw SnO_4 and one distorted square-pyramidal SnO_5 polyhedron are observed (the shaded area marks the basal form formed by $\text{O1}, \text{O3}^{\text{i}}, \text{O3}^{\text{iii}}$ and O6^{iv}). Edge sharing leads to tetrameric Sn_4O_{12} clusters. [Symmetry codes: (i) $-x, -y + 1, -z + 1$; (ii) $x - 1, y, z + 1$; (iii) $x - 1, y, z$; (iv) $-x, -y + 2, -z$; (vi) $-x - 1, -y + 1, -z + 1$; (vii) $x - 1, y - 1, z + 1$; (viii) $-x, -y + 1, -z$.]

Maniam *et al.*, 2010). Looking along the $\text{P1} \cdots \text{S1}$ axis, the O atoms of the phosphonate and sulfonate groups are located in a staggered conformation but, in contrast to the ideal torsion angle of 60° , the $\text{O}-\text{P} \cdots \text{S}-\text{O}$ torsion angles vary from $40.79(19)$ to $76.92(18)^\circ$.

The crystal structure of (I) is built of Sn–O polyhedra containing sterically active lone pairs of electrons. These are also observed in many tin(II) phosphonates, such as $[\text{Sn}_2(\text{O}_3\text{PCH}_3)(\text{C}_2\text{O}_4)]$, $[\text{Sn}_4(\text{O}_3\text{PCH}_2\text{CH}_2\text{CO}_2)_2(\text{C}_2\text{O}_4)]$, $[\text{Sn}(\text{C}_6\text{H}_5\text{O}_3\text{P})]$ and $[\text{Sn}(\text{O}_3\text{PCH}_2\text{NHC}_4\text{H}_8\text{NHCH}_2\text{PO}_3)]$, which contain SnO_3 , SnO_4 and Sn_2O_7 polyhedra (Adair *et al.*, 1998; Stock *et al.*, 2000; Lansky *et al.*, 2001; Zhang *et al.*, 2008). Depending on how the Sn–O bond distances are taken into account, the crystal structure of (I) can be described in different ways.

Including only Sn–O distances less than 2.7 \AA , two distorted seesaw-type SnO_4 polyhedra are observed. Sn1 is connected to atoms $\text{O1}, \text{O2}^{\text{i}}, \text{O5}^{\text{ii}}$ and O7 (all symmetry codes are as in Fig. 2), with bond lengths in the range $2.124(3)$ – $2.425(3) \text{ \AA}$ (Table 1) and $\text{O}-\text{Sn1}-\text{O}$ angles in the range $69.82(10)$ – $140.63(10)^\circ$. The two longest Sn1–O bonds (to O1 and O5^{ii}) lie in the pseudo-axial positions, while the two shorter Sn1–O bonds (to O2^{i} and O7) and the lone pair are in the equatorial plane. Sn2 is connected to atoms $\text{O1}^{\text{vi}}, \text{O3}^{\text{i}}, \text{O6}^{\text{iv}}$ and O7 , with bond lengths in the range $2.108(3)$ – $2.587(3) \text{ \AA}$. The $\text{O}-\text{Sn2}-\text{O}$ angles in the distorted seesaw geometry vary from $73.59(10)$ to $152.13(10)^\circ$. The observed Sn–O distances and $\text{O}-\text{Sn}-\text{O}$ angles are in very good agreement with those reported in the seesaw-type SnO_4 units of the layered tin(II) phosphonate $[\text{Sn}_2(\text{O}_3\text{PCH}_3)(\text{C}_2\text{O}_4)]$ and the three-dimensional structure of $[\text{Sn}_4(\text{O}_3\text{PCH}_2\text{CH}_2\text{CO}_2)_2(\text{C}_2\text{O}_4)]$ (Adair *et al.*, 1998; Stock *et al.*, 2000). This form of polyhedron is also similar to those observed in α - SnO , with Sn–O distances of 2.223 \AA and an $\text{O}-\text{Sn}-\text{O}$ -angle range of 74.36 – 117.44° (Levi, 1924). Edge sharing of the two distorted seesaw-type SnO_4


Figure 3

Packing diagram showing the interconnection of dimeric clusters *via* phosphonate and sulfonate groups to form chains. Taking the $\text{Sn2}-\text{O3}^{\text{iii}}$ bond of $2.726(3) \text{ \AA}$ (thick dashed lines) into account, tetrameric Sn_4O_{12} clusters are formed and the formerly described chains are connected to form layers in the ab plane. The positions of lone pairs are indicated by the narrow voids between the opposing Sn1^{2+} ions. Hydrogen bonds are shown as thin dashed lines. The layers are then linked to each other by the benzene groups along the c axis. Atoms C2, C3, C5 and C6 and their respective H atoms have been omitted for clarity. [Symmetry code: (iii) $x - 1, y, z$.]

polyhedra in (I) leads to dimeric units which are in close proximity to each other [$\text{Sn2}-\text{O3}^{\text{iii}} = 2.726(3) \text{ \AA}$] and are connected through the phosphonate and sulfonate groups to form chains (Fig. 3). These chains are connected by the benzene rings of the phosphonobenzenesulfonate ions to form a layered structure.

If the additional Sn–O distance of $2.726(3) \text{ \AA}$ is taken into account as a genuine bond, two kinds of polyhedra are observed, *viz.* distorted seesaw-type SnO_4 and irregular square-pyramidal Sn_2O_5 polyhedra. The irregular SnO_5 square pyramid consists of the apical $\text{Sn2}-\text{O7}$ bond and the four basal Sn–O bonds to atoms $\text{O1}, \text{O3}^{\text{i}}, \text{O3}^{\text{iii}}$ and O6^{iv} (symmetry codes as in Fig. 2). Associated with the influence of the lone pair, the Sn^{2+} ion is located $0.514(1) \text{ \AA}$ below the basal plane, whereas apical atom O7 is positioned $1.591(3) \text{ \AA}$ above the plane (Fig. 2). Although this distance is much larger than the sum of the ionic radii (2.35 \AA ; McDonald *et al.*, 1980), it is much smaller than the sum of the van der Waals radii (3.70 \AA ; Kawamura *et al.*, 1999). A search of the Cambridge Structural Database (Allen, 2002) for Sn–O bond lengths in tin phosphonates yields values between 1.9 and 2.8 \AA , with a mean value around 2.2 \AA and, in the literature, bond lengths of up to 3 \AA are discussed (Ramaswamy *et al.*, 2008; Holt *et al.*, 1987). Accordingly, the next largest Sn–O distances in (I), which are $3.094(3)$ and $3.292(3) \text{ \AA}$ for $\text{Sn1} \cdots \text{O4}^{\text{iv}}$ and $\text{Sn2} \cdots \text{O2}$, respectively, were not considered in the structural description. Using Sn–O distances up to 2.73 \AA , edge sharing of the SnO_5 polyhedra is observed and thus Sn_4O_{12} clusters are formed (Fig. 2). These tetrameric clusters are connected by the phosphonate and sulfonate groups to form layers in the ab plane (Fig. 3), which are further connected by the benzene

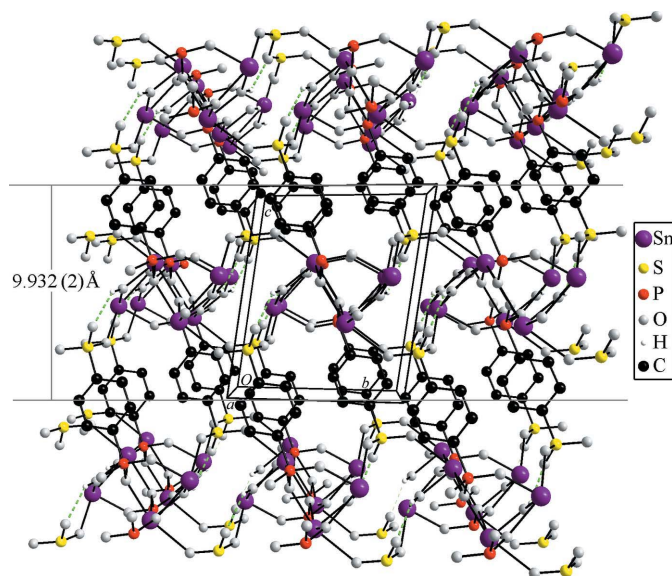


Figure 4
Schematic representation of the three-dimensional pillared layered structure of (I), viewed along the *a* axis, with an interlayer distance of 9.932 (2) Å. Aromatic H atoms have been omitted for clarity.

rings of the phosphonobenzenesulfonate ions to form a pillared layered structure (Fig. 4). An interlayer distance of 9.932 (2) Å separates the layers from each other along the *c* axis. In this arrangement, the presence of narrow voids indicates the position of the sterically active lone pairs. These are observed between opposing Sn1²⁺ ions [Sn1...Sn1(−*x*, −*y* + 2, −*z* + 1) = 4.335 (1) Å] (Fig. 3), whereas for Sn2²⁺ the lone pairs point towards the interlayer space occupied by the benzene rings.

Only one hydrogen bond is observed in (I) which involves the bond between the μ(O—H) hydroxide ion and an O atom of the sulfonate group (Fig. 3 and Table 2). This bond can be considered as a weak hydrogen bond (Libowitzky, 1999).

Experimental

All reagents and solvents were obtained commercially and used without further purification. 4-Phosphonobenzenesulfonic acid dihydrate (H₃L) was synthesized according to Montoneri *et al.* (2007). The reaction mixture consisted of tin(II) chloride dihydrate (6.8 mg, 0.03 mmol), H₃L (5.48 mg, 0.02 mmol), NaOH (0.06 mmol) and deionized water (200 μl). The mixture was heated in a 300 μl Teflon-lined high-throughput reactor at 423 K for 36 h (Stock, 2010). The mixture was cooled to room temperature over a period of 8 h, and colourless plate-like crystals were formed.

Crystal data

[Sn ₂ (C ₆ H ₄ O ₆ PS)(OH)]	$\gamma = 75.25 (3)^\circ$
$M_r = 489.56$	$V = 571.0 (2) \text{ \AA}^3$
Triclinic, $P\bar{1}$	$Z = 2$
$a = 7.0045 (14) \text{ \AA}$	Mo $K\alpha$ radiation
$b = 8.487 (2) \text{ \AA}$	$\mu = 4.72 \text{ mm}^{-1}$
$c = 10.0570 (17) \text{ \AA}$	$T = 293 \text{ K}$
$\alpha = 81.10 (2)^\circ$	$0.14 \times 0.10 \times 0.07 \text{ mm}$
$\beta = 86.17 (2)^\circ$	

Data collection

Stoe IPDS-1 diffractometer	6691 measured reflections
Absorption correction: numerical (<i>X-RED</i> and <i>X-SHAPE</i> ; Stoe & Cie, 2008)	2550 independent reflections
$T_{\min} = 0.380$, $T_{\max} = 0.581$	2146 reflections with $I > 2\sigma(I)$
	$R_{\text{int}} = 0.048$

Refinement

$R[F^2 > 2\sigma(F^2)] = 0.026$	155 parameters
$wR(F^2) = 0.071$	H-atom parameters constrained
$S = 1.03$	$\Delta\rho_{\max} = 0.82 \text{ e \AA}^{-3}$
2550 reflections	$\Delta\rho_{\min} = -1.10 \text{ e \AA}^{-3}$

Table 1

Selected geometric parameters (Å, °).

Sn1—O1	2.425 (3)	P1—O1	1.548 (3)
Sn1—O2 ⁱ	2.124 (3)	P1—O2	1.532 (3)
Sn1—O5 ⁱⁱ	2.412 (3)	P1—O3	1.532 (3)
Sn1—O7	2.156 (3)	P1—C1	1.798 (3)
Sn2—O1	2.243 (3)	S1—O4	1.460 (3)
Sn2—O3 ⁱ	2.345 (3)	S1—O5	1.469 (4)
Sn2—O3 ⁱⁱⁱ	2.726 (3)	S1—O6	1.460 (3)
Sn2—O6 ^{iv}	2.587 (3)	S1—C4	1.780 (4)
Sn2—O7	2.108 (3)		
O2 ⁱ —Sn1—O7	91.86 (11)	O3 ⁱ —Sn2—O3 ⁱⁱⁱ	74.32 (10)
O2 ⁱ —Sn1—O5 ⁱⁱ	78.78 (11)	O3 ⁱⁱⁱ —Sn2—O6 ^{iv}	119.16 (10)
O7—Sn1—O5 ⁱⁱ	80.57 (11)	O6 ^{iv} —Sn2—O1	73.59 (10)
O2 ⁱ —Sn1—O1	76.92 (10)	O7—Sn2—O1	74.32 (10)
O7—Sn1—O1	69.82 (10)	O6 ^{iv} —Sn2—O3 ⁱ	152.13 (10)
O5 ⁱⁱ —Sn1—O1	140.63 (10)	O1—Sn2—O3 ⁱⁱⁱ	147.69 (10)
O1—Sn2—O3 ⁱ	83.12 (9)		

Symmetry codes: (i) $-x, -y + 1, -z + 1$; (ii) $x - 1, y, z + 1$; (iii) $x - 1, y, z$; (iv) $-x, -y + 2, -z$.

Table 2

Hydrogen-bond geometry (Å, °).

$D-H \cdots A$	$D-H$	$H \cdots A$	$D \cdots A$	$D-H \cdots A$
O7—H7 [·] ··O4 ⁱⁱ	0.84	2.19	2.874 (4)	139

Symmetry code: (ii) $x - 1, y, z + 1$.

All H atoms were located in difference Fourier maps. Idealized values for the bond lengths (C—H = 0.93 Å and O—H = 0.84 Å) and angles were used and the H-atom parameters were refined using a riding model. The highest peak of 0.82 e Å^{−3} in the residual electron-density map is located 1.34 Å from H3 and the deepest hole of 1.10 e Å^{−3} is located 0.72 Å from Sn2.

Data collection: *X-AREA* (Stoe & Cie, 2008); cell refinement: *X-AREA*; data reduction: *X-AREA*; program(s) used to solve structure: *SHELXS97* (Sheldrick, 2008); program(s) used to refine structure: *SHELXL97* (Sheldrick, 2008); molecular graphics: *DIAMOND* (Brandenburg, 2010); software used to prepare material for publication: *XCIF* in *SHELXTL* (Sheldrick, 2008).

The authors thank Professor Dr Christian Näther and Inke Jess (University of Kiel) for the acquisition of the single-crystal data. This work was supported by the State of Schleswig–Holstein, Germany. We also acknowledge financial support from the Deutsche Forschungsgemeinschaft (grant No. DFG-STO-643/2–3).

Supplementary data for this paper are available from the IUCr electronic archives (Reference: JZ3200). Services for accessing these data are described at the back of the journal.

References

- Adair, B., Natarajan, S. & Cheetham, A. K. (1998). *J. Mater. Chem.* **8**, 1477–1479.
- Adani, F., Casciola, M., Jones, D. J., Massinelli, L., Montoneri, E., Rozière, J. & Vivani, R. (1998). *J. Mater. Chem.* **8**, 961–964.
- Alberti, G. & Casciola, M. (2003). *Annu. Rev. Mater. Res.* **33**, 129–154.
- Alberti, G., Casciola, M., Costantino, U., Peraio, A. & Montoneri, E. (1992). *Solid State Ionics*, **50**, 315–322.
- Alberti, G., Casciola, M., Costantino, U. & Vivani, R. (1996). *Adv. Mater.* **8**, 291–303.
- Alberti, G. M., Costantino, U., Allulli, S. & Tomassini, N. (1978). *J. Inorg. Nucl. Chem.* **40**, 1113–1117.
- Allen, F. H. (2002). *Acta Cryst.* **B58**, 380–388.
- Brandenburg, K. (2010). *DIAMOND*. Release 3.2f. Crystal Impact GbR, Bonn, Germany.
- Clearfield, A. (1998). *Prog. Inorg. Chem.* **47**, 371–510.
- Clearfield, A. & Stynes, J. A. (1964). *J. Inorg. Nucl. Chem.* **26**, 117–129.
- Du, Z.-Y., Xu, H.-B. & Mao, J.-G. (2006). *Inorg. Chem.* **45**, 9780–9788.
- Holt, E. M., Kläui, W. & Zuckerman, J. J. (1987). *J. Organomet. Chem.* **335**, 29–42.
- Kawamura, K., Nakazawa, H. & Miyoshi, K. (1999). *Organometallics*, **18**, 4785–4794.
- Lansky, D. E., Zavalij, P. Y. & Oliver, S. R. J. (2001). *Acta Cryst.* **C57**, 1051–1052.
- Levi, G. R. (1924). *Nuovo Cimento*, **1**, 335–346.
- Libowitzky, E. (1999). *Monatsh. Chem.* **130**, 1047–1059.
- Maniam, P., Näther, C. & Stock, N. (2010). *Eur. J. Inorg. Chem.* pp. 3866–3874.
- McDonald, R. C. & Eriks, K. (1980). *Inorg. Chem.* **19**, 1237–1241.
- Montoneri, E. & Ricca, G. (1991a). *Phosphorus Sulfur Silicon Relat. Elem.* **55**, 111–115.
- Montoneri, E. & Ricca, G. (1991b). *Phosphorus Sulfur Silicon Relat. Elem.* **55**, 201–204.
- Montoneri, E., Viscardi, G., Bottigliengo, S., Gobetto, R., Chierotti, M. R., Buscaino, R. & Quagliotto, P. (2007). *Chem. Mater.* **19**, 2671–2678.
- Poojary, D. M., Zhang, B., Bellinghausen, P. & Clearfield, A. (1996a). *Inorg. Chem.* **35**, 5254–5263.
- Poojary, D. M., Zhang, B., Bellinghausen, P. & Clearfield, A. (1996b). *Inorg. Chem.* **35**, 4942–4949.
- Ramaswamy, P., Datta, A. & Natarajan, S. (2008). *Eur. J. Inorg. Chem.* pp. 1376–1385.
- Sheldrick, G. M. (2008). *Acta Cryst.* **A64**, 112–122.
- Sonnauer, A., Feyand, M. & Stock, N. (2009). *Cryst. Growth Des.* **9**, 586–592.
- Sonnauer, A., Lieb, A. & Stock, N. (2008). *Acta Cryst.* **E64**, m1417–m1418.
- Sonnauer, A., Näther, C., Höpfe, H. A., Senker, J. & Stock, N. (2007). *Inorg. Chem.* **46**, 9968–9974.
- Sonnauer, A. & Stock, N. (2008). *J. Solid State Chem.* **181**, 473–479.
- Stein, E. W., Clearfield, A. & Subramanian, M. A. (1996). *Solid State Ionics*, **83**, 113–124.
- Stock, N. (2010). *Microporous Mesoporous Mater.* **129**, 287–295.
- Stock, N., Stucky, G. D. & Cheetham, A. K. (2000). *Chem. Commun.* pp. 2277–2278.
- Stoe & Cie (2008). *X-AREA, X-RED, X-SHAPE and X-STEP32*. Stoe & Cie, Darmstadt, Germany.
- Yang, C. Y. & Clearfield, A. (1987). *React. Polym.* **5**, 13–21.
- Zhang, J., Li, J., Sun, Z.-G., Zhao, Y., Zhu, Y.-Y., Zhang, N., Liu, L. & Lu, X. (2008). *Z. Anorg. Allg. Chem.* **634**, 2629–2633.

4.3.3 Synthesis and characterization of the mixed-linker copper(II) coordination polymer $[\text{Cu}(\text{HO}_3\text{PC}_6\text{H}_4\text{SO}_3)(\text{C}_{10}\text{N}_2\text{H}_8)] \cdot \text{H}_2\text{O}$

This is the pre-peer reviewed version of the above-mentioned article which has been published in its final form in "Zeitschrift für Anorganische und Allgemeine Chemie": DOI: 10.1002/zaac.201100202. Copyright © 2011 WILEY-VCH Verlag GmbH & Co. KGaA, Weinheim. The supporting information of this article is placed in the Appendix section (Appendix 3).

So far, all high-throughput investigations involving the 4-phosphonobenzenesulfonic acid linker were performed without any co-ligands (section 4.3.1-4.3.2). The crystal structures of the single linker systems are mostly three-dimensional pillared-layered networks containing polynuclear M-O-M clusters. The previous investigations have also shown that copper(II) ions display diverse M-O-M connectivities and therefore, warrants a further study in a mixed-ligand environment especially with amine ligands. As discussed in Section 4.1.1, the incorporation of amines as co-ligand with 3-phosphonobenzenesulfonic acid have produced a variety of new metal phosphonosulfonates with 1,10-phenanthroline (*phen*) and 4,4'-bipyridine (*bipy*). The chemistry of the *para*-bridging mode of *bipy* is much more of interest, as the chelating *phen* ligand is more likely to form cluster networks. Therefore, this work focuses on the system $\text{Cu}^{2+} / \text{H}_2\text{O}_3\text{PC}_6\text{H}_4\text{SO}_3\text{H} / \textit{bipy} / \text{solvent}$. The screening of solvents with various polarities (water, acetonitrile, dimethylformamide and isopropanol) delivered important preliminary information for the pure-phase synthesis of a new mixed-ligand compound because the solubility of each reactant can influence the product formation. Water was determined to be optimal solvent which generated pure-phase material $[\text{Cu}(\text{HO}_3\text{PC}_6\text{H}_4\text{SO}_3)(\text{H}_2\text{O})]$ (**1**). The subsequent screening of copper(II) salts has helped to further optimize the hydrothermal synthesis of **1**. Compound **1** is built of isolated Jahn-Teller distorted CuN_2O_4 octahedra which are interconnected by phosphonate and sulfonate groups to form chains. These chains are cross-linked by the phenyl rings and the *bipy* ligands to form a three-dimensional framework assembly. One oxygen atom from each phosphonate and sulfonate groups does not coordinate to the metal ions but are engaged in hydrogen bonds. Rietveld analysis as well as temperature dependent investigations via TG and XRPD experiments have revealed a directional switching of Jahn-Teller distortion upon the loss of the water molecules. The phase transition of **1** to the dehydrated structure of $[\text{Cu}(\text{HO}_3\text{PC}_6\text{H}_4\text{SO}_3)]$ (**1-h**) is reversible upon exposure to water. Magnetic susceptibility studies have shown that compound **1** displays weak ferro-/ferrimagnetic behaviour in the 3.5 to 300 K range and a sudden change to antiferromagnetic interaction is observed at 3.5 K.

Synthesis and characterization of the mixed-linker copper(II) coordination polymer [Cu(HO₃PC₆H₄SO₃)(C₁₀N₂H₈)]·H₂O

Palanikumar Maniam^[a] and Norbert Stock^{*[a]}

Dedicated to Prof. Dr. Hanskarl Müller-Buschbaum on the Occasion of His 80th Birthday

Keywords: high-throughput screening; copper; coordination polymer; Phosphonato-sulfonates; crystal structure

A new copper(II) phosphonatobenzenesulfonate incorporating 4,4'-bipyridine (4,4'-*bipy*) as auxiliary ligand has been discovered through systematic high-throughput (HT) screening of the system Cu(NO₃)₂·3H₂O/H₂O₃PC₆H₄SO₃H/4,4'-*bipy* using different solvents. The hydrothermal synthesis of [Cu(HO₃PC₆H₄SO₃)(C₁₀H₈N₂)]·H₂O (**1**) was further optimized by screening various copper(II) salts. The crystal structure of **1** was determined by single crystal X-ray diffraction and unveiled the presence of isolated sixfold coordinated Jahn-Teller distorted Cu²⁺ ions. The isolated CuN₂O₄ octahedra are interconnected by phosphonate and sulfonate groups to form chains along the *c*-axis. The organic groups, namely phenyl rings and 4,4'-*bipy* molecules cross-link the chains into a three-dimensional framework.

Water molecules are found in the narrow voids in the structure which are held by weak hydrogen bonds. Upon dehydration, the structure of **1** undergoes a phase transition which was confirmed by TG measurements and temperature dependent X-ray powder diffraction. The new structure of **1-h** was refined with Rietveld methods. Detailed inspection of the structure revealed the directional switching of the Jahn-Teller distortion upon de/rehydration. Weak ferro-/ferrimagnetic interactions were observed by magnetic investigations of **1** which switch to antiferromagnetic below 3.5 K. Compounds **1** and **1-h** are further characterized by thermogravimetric and elemental analysis as well as IR spectroscopy.

* Prof. Dr. Norbert Stock
E-Mail: stock@ac.uni-kiel.de

[a] Institut für Anorganische Chemie,
Christian-Albrechts-Universität,
Max-Eyth-Strasse 2, 24118 Kiel, Germany.

Supporting information for this article is available on the
WWW under <http://dx.doi.org/10.1002/zaac.201100202>
from the author

Introduction

The field of inorganic-organic hybrid compounds encompasses many types of materials; i.e. amorphous nanocomposites, such as self-assembled mesoporous materials, to crystalline products [1]. One intensively studied class of these compounds is coordination polymers [2,3]. The organic building units that are mostly deployed in these materials are based on carboxylates (R-CO₂⁻) and amines [4,5,6,7]. On the other hand, sulfonate (R-SO₃⁻) and phosphonate (R-PO₃²⁻) based compounds have been less intensively investigated [8,9,10,11]. The restriction of structural diversity with these functional groups compared to the -CO₂⁻ counterpart is mostly caused by the more flexible coordination modes as well as the higher number of coordinating atoms. Therefore, in general dense materials are formed [12,13]. We are interested in the utilization of organic linker molecules containing two or more different functional groups for the synthesis of inorganic-organic hybrid compounds. In addition to the number of functional groups, their geometry, coordination modes, as well as charge and acidity have a strong effect on the final crystal structure formation.

Examples from our previous work comprise the use of linkers containing phosphonate and carboxylate groups, [14,15] phosphonate and amine groups such as iminobis-(methylphosphonate) units [16] or iminobis-(methylphosphonate) and carboxylate units [17,18]. Linkers containing a phosphonic and a sulfonic acid groups have only been recently investigated. By using the flexible linkers 2-phosphonoethane- and 4-phosphonobutane-sulfonic acid, our group has explored the synthesis of several hybrid compounds with different ions such as Cu²⁺ [19,20], Sr²⁺ [21], Ba²⁺ [22], and lanthanide ions [23,24,25]. Rigid phosphonoarylsulfonic acids, i.e. 3-phosphonobenzenesulfonic acid were employed by the group of Mao [26,27,28,29,30], 5-phosphono-1,3-disulfonic acid and 4-fluoro-3-sulfobenzylphosphonic acid by the group of Montoneri [31,32], mostly in combination with amine linkers.

The synthesis of most metal phosphonates is accomplished under hydrothermal conditions. Such reactions are often known to be strongly dependent on the process parameters, e.g. reaction time, temperature, heating rate, and the compositional parameters, e.g. molar composition of the starting materials, pH of the reaction mixture or overall concentration. An elegant way for the exploration of these complex systems can be carried out using high-throughput (HT) methods [33,34,35]. These allow a systematic and efficient investigation of large parameter spaces giving rise to the accelerated discovery of new compounds and optimization of synthesis parameters. Due to the large amounts of data, reaction and structural trends can be derived. Our recent work on 4-phosphonobenzenesulfonic acid (H₃L) with HT methods

has highlighted the discovery of several compounds incorporating this linker and Cu^{2+} ions [36]. Various CuO clusters ranging from mononuclear CuO_6 , binuclear Cu_2O_8 , hexanuclear Cu_6O_{24} to infinite chains of edge-sharing $\text{CuO}_5/\text{CuO}_6$ were observed in these phosphonosulfonate compounds. We concentrated on the usage of copper(II) as the metal ion as it usually displays diverse coordinating characteristics arising from Jahn-Teller distortion as well as the catalytic potential through coordinatively unsaturated copper sites [37,38]. By inserting auxiliary ligands such as amines, new structural motives could be obtained as seen in the work of Mao et al. [26,27,28,29,30]. In order to gain insight into these structural possibilities, HT-screening of various solvents and copper(II) salts with an auxiliary diamine ligand, namely 4,4'-bipyridine (4,4'-*bipy*) was performed. This systematic investigation has resulted in the discovery and the synthesis optimization of a new mixed-ligand coordination polymer. Here, we report the synthesis, structural and magnetic characterization of a new copper(II)-coordination polymer containing H_3L and 4,4'-*bipy*, $[\text{Cu}(\text{HL})(4,4'\text{-bipy})]\cdot\text{H}_2\text{O}$ (**1**) and its structural conversion to the dehydrated compound $[\text{Cu}(\text{HL})(4,4'\text{-bipy})]$ (**1-h**).

Results and Discussion

HT-screening of solvents

Solubility of each reactant in the respective solvent plays an essential role in determining the outcome of a synthesis [39]. Nonetheless, most metal phosphonates or sulfonates are synthesized in aqueous solutions. In order to see the effects of other solvents on the synthesis, acetonitrile, isopropanol and N,N-dimethylformamide (DMF) were also screened with $\text{Cu}(\text{NO}_3)_2\cdot 3\text{H}_2\text{O}$, H_3L and 4,4'-*bipy* (Tab. S1). All screening reactions in this stage were performed at a reaction temperature of 130 °C. The molar ratios of $\text{Cu}^{2+} : \text{H}_3\text{L} : 4,4'\text{-bipy}$ were varied in the range of 1 to 3 in 1.0 steps. According to the X-ray powder diffraction (XRPD) measurements of the products, isopropanol-based syntheses yielded various mixed-phase products most of which contained **1**. Due to strong overlap of the reflections the identification of the other products was not accomplished. DMF based reactions generated mixed phases mostly comprised of **1**, elemental Cu, Cu_2O and $[\text{Cu}(4,4'\text{-bipy})(\text{OH})]$ [40] which indicates that DMF can also act as a reducing agent under certain conditions [41]. Acetonitrile based reactions produced mixed phases in which green crystals were obtained. These were determined by XRPD measurements to be the known compound $[\text{Cu}_2(\text{CH}_3\text{COO})_4(4,4'\text{-bipy})]\cdot\text{CH}_3\text{CN}$ [42]. The acetate ion resulted from the in situ hydrolysis of acetonitrile. In general, the organic solvents are advantageous to increase the solubility of some amine ligands. Nevertheless, the usage of organic solvent is disadvantageous for our purposes as no new mixed-ligand coordination polymer was obtained. Only with water based synthesis led unequivocally to a new mixed-ligand compound, $[\text{Cu}(\text{HL})(4,4'\text{-bipy})]\cdot\text{H}_2\text{O}$ (**1**).

HT-screening of copper(II) salts

The counter-ions of the copper salts affect the pH of the reaction mixture and can also induce in situ side-reactions such as oxidation during the synthesis [18]. In addition, the

deployment of the suitable copper(II) salt could also prevent the co-crystallization of unwanted phases [36]. In a HT-screening experiment with 24 individual reactions, other copper salts in addition to $\text{Cu}(\text{NO}_3)_2\cdot 3\text{H}_2\text{O}$ were tested with 4,4'-*bipy* under hydrothermal conditions (Tab. S2). The reaction involving $\text{CuCl}_2\cdot 2\text{H}_2\text{O}$ only yielded $\alpha\text{-}[\text{Cu}(4,4'\text{-bipy})\text{Cl}_2]$ which was identified via XRPD and elemental analysis [43]. $\text{Cu}(\text{CH}_3\text{COO})_2\cdot\text{H}_2\text{O}$ always generated mixed phases of **1** with unidentified crystalline impurities and traces of Cu_2O . The use of $\text{CuSO}_4\cdot 5\text{H}_2\text{O}$ resulted only in mixtures of **1** with a small amount of crystalline impurities. The most suitable copper salt was determined to be $\text{Cu}(\text{NO}_3)_2\cdot 3\text{H}_2\text{O}$ since it resulted mostly in the pure phase **1** depending on the molar composition of the reaction mixtures. Looking closely at the various $\text{Cu}(\text{NO}_3)_2\cdot 3\text{H}_2\text{O} / \text{H}_3\text{L} / 4,4'\text{-bipy}$ molar ratios used, the optimal reactant composition was determined to be 1 : 1 : 1. This molar ratio was successfully used for the synthesis scale up in glass tubes (see Experimental Section).

Crystal structure

The asymmetric unit of **1** is comprised of two Cu^{2+} ions, one doubly deprotonated $(\text{HL})^{2-}$ ion, two 4,4'-*bipy* and a single water molecule (Fig. 1).

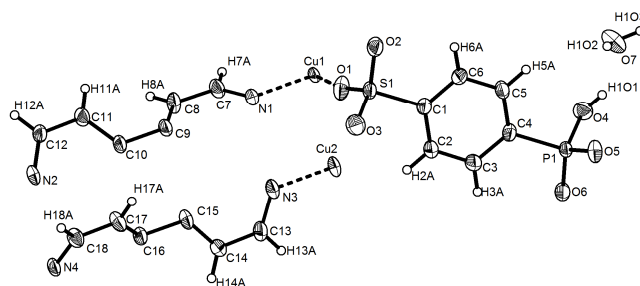


Figure 1. The asymmetric unit of compound **1**. The coordinative Cu-N and Cu-O bonds are depicted by broken lines. Thermal ellipsoids are drawn at 50 % probability.

The X-ray scattering factors of phosphorus and sulfur are very similar. Nevertheless, the distinction can be made by comparison of the P-O and S-O bond lengths. The P-O bond lengths of 1.489(2)-1.571(2) Å in **1** are longer than the S-O bonds which are between 1.438(2) and 1.456(3) Å. These observations agree well with the values in the literature and facilitate the assignment of S and P atoms [19, 36, 44].

The Cu^{2+} ions are surrounded by four oxygen atoms of the sulfonate and phosphonate ions as well as two nitrogen atoms of the 4,4'-*bipy* molecules to form a distorted CuN_2O_4 octahedra. The O-atoms of phosphonate ions and the N-atoms lie on the equatorial positions in the octahedra while the O-atoms from the sulfonate ions are in the axial positions. The typical Jahn-Teller distortion can be observed with the elongated Cu-O axial bonds in the 2.556(2)-2.620(3) Å range (Fig. 2A). The equatorial Cu-O and Cu-N bonds are in the range of 1.930(2)-1.942(2) Å and 2.008(3)-2.025(3) Å, respectively. These octahedra are interconnected via S- and P-atoms along the *c*-axis to form infinite chains (Fig. 2A). The chains are cross-linked along the *b*-axis through 4,4'-*bipy* molecules and also through $(\text{HL})^{2-}$ ions in the (101) plane (Fig. 3). A three-dimensional structure is thus formed. Weak H-bonds ($D\cdots A = 2.614(3)\text{-}$

2.819(3) Å) are observed between the water molecule and the oxygen atoms from the phosphonate and sulfonate ions (Fig. 2A). The water molecules act twice as H-donor and once as H-acceptor.

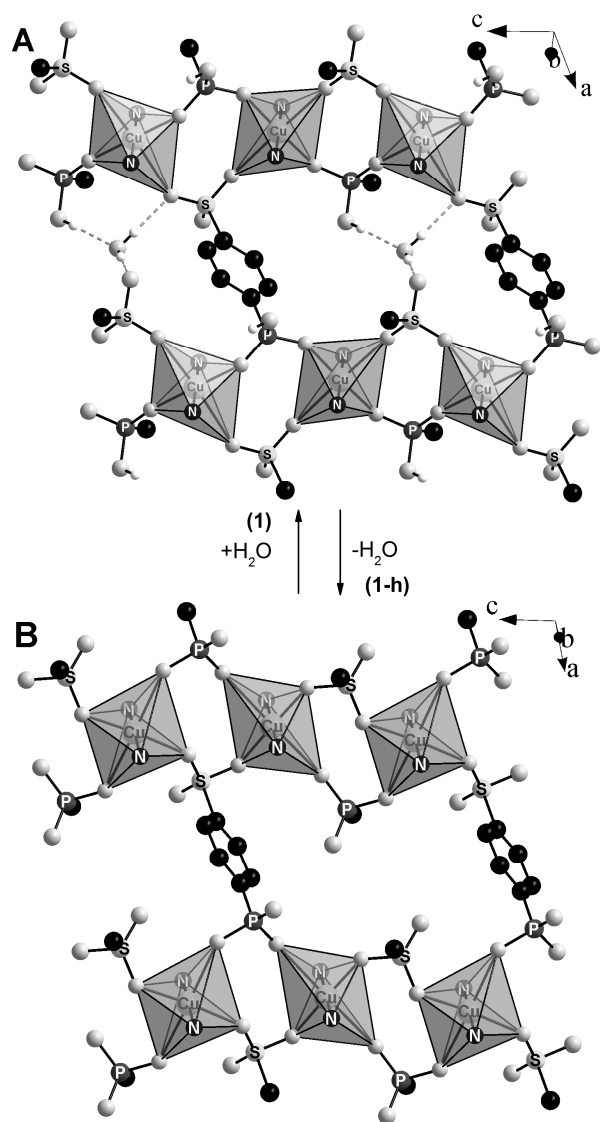


Figure 2. The chain-like interconnection of the CuN_2O_4 Jahn-Teller distorted octahedra by the sulfonate and phosphonate groups along the c -axis for the compound **1** (A) and **1-h** (B). The chains are linked to each other via the phenyl rings of the $(\text{HL})^{2-}$ ions. The elongated Cu-O axial bonds in **1** originate from sulfonate groups (A). In **1-h**, the elongation of Cu-O axial bonds involves the O-atoms of the phosphonate groups (B). H-atoms from the aromatic groups were omitted for clarity.

Thermal treatment at 250 °C leads to the removal of the H_2O molecules (see Thermal investigations). Changes in the unit cell parameters were observed with no symmetry changes. The most apparent changes are a longer cell parameter a (+7.8 %) and a shorter cell parameter c (-3.7 %). The cell parameter b , which is exactly the distance between the chains connected by the 4,4'-*bipy* ligands, does not change significantly (Fig. 3).

Typically, structural phase transitions are due to temperature changes [45], but in the compound **1**, the transition to **1-h** seems to be caused by the dehydration of the compound as the dehydrated phase **1-h** is stable at room

temperature. By exposing **1-h** to moisture, the structure converts gradually to the crystal structure of **1** which was confirmed by XRPD analysis (Fig. S1).

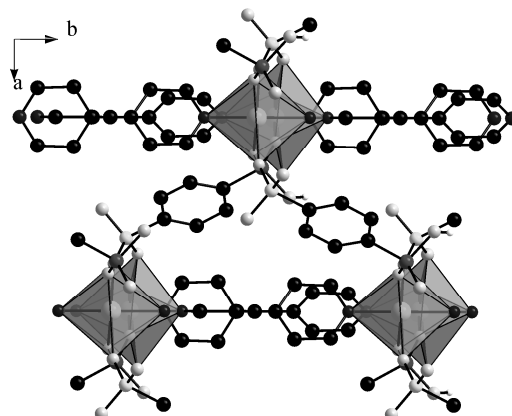


Figure 3. View along [001] showing the linkage of the chains of CuN_2O_4 octahedra to each other by the phenyl rings of $(\text{HL})^{2-}$ ions, and by the 4,4'-*bipy* ligands. The same arrangement is observed in both compounds **1** and **1-h**. H-atoms from the aromatic groups were omitted for clarity.

A possible explanation for the lengthening of cell parameter a could be the lack of the hydrogen bonds from the water molecules in **1**. This produces a repulsion of the chains from each other and thus increasing the cell length along the a -axis.

Looking closer at the atomic arrangements in **1-h**, the elongated Cu-O axial bonds of the Jahn-Teller distorted CuN_2O_4 octahedra are no longer between the oxygen atoms of sulfonate groups, but instead between the oxygen atoms of the phosphonate groups (Fig. 2A, 2B). This is similar to a so-called “Jahn-Teller switching” which has been reported with several copper(II) containing compounds. In a Jahn-Teller distorted $\text{Cu}(\text{D}_2\text{O})_6^{2+}$ octahedra in the deuterated Tutton salt, $\text{Cu}(\text{D}_2\text{O})_6(\text{ND}_4)_2(\text{SO}_4)_2$, the elongated axial bonds flip to different pairs of water molecules compared to hydrogenous compound [46]. A pressure dependent “switching” also occurs in this compound upon raising the pressure from 1 to 1.5 bar [47]. The changes in the local coordination environment of Cu^{2+} ion between compounds **1** and **1-h** can be attributed to the lack of hydrogen bonding from water molecules. Nevertheless, the reasoning behind this observation cannot be solely dependent on the water molecules, but also on the influence of the remainder of the whole structure.

Magnetic investigations

To investigate the magnetic properties of **1**, the temperature dependence of its susceptibility was investigated by applying a magnetic field of $H = 1$ T in the temperature range of 2-300 K. The Cu^{2+} ions are only found in isolated CuN_2O_4 polyhedra and are connected by phosphonate and sulfonate groups ($\text{Cu}\cdots\text{Cu} = 5.356(1)$ Å). Due to the long exchange pathway, weak magnetic interactions are expected. Looking at the χ^{-1} versus T plot fitted using the Curie-Weiss law $\chi = C/(T-\theta_w)$, an almost linear curve is observed which confirms the Curie-Weiss paramagnetism (Fig. 4, top). A Weiss constant of 10.2 K was determined which indicates weak ferro-/ferrimagnetic

interactions. This result is also supported by the plot of $\chi \cdot T$ versus T in Fig. 4 (bottom) that shows the domination of weak ferro-/ferrimagnetic behaviour from 300 K to 3.5 K. At 3.5 K, the interaction switches to antiferromagnetic (see inset in Fig. 4, bottom). The average effective magnetic moment of $1.69(4) \mu_B$ calculated from the fitted data from 40-300 K compares well with the theoretical spin-only value of $1.73 \mu_B$ (Fig. 4). Upon further cooling from 40 K to 2 K, the μ_{eff} value dips exponentially which indicates complex magnetic interactions.

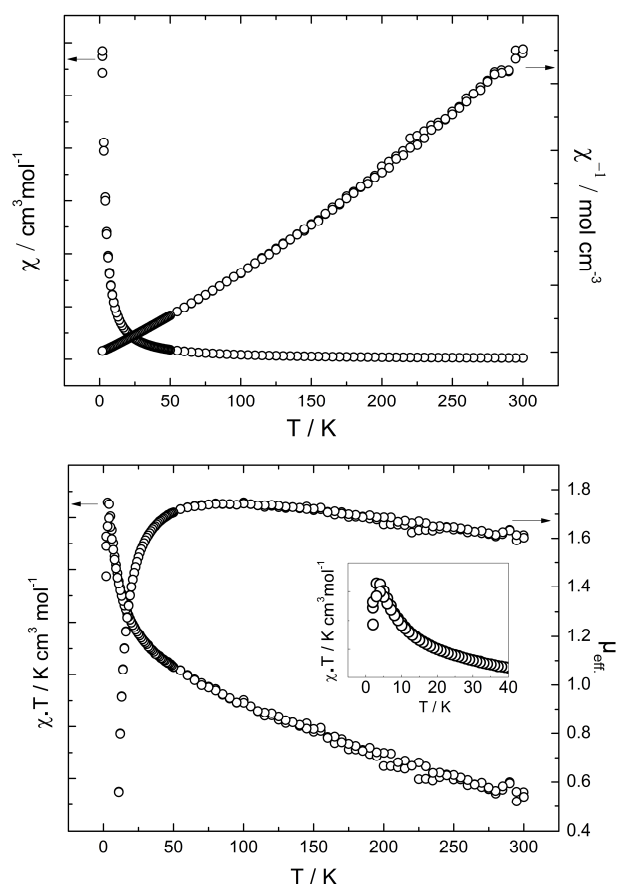


Figure 4. Results of the magnetic susceptibility measurements for **1**. Plots of paramagnetic and reciprocal paramagnetic susceptibility (top) as well as $\chi \cdot T$ and effective magnetic moment as function of temperature are shown. The inset graph displays the switching from ferro-/ferrimagnetic to antiferromagnetic interactions at 3.5 K.

Thermal investigations

TG/DTA measurements have yielded much insight in the composition and the thermal stability of compound **1** (Fig. S3). The solid product after the TG analysis was characterized by XRPD measurement. The endothermic dehydration of **1** is observed at 200 °C (weight loss % calc./obs.: 3.9/4.1). The second weight loss stage (200-450 °C) is attributed to the loss of 4,4'-*bipy* molecules (% calc./obs.: 32.9/32.0). The final step in the TG curve can be assigned to the disintegration of the -C₆H₄-SO₃ fragment of the (HL)²⁻ ions (% calc./obs.: 33.0/32.1). The light blue colored solid residue was identified as Cu₂P₂O₇ by XRPD (% calc./obs.: 31.8/31.7).

Temperature dependent XRPD measurements gave important evidence on the phase transition of **1** to **1-h** (Fig. 5). Compound **1** is stable in the temperature range of 20-250 °C. Upon complete dehydration at 250 °C, **1-h** is formed which decomposes at 340 °C. The obvious discrepancy in phase transition temperatures between TG (200 °C) and temperature dependent XRPD analyses (250 °C) is due to the difference in the sample setup (refer to Experimental Section).

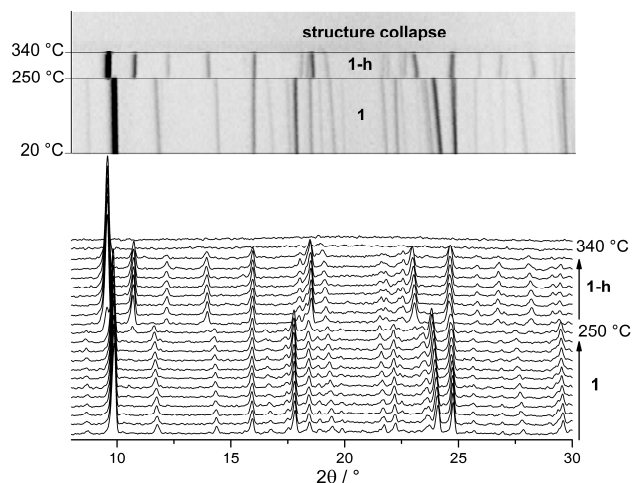


Figure 5. Results of the temperature dependent XRPD investigation of a capillary tube sample shows the phase transition from **1** to **1-h** at 250 °C.

Conclusions

High-throughput methods have helped to identify and optimize the reaction conditions that led to the new mixed-linker coordination polymer [Cu(HL)(4,4'-*bipy*)]·H₂O. Surprisingly the choice of Cu-salt and solvent has a strong influence on the structure formed. Thus, only the reaction in water led to a single-phase product of **1**. Although only very small pores are present in the structure of **1**, occluded water molecules can be reversibly removed. The often in coordination polymers observed structural flexibility leads to a substantial change in the coordination environment of the Jahn-Teller distorted CuN₂O₄ polyhedra in **1**. In **1** the elongated axial bonds stem from the sulfonate groups Cu-O-S and upon dehydration, they are instead between the phosphonate groups. Such switching phenomenon in the coordination environment of the Jahn-Teller distorted octahedra has been rarely observed in the literature.

Table 1. Crystallographic data and details on the structure determination from single crystal of [Cu(HL)(4,4'-*bipy*)]·H₂O (**1**) and from Rietveld refinement of [Cu(HL)(4,4'-*bipy*)] (**1-h**).

	1	1-h
formula	C ₁₆ H ₁₅ CuN ₂ O ₇ PS	C ₁₆ H ₁₃ CuN ₂ O ₆ PS
MW (g·mol ⁻¹)	473.87	455.89
crystal system	monoclinic	monoclinic
space group	C2 (no. 5)	C2 (no. 5)
<i>a</i> / Å	15.7374(12)	16.9581(7)
<i>b</i> / Å	11.0896(6)	11.1033(3)
<i>c</i> / Å	10.6253(8)	10.2310(5)
β / °	108.243(6)	103.866(2)
<i>V</i> / Å ³	1761.14(22)	1870.27(10)

Z	4	4
$\rho_{\text{calc.}} / \text{g} \cdot \text{cm}^{-3}$	1.787	1.572
T / K	293 (5)	583 (5)
μ / mm^{-1}	1.495	-
min/max transm.	0.770 / 0.862	-
$\theta_{\text{min}}, \theta_{\text{max}} / ^{\circ}$	2-29.2	4-40
meas. reflns.	16314	-
unique reflns.	4619	-
reflns. [$F_o > 4\sigma(F_o)$]	4368	-
parameter	258	70
R-values	$R_{\text{int}} = 0.038$	$R_{\text{exp}} = 0.023$
	$R_{1,w}R_2$ [all data]	$R_{\text{Bragg}} = 0.008$
	0.036, 0.071	
	$R_{1,w}R_2$ [$F_o > 4\sigma(F_o)$]	$R_p = 0.032$
	0.032, 0.069	$R_{\text{wp}} = 0.042$
GoF	1.085	1.805
$\Delta\rho_{\text{max}}, \Delta\rho_{\text{min}} / \text{e} \cdot \text{\AA}^{-3}$	0.43, -0.38	-

Experimental Section

Materials and characterization methods: All chemicals were commercially available and used without further purification (Sigma-Aldrich and ABCR), except for 4-phosphonobenzenesulfonic acid (H_3L) which was synthesized according to the procedure reported previously [48]. The three step synthesis of H_3L was performed with 4-bromobenzenesulfonyl chloride as the starting reactant. High-throughput XRPD experiments were carried out in transmission mode using a STOE high-throughput powder diffractometer ($\text{CuK}_{\alpha 1}$, $\lambda = 1.5406 \text{ \AA}$) equipped with an image-plate position-sensitive detector (IPPSD). MIR spectra were recorded with an ATI Matheson Genesis spectrometer in the spectral range $4000\text{--}400 \text{ cm}^{-1}$ using the KBr disc method as well as an ALPHA-ST-IR Bruker spectrometer equipped with an ATR unit. Thermogravimetric analyses were carried out in air atmosphere (75 mL min^{-1} , $30\text{--}800 \text{ }^{\circ}\text{C}$, $4 \text{ }^{\circ}\text{C min}^{-1}$) using a NETZSCH STA 409 CD analyzer. The temperature dependent XRPD analysis in Debye-Scherrer mode was carried out on a STOE Stadi-P diffractometer ($\text{CuK}_{\alpha 1}$, $\lambda = 1.5406 \text{ \AA}$), equipped with a STOE high temperature capillary furnace, using 0.3 mm quartz capillary tubes. CHNS analyses were performed with an Eurovektor EuroEA Elemental Analyzer. The semiquantitative elemental analyses were performed with a Phillips ESEM XL 30 hot cathode scanning electron microscope equipped with energy dispersive X-ray (EDX) EDAX analyzer for elemental analysis. Magnetic measurements for compound **1** was performed with a Physical Property Measuring System (PPMS) from Quantum Design (9 T magnet), at 1 T (DC field), respectively, in the temperature range of 2 to 300 K (ZFC). Diamagnetic susceptibility of compound **1** ($-237.51 \cdot 10^{-6} \text{ cm}^3 \text{ mol}^{-1}$) was calculated using the tables in the literature and diamagnetic correction was applied during the data analysis [49].

High-Throughput Experiments: The reaction system $\text{Cu}^{2+}/\text{H}_3\text{L}/4,4'\text{-bipy}/\text{solvent}$ was investigated using various molar ratios $\text{Cu}^{2+}/\text{H}_3\text{L}/4,4'\text{-bipy}$ employing high-throughput methods (process and compositional parameters are listed in Tab. S1–S2 in the Supporting Information). Each HT experiment was performed under solvothermal conditions in a custom-made stainless steel high-throughput reactor system containing 48 PTFE inserts each. The PTFE inserts have a maximum volume of $300 \text{ }\mu\text{L}$ [34]. All reagents were manually dosed using aqueous solutions of the

reactants. The concentrations as well as the exact amounts of starting materials are given in the Table S1–S2. The evaluation of the HT experiments are based on XRPD measurements.

[Cu(HL)(4,4'-bipy)]·H₂O (1): In a typical HT experiment **1** was obtained by the following procedure (molar ratio $\text{Cu}^{2+}:\text{H}_3\text{L}:4,4'\text{-bipy} = 1 : 1 : 1$). Aqueous solutions of $\text{Cu}(\text{NO}_3)_2 \cdot 3\text{H}_2\text{O}$ (0.02 mmol, $40 \text{ }\mu\text{L}$), H_3L (0.02 mmol, $20 \text{ }\mu\text{L}$), $4,4'\text{-bipy}$ (0.02 mmol, $20 \text{ }\mu\text{L}$) and additional H_2O ($120 \text{ }\mu\text{L}$) were mixed in a $300 \text{ }\mu\text{L}$ reactor and heated for 48 h at $130 \text{ }^{\circ}\text{C}$. The scale-up of **1** was accomplished using glass tubes (DURAN® culture tubes $12 \times 100 \text{ mm}$ D50 GL 14 M.KAP, SCHOTT 261351155). $\text{Cu}(\text{NO}_3)_2 \cdot 3\text{H}_2\text{O}$ ($500 \text{ }\mu\text{L}$, 0.2 mmol), H_3L ($500 \text{ }\mu\text{L}$, 0.2 mmol), and $4,4'\text{-bipy}$ ($1000 \text{ }\mu\text{L}$, 0.2 mmol) were combined and sonicated for 10 min. The mixture was heated at $130 \text{ }^{\circ}\text{C}$ for 48 h. The synthesis yielded a light blue powder (40 mg, 42 mol% based on H_3L , final pH value of reaction mixture = 1-2) which was identified by XRPD. $\text{C}_{16}\text{H}_{15}\text{CuN}_2\text{O}_7\text{PS}$ (molecular mass: 473.87 g/mol); C 40.6 (calc. 40.5); H 2.9 (3.2); N 6.2 (6.0); S 6.8 (6.8)%. IR (KBr): $\nu(\text{OH})$ 3410 cm^{-1} , $\nu(\text{Ar-H})$ 3080 w , $\delta(\text{OH})$ 1650 m , $\nu(\text{C=C})$ 1600 m , $\nu(\text{C=N})$ 1410 m , $\nu_{\text{asym}}(\text{P-O, S-O})$ 1190 s , $\nu_{\text{sym}}(\text{P-O, S-O})$ 1090 m , $\delta(\text{Ar-H})$ 810 m , 645 s .

[Cu(HL)(4,4'-bipy)] (1-h): **1-h** is obtained by activating compound **1** at $200 \text{ }^{\circ}\text{C}$ under vacuum for 12 h. To avoid rehydration of **1-h** to **1**, the dehydrated substance is stored in a vacuum desiccator with KOH and P_2O_5 as the desiccant. $\text{C}_{16}\text{H}_{13}\text{CuN}_2\text{O}_6\text{PS}$ (molecular mass: 455.88 g/mol); C 42.0 (calc. 42.2); H 3.1 (2.9); N 6.1 (6.1); S 6.8 (7.0)%. IR (ATR): $\nu(\text{Ar-H})$ $3070 \text{ cm}^{-1} \text{ w}$, $\nu(\text{C=C})$ 1610 m , $\nu(\text{C=N})$ 1410 m , $\nu_{\text{asym}}(\text{P-O, S-O})$ 1140 s , $\nu_{\text{sym}}(\text{P-O, S-O})$ 1000 m , $\delta(\text{Ar-H})$ 810 m , 642 s .

X-ray Crystallography: A suitable crystal of the compound was carefully selected from the HT experiments using a polarizing microscope. Single-crystal X-ray diffraction for **1** was performed with a STOE IPDS-1 diffractometer equipped with a fine-focus sealed tube (Mo- K_{α} radiation, $\lambda = 0.71073 \text{ \AA}$). For data reduction and absorption correction the programs XRED and XSHAPE were used [50]. The single crystal structure was solved by direct methods and refined using the program package SHELXTL [51]. Experimental data and results of the structure determination of **1** are given in Table 1.

The crystal structure of **1-h** was determined on the basis of X-ray powder diffraction data. The XRPD pattern of a capillary-filled sample was recorded with a STOE Stadi-P powder diffractometer in Debye-Scherrer geometry using Ge(111) monochromated $\text{CuK}_{\alpha 1}$ radiation. The details of XRPD measurements are as following; 2θ range = $8\text{--}80^{\circ}$, step width = 0.01 , data points = 4800, no. of observed reflections = 105, T = $583(5) \text{ K}$. EXPO2009 software with TREOR indexing algorithm was used to determine the cell parameters [52]. The Rietveld refinement (Fig. 6) was performed with the TOPAS package[53] using the structure of **1** as the starting model. Preferred orientation of the crystallites was described with a spherical harmonics function of 4th order. 32 atomic, 18 profile and 20 background parameters (Chebyshev) were refined. The relevant crystallographic data and further details of the data collection are summarized in Table 1.

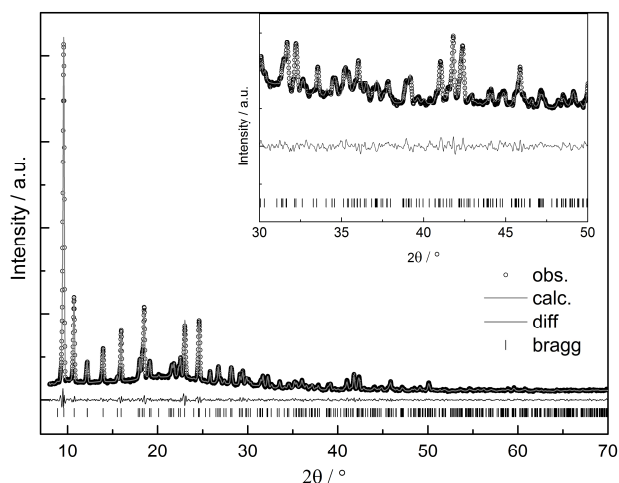


Figure 6. Observed (circles) and calculated (line) XRPD pattern as well as the difference profile of the Rietveld refinement of **1-h**; Allowed Bragg reflex positions are marked by vertical lines.

Crystallographic data (excluding structure factors) for the structures **1** and **1-h** reported in this paper have been deposited with the Cambridge Crystallographic Data Centre as supplementary publication no. CCDC-822923 (**1**) and 823351 (**1-h**). Copies of the data can be obtained free of charge on application to CCDC, 12 Union Road, Cambridge CB2 1EZ, UK [fax.: (internat.) + 44 1223/336-033; e-mail: deposit@ccdc.cam.ac.uk].

Supporting Information (see footnote on the first page of this article): Experimental details of the HT-investigations; selected bond lengths and angles; comparison of measured and simulated XRPD patterns, IR spectroscopic data; TG / DTA analysis of **1**.

Acknowledgement

The authors thank Inke Jess and Professor Christian Näther for the acquisition of the single-crystal data, Beatrix Seidlhofer for TG measurements, Henning Lühmann and Maren Rassmussen for magnetic measurements. This work was supported by the Deutsche Forschungsgemeinschaft (DFG) (STO 643/2).

- [1] C. Sanchez, B. Julian, P. Belleville, M. Popall, *J. Mater. Chem.* **2005**, *15*, 3559–3592.
- [2] A. Y. Robin, K. M. Fromm, *Coor. Chem. Rev.* **2006**, *250*, 2127–2157.
- [3] S. Kitagawa, R. Kitaura, S. Noro, *Angew. Chem. Int. Ed.* **2004**, *43*, 2334–2375; *Angew. Chem.* **2004**, *116*, 2388–2430.
- [4] H. Li, M. Eddaoudi, M. O’Keefe, O. M. Yaghi, *Nature*, **1999**, *402*, 276–279.
- [5] A. Sonnauer, F. Hoffmann, M. Froba, L. Kienle, V. Duppel, M. Thommes, C. Serre, G. Férey, N. Stock, *Angew. Chem. Int. Ed.* **2009**, *48*, 3791–3794; *Angew. Chem.* **2009**, *121*, 3849–3852.
- [6] D. N. Dybtsev, H. Chun, K. Kim, *Angew. Chem. Int. Ed.* **2004**, *43*, 5033–5036; *Angew. Chem.* **2004**, *116*, 5143–5146.
- [7] K. S. Park, Z. Ni, A. P. Cote, J. Y. Choi, R. Huang, F.J. Uribe-Romo, H.K. Chae, M. O’Keefe, O.M. Yaghi, *P. Natl. Acad. Sci USA.* **2006**, *103*, 10186–10191.
- [8] A. Clearfield, *Curr. Opin. Solid State Mater. Sci.* **2002**, *6*, 495–506.
- [9] D. K. Cao, S. Gao, L.-M. Zheng, *J. Solid State Chem.* **2004**, *177*, 2311–2315.
- [10] K. Maeda, *Micropor. Mesopor. Mater.* **2004**, *73*, 47–55.
- [11] R.-G. Xiong, J. Zhang, Z.-F. Chen, X.-Z. You, C.-M. Che, H.-K. Fun, *J. Chem. Soc., Dalton Trans.* **2001**, 780–782.
- [12] G. K. H. Shimizu, R. Vaidyanathan, J. M. Taylor, *Chem. Soc. Rev.* **2009**, *38*, 1430–1449.
- [13] S. Natarajan, P. Mahata, *Curr. Opin. Solid State Mater. Sci.* **2009**, *13*, 46–53.
- [14] N. Stock, T. Bein, *J. Mater. Chem.* **2005**, *15*, 1384–1391.
- [15] C. Serre, N. Stock, T. Bein, G. Férey, *Inorg. Chem.* **2004**, *43*, 3159.
- [16] N. Stock, A. Stoll, T. Bein, *Micropor. Mesopor. Mater.* **2004**, *69*, 65–69.
- [17] S. Bauer, T. Bein, N. Stock, *J. Solid State Chem.* **2006**, *179*, 145–155.
- [18] S. Bauer, T. Bein, *Inorg. Chem.* **2005**, *44*, 5882–5899.
- [19] A. Sonnauer, N. Stock, *Eur. J. Inorg. Chem.* **2008**, 5038–5045.
- [20] A. Sonnauer, M. Feyand, N. Stock, *Cryst. Growth Des.* **2009**, *9*, 586–592.
- [21] A. Sonnauer, N. Stock, *Solid State Sci.* **2009**, *11*, 358–363.
- [22] A. Sonnauer, N. Stock, *J. Solid State Chem.* **2008**, *181*, 473–479.
- [23] A. Sonnauer, C. Näther, H. A. Hoppe, J. Senker, N. Stock, *Inorg. Chem.* **2007**, *46*, 9968–9974.
- [24] A. Sonnauer, N. Stock, *J. Solid State Chem.* **2008**, *181*, 3065–3070.
- [25] M. Feyand, C. Näther, A. Rothkirch, N. Stock, *Inorg. Chem.* **2010**, *49*, 11158–11163.
- [26] Z.-Y. Du, H.-B. Xu, J.-G. Mao, *Inorg. Chem.* **2006**, *45*, 9780–9788.
- [27] Z.-Y. Du, H.-B. Xu, J.-G. Mao, *Inorg. Chem.* **2006**, *45*, 6424–6430.
- [28] Z.-Y. Du, V. A. Prosvirin, J.-G. Mao, *Inorg. Chem.* **2007**, *46*, 9884–9894.
- [29] Z.-Y. Du, X.-L. Li, Q.-Y. Liu, J.-G. Mao, *Cryst. Growth Des.* **2007**, *7*, 1501–1507.
- [30] Z.-Y. Du, H.-B. Xu, X.-L. Li, J.-G. Mao, *Eur. J. Inorg. Chem.* **2007**, 4520–4529.
- [31] F. Adani, M. Casciola, D. J. Jones, L. Massinelli, E. Montoneri, J. Rozière, R. Viviani, *J. Mater. Chem.* **1998**, *8*, 961–964.
- [32] A. F. Benedetto, P. J. Squattrito, F. Adani, E. Montoneri, *Inorg. Chim. Acta.* **1997**, *260*, 207–216.
- [33] N. Stock, T. Bein, *Angew. Chem. Int. Ed.* **2004**, *43*, 749–752; *Angew. Chem.* **2004**, *116*, 767–770.
- [34] N. Stock, *Micropor. Mesopor. Mater.* **2010**, *129*, 287–295.
- [35] S. Bauer, N. Stock, *Angew. Chem. Int. Ed.* **2007**, *46*, 6857–6860; *Angew. Chem.* **2007**, *119*, 6981–6984.
- [36] P. Maniam, C. Näther, N. Stock, *Eur. J. Inorg. Chem.* **2010**, 3866–3874.
- [37] H. A. Jahn, E. Teller, *Proc. R. Soc. A*, **1937**, *161*, 220–235.
- [38] L. Alaerts, E. Séguin, H. Poelman, F. Thibault-Starzyk, P. A. Jacobs, D. E. De Vos, *Chem. Eur. J.* **2006**, *12*, 7353–7363.
- [39] J. Fan, M. H. Shu, T. Okamura, Y. Z. Li, W. Y. Sun, W. X. Tang, N. Ueyama, *New J. Chem.* **2003**, *27*, 1307–1309.
- [40] S. P. Chen, G. Fan, S. L. Gao, *Acta Chimica Sinica*, **2007**, *65*, 1385–1388.
- [41] I. Pastoriza-Santos, L. M. Liz-Marzán, *Pure Appl. Chem.* **2000**, *72*, 83–90.
- [42] Y. H. Wen, Y. H. He, Y. L. Feng, *Chin. J. Struct. Chem.* **2007**, *26*, 29–32.
- [43] N. Masciocchi, P. Cairati, L. Carlucci, G. Mezza, G. Ciani, A. Sironi, *J. Chem. Soc., Dalton Trans.* **1996**, 2739–2746.

-
- [44] P. Maniam, N. Stock, *Acta Cryst.* **2011**, *C67*, m73-m76.
- [45] Y. Liu, J. H. Her, A. Dailly, A. J. Ramirez-Cuesta, D. A. Neumann, C. M. Brown, *J. Am. Chem. Soc.* **2008**, *130*, 11813-11818.
- [46] B. J. Hathaway, A. W. Hewat, *J. Solid State Chem.* **1984**, *51*, 364-375.
- [47] C. J. Simmons, M. A. Hitchman, H. Stratemeier, A. J. Schultz, *J. Am. Chem. Soc.* **1993**, *115*, 11304-11311.
- [48] E. Montoneri, G. Viscardi, S. Bottigliengo, R. Gobetto, M. R. Chierotti, R. Buscaino, P. Quagliotto, *Chem. Mater.* **2007**, *19*, 2671-2678.
- [49] G. A. Bain, J. F. Berry, *J. Chem Educ.* **2008**, *85*, 532-536.
- [50] *XRED version 1.19, XSHAPE version 1.06*, Stoe & Cie GmbH, Darmstadt, Germany, **1999**.
- [51] G. M. Sheldrick, *Acta Cryst.* **2008**, *A64*, 112-122.
- [52] A. Altomare, M. Camalli, C. Cuocci, C. Giacovazzo, A. Moliterni and R. Rizzi, *J. Appl. Cryst.* **2009**, *42*, 1197-1202.
- [53] A. A. Coelho, *TOPAS-Academic v4.1*; Coelho Software, Brisbane, **2007**.

4.4 Polycarboxylate based MOFs

Porous materials have been studied for various potential applications, for example gas storage, gas separation, catalysis and drug storage.^[1] Especially, well ordered crystalline porous materials such as metal-organic frameworks (MOF) are of much importance in this case. The nature of such size- and shape-selective applications requires well defined pores and chemical properties. Since the first conceptual work on polycarboxylate based coordination polymers in 1965 by Tomic, metal polycarboxylate materials have established a strong foothold in the MOF research area.^[2] This current flood of interest in MOFs is spurred by Férey^[3], Kitagawa^[4] and Yaghi^[5] whose groups have discovered well investigated MOFs such as MIL-101^[6] and MOF-5^[7] which, curiously enough, are made of polycarboxylate ligands. Another essential polycarboxylate MOF which promoted various studies on its synthesis, characterization and possible applications is HKUST-1, $[\text{Cu}_3(\text{BTC})_2(\text{H}_2\text{O})_3]$, BTC = 1,3,5-benzenetricarboxylate.^[8] A closer look at these MOFs shows that they are constructed of different type of M-O clusters which can be defined as so-called inorganic building bricks or sometimes “secondary building units” (SBU) (Figure 4.14).

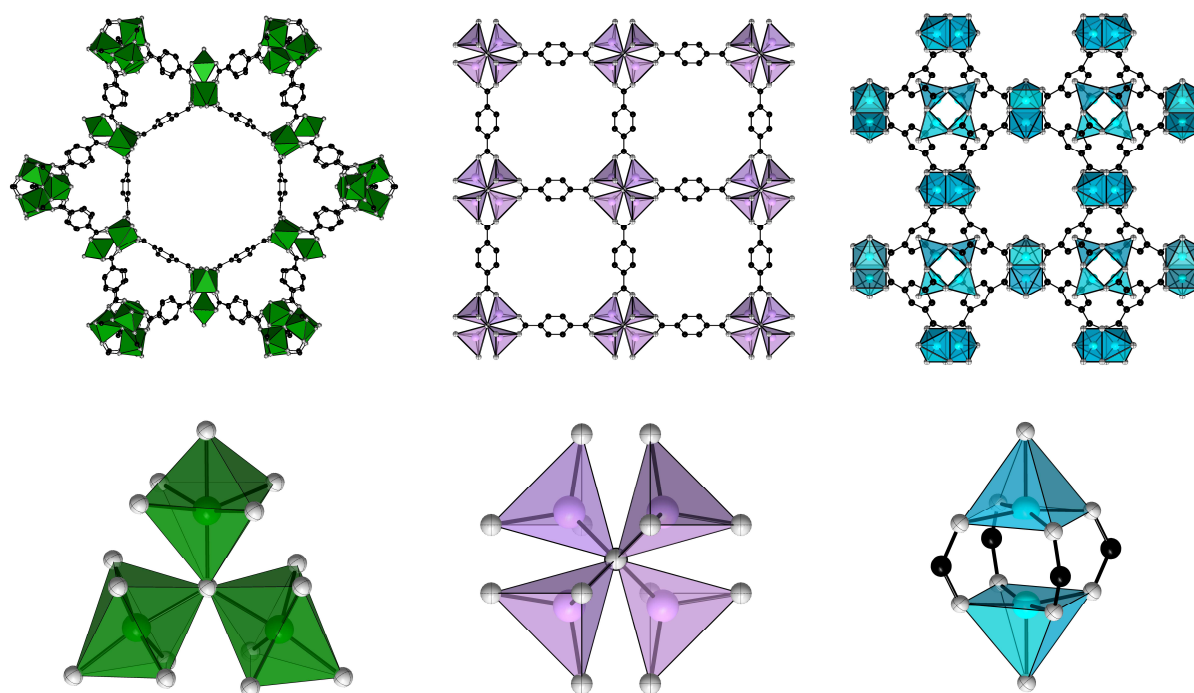


Figure 4.14 (top row from left): Supertetrahedra forming hexagonal ring in MIL-101, square rings in MOF-5, a section of HKUST-1 structure and their respective building bricks (bottom row from left): Cr_3O_{16} trimer, $\text{Zn}_4(\text{O})\text{O}_{12}$ tetrameric cluster and dimeric $\text{Cu}_2\text{O}_{10}\text{C}_4$ paddle-wheel units.

Instead of working on larger metal clusters such as in MIL-101 and MOF-5, the focus point of this work is the simple paddle-wheel metal cluster which is known to form highly symmetrical MOF structures. The four-bladed paddle-wheel unit in HKUST-1 contains two Cu^{2+} ions, four bridging carboxylate groups in the equatorial positions as well as two terminal water ligands in the axial positions and all together they form pseudo-octahedral or square pyramidal coordination geometries. Although three-bladed paddle-wheel unit based crystal structures are also occasionally reported,^[9] the four-bladed paddle-wheel units are observed more often in crystal structures, even in simple metal salts such as copper(II) acetate dihydrate.^[10] Furthermore, the short Cu-Cu distance of 2.64 Å is close to the interatomic distances in metallic copper (2.56 Å) and thus, the dimers are subjected to strong magnetic exchange interactions.^[11]

To further understand the metal ion-carboxylate interactions, one needs to look into the possible bonding modes offered by the -COO^- ions. According to the review by Glusker *et al.*, three coordination modes depending on the $\text{C-O}\cdots\text{M}^{n+}$ angle can be distinguished (Figure 4.15), namely: (1) equal sharing of metal ion by two oxygen atoms (*direct*-bonding), (2) $\text{M}^{n+}\cdots\text{O-C}$ angle of $0\text{-}80^\circ$ (*syn*-bonding) and (3) energetically less favourable angle of $-90\text{-}0^\circ$ (*anti*-bonding).^[12] Therefore, each blade in the paddle-wheel based unit is considered to have a *syn-syn*-bonding $\{\mu\text{-(OCO)}(\text{M}^{n+})_2\}$. Their observations also noted that most compounds containing carboxylate groups have *syn*-bonding compared to *anti*- and *direct*-bonding in which the latter type of bonds normally have weaker and longer M-O bond distances of > 2.3 Å.

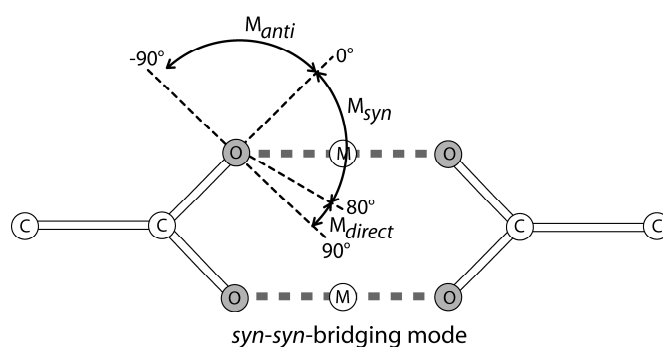


Figure 4.15 Three types of carboxylate ion coordination modes to metal ions. *Syn*-bonding: $0\text{-}80^\circ$, *direct*-bonding: $80\text{-}90^\circ$ and *anti*-bonding: $-90\text{-}0^\circ$. Thus, a paddle-wheel unit has a bridging *syn-syn* mode.^[12]

An interesting property of paddle-wheel units is the accessibility of coordinative unsaturated metal sites and the chemical stability after the removal of terminal axial ligands such as water via thermal activation. This feature enables the activated MOF to act as Lewis acid catalyst

for organic reactions such as isomerization, oxidation and cyanosilylation.^[13,14,15] Inelastic neutron scattering and *in situ* IR spectroscopy studies have also determined that the free metal sites are important binding sites for H₂ adsorption.^[16,17] Recent investigations have also shown that the free Mⁿ⁺ sites in paddle-wheel based MOFs can be occupied by various gases including NO, CO₂, CH₄ and O₂.^[18,19,20,21] Due to all these properties, HKUST-1 became one of first MOFs to be produced in a commercial scale under the name BASOLITE® C300 by BASF SE. The industrial MOF materials can be easily shaped into tablets, extrudates and honeycomb bodies for application purposes.

4.4.1 Isoreticular chemistry

The area of metal-organic frameworks is expanding at a very rapid rate in the recent years.^[22] Each research group is trying to find new niches which others have overlooked. It could be either in the field of synthesis, characterization or finding a new application for a MOF. Nevertheless, all fields provide ample opportunities to make new discoveries in order to fully understand the nature of MOFs. As MOFs are crystalline materials, the precise atomic or molecular positions are known and by specifically changing the metal ion or the organic linker which interconnects the metal ions, the framework properties can be manipulated while maintaining the structure topology. This type of chemistry is termed as *isoreticular chemistry*. An elegant example was demonstrated by the group of Yaghi, where they have systematically modified the pore sizes of the parent structure of MOF-5 [Zn₄O(BDC)₃] by replacing the original terephthalate (BDC) linkers with similar but longer dicarboxylates.^[23] They also showed that functional groups can be incorporated in the pores by directly using functionalized linkers such amino-, bromo- and alkoxy-terephthalic acids, but the functionalization does not stop there. Although extreme solvothermal conditions limit the possible functional groups that could be used, existing functional groups such –NH₂ can also be further modified by post-synthetic reactions.^[24] Such examples include covalent modification of aminoterephthalate linkers in IRMOF-3 into acetylamino-terephthalate and other derivatives with longer alkyl chains via room temperature reactions.^[25]

So far, most isoreticular functionalizations are conducted on the organic building unit of MOFs. Changing metal ions is a more complex subject due to different coordination chemistry of each metal. Only few reports have emerged from this line of research. For example, the structure of Cr-MIL-101^[6] can also reproduced with Fe³⁺ and Al³⁺ ions.^[26,27] The MOF-5 structure has been reported with Zn²⁺, Be²⁺, Co²⁺ ions^[7,28] and isostructural compounds of HKUST-1 were discovered with Mo²⁺, Fe^{2+/3+} and Cr²⁺ ions.^[29,30,21] Nevertheless, the synthesis conditions are no longer the same for each metal ion. Reactants such metal salts and solvents have to be screened to get the desired structure, otherwise other energetically

favorable compounds will be formed. Sometimes, the organic linkers also have to possess certain functional groups in order to obtain isorecticular structures. For example, the structure of Al-MIL-101 can only be obtained by employing $\text{Al}(\text{NO}_3)_3 \cdot 6\text{H}_2\text{O}$, aminoterephthalic acid and dimethylformamide. $\text{AlCl}_3 \cdot 6\text{H}_2\text{O}$, terephthalic acid and water lead to Al-MIL-53.^[27] A recent comparison of reaction kinetics of MIL-53 isostructures by Jung *et al.* has elucidated that reaction rates are very much dependent of the metal ions used. At the same temperatures irrespective of nucleation or crystal growth stages, the relative synthesis rate increases in the following order: $r_{\text{Cr-MIL-53}} < r_{\text{Al-MIL-53}} < r_{\text{V-MIL-47}}$.^[31] Taking into account all these factors, this part of the Ph.D work concentrates on the isorecticular metal-ion chemistry.

4.4.2 Porous nickel-based MOFs with paddle-wheel building units

A potential metal ion candidate for isorecticular MOF investigation in the paddle-wheel structure class is nickel(II). A structure-based search in the Cambridge Structural Database (CSD) shows that most of the compounds with paddle-wheel building units are based on Cu^{2+} and Zn^{2+} ions.^[32] Nickel(II) compounds account for only 23 of the 2487 total number of structures (Figure 4.16 *left*). None of these 23 nickel(II) compounds with paddle-wheel units has porous frameworks. An example of such a non-porous nickel compound is $[\text{Ni}_3(2,6\text{-NDC})_3(\text{bipy})_{1.5}]$ and this structure highlights the difficulty of obtaining non-interpenetrated frameworks when relatively long or larger linkers, in this case 2,6-naphthalenedicarboxylic acid ($\text{H}_2\text{-2,6-NDC}$) and a pillaring ligand, 4,4'-bipyridine (*bipy*) were employed (Figure 4.17 *left*).^[33] Only one porous nickel MOF with paddle-wheel units has emerged from a keyword-based search in Scifinder ® (Figure 4.16 *right*).^[34] This very recent report describes a fully characterized porous nickel(II) MOF containing paddle-wheel building units (Figure 4.17 *right*).^[35]

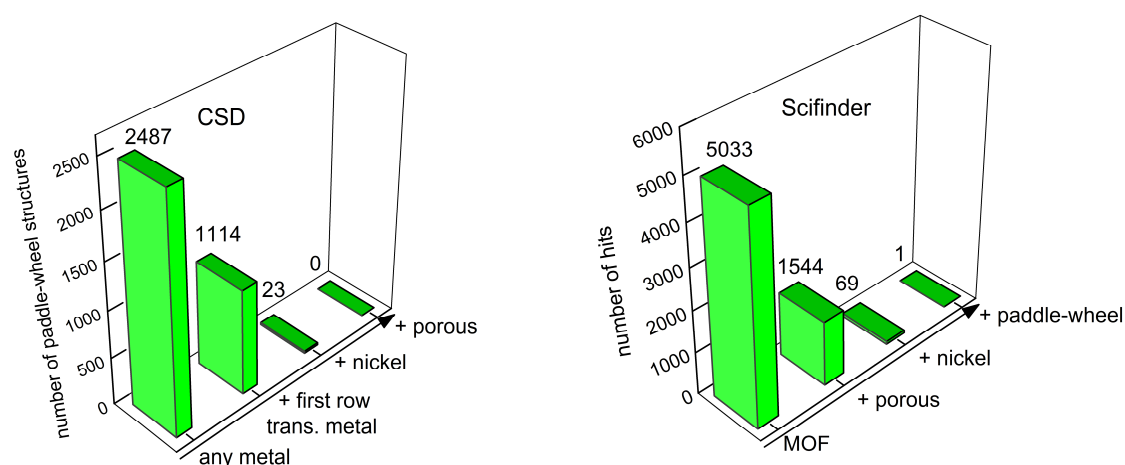


Figure 4.16 (*left*) CSD structural database search of paddle-wheel structure entries. (*right*) Scifinder keyword database search of MOF report entries. Time of search: December 2010.

In that study, a smaller pillaring ligand DABCO (1,4-diazabicyclo[2.2.2]octane) was employed and a highly porous but non-interpenetrating paddle-wheel containing nickel compound $[\text{Ni}_2(2,6\text{-NDC})_2(\text{DABCO})]$ was discovered. The results of these database search clearly show that there is a substantial lack of porous nickel(II) based MOFs and therefore, this gap motivates new studies of such structures. Furthermore, the combination of porosity and the presence of coordinatively unsaturated Ni^{2+} sites in the dimeric paddle-wheel units are also of special interest due to potential catalytic properties. Some examples of heterogeneous catalysis involving Ni^{2+} containing structures are hydrogenation of dienes and oxidation of CO to CO_2 .^[36,37] Based on experimental isosteric heats of adsorption values, Ni^{2+} ions with open metal sites also display the highest H_2 binding strength in comparison to Zn^{2+} , Mn^{2+} , Mg^{2+} and Co^{2+} in a series of $[\text{M}_2(2,5\text{-diolate-terephthalate})]$ isostructures.^[38] The accessibility of such open metal sites is much more enhanced in paddle-wheel units and thus, improve Ni^{2+} ion-guest interactions.^[39]

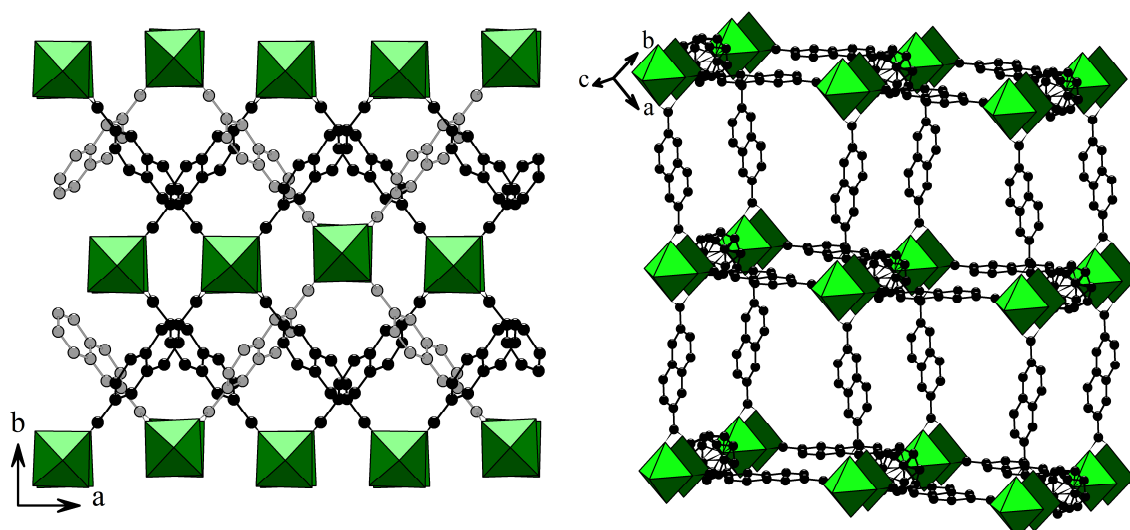
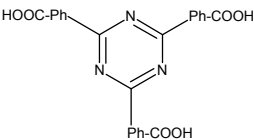
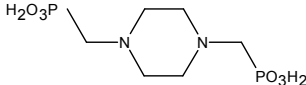
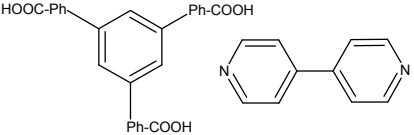
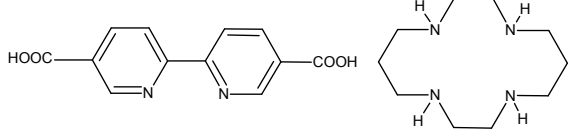
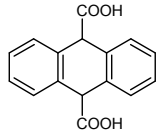
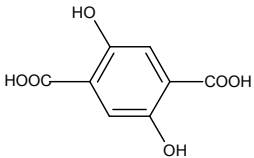
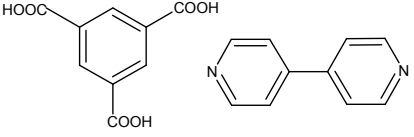
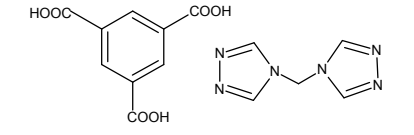
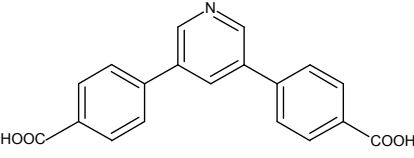
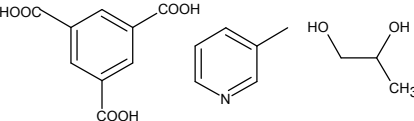


Figure 4.17 (left) The structure of $[\text{Ni}_3(2,6\text{-NDC})_3(\text{bipy})_{1.5}]$ (*bipy* ligands are located behind the Ni-O clusters along the *c*-axis). Triply interpenetrating networks render the structure non-porous. (right) The porous paddle-wheel structure of $[\text{Ni}_2(2,6\text{-NDC})_2(\text{DABCO})]$ with $9.6 \times 9.6 \text{ \AA}$ main pores and a smaller $2.5 \times 7.4 \text{ \AA}$ side pores (specific surface area_{BET} = $2330 \text{ m}^2 \text{ g}^{-1}$). 2,6-NDC = 2,6-naphthalenedicarboxylate, DABCO = 1,4-diazabicyclo[2.2.2.]octane.

Structural comparison of known porous nickel polycarboxylate MOFs has indicated that Ni^{2+} ions form octahedral coordination geometries and dimeric nickel clusters are very rare (Table 4.3). Most of these MOFs have either isolated NiX_6 octahedra, one dimensional NiX_6 edge-sharing chains or corner-sharing trinuclear Ni_3X_n clusters containing one μ_3 -oxygen atom ($\text{X} = \text{O}, \text{N}$). Dimeric Ni-O/N motifs are rarely reported and it is possible that such clusters require special synthesis conditions or additives/modulators in order for them to crystallize preferentially. In this situation, the paddle-wheel type building unit comes into mind as a promising dimeric cluster to be investigated with polycarboxylic acid linkers. The following

section discusses the crystal structures containing paddle-wheel building units which were investigated in this Ph.D. thesis.

Table 4.3 List of non-paddle-wheel based porous nickel(II) MOFs, the respective Ni_mX_n -cluster assembly and the experimental total pore volume (* = calculated with PLATON^[40], † = mixed-valent $Ni^{II,III}$ ions).

Linkers employed	Ni-cluster type	Pore volume (cm ³ g ⁻¹)	Lit.
	trimeric μ_3 -O-corner-sharing Ni_3O_{16}	0.13	41
	chains of edge-sharing $NiNO_5$ octahedra	0.21	42
	isolated NiN_2O_4 octahedra	0.21*	43
	isolated NiN_4O_2 octahedra	0.37	44
	trimeric μ_3 -O-corner-sharing Ni_3O_{16}	0.38	45
	chains of edge-sharing NiO_6 octahedra	0.41	46
	isolated NiO_6 octahedra	0.43	47
	trimeric corner-sharing $Ni_3N_8O_8$	0.51*	48
	trimeric μ_3 -OH-corner-sharing Ni_3O_{16} [†]	0.52*	49
	isolated NiN_2O_4 octahedra	0.63	50

	trimeric μ_3 -OH-corner-sharing $\text{Ni}_3\text{O}_{16}^\dagger$	0.93	51
	pentameric $(\mu_3\text{-O})_2$ edge-sharing pentanuclear Ni_5O_{22}	2.18	52

1) $[\text{M}_3(\text{BTC})_2(\text{X})_3]$ (HKUST-1): The highly porous compound is considered as the simplest cubic framework structure (space group = $Fm\bar{3}m$) attainable with the H_3BTC linker (H_3BTC = 1,3,5-benzenetricarboxylic acid).^[8] The dimeric paddle-wheel $\text{M}_2\text{O}_8\text{X}_2$ clusters with a relatively short internuclear M-M distance have eight oxygen atoms from four carboxylate fragments in the equatorial positions and two terminal atoms (X) in the axial positions. Each cluster is connected to four organic fragments of BTC linkers in a fourfold symmetry and the BTC linker itself is linked to three paddle-wheel clusters (threefold symmetry), hence leading to a (3,4)-connected network in compliance with Wells notation.^[53] The simplified network can be assigned as an augmented twisted boracite structure (**tbo-a**) according to RCSR database.^[54] A three-dimensional (9 Å pore diameter) pore system is observed in the structure in addition to smaller 5 Å pores in octahedral cages (Figure 4.18).

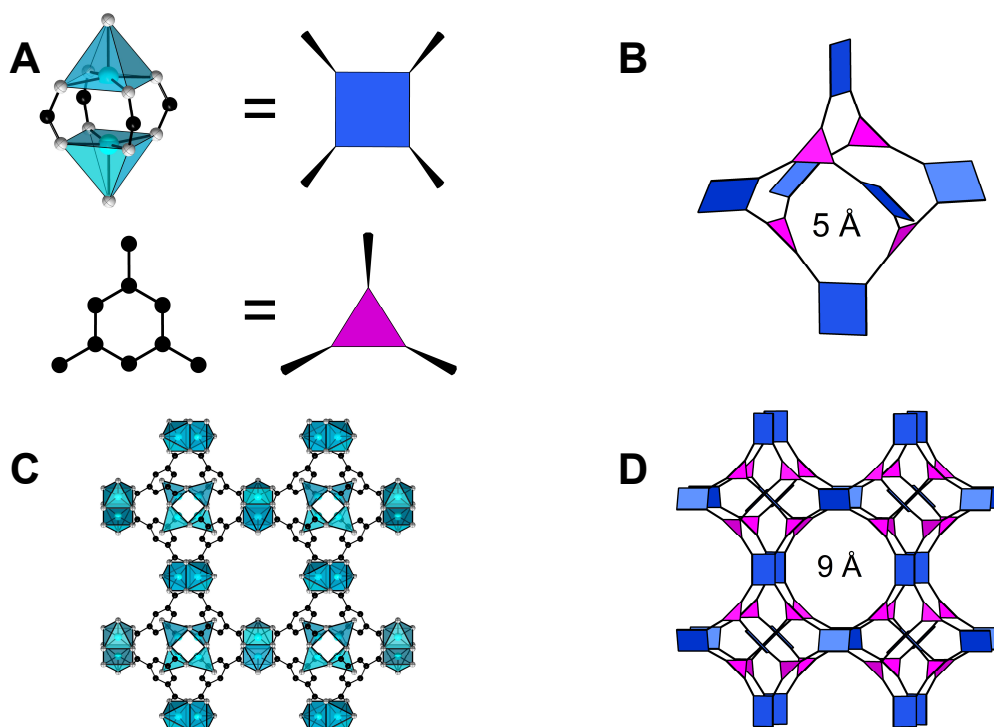


Figure 4.18 The paddle-wheel clusters and BTC linkers can be simplified as squares and triangles, respectively (A). The (3,4)-interconnection of the squares and triangles forms an octahedral cage (B) with an approximate pore diameter of 5 Å. Corner-sharing of these octahedra forms a 3D structure with 9 Å pores. A section of HKUST-1 is displayed as ball-stick model (C) and as simplified **tbo-a** framework (D).

This structure was originally reported with Cu^{2+} ions and was synthesized using solvothermal methods with 50:50 water:ethanol solvent mixture. Current literature reports that the copper-based compound can be now produced with various methods such as microwave-assisted heating^[55], electrochemical^[56], sonothermal^[57] and mechanochemical syntheses^[58]. So far, isorecticular structures have been obtained with Mo^{2+} , $\text{Fe}^{2+}/^{3+}$ and Cr^{2+} ions via solvothermal synthesis.^[29,30,21]

2) $[\text{M}_3(\text{BTB})_2(\text{X})_3]$ MOF-14: This porous structure is related to HKUST-1 in many perspectives as it also has a cubic framework structure and consists of a similar but larger tripodal linker H_3BTB ($\text{H}_3\text{BTB} = 4,4',4''\text{-benzene-1,3,5-triyl-tris(benzoic acid)}$) as well as the paddle-wheel clusters.^[59] Unlike HKUST-1, the symmetry of MOF-14 is reduced to $Im\bar{3}$ due to freely rotating phenyl rings around the central phenyl ring in the BTB linker (35° torsion angle). Each (3,4)-connected sub-framework can be simplified to an augmented Pt_3O_4 (**pto-a**) structure (Figure 4.19 B).^[54] In addition, the spatial arrangement leads to an interwoven framework where the phenyl rings from two sub-frameworks are minimally displaced from each other (3–4 Å) with strong π - π interactions (Figure 4.19 C, D).

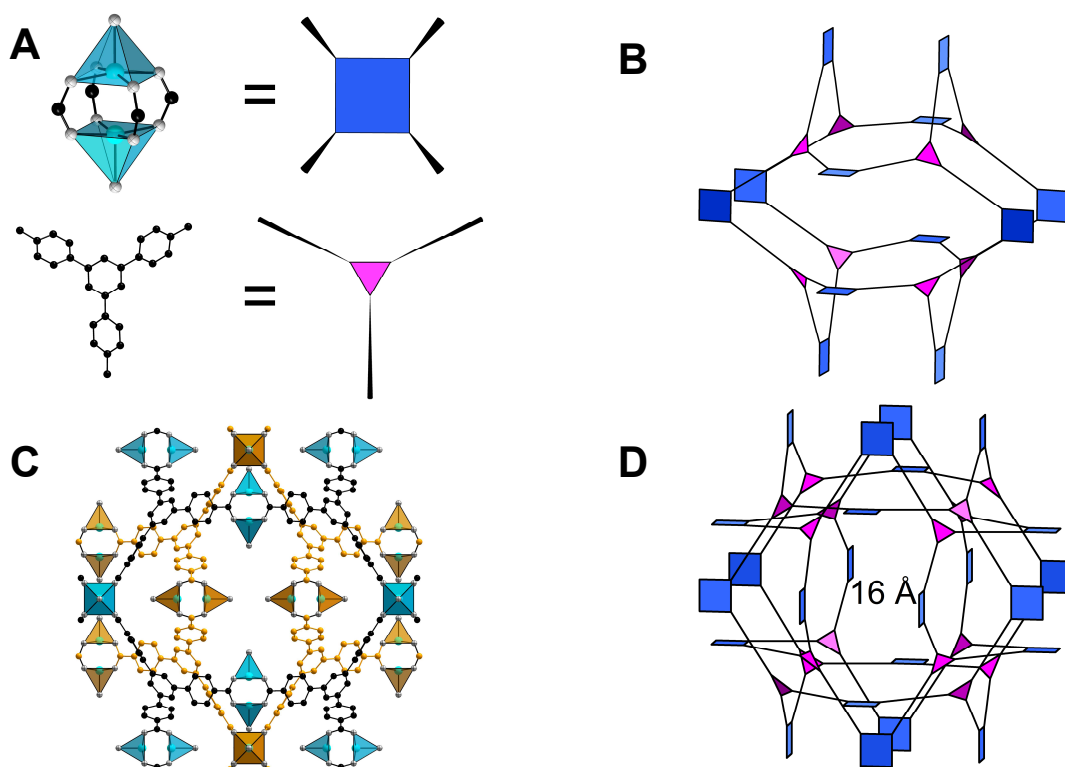


Figure 4.19 The paddle-wheel clusters and BTB linkers can be simplified as squares and triangles, respectively (A). The (3,4)-interconnection of the squares and triangles forms a **pto-a** cage (B) with ellipsoid shaped windows. Two cages (orange and black) interweave each other with minimal displacement and thus inner cavities of 16 Å (C and D) are formed.

This structure was also originally reported with Cu^{2+} ions and was synthesized at $65\text{ }^\circ\text{C}$ with an ethanol/DMF/water/pyridine solvent mixture. Mechanochemical synthesis of Cu-MOF-14 was recently reported^[60], but no isostructural compounds is reported with other metal ions until now.

3) $[\text{M}_2(\text{BDC})_2(\text{DABCO})]$ -tetragonal: Compared to HKUST-1 and MOF-14 which are based on a single polycarboxylate linker, this MOF structure has dimeric paddle-wheel clusters comprising of rigid dicarboxylate linkers BDC (H_2BDC = benzene-1,4-dicarboxylic acid) and also terminal N-bridging DABCO ligands (DABCO = 1,4-diazabicyclo[2.2.2]octane) (Figure 4.20 A).^[61] The (4,4)-interconnection of BDC linkers and paddle-wheel clusters lead to the formation of a 2D square lattice layer and hence the assignment of **sql** topological symbol is used which is typical for structures with tetragonal $P4/mmm$ space group. This layered arrangement can be clearly seen by simplifying the paddle-wheel units as spherical nodes and BDC linkers as joining struts (Figure 4.20 A, B). Square-shaped pores of 7 \AA are observed in the layers. The final assembly of a pillared-layered 3D framework is accomplished through the pillaring of DABCO ligands which results in smaller 4 \AA pores between the layers (Figure 4.20 C, D).

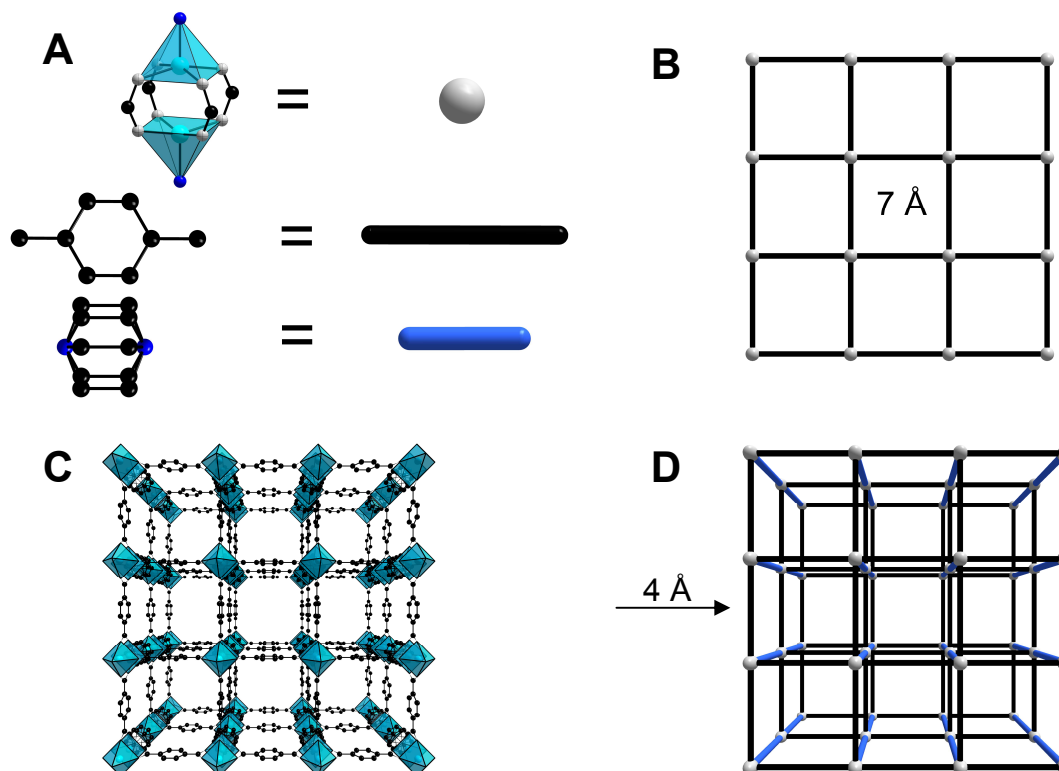


Figure 4.20 The paddle-wheel clusters and BDC linkers as well as the DABCO ligands can be simplified as spherical nodes and linear struts, respectively (A). The (4,4)-interconnection of the nodes and BDC struts leads to a **sql** layer (B) with square-shaped pore windows. Pillaring by the bridging DABCO ligands connects the layers to form the final pillared-layered framework. This framework represents the activated compound $[\text{M}_2(\text{BDC})_2(\text{DABCO})]$ with no guest molecules.

The $[M_2(\text{BDC})_2(\text{DABCO})]$ compound also displays structural flexibility depending on the guest molecules residing in the pores. The as-synthesized structure ($I4/mcm$ space group) has bent BDC linkers and once activated, the linkers become planar which results in the presence of a mirror plane and the change to the space group $P4/mmm$. Inclusion of large molecules such as benzene leads to the loss of the fourfold symmetry and the $[M(\text{BDC})]$ layers have no longer square motif but instead a rhombic grid pattern ($Cmmm$ spacegroup).^[61]

The structure model of $[M_2(\text{BDC})_2(\text{DABCO})]$ was originally reported in 2001 with Cu^{2+} ions and the compound was produced using a stepwise synthesis whereby the Cu^{2+} ions was reacted first with H_2BDC linkers in methanol at 40 °C and later mixed together with a toluene solution of DABCO at 160 °C.^[62] The full structural characterization of the framework type and the investigation of structure flexibility was performed on the Zn-based isostructural compound.^[61] Isostructural materials with Co^{2+} and Ni^{2+} ions were also reported, but with the exception that the synthesis of the Ni^{2+} -based compound was not optimized and no full characterization of the structure was performed.^[63,64]

4) $[M_2(\text{BDC})_2(\text{DABCO})]$ -trigonal: Although the angles in the paddle-wheel clusters stays similar, different connectivities to BDC linkers can occur. Instead of (4,4)-connection in the tetragonal structure, a (3,4) connection was observed in the layers in the trigonal structure with the same structural composition and hence, framework polymorphism is observed. The shortest possible loop/polygon originating from a node is now a triangle while the number of connections radiating from a node is still four. Corner-sharing of triangles also creates larger hexagonal rings. The combination of these triangular and hexagonal rings leads to a pattern which commonly called “Kagomé” layer or **kgm** topology (Figure 4.21 B).^[54,65] Van der Waals spheres of 14 Å and 4.5 Å can fit the hexagonal and triangular windows, respectively. Similar to the tetragonal structure, the DABCO ligands act as pillars to connect the Kagomé layers (Figure 4.21 C, D). Comparing both pseudo-polymorphs, this so-called trigonal framework exhibits lower density than the tetragonal framework and hence, higher surface area and micropore volume are expected for the Kagomé layer-based structure.

This structure was previously selectively synthesized by Chun et al. with Zn^{2+} ions using a DMF/acetonitrile/ethyleneglycol mixture at a reaction temperature of 120 °C.^[66] They have also postulated that acetonitrile molecules act as template for the triangular cages via π - π interactions and hydrogen bonds between the other solvent molecules assisted the formation of the hexagonal cages. Further studies by Kitagawa et al. on the Zn-based pseudo-polymorphs has shown that each phase can be selectively synthesized by controlling the reaction time. The trigonal phase prefers to form at short reaction times. So far, no report has mentioned any isostructural compound of such a trigonal framework with other metal ions.

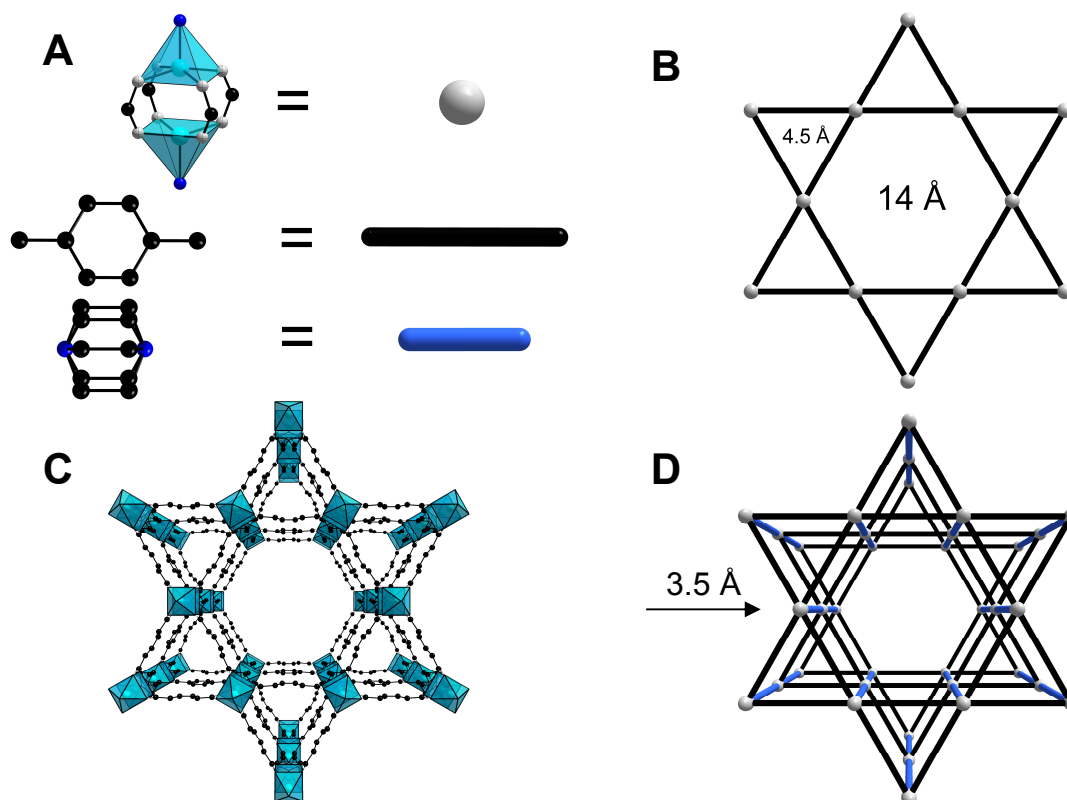


Figure 4.21 The paddle-wheel clusters and BDC linker as well as the DABCO ligand can be simplified as spherical nodes and linear struts, respectively (A). The (3,4)-interconnection of the nodes and BDC struts forms a **kgm** layer (B) with triangular and hexagonal shaped pore windows. Pillaring by the bridging DABCO ligands connects the layers to form the final pillared-layered framework. This framework represents the activated compound $[M_2(BDC)_2(DABCO)]$ with no guest molecules.

References

- [1] S. T. Meek, J. A. Greathouse, M. D. Allendorf, *Adv. Mater.* **2011**, *23*, 249-267.
- [2] E. A. Tomic, *J. Appl. Polym. Sci.* **1965**, *9*, 3745-3752.
- [3] A. K. Cheetham, G. Férey, T. Loiseau, *Angew. Chem Int. Ed.* **1999**, *38*, 3268-3292; *Angew. Chem.* **1999**, *111*, 3466-3492.
- [4] S. Kitagawa, R. Kitaura, S.-I. Noro, *Angew. Chem Int. Ed.* **2004**, *43*, 2334-2375; *Angew. Chem.* **2004**, *116*, 2388-2430.
- [5] M. Eddaoudi, D. B. Moler, H. Li, B. Chen, T. M. Reineke, M. O'Keeffe, O. M. Yaghi, *Acc. Chem. Res.* **2001**, *34*, 319-330.
- [6] G. Férey, C. Mellot-Draznieks, C. Serre, F. Millange, J. Dutour, S. Surblé, I. Margiolaki, *Science*, **2005**, *309*, 2040-2042.
- [7] H. Li, M. Eddaoudi, M. O'Keeffe, O. M. Yagi, *Nature*, **1999**, *402*, 276-279.
- [8] S. S.-Y. Chui, S. M.-F. Lo, J. P. H. Charmant, A. Guy Orpen, I. D. Williams, *Science*, **1999**, *283*, 1148-1150.
- [9] S. M. F. Lo, S. S. Y. Chui, L. Y. Shek, Z. Lin, X. X. Zhang, G. H. Wen, I. D. Williams, *J. Am. Chem. Soc.* **2000**, *122*, 6293-6294.

- [10] J. N. Van Niekerk, F. R. L. Schoening, *Acta Cryst.* **1953**, *6*, 227-232.
- [11] B. Bleaney, K. D. Bowers, *Proc. R. Soc. London A*, **1952**, *214*, 451-465.
- [12] C. J. Carrell, H. L. Carrell, J. Erlebacher, J. P. Glusker, *J. Am. Chem. Soc.* **1988**, *110*, 8651-8656.
- [13] L. Alaerts, E. Séguin, H. Poelman, F. Thibault-Starzyk, P. A. Jacobs, D. E. De Vos, *Chem.-Eur. J.* **2006**, *12*, 7353-7363.
- [14] S. De Rosa, G. Giordano, T. Granato, A. Katovic, A. Siciliano, F. Tripicchio, *J. Agric. Food Chem.* **2005**, *53*, 8306-8309.
- [15] K. Schlichte, T. Kratzke, S. Kaskel, *Microporous Mesoporous Mater.* **2004**, *73*, 81-88.
- [16] P. M. Forster, J. Eckert, B. D. Heiken, J. B. Parise, J. W. Yoon, S. H. Jung, *J. Am. Chem. Soc.* **2006**, *128*, 16846-16850.
- [17] C. Lamberti, A. Zecchina, E. Groppo, S. Bordiga, *Chem. Soc. Rev.* **2010**, *39*, 4951-5001.
- [18] B. Xiao, P. S. Wheatley, X. Zhao, A. J. Fletcher, S. Fox, A. G. Rossi, I. L. Megson, S. Bordiga, L. Regli, K. M. Thomas, R. E. Morris, *J. Am. Chem. Soc.* **2007**, *129*, 1203-1209.
- [19] M. D. Allendorf, R. J. T. Houk, L. Andruszkiewicz, A. A. Talin, J. Pikarsky, A. Choudhury, K. A. Gall, P. J. Hesketh, *J. Am. Chem. Soc.* **2008**, *130*, 14404-14405.
- [20] H. Wu, J. Simmons, Y. Liu, C. Brown, X. S. Wang, S. Ma, V. Peterson, P. Southon, C. Kepert, H. C. Zhou, T. Yildirim, W. Zhou, *Chem.-Eur. J.* **2010**, *16*, 5205-5214.
- [21] L. J. Murray, M. Dinca, J. Yano, S. Chavan, S. Bordiga, C. M. Brown, J. R. Long, *J. Am. Chem. Soc.* **2010**, *132*, 7856-7857.
- [22] J. R. Long, O. M. Yaghi, *Chem. Soc. Rev.* **2009**, *38*, 1213-1214.
- [23] M. Eddaoudi, J. Kim, N. Rosi, D. Vodak, J. Wachter, M. O'Keeffe, O. M. Yaghi, *Science*, **2002**, *295*, 469-472.
- [24] Z. Wang, S. M. Cohen, *J. Am. Chem. Soc.* **2007**, *129*, 12368-12369.
- [25] K. K. Tanabe, Z. Wang, S. M. Cohen, *J. Am. Chem. Soc.* **2008**, *130*, 8508-8517.
- [26] S. Bauer, C. Serre, T. Devic, P. Horcajada, J. Marrot, G. Férey, N. Stock, *Inorg. Chem.* **2008**, *47*, 7568-7576.
- [27] P. Serra-Crespo, E. V. Ramos-Fernandez, J. Gascon, F. Kapteijn, *Chem. Mater.* **2011**, *23*, 2565-2572.
- [28] S. Hausdorf, F. Baitalow, T. Böhle, D. Rafaja, F. O. R. L. Mertens, *J. Am. Chem. Soc.* **2010**, *132*, 10978-10981.
- [29] M. Kramer, U. Schwarz, S. Kaskel, *J. Mater. Chem.* **2006**, *16*, 2245-2248.
- [30] L. Xie, S. Liu, C. Gao, R. Cao, J. Cao, C. Sun, Z. Su, *Inorg. Chem.* **2007**, *46*, 7782-7788.
- [31] E. Haque, J. H. Jeong, S. H. Jung, *CrystEngComm*, **2010**, *12*, 2749-2754.
- [32] F. H. Allen, *Acta Cryst.* **2002**, *B58*, 380-388. Databank search in CSD Conquest version 5.31 with Feb 2010 update.
- [33] S. W. Lee, H. J. Kim, Y. K. Lee, K. Park, J. H. Son, Y. U. Kwon, *Inorg. Chim. Acta*, **2003**, *353*, 151-158.
- [34] Scifinder®, version 2011; Chemical Abstracts Service: Columbus, Ohio, USA.

- [35] N. Klein, C. Herzog, M. Sabo, I. Senkovska, J. Getzschmann, S. Paasch, M. R. Lohe, E. Brunner, S. Kaskel, *Phys. Chem. Chem. Phys.* **2010**, *12*, 11778-11784.
- [36] N. Guillou, Q. Gao, P. M. Forster, J. S. Chang, M. Noguès, S. E. Park, G. Férey, A. K. Cheetham, *Angew. Chem., Int. Ed.* **2001**, *40*, 2831–2834. *Angew. Chem.* **2001**, *113*, 2913–2916.
- [37] R.-Q. Zou, H. Sakurai, Q. Xu, *Angew. Chem., Int. Ed.* **2006**, *45*, 2542–2546. *Angew. Chem.* **2006**, *118*, 2604–2608.
- [38] W. Zhou, H. Wu, T. Yildirim, *J. Am. Chem. Soc.* **2008**, *130*, 15268-15269.
- [39] S. I. Vagin, A. K. Ott, B. Rieger, *Chem. Ing. Tech.* **2007**, *79*, 767-780.
- [40] A. L. Spek, *J. Appl. Cryst.* **2003**, *36*, 7-13.
- [41] S. Ma, X. S. Wang, E. S. Manis, C. D. Collier, H. C. Zhou, *Inorg. Chem.* **2007**, *46*, 3432-3434.
- [42] S. R. Miller, G. M. Pearce, P. A. Wright, F. Bonino, S. Chavan, S. Bordiga, I. Margiolaki, N. Guillou, G. Férey, S. Bourrelly, P. L. Llewellyn, *J. Am. Chem. Soc.* **2008**, *130*, 15967-15981.
- [43] R. Heck, J. Bacsá, J. E. Warren, M. J. Rosseinsky, D. Bradshaw, *CrystEngComm.* **2008**, *10*, 1687-1692.
- [44] E. Y. Lee, M. P. Suh, *Angew. Chem. Int. Ed.* **2004**, *43*, 2798–2801; *Angew. Chem.* **2004**, *116*, 2858–2861.
- [45] S. Ma, J. M. Simmons, D. Yuan, J. R. Li, W. Weng, D. J. Liu, H. C. Zhou, *Chem. Commun.* **2009**, 4049-4051.
- [46] P. D. C. Dietzel, B. Panella, M. Hirscher, R. Blom, H. Fjellvag, *Chem. Commun.* **2006**, 959-961.
- [47] C. Gao, S. Liu, L. Xie, Y. Ren, J. Cao, C. Sun, *CrystEngComm.* **2007**, *9*, 545-547.
- [48] H. A. Habib, J. Sanchiz, C. Janiak, *Dalton Trans.* **2008**, 1734-1744.
- [49] J. Jia, X. Lin, C. Wilson, A. J. Blake, N. R. Champness, P. Hubberstey, G. Walker, E. J. Cussen, M. Schröder, *Chem. Commun.* **2007**, 840-842.
- [50] D. Bradshaw, T. J. Prior, E. J. Cussen, J. B. Claridge, M. J. Rosseinsky, *J. Am. Chem. Soc.* **2004**, *126*, 6106-6114.
- [51] Y. B. Zhang, W. X. Zhang, F. Y. Feng, J. P. Zhang, X. M. Chen, *Angew. Chem. Int. Ed.* **2009**, *48*, 5287-5290; *Angew. Chem.* **2009**, *121*, 5391-5394.
- [52] K. Gedrich, I. Senkovska, N. Klein, U. Stoeck, A. Henschel, M. R. Lohe, I. A. Baburin, U. Mueller, S. Kaskel, *Angew. Chem. Int. Ed.* **2010**, *49*, 8489-8492; *Angew. Chem.* **2010**, *122*, 8667-8670.
- [53] A. F. Wells, **1977**, *Three-dimensional Nets and Polyhedra*, Wiley-Interscience, New York, USA.
- [54] M. O’Keeffe, M. A. Peskov, S. J. Ramsden, O. M. Yaghi, *Acc. Chem. Res.* **2008**, *41*, 1782-1789.
- [55] Y. K. Seo, G. Hundal, I. T. Jang, Y. K. Hwang, C. H. Jun, J. S. Chang, *Microporous Mesoporous Mater.* **2009**, *119*, 331-337.
- [56] U. Mueller, M. Schubert, F. Teich, H. Puetter, K. Schierle-Arndt and J. Pastré, *J. Mater. Chem.* **2006**, *16*, 626-636.

- [57] Z.-Q. Li, L.-G. Qiu, T. Xu, Y. Wu, W. Wang, Z.-Y. Wu, X. Jiang, *Mater. Lett.* **2009**, *63*, 78-80.
- [58] M. Schlesinger, S. Schulze, M. Hietschold, M. Mehring, *Microporous Mesoporous Mater.* **2010**, *32*, 121-127.
- [59] B. Chen, M. Eddaoudi, S. T. Hyde, M. O'Keeffe, O. M. Yaghi, *Science*, **2001**, *291*, 1021-1023.
- [60] M. Klimakow, P. Klobes, A. F. Thünemann, K. Rademann, F. Emmerling, *Chem. Mater.* **2010**, *22*, 5216-5221.
- [61] D. N. Dybtsev H. Chun, K. Kim, *Angew. Chem. Int. Ed.* **2004**, *43*, 5033-5036; *Angew. Chem.* **2004**, *116*, 5143-5146.
- [62] K. Seki, S. Takamizawa, W. Mori, *Chem. Lett.* **2001**, *30*, 332-333.
- [63] T. Takei, T. Ii, J. Kawashima, T. Ohmura, M. Ichikawa, M. Hosoe, Y. Shinya, I. Kanoya, W. Mori, *Chem. Lett.* **2007**, *36*, 1136-1137.
- [64] B. Arstad, H. Fjellvåg, K. O. Kongshaug, O. Swang, R. Blom, *Adsorption*, **2008**, *14*, 755-762.
- [65] I. Syozi, *Prog. Theor. Phys.* **1951**, *6*, 306-308.
- [66] H. Chun, J. Moon, *Inorganic Chemistry*, **2007**, *46*, 4371-4373.

4.4.3 Investigation of Porous Ni-Based Metal Organic Frameworks Containing Paddle-Wheel Type Inorganic Building Units via High-Throughput Methods

The above-mentioned article has been published in its final form in "Inorganic Chemistry": DOI: 10.1021/ic200381f. The article is reprinted here with permission from American Chemical Society, Copyright © 2011. The supporting information of this article is placed in the Appendix section (Appendix 4).

Four porous nickel-based MOFs with paddle-wheel building units (**1a**, **2**, **3a**, **3b**) were synthesized. Starting from H₃BTC linker (H₃BTC = 1,3,5-benzenetricarboxylic acid), high-throughput (HT) screening was performed with various nickel salts, organic bases and solvents. The results showed that Ni(NO₃)₂·6H₂O, 2-methylimidazole and dimethylformamide (DMF) were the optimal starting materials for the synthesis of the porous MOF [Ni₃(BTC)₂(Me₂NH)₃](DMF)₄(H₂O)₄ (**1a**) which is isostructural to HKUST-1. Through the HT screening of reaction temperatures (150-180 °C), the optimal formation fields of **1a** and two dense phases, **1b** [Ni₆(BTC)₂(DMF)₆(HCOO)₆] and **1c** were determined. In **1a**, the dimethylamine (Me₂NH) terminal axial ligands are formed via *in situ* hydrolysis of DMF solvent molecules. Applying the previous reactants, reaction conditions and employing the larger linker H₃BTB (4,4',4''-benzene-1,3,5-triyl-tris-(benzoic acid)), another porous MOF [Ni₃(BTB)₂(2-MelmH)_{1.5}(H₂O)_{1.5}](DMF)₉(H₂O)_{6.5} (**2**), isostructural to MOF-14, with interwoven frameworks was obtained. For the synthesis of **1a** as well as **2**, the addition of 2-methylimidazole (2-MelmH) and conventional heating are very important. Microwave-assisted heating (MW) was applied for the phase-selective synthesis of pseudo-polymorphic MOFs [Ni₂(BDC)₂(DABCO)]·(DMF)₄(H₂O)_{1.5} (**3a**) and [Ni₂(BDC)₂(DABCO)]·(DMF)₄(H₂O)₄ (**3b**). Rapid nucleation with MW assisted heating, low overall concentration, stirring and excess of DABCO leads to the formation of trigonal framework (**3b**) while the synthesis of tetragonal framework (**3a**) is accomplished using low DABCO amounts, high overall concentration and no stirring. A new dense phase **3c** [Ni(BDC)(DABCO)] was also discovered during the HT experiments. Adsorption isotherm experiments have confirmed the microporosity of **1a**, **2**, **3a** and **3b**. Although compound **2** exhibits no adsorption of N₂, the uptake of gas/vapors molecules with smaller kinetic diameters is possible. In addition, strong hysteresis has been observed with H₂O and H₂. The crystal structures of **1a**, **1b** and **2** were determined by single crystal X-ray diffraction. Rietveld refinement of the structures of **3a**, **3b** and **3c** had to be carried out since only microcrystalline products were obtained. Further characterization of the compounds was carried out with thermogravimetric, IR and elemental analysis which helped to identify and quantify the guest molecules in the compounds.

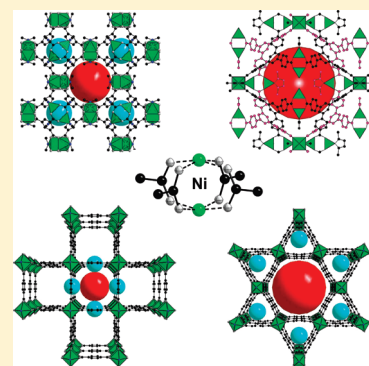
Investigation of Porous Ni-Based Metal–Organic Frameworks Containing Paddle-Wheel Type Inorganic Building Units via High-Throughput Methods

Palanikumar Maniam and Norbert Stock*

Institut für Anorganische Chemie, Christian-Albrechts-Universität zu Kiel, Max-Eyth-Strasse 2, D-24118 Kiel, Germany

Supporting Information

ABSTRACT: In the search of Ni based metal–organic frameworks (MOFs) containing paddle-wheel type building units, three chemical systems $\text{Ni}^{2+}/\text{H}_n\text{L}/\text{base}/\text{solvent}$ with $\text{H}_n\text{L} = \text{H}_3\text{BTC}$ (1,3,5-benzenetricarboxylic acid), H_3BTB (4,4',4'',-benzene-1,3,5-triyl-tris-(benzoic acid)), and H_2BDC (terephthalic acid) were investigated using high-throughput (HT) methods. In addition to the conventional heating, for the first time HT microwave assisted synthesis of MOFs was carried out. Six new compounds were discovered, and their fields of formation were established. In the first system, H_3BTC was employed and a comprehensive HT-screening of compositional and process parameters was conducted. The synthesis condition for the Ni paddle-wheel unit was determined and two compounds $[\text{Ni}_3(\text{BTC})_2(\text{Me}_2\text{NH})_3] \cdot (\text{DMF})_4(\text{H}_2\text{O})_4$ (**1a**) and $[\text{Ni}_6(\text{BTC})_2(\text{DMF})_6(\text{HCOO})_6]$ (**1b**) were discovered ($\text{Me}_2\text{NH} = \text{dimethylamine}$, $\text{DMF} = \text{dimethylformamide}$). In the second system, the use of the extended tritopic linker H_3BTB and the synthesis conditions for the paddle-wheel units led to the porous MOF, $[\text{Ni}_3(\text{BTB})_2(2\text{-MeIm})_{1.5}(\text{H}_2\text{O})_{1.5}] \cdot (\text{DMF})_9(\text{H}_2\text{O})_{6.5}$ (**2**), (2-MeIm = 2-methylimidazole). This compound shows a selective adsorption of H_2O and H_2 with a strong hysteresis. In the third system, H_2BDC was used, and the base (DABCO) was incorporated as a bridging ligand into all structures. Thus, two pillared layered porous MOFs $[\text{Ni}_2(\text{BDC})_2(\text{DABCO})] \cdot (\text{DMF})_4(\text{H}_2\text{O})_{1.5}$ (**3a**) and $[\text{Ni}_2(\text{BDC})_2(\text{DABCO})] \cdot (\text{DMF})_4(\text{H}_2\text{O})_4$ (**3b**) as well as a layered compound $[\text{Ni}(\text{BDC})(\text{DABCO})] \cdot (\text{DMF})_{1.5}(\text{H}_2\text{O})_2$ (**3c**) were isolated. The **3a** and **3b** polymorphs of the $[\text{Ni}_2(\text{BDC})_2(\text{DABCO})]$ framework can be selectively synthesized. The combination of microwave assisted heating, low overall concentration, stirring of the reaction mixtures, and an excess of DABCO yields a highly crystalline pure phase of **3b**. The fields of formation of all compounds were established, and scale-up was successfully performed for **1b**, **2**, **3a**, **3b**, and **3c**. All compounds were structurally characterized. In addition to IR, elemental and TG analyses, gas and vapor sorption experiments were carried out.



INTRODUCTION

High-throughput (HT) methodologies which are regarded as a core component in the screening of new drugs in the pharmaceutical field are also very helpful in the area of solid state chemistry.^{1–3} By implementing this alternative method in solvothermal syntheses, many groups have discovered new compounds such as zeolites, metal-arsenates, -phosphonates, -carboxylates and -imidazolates.^{4–8} In contrast to conventional methods, HT methods allow the rapid and systematic investigation of large synthesis fields.^{3,9} This enables the efficient discovery of new compounds, the fast optimization of synthesis conditions, and because of the large amount of data, it allows the extraction of reaction trends. HT methods have been successfully applied in the investigation of porous metal–organic frameworks (MOFs), which are of interest because of their potential application in fields such as gas storage, gas separation, catalysis, and drug delivery.^{10,11} Using HT methods, compounds such as MIL-101-NDC,¹² the amino-functionalized MOFs MIL-53, MIL-88, and MIL-101^{13,14} and imidazolate based compounds such as ZIF-8 have been discovered.⁸

One of the most intensively investigated MOF to-date is HKUST-1 $[\text{Cu}_3(\text{BTC})_2(\text{H}_2\text{O})_3]$ which contains paddle-wheel

type inorganic building units.¹⁵ The chemical and thermal stability as well as the presence of accessible Lewis acid sites are some of the reasons why HKUST-1 has been studied by many groups. A search in the CSD database shows that most of the compounds containing paddle-wheel units are based on Cu and Zn, but examples with other ions such as Mo, Fe, and Cr were also reported.¹⁶ Only few nickel carboxylates with paddle-wheel units have been described. While most of these nickel compounds exhibit no porosity,^{17–20} only two porous structures were recently reported.^{21,22} The combination of porosity and the presence of coordinatively unsaturated Ni^{2+} sites is also of special interest because of catalytic properties^{23,24} and the strong H_2 binding affinity.^{25,26} The accessibility of the metal sites in these compounds depends very much on the nature and size of Ni-based inorganic units. Simple dimeric clusters such paddle-wheel units provide much less steric hindrance and thus, could enhance host–guest interactions. For these reasons, we started a systematic investigation to explore the feasibility of synthesizing

Received: February 23, 2011

Published: May 03, 2011

porous Ni²⁺ based MOFs with paddle-wheel units. Starting from the well established linkers 1,3,5-benzenetricarboxylic acid (H₃BTC), 4,4',4''-benzene-1,3,5-triyl-tris(benzoic acid) (H₃BTB) and terephthalic acid (H₂BDC), we investigated the three chemical systems Ni²⁺/H_nL/base/solvent with H_nL = H₃BTC, H₃BTB, and H₂BDC. Here we report the fields of formation of six compounds, four containing Ni paddle-wheel units, in these three systems, and their structural elucidation, as well as their detailed characterization.

EXPERIMENTAL SECTION

Material and Methods. All reagents are of analytical grade (Sigma-Aldrich and ABCR) and were used without any further purification. H₃BTB was provided by BASF SE. High-throughput X-ray powder diffraction (XRPD) experiments were carried out in transmission mode using a STOE Stadi P combi high-throughput X-ray powder diffractometer equipped with an image-plate position-sensitive detector (IPSPD). MIR spectra were recorded with an ATI Matheson Genesis spectrometer in the spectral range 4000–400 cm⁻¹ using the KBr disk method. Thermogravimetric analyses were carried out in air (75 mL min⁻¹, 30–800 °C, 4 °C min⁻¹) or nitrogen (75 mL min⁻¹, 30–800 °C, 4 °C min⁻¹) atmosphere using a NETZSCH STA 409 CD analyzer. CHN analyses were performed with a Eurovektor EuroEA Elemental Analyzer. The SEM images and semiquantitative elemental analyses were performed with a Phillips ESEM XL 30 and JEOL JSM-6500F hot cathode scanning electron microscope equipped with an energy dispersive X-ray (EDX) EDAX analyzer for elemental analysis. N₂, CO₂, Ar, and H₂O sorption experiments were performed using a Belsorp-max apparatus (BEL JAPAN INC.). Low pressure volumetric hydrogen sorption measurements were conducted with a Quantachrome Autosorb 1-C instrument at 77 K; H₂ as well as He gases of 99.999% purity were used. For the activation prior to sorption measurement, all samples were heated overnight at 150 °C in vacuum (10⁻³ mbar).

High-Throughput Experiments (Conventional Heating). The reaction system Ni²⁺/H_nL/base/solvent was investigated using various molar ratios Ni²⁺:H_nL:base (discovery and focused arrays) employing high-throughput methods. The process and compositional parameters are listed in the Supporting Information, Tables S1–S15. The HT experiments via conventional heating were performed under solvothermal conditions in a custom-made stainless steel high-throughput reactor system containing 48 PTFE inserts each with a maximum volume of 300 μL.²⁷ For most of the HT-experiments, standard solutions of starting materials were made by dissolving all solid reagents in the solvent under magnetic stirring (Supporting Information, Tables S1–S15). Respective volumes of each reactant were manually dosed into the PTFE inserts. In some of the HT-experiments, solid reactants with low solubility were weighed in directly into the Teflon inserts. The exact amounts of starting materials are given in the Supporting Information, Table S1–S15. The evaluations of the HT experiments are based on XRPD measurements.

High-Throughput Experiments (Microwave Heating). The system Ni²⁺/H₂BDC/DABCO/DMF was investigated under microwave assisted heating. All reactions were performed using Anton Paar Synthos 3000 multimode microwave unit employing a 4 × 24MG5 rotor. Sealed borosilicate glass vials with reaction mixtures were used, which were inserted into the silicon carbide plate (6 × 4 matrix). The temperature of the plates is monitored using an IR sensor located at the bottom of the microwave unit. Samples requiring stirring were agitated with 10 mm magnetic stir bars during synthesis. The exact amounts of starting materials and reaction conditions are given in the Supporting Information, Tables S16–S19. The evaluations of the HT experiments are based on XRPD measurements.

[Ni₃(BTC)₂(Me₂NH)₃]·(DMF)₄(H₂O)₄ (**1a**). In a HT experiment **1a** was obtained by the following procedure (molar ratio Ni(NO₃)₂·6H₂O/H₃BTC/2-MeIm = 2:1.5:1). DMF solutions of Ni(NO₃)₂·6H₂O (0.03 mmol, 30 μL), H₃BTC (0.015 mmol, 60 μL), 2-MeIm (0.01 mmol, 10 μL), and DMF (100 μL) were pipetted into a 300 μL reactor. The mixture was heated at 170 °C for 48 h in a conventional oven. The synthesis of compound **1a** could not be scaled-up in glass reactors or larger Teflon reactors. Therefore, a larger amount of the pure phase product was collected from a separate HT experiment containing 24 identical reaction mixtures with the molar ratio Ni(NO₃)₂·6H₂O/H₃BTC/2-MeIm = 2:1.5:1. The product (69 mg, 35% based on H₃BTC) containing dark green octahedral crystals (SEM micrograph Supporting Information, Figure S1) was washed with fresh DMF and identified by XRPD measurements. The measured and simulated XRPD patterns (Supporting Information, Figure S4) compare well. Elemental analysis of [Ni₃(BTC)₂(Me₂NH)₃]·(DMF)₄(H₂O)₄ (**1a**), *M* = 1090.02 g mol⁻¹: found C 39.6, H 5.1, N 9.3; calcd C 39.6, H 5.8, N 9.0.

[Ni₆(BTC)₂(HCOO)₆(DMF)₆] (**1b**). In a HT experiment, **1b** was obtained by the following procedure (molar ratio Ni(ClO₄)₂·6H₂O/H₃BTC/2-MeIm = 3:1:1). DMF solutions of Ni(ClO₄)₂·6H₂O (0.03 mmol, 60 μL), H₃BTC (0.01 mmol, 40 μL), 2-MeIm (0.01 mmol, 20 μL), and DMF (80 μL) were pipetted into a 300 μL reactor. The mixture was heated at 150 °C for 48 h in a conventional oven. The scale-up of **1b** was accomplished in DURAN glass tubes with *V*_{max} = 4 mL by employing Ni(ClO₄)₂·6H₂O (0.3 mmol, 109.7 mg), H₃BTC (0.1 mmol, 21.0 mg), 2-MeIm (0.1 mmol, 8.2 mg) and 2 mL of DMF. The product (49.4 mg, 67% based on H₃BTC) containing green hexagonal plates (SEM micrograph Supporting Information, Figure S1) was washed with fresh DMF and identified by XRPD measurements. The measured and simulated XRPD patterns (Supporting Information, Figure S4) compare well. Elemental analysis of [Ni₆(BTC)₂(HCOO)₆(DMF)₆] (**1b**), *M* = 1475.05 g mol⁻¹: found C 34.5, H 4.0, N 5.8; calcd C 34.2, H 3.7, N 5.7.

[Ni₃(BTB)₂(2-MeIm)_{1.5}(H₂O)_{1.5}]·(DMF)₉(H₂O)_{6.5} (**2**). In a HT experiment under conventional heating **2** was obtained by the following procedure (molar ratio Ni(NO₃)₂·6H₂O/H₃BTB/2-MeIm = 1.5:3:3.5). DMF solutions of Ni(NO₃)₂·6H₂O (0.015 mmol, 15 μL), H₃BTB (0.03 mmol, 105 μL), 2-MeIm (0.035 mmol, 35 μL), and DMF (45 μL) were pipetted into a 300 μL reactor. The mixture was heated at 170 °C for 48 h. The scale-up of **2** was accomplished in a batch Teflon-lined steel autoclave with *V*_{max} = 20 mL by employing Ni(NO₃)₂·6H₂O (1.5 mmol, 436 mg), H₃BTB (3 mmol, 1314 mg), 2-MeIm (3.5 mmol, 287 mg), and 20 mL of DMF. The product (769 mg, 78% based on Ni(NO₃)₂·6H₂O) containing dark brown blocks (SEM micrograph Supporting Information, Figure S1) was washed with fresh DMF and identified by XRPD measurements. The measured and simulated XRPD patterns (Supporting Information, Figure S5) compare well. Elemental analysis of [Ni₃(BTB)₂(2-MeIm)_{1.5}(H₂O)_{1.5}]·(DMF)₉(H₂O)_{6.5} (**2**), *M* = 1971.83 g mol⁻¹: found C 52.6, H 5.4, N 8.8; calcd C 52.9, H 6.0, N 8.5.

[Ni₂(BDC)₂(DABCO)]·(DMF)₄(H₂O)_{1.5} (**3a**). In a HT experiment under conventional heating, **3a** was obtained by the following procedure (molar ratio Ni(NO₃)₂·6H₂O/H₂BDC/DABCO = 2:2:1). DMF solutions of Ni(NO₃)₂·6H₂O (0.02 mmol, 20 μL), H₂BDC (0.02 mmol, 60 μL), DABCO (0.01 mmol, 10 μL), and DMF (110 μL) were pipetted into a 300 μL reactor. The mixture was heated at 110 °C for 48 h. The scale-up of **3a** was accomplished in a batch Teflon-lined steel autoclave with *V*_{max} = 20 mL by employing Ni(NO₃)₂·6H₂O (2 mmol, 580 mg), H₂BDC (2 mmol, 332 mg), DABCO (1 mmol, 112 mg) and 20 mL of DMF. The product (614 mg, 70% based on H₂BDC) containing green microcrystalline powder (SEM micrograph Supporting Information, Figure S1) was washed with fresh DMF and identified by XRPD measurements (Supporting Information, Figure S6). Elemental analysis of [Ni₂(BDC)₂(DABCO)]·(DMF)₄(H₂O)_{1.5} (**3a**), *M* = 877.12 g mol⁻¹: found C 46.2, H 5.4, N 9.3; calcd C 46.5, H 5.8, N 9.6.

Table 1. Crystallographic Data for $[\text{Ni}_3(\text{BTC})_2(\text{Me}_2\text{NH})_3] \cdot (\text{DMF})_4(\text{H}_2\text{O})_4$ (**1a**), $[\text{Ni}_6(\text{BTC})_2(\text{DMF})_6(\text{HCOO})_6]$ (**1b**), and $[\text{Ni}_3(\text{BTB})_2(2\text{-MeIm})_{1.5}(\text{H}_2\text{O})_{1.5}] \cdot (\text{DMF})_9(\text{H}_2\text{O})_{6.5}$ (**2**)

	1a^a	1b	2a^a
chemical formula	$\text{Ni}_3\text{C}_{36}\text{H}_{63}\text{N}_7\text{O}_{20}$	$\text{Ni}_6\text{C}_{42}\text{H}_{54}\text{N}_6\text{O}_{30}$	$\text{Ni}_3\text{C}_{87}\text{H}_{118}\text{N}_{12}\text{O}_{29}$
formula weight (g/mol)	1090.02	1475.05	1971.83
crystal system	cubic	trigonal	cubic
space group	$Fm\bar{3}m$ (No. 225)	$P\bar{3}$ (No. 147)	$Im\bar{3}$ (No. 204)
<i>a</i> (Å)	26.5941(7)	13.8230(4)	26.816(3)
<i>b</i> (Å)	26.5941(7)	13.8230(4)	26.816(3)
<i>c</i> (Å)	26.5941(7)	7.9625(2)	26.816(3)
α (deg)	90	90	90
β (deg)	90	90	90
γ (deg)	90	120	90
<i>V</i> (Å ³)	18808.6(9)	1317.60(6)	19283(6)
<i>Z</i>	16	1	8
λ (Å)	0.71013	0.71013	0.71013
<i>D</i> _{calcd} (g cm ⁻³)	1.025	1.859	0.831
μ (mm ⁻¹)	1.23	2.20	0.62
temp (K)	293	120	293
R1 (on <i>F</i> _o ² , <i>I</i> > 2σ(<i>I</i>))	0.068	0.040	0.076
wR2 (on <i>F</i> _o ² , <i>I</i> > 2σ(<i>I</i>))	0.180	0.070	0.239

^aThe SQUEEZE routine of the program PLATON was used to eliminate the contribution of disordered solvents molecules.²⁹

$[\text{Ni}_2(\text{BDC})_2(\text{DABCO})] \cdot (\text{DMF})_4(\text{H}_2\text{O})_4$ (**3b**). In a HT-MW experiment **3b** was obtained by the following procedure (molar ratio Ni(NO₃)₂·6H₂O/H₂BDC/DABCO = 1:1:4). DMF solutions of Ni(NO₃)₂·6H₂O (0.1 mmol, 200 μL), H₂BDC (0.1 mmol, 300 μL), DABCO (0.4 mmol, 800 μL), and DMF (700 μL) were pipetted into a 4 mL glass vial. The mixture was heated under stirring in the microwave unit at 110 °C for 2 h (set power value = 400 W). Larger amounts of **3b** were obtained by using a separate HT-MW experiment containing six identical reaction mixtures with the molar ratio Ni(NO₃)₂·6H₂O/H₂BDC/DABCO = 1:1:4. The product (163 mg, 59% based on H₂BDC) containing green microcrystalline powder (SEM micrograph Supporting Information, Figure S1) was washed with fresh DMF and identified by XRPD measurements (Supporting Information, Figure S6). Elemental analysis of $[\text{Ni}_2(\text{BDC})_2(\text{DABCO})] \cdot (\text{DMF})_4(\text{H}_2\text{O})_4$ (**3b**), *M* = 922.23 g mol⁻¹: found C 43.8, H 5.7, N 9.2; calcd C 44.3, H 6.1, N 9.1.

$[\text{Ni}(\text{BDC})(\text{DABCO})] \cdot (\text{DMF})_{1.5}(\text{H}_2\text{O})_2$ (**3c**). In a HT-MW experiment **3c** was obtained by the following procedure (molar ratio Ni(NO₃)₂·6H₂O/H₂BDC/DABCO = 3:1:4). DMF solutions of Ni(NO₃)₂·6H₂O (0.3 mmol, 600 μL), H₂BDC (0.1 mmol, 300 μL), DABCO (0.4 mmol, 800 μL), and DMF (300 μL) were pipetted into a 4 mL glass vial. The mixture was heated in the microwave unit at 110 °C for 2 h (set power value = 400 W). Larger amounts of **3c** were obtained using a separate HT-MW experiment containing six identical reaction mixtures with the molar ratio Ni(NO₃)₂·6H₂O/H₂BDC/DABCO = 3:1:4. The product (153 mg, 53% based on H₂BDC) containing pale green microcrystalline powder (SEM micrograph Supporting Information, Figure S1) was washed with fresh DMF and identified by XRPD measurements (Supporting Information, Figure S6). Elemental analysis of $[\text{Ni}(\text{BDC})(\text{DABCO})] \cdot (\text{DMF})_{1.5}(\text{H}_2\text{O})_2$ (**3c**), *M* = 480.65 g mol⁻¹: found C 46.2, H 6.0, N 10.4; calcd C 46.2, H 6.4, N 10.2.

X-ray Crystallography. Suitable crystals of the compounds were carefully selected from the HT experiments using a polarizing microscope. Single-crystal X-ray diffraction for **1a** and **2** were performed with a STOE IPDS-1 diffractometer equipped with a fine-focus sealed tube (Mo-Kα radiation, λ = 71.073 pm). For data reduction and absorption correction the programs XRED and XSHAPE were used.²⁸ For **1a** and **2**, contributions from disordered solvent molecules were removed by the

SQUEEZE routine (PLATON).²⁹ The single crystal of **1b** was measured using a Bruker–Nonius APEX II CCD diffractometer equipped with a Bruker–Nonius FR591 rotating anode Mo-Kα radiation source. Absorption correction was done using the SADABS software.³⁰ The single crystal structures were solved by direct methods and refined using the program package SHELXTL.³¹ The results of single crystal structure determinations are summarized in Table 1. The structure of compound **3c** was solved using the following software programs: EXPO2009,³² Material Studio,³³ and FOX.³⁴ The full Rietveld refinement of compounds **3a**, **3b**, and **3c** were carried out with TOPAS.³⁵ Results and final Rietveld refinement plots are given in Table 2 and Supporting Information, Figures S7–S9. Comparison of Ni–O and Ni–N bond lengths of the paddle-wheel based Ni(II) compounds are summarized in the Supporting Information, Table S20.

RESULTS AND DISCUSSION

The systematic investigation of a chemical system comprises a large number of parameters. Many chemical parameters such as molar ratios of starting materials, the overall concentration, additives (e.g., a base), the solvent, or the metal salt employed have a strong influence on the product formation and the phase purity.^{36,37} Furthermore, process parameters such as the heating program, the reaction time, and the reaction temperature have to be taken into account.³⁸ To identify the reaction conditions leading to Ni-based paddle-wheel units, all these parameters were investigated. Starting from so-called discovery arrays, large parts of the parameter fields are scanned. Once a new compound is discovered, focused arrays are set up which focus on a smaller part or the parameter space and thus allow us to establish the optimized synthesis conditions.²⁷ In the following sections the results of our HT- investigations of the three respective systems are described and discussed.

HT-Investigation of the System Ni²⁺/H₃BTC/Base/Solvent. The first and most extensive screening of the reaction parameters was carried out in the first system Ni²⁺/H₃BTC/base/solvent (Figure 1). At first the influence of different bases,

Table 2. Crystallographic Data for $[\text{Ni}_2(\text{BDC})_2(\text{DABCO})] \cdot (\text{DMF})_4(\text{H}_2\text{O})_{1.5}$ (**3a**), $[\text{Ni}_2(\text{BDC})_2(\text{DABCO})] \cdot (\text{DMF})_4(\text{H}_2\text{O})_4$ (**3b**), and $[\text{Ni}(\text{BDC})(\text{DABCO})] \cdot (\text{DMF})_{1.5}(\text{H}_2\text{O})_2$ (**3c**)

	3a	3b	3c
chemical formula	$\text{Ni}_2\text{C}_{34}\text{H}_{51}\text{N}_6\text{O}_{13.5}$	$\text{Ni}_2\text{C}_{34}\text{H}_{56}\text{N}_6\text{O}_{16}$	$\text{NiC}_{18.5}\text{H}_{30.5}\text{N}_{3.5}\text{O}_{7.5}$
formula weight (g/mol)	877.12, 557.75 ^a	922.23, 557.75 ^a	480.65, 334.98 ^a
crystal system	tetragonal	trigonal	monoclinic
calculated density ($\text{g} \cdot \text{cm}^{-3}$)	1.360, 0.861 ^a	1.215, 0.735 ^a	1.762, 1.228 ^a
space group	<i>I4/mcm</i> (No. 140)	<i>P3m1</i> (No. 164)	<i>P2/m</i> (No. 10)
<i>a</i> (Å)	15.1496(7)	21.5930(3)	10.6682(7)
<i>b</i> (Å)	15.1496(7)	21.5930(3)	7.0125(4)
<i>c</i> (Å)	18.6597(8)	9.3672(1)	6.0822(4)
α (deg)	90	90	90
β (deg)	90	90	95.269(5)
γ (deg)	90	120	90
<i>V</i> (Å ³)	4282.6(4)	3782.4(1)	453.1(1)
<i>Z</i>	4	3	1
λ (Å)	1.5406	1.5406	1.5406
2θ range (deg)	2.0 to 80.0	2.0 to 80.0	2.0 to 80.0
no. of non H-atoms	13	11	17
GoF	1.158	2.930	3.570
no. structural parameters	39	40	79
<i>R</i> _{wp}	0.044	0.054	0.139
<i>R</i> _p	0.033	0.039	0.097
<i>R</i> _{Bragg}	0.009	0.032	0.055

^a The values are calculated without guest molecules.

imidazole (Im), 2-methylimidazole (2-MeIm), 1,4-diazabicyclo-[2.2.2]octane (DABCO), and 4,4-bipyridine (4,4-Bipy) in the system $\text{NiCl}_2 \cdot 6\text{H}_2\text{O}/\text{H}_3\text{BTC}/\text{base}/\text{DMF}$, was investigated varying the molar ratio $\text{Ni}^{2+}/\text{H}_3\text{BTC}$. At 150 °C, only 2-MeIm led to a new, well crystalline phase which was identified as $[\text{Ni}_3(\text{BTC})_2(\text{Me}_2\text{NH})_3] \cdot (\text{DMF})_4(\text{H}_2\text{O})_4$ (**1a**) and is isostructural to HKUST-1 (Supporting Information, Table S1).¹⁵ In contrast to the copper-analogue HKUST-1 which can be obtained in various solvents without any additives via solvothermal, electrochemical, microwave, or sonothermal methods (Supporting Information, Table S21), the presence of the base 2-MeIm is essential for the formation of **1a**. The role of 2-MeIm can not be explained up to now. It is not a structure directing agent since no 2-MeIm could be found in the final product **1a**.

To find the optimal Ni^{2+} source for the synthesis, different salts, that is, $\text{NiCl}_2 \cdot 6\text{H}_2\text{O}$, $\text{NiSO}_4 \cdot 6\text{H}_2\text{O}$, $\text{Ni}(\text{ClO}_4)_2 \cdot 6\text{H}_2\text{O}$, $\text{Ni}(\text{CH}_3\text{COO})_2 \cdot 4\text{H}_2\text{O}$, and $\text{Ni}(\text{NO}_3)_2 \cdot 6\text{H}_2\text{O}$, were screened in combination with H_3BTC , 2-MeIm, and DMF at a reaction temperature of 150 °C (Figure 1, Supporting Information, Table S2). On the basis of the results of the XRPD measurements, $\text{NiSO}_4 \cdot 6\text{H}_2\text{O}$ and $\text{Ni}(\text{CH}_3\text{COO})_2 \cdot 4\text{H}_2\text{O}$ produce only X-ray amorphous products while $\text{Ni}(\text{ClO}_4)_2 \cdot 6\text{H}_2\text{O}$ led exclusively to the new dense compound $[\text{Ni}_6(\text{BTC})_2(\text{DMF})_6(\text{HCOO})_6]$ (**1b**). $\text{Ni}(\text{NO}_3)_2 \cdot 6\text{H}_2\text{O}$ yields most often a mixture of both phases **1a** and **1b** depending on the molar ratio of the reactants (Supporting Information, Table S2). Although the use of $\text{NiCl}_2 \cdot 6\text{H}_2\text{O}$ resulted always in the formation of **1a**, EDX measurements showed the presence of large amounts of Cl^- ions in the as synthesized product ($\text{Ni}/\text{Cl} = 1:4\text{--}5$). Removal of the Cl^- ions was investigated but always led to the structural decomposition. Therefore, $\text{Ni}(\text{NO}_3)_2 \cdot 6\text{H}_2\text{O}$ was used for all further investigations.

The use of various solvents well-known for the synthesis of MOFs and mixtures thereof were screened for the synthesis

optimization of **1a** (Figure 1, Supporting Information, Table S3). On the basis of the results of the XRPD measurements, only pure, dry DMF led to the most crystalline and pure phase product **1a**. Nevertheless, small amounts of H_2O introduced through the use of $\text{Ni}(\text{NO}_3)_2 \cdot 6\text{H}_2\text{O}$ lead to the partial hydrolysis of DMF and the formation of dimethylamine (Me_2NH) and formic acid. While formate ions can act as anionic ligands, dimethylamine can act as a monodentate ligand or in the protonated form as a counterion to balance the framework charge.^{39,40} In **1a** and **1b** dimethylamine and formate ions are observed, respectively.

The reaction temperature also plays a crucial role in solvothermal syntheses, especially with respect to the crystallinity and the yield of the phase.^{38,41} Therefore, the reaction system $\text{Ni}^{2+}/\text{H}_3\text{BTC}/2\text{-MeIm}$ in DMF was investigated at five different temperatures between 140 and 180 °C using 48 different starting compositions, each (Figure 2, Supporting Information, Tables S4–S8). The products were analyzed per XRPD measurements, and the results are plotted in ternary crystallization diagrams (Figure 2). In addition to **1a** and **1b**, a new crystalline phase was detected (**1c**) at temperatures between 150 and 170 °C, which rapidly decomposed upon exposure to air. This phase is only found at the edge of the crystallization diagram in the area of high 2-MeIm and low Ni^{2+} concentrations. **1a** and **1c** crystallize as dark green octahedral and rod-shaped crystals, respectively, while **1b** forms light green hexagonal crystals (Supporting Information, Figure S1). Figure 2 shows that **1a** preferentially forms at temperatures of 160–180 °C, but only at 170 °C crystals with a well-defined shape (octahedral morphology) were obtained (Supporting Information, Figure S1). Pure phase **1a** with high crystallinity was observed at the molar ratio $\text{Ni}(\text{NO}_3)_2/\text{H}_3\text{BTC}/2\text{-MeIm} = 2:1.5:1$ at 170 °C. Large amounts of **1a** could only be obtained in our 48-er reactor system. Title compound **1b** is the

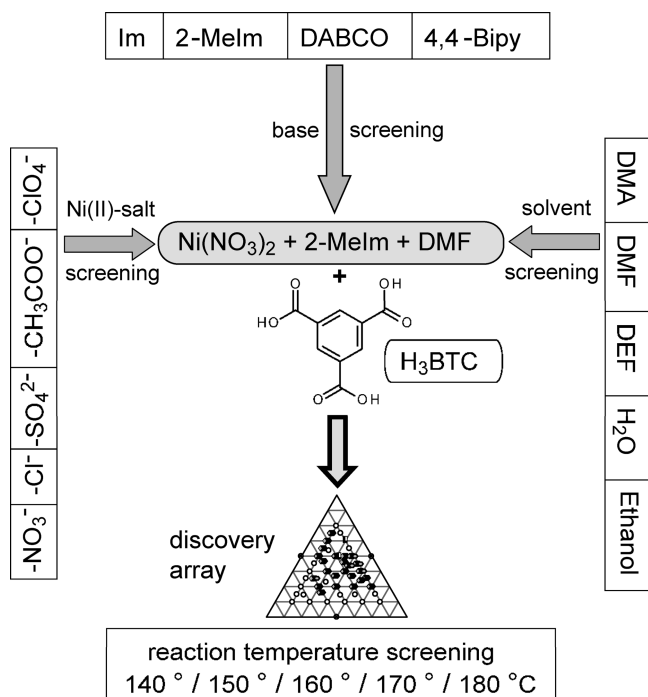


Figure 1. Summary of the HT screening of nickel(II) salts, bases, and solvents which provided the optimal reactants (shaded box) for the subsequent reaction temperature screening in HT-investigation of the system $\text{Ni}^{2+}/\text{H}_3\text{BTC}/\text{base}/\text{solvent}$. The definitions of the abbreviations used are following: Im = imidazole, 2-Melm = 2-methylimidazole, DABCO = 1,4-diazabicyclo[2.2.2]octane, 4,4-Bipy = 4,4-bipyridine, DMA = dimethylacetamide, DMF = dimethylformamide, DEF = diethylformamide, H_3BTC = 1,3,5-benzenetricarboxylic acid. Details of the experiments are given in Supporting Information, Tables S1–S3.

dominant phase at lower temperatures, and scale-up was easily accomplished.

HT-Investigation of $\text{Ni}(\text{NO}_3)_2/\text{H}_3\text{BTC}/2\text{-Melm}$ System. Once the synthesis condition of the Ni paddle-wheel unit for **1a** was established, H_3BTC was replaced with the extended linker H_3BTB and the optimal reactants and solvent, that is, nickel(II)-nitrate salt, 2-methylimidazole, and DMF, were employed. Using an initial reaction temperature of 150°C and a reaction time of 72 h, a discovery array containing 48 different molar ratios of $\text{Ni}(\text{NO}_3)_2/\text{H}_3\text{BTB}/2\text{-Melm}$ were investigated. As shown in the crystallization diagram (Figure 3), only one crystalline phase is observed. Large dark brown cubic crystals of the paddle-wheel based structure $[\text{Ni}_3(\text{BTB})_2(2\text{-Melm})_{1.5}(\text{H}_2\text{O})_{1.5}] \cdot (\text{DMF})_9(\text{H}_2\text{O})_{6.5}$ (**2**) were obtained (Supporting Information, Figure S2). Upon exposure to air the crystals change their color to green in minutes without the loss of crystallinity. The title compound is only formed in a small, well-defined area of the crystallization diagram (Figure 3). A focused array was set up to narrow down the compositional parameters, and the reaction temperature was varied between 130 and 170°C . Well crystalline product of **2** is obtained at the molar ratio range $\text{Ni}(\text{NO}_3)_2/\text{H}_3\text{BTC}/2\text{-Melm} = 1.25\text{--}1.5:1.25\text{--}3.8:3\text{--}5.5$ at 170°C . Employing these conditions, the synthesis scale-up was carried out without any problems. In comparison to analogous Cu-based MOF-14 which is formed under mild synthesis conditions,⁴² compound **2** prefers relatively high reaction temperatures and 2-methylimidazole as an additive.

HT-Investigation of $\text{Ni}^{2+}/\text{H}_2\text{BDC}/\text{DABCO}$ System. Series of $[(\text{M}^{2+})_2(\text{BDC})_2(\text{DABCO})]$ ($\text{M} = \text{Ni}, \text{Co}, \text{Cu}, \text{Zn}$) paddle-wheel

based porous MOFs with tetragonal framework structures were reported in recent years.^{21,43–45} On the basis of the Cu-compound, Seki et al. proposed the structure model in 2001.⁴⁴ The tetragonal structure was later refined from single crystal XRD data of the isorecticular Zn-based compound.^{45,46} A Zn-based polymorph of this MOF with a trigonal framework (Kagomé net topology⁴⁷) was first synthesized by Chun et al. in a ternary solvent system.⁴⁸ The polymorph formation, tetragonal phase versus trigonal phase, can be controlled using different reaction times or using anion-templating as observed in mechanochemical synthesis.^{49,50} While the Zn-based compounds have been studied in detail, almost no data is available on the Ni-based systems.^{21,22} Rather than focusing only on the solvent system or the reaction time, we decided to study the polymorph formation by systematically investigating the compositional parameters as well as the reaction temperature. By employing the HT-reactor system, a discovery array was setup with 48 different $\text{Ni}(\text{NO}_3)_2/\text{H}_2\text{BDC}/\text{DABCO}$ compositions using DMF as the sole solvent (Supporting Information, Figure S3 and Supporting Information, Tables S11–S14). Four temperatures (90° , 110° , 130° , and 150°C) were chosen, and the reactors were subjected to conventional heating for 48 h. Both polymorphs, the tetragonal $[\text{Ni}_2(\text{BDC})_2(\text{DABCO})] \cdot (\text{DMF})_4(\text{H}_2\text{O})_{1.5}$ (**3a**) and trigonal $[\text{Ni}_2(\text{BDC})_2(\text{DABCO})] \cdot (\text{DMF})_4(\text{H}_2\text{O})_4$ (**3b**) phases were observed, and the new structure $[\text{Ni}(\text{BDC})(\text{DABCO})] \cdot (\text{DMF})_{1.5}(\text{H}_2\text{O})_2$ (**3c**) was discovered.

Title compound **3a** is the prevalent phase in the upper part of the crystallization diagram within the molar ratio range $\text{Ni}(\text{NO}_3)_2/\text{H}_2\text{BDC}/\text{DABCO} = 1\text{--}5:2\text{--}6:1\text{--}4$, whereas phase **3c** dominates the lower part in the molar ratio range $\text{Ni}(\text{NO}_3)_2/\text{H}_2\text{BDC}/\text{DABCO} = 1\text{--}4:1:3\text{--}6$. A scale-up synthesis of **3a** could be performed successfully using a 20 mL Teflon batch reactor with the optimal molar ratio $\text{Ni}(\text{NO}_3)_2/\text{H}_2\text{BDC}/\text{DABCO} = 2:2:1$ at 110°C for 48 h. In the overlapping section of the **3a** and **3c** formation fields, title compound **3b** was observed. It always cocrystallizes as the minor phase with **3a** or **3c**. Comparing the number of occurrences of **3b** at different temperatures, this compound was predominantly formed at 110°C (Supporting Information, Figure S3). Since in the corresponding Zn-based system, a short reaction time leads to the formation of the trigonal phase,⁴⁹ we also investigated the influence of the reaction time. A decrease to 1 h helps to increase the yield of **3b**, but the cocrystallization of **3a** could not be avoided (Figure 4, Supporting Information, Table S15). The results of HT-investigations via conventional heating at different reaction times have generally shown that both **3a** and **3b** are rapidly formed in relatively short time. In addition, only microcrystalline products of **3a** and **3b** have been obtained in all experiments. These factors indicate that the nucleation rate of both phases is high which usually leads to many small crystals.⁵¹ To further investigate the polymorph formation, high-throughput experiments using microwave-assisted heating (HT-MW) with magnetic stirring were conducted (Figure 5). Microwave heating, which has been mostly utilized in the field of organic chemistry, is reported to have many advantages such as short reaction times, higher product yields, and increased product purity.^{52,53} Recent reports have also shown that porous materials can be synthesized with microwave heating and most importantly, phase selectivity has been demonstrated, for example, for silicoaluminium phosphates.^{54,55} Therefore, the following studies were carried out: (a) influence of the molar ratios $\text{Ni}^{2+}/\text{H}_2\text{BDC}/\text{DABCO}$ (Figure 5A), (b) role of stirring during the reaction (Figure 5B), (c) influence of the overall

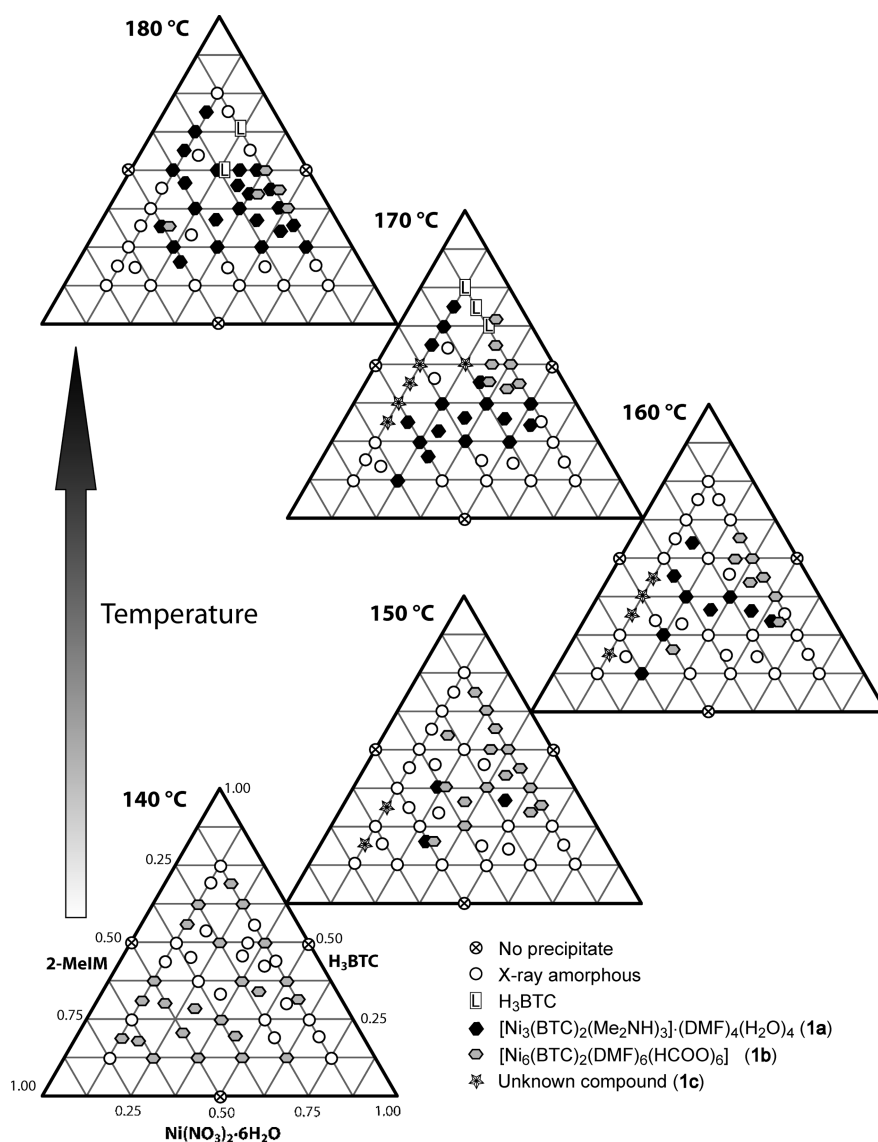


Figure 2. Ternary crystallization diagrams showing the results of HT reaction temperature screening between 140° and 180 °C. Compound **1b** dominates the formation fields at lower temperatures. **1a** forms preferentially at higher temperatures, mostly in the center of the diagram. **1c** crystallizes in a small formation field with high 2-MeIm amounts at 150–170 °C. Overlapping symbols stand for mixed phases. Results are based on XRPD measurements. Molar ratios of reactants are normalized to 1.00. Details of the experiments are given in Supporting Information, Tables S4–S8.

concentration (Figure 5C), and (d) influence of the Ni salt counterion (Figure 5D). These experiments were carried out repeatedly (2–3 times each) to confirm the trends observed.

On the basis of the previous results (Figure 4), molar ratios $\text{Ni}(\text{NO}_3)_2/\text{H}_2\text{BDC} = 1:1$, $1.5:1$, and $2:1$ were chosen for the HT-MW experiment and the amount of DABCO was varied (Figure 5A, Supporting Information, Table S16). In contrast to the experiments under conventional heating (no stirring), pure phase **3b** could be obtained by applying the same reaction time and temperature. Employing a molar ratio of $\text{Ni}(\text{NO}_3)_2/\text{H}_2\text{BDC}/\text{DABCO}/\text{DMF} = 1:1:4:260$ and microwave heating at 110 °C for 1 h under stirring yields a highly crystalline single-phase product of **3b**. Another HT-MW experiment was performed to cross-examine the stirring effect on the selective crystallization of **3a** and **3b** (Figure 5B, Supporting Information, Table S17). Interestingly, in this concentration regime pure phase of **3b** only forms under stirring and using large molar excess of DABCO, while the

nonstirred reaction mixtures and smaller amounts of DABCO lead to the formation of **3a**. The effect of stirring on the phase selectivity is a relatively undeveloped field, and so far, it has been reported in the area of selective asymmetric synthesis^{56,57} and synthesis of zeolites, for example, for zeolite Y polymorphs.⁵⁸

The overall concentration has also a large influence on the product formation. In a HT-MW experiment, the $\text{Ni}(\text{NO}_3)_2/\text{H}_2\text{BDC}/x \cdot \text{DABCO}/y \cdot \text{DMF}$ ($x = 0.5$ and 4) reaction mixtures with y ranging from 65 to 5200 were investigated (Figure 5C, Supporting Information, Table S18, previously used concentrations in experiment 5B are marked by an asterisk). The results show that under highly diluted conditions and independent of stirring or base amount, only phase **3b** forms. Thus, the overall concentration exerts a greater influence on the product formation than the base amount. Under higher overall concentrations, the influence of stirring and base amount is observed. Phase **3a** crystallizes preferentially at concentrated conditions and low

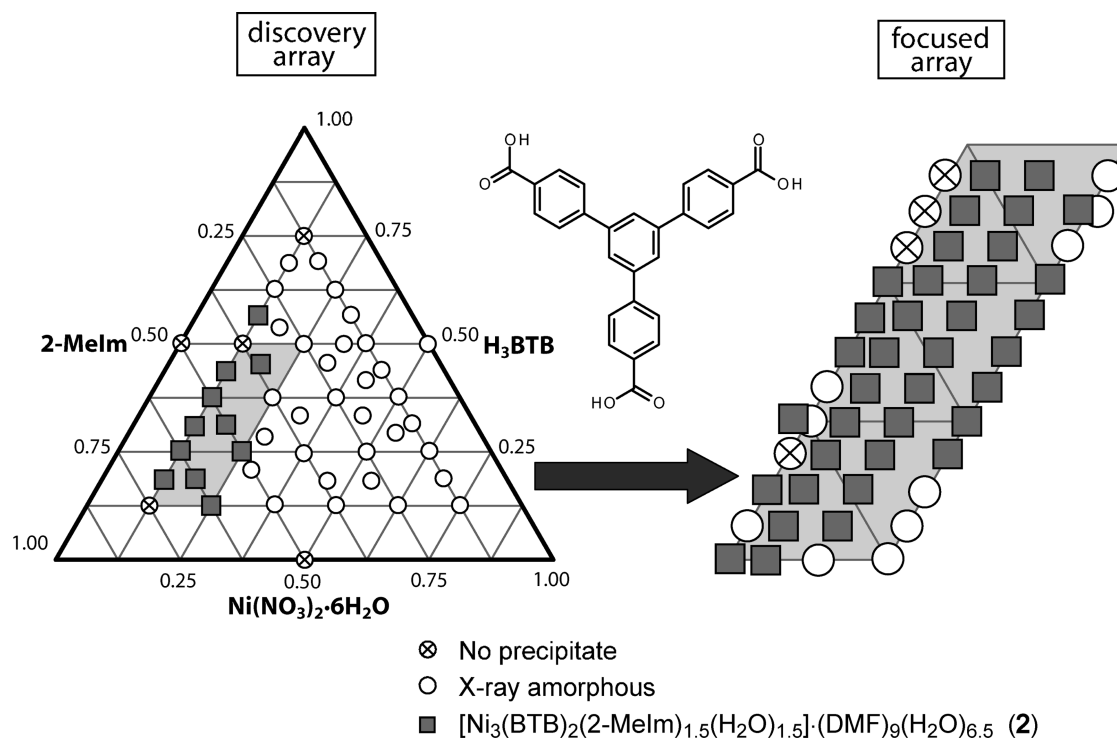


Figure 3. Crystallization diagram displaying the results of HT-investigations of the system $\text{Ni}^{2+}/\text{H}_3\text{BTB}/2\text{-Melm}/\text{DMF}$. Reactions were conducted at 150°C for 72 h in a conventional oven. Left: discovery array showing the approximate formation field of **2**. Right: focused array confirming the specific formation field of **2**. Results are based on XRPD measurements. Molar ratio values are normalized to 1.00. Details of the HT-experiment are given in Supporting Information, Tables S9–S10.

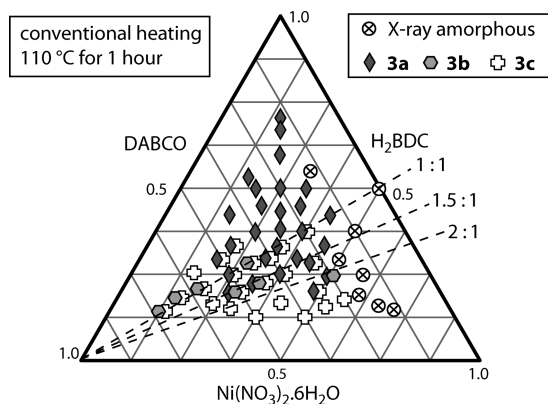


Figure 4. Crystallization diagram displaying the results of HT-investigations of the system $\text{Ni}(\text{NO}_3)_2/\text{H}_2\text{BDC}/\text{DABCO}$. Reactions were conducted at 110°C for 1 h in a conventional oven. Formation of **3b** was observed at molar ratios $\text{Ni}(\text{NO}_3)_2/\text{H}_2\text{BDC} = 1:1, 1.5:1,$ and $2:1$ (dashed lines). These parameters were used in the HT-MW setup for further investigations (Figure 5). Details of the HT-experiment are given in Supporting Information, Table S15.

amounts of base and phase **3c** forms exclusively at high overall concentration, an excess of DABCO and under stirring. Similar observations were also reported in the hydrothermal synthesis of Al/Cr-MIL-101 and Al/Cr-MIL-53, in which the former prefers dilute and more basic conditions whereas Al/Cr-MIL-53 requires concentrated and acidic conditions.^{60,61} Recently Friscic et al. have demonstrated the anion-templating effect of nitrate and sulfate ions in the liquid assisted mechanochemical synthesis of the analogue Zn-based polymorphs.⁵⁰ Because of their synthesis

procedure, the added anions were incorporated into the structure and lead to the phase selectivity. The addition of nitrate salts led to the formation of the tetragonal framework, while sulfate salts resulted in the formation of the trigonal framework structure. Therefore, we also investigated the role of NO_3^- and SO_4^{2-} anions of the Ni^{2+} salt on the product formation (Figure S19, Supporting Information, Table S19). In the solvothermal HT-MW experiment, the NO_3^- salt leads to better crystalline products of **3a** and **3b**. Pure phase **3b** could not be obtained starting from the SO_4^{2-} salt. Thus the anion-templating effect cannot be transferred to the Ni-system with solvothermal reaction conditions.

Crystal Structure Description. The coordination of carboxylate ions to metal ions can be categorized in three types depending on the $\text{C}-\text{O}\cdots\text{M}$ angle.⁶² Paddle-wheel units are defined as two M^{n+} ions which are bridged by four $(\text{COO})^-$ ions in *syn-syn* mode (Figure 6). In this work, four porous nickel(II) based MOFs with paddle-wheel building units and two dense non paddle-wheel containing compounds were synthesized. Crystal structures of compounds **1a**, **1b**, and **2** were determined via single crystal X-ray diffraction, and Rietveld refinement was applied for the microcrystalline compounds **3a**, **3b**, and **3c**. Suitable starting structures were only available for **3a**, **3b**, and for **3c**, the structure solution was accomplished using in-house XRPD data.

$[\text{Ni}_3(\text{BTC})_2(\text{Me}_2\text{NH})_3]\cdot(\text{DMF})_4(\text{H}_2\text{O})_4$ (**1a**). Title compound **1a** has a 3D framework built of Ni(II) paddle-wheel units and tritopic BTC linker molecules. The paddle-wheel unit consists of four carboxylate fragments in the equatorial positions and two dimethylamine molecules in the axial positions (Figure 7*i*). The axial ligands were formed in situ through the partial hydrolysis of

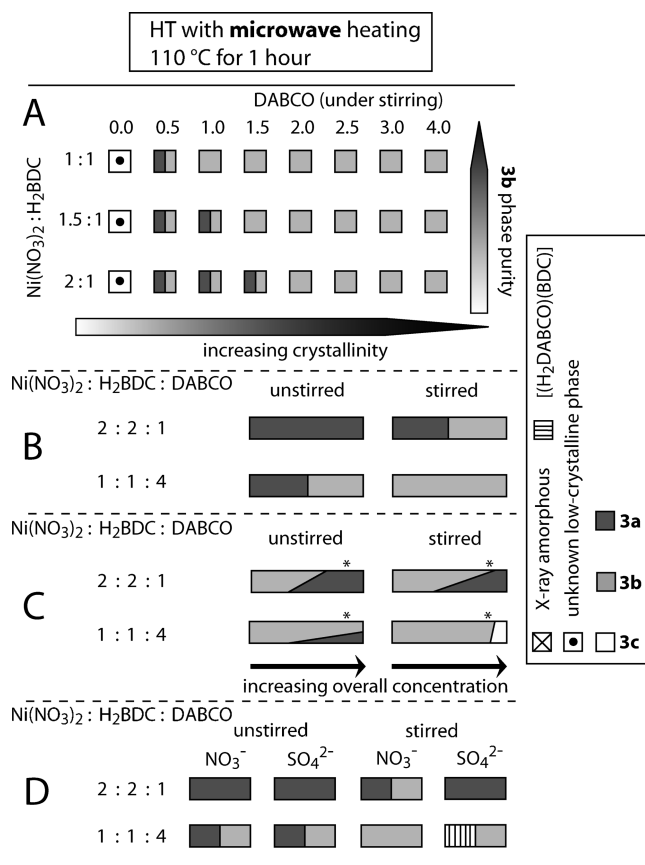


Figure 5. Results of HT-MW investigations of the system $\text{Ni}(\text{NO}_3)_2/\text{H}_2\text{BDC}/\text{DABCO}/\text{DMF}$. Under stirring, pure phase and highly crystalline **3b** was synthesized using large amounts of DABCO (A). In B, the effect of stirring on the product formation was studied with the optimal reactant molar ratios for **3a** (2:2:1:130) and **3b** (1:1:4:260). In C, the effect of the increasing overall concentration is shown for unstirred and stirred reaction mixtures, respectively [1 $\text{Ni}(\text{NO}_3)_2/1 \text{H}_2\text{BDC}/x \text{DABCO}/y \text{DMF}$, with $x = 0.5, 4$ and $y = 65\text{--}5200$]. The influence of sulfate and nitrate ions on the **3a/3b** formation is shown in diagram D. $[(\text{H}_2\text{DABCO})(\text{BDC})]$ is the salt formed from protonated DABCO and benzenedicarboxylate ions.⁵⁹

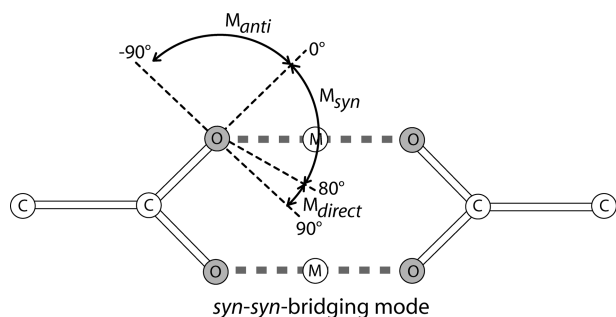


Figure 6. Three types of carboxylate ion coordination modes to metal ions. *Syn*-bonding: $0\text{--}80^\circ$, *direct* bonding: $80\text{--}90^\circ$, and *anti*-bonding: $-90\text{--}0^\circ$. Thus, a paddle-wheel unit has a *syn-syn* bridging mode.⁶²

DMF. Thus, each paddle-wheel unit contains two five-coordinated Ni^{2+} ions with distorted square pyramidal polyhedra. These units are connected to four carboxylate groups of the BTC linker to form a 3D (3,4)-connected **tbo-a**⁶³ framework

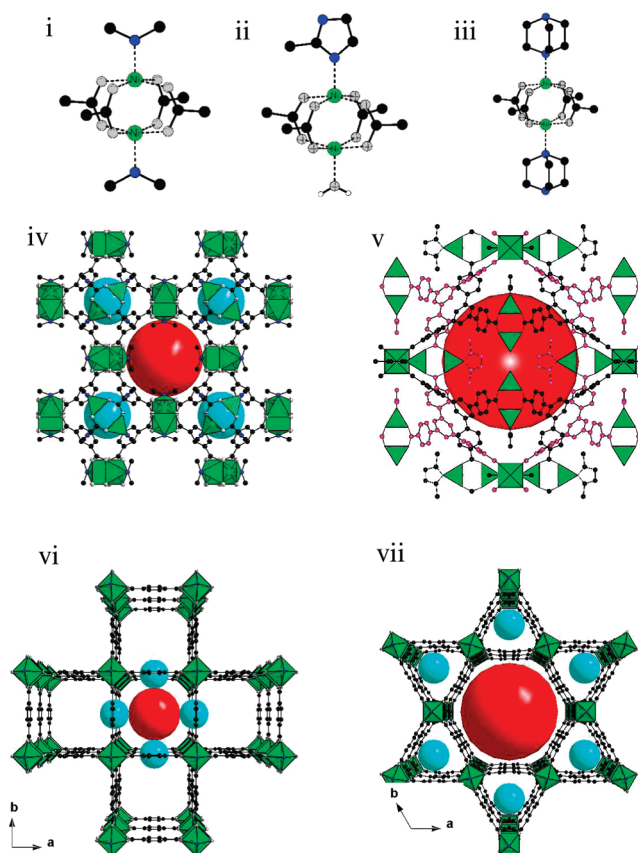


Figure 7. Paddle-wheel building units of (i) **1a** with two axial dimethylamine ligands, (ii) **2** with one axial water and one axial 2-methylimidazole ligand, (iii) **3a/3b** with two axial 1,4-diazabicyclo[2.2.2]octane ligands. Section of the crystal structures of **1a** (iv), view along $[100]$, ~ 9 and ~ 5 Å pores, **2** with two interwoven nets (v), view along $[100]$, 16 Å cavities, activated **3a** (vi), view along $[001]$, 7 Å along c axis and 4 Å pores along the a and b axes, **3b** (vii), view along $[001]$ 14 Å and 4 Å pores along the c axis and 3.5 Å pore windows along a and b axes. Square pyramidal $\text{NiO}_5/\text{NiO}_4\text{N}$ units are displayed as green polyhedra.

with $Fm\bar{3}m$ symmetry. The structure of **1a** has two cages with inner pore diameters of ~ 9 and ~ 5 Å, respectively (Figure 7,iv). To the best of our knowledge, isostructural compounds have only been reported with copper, iron, molybdenum, and chromium.^{15,64–66} The pores are occupied by DMF and H_2O molecules, which can be removed by thermal activation and renders the pores accessible to gas molecules.

$[\text{Ni}_3(\text{BTB})_2(2\text{-MeIm})_{1.5}(\text{H}_2\text{O})_{1.5}] \cdot (\text{DMF})_9(\text{H}_2\text{O})_{6.5}$ (**2**). Compound **2** is built of $\text{Ni}(\text{II})$ paddle-wheel units which are composed of four carboxylate groups in equatorial positions and one water molecule as well as one 2-methylimidazole (2-MeIm) ligand in the axial positions. Similar to **1a**, the paddle-wheel units are connected to BTB linker molecules to construct an extended 3D (3,4)-connected **pto-a** network.^{42,63} Because of freely rotating phenyl rings around the central phenyl ring of BTB linker (35° torsion angle), the symmetry of **2** is reduced to $Im\bar{3}$.⁶⁷ In analogy to the isostructural $\text{Cu}(\text{II})$ -based compound (MOF-14),⁴² title compound **2** has a 2-fold interwoven network with a minimum displacement of 3 Å between the subframeworks (Figure 7,v). Although large cavities of approximately 16 Å are observed, the pore opening is restricted to a window of 3×4 Å (without the axial water ligands). The cavities are

occupied by DMF and water molecules. Upon thermal activation the guest molecules are removed. The crystallinity of sample increases drastically, and a structural transformation takes place (Supporting Information, Figure S5). The new reflections observed in the XRPD pattern of activated **2** can be explained by using a larger isomorphous unit cell (**2-ht**) and same space group $Im\bar{3}$ with cell parameters $3 \cdot (a, b, c)$.⁶⁸

$[Ni_2(BDC)_2(DABCO) \cdot (DMF)_4(H_2O)_{1.5}]$ (**3a**). Rietveld refinement of the compound **3a** was performed starting from the structure model of the isostructural Zn-based compound as it always crystallizes as a microcrystalline powder (Supporting Information, Figure S1, Table 2, Supporting Information, Figure S7).⁴⁵ As seen in Figure 7,iii, the paddle-wheel unit is comprised of four carboxylate groups and the DABCO ligands are located in the axial positions. A 2D layer with a (4,4) sql^{63} grid is formed by the connection of the paddle-wheel units with BDC linkers in the *ab* plane. The layers are interconnected to form a pillared layered 3D structure via DABCO ligands along [001]. Two pore sizes of ~ 7 (along *c* axis) and ~ 4 Å (along *a* and *b* axes) are observed in the microporous structure of activated **3a** (Figure 7,vi). The as-synthesized compound crystallizes in the space group $I4/mcm$ because of bent BDC linker molecules. Upon activation the symmetry changes to $P4/mmm$ since the BDC linkers are now planar. This flexibility is caused by the presence and the type of guest molecules residing in the pores.⁴⁵

$[Ni_2(BDC)_2(DABCO) \cdot (DMF)_4(H_2O)_4]$ (**3b**). Title compounds **3b** and **3a** exhibit polymorphic framework structures, containing different amounts of H_2O guest molecules. Rietveld refinement of the compound **3b** was performed starting from the structure model of the isostructural Zn-based compound as it always crystallizes as a microcrystalline powder (Supporting Information, Figure S1, Table 2, Supporting Information, Figure S8).⁴⁸ The structure consists of (3,4)-connected kgm^{63} layers build by the paddle-wheel units and linked by the BDC molecules. These layers are interconnected by the DABCO molecules along the *c* axis, and a pillared 3D network is obtained. Along the *a* and *b* axes ~ 3.5 Å rectangular windows and along the *c* axis two types of pores with trigonal (4.5 Å) and hexagonal (14 Å) shapes are observed (Figure 7,vii). The pores are occupied by the DMF and water molecules. These can be removed by thermal activation, but under ambient conditions the structure decomposes gradually.

Whereas Zn^{2+} ions have a very flexible coordination environment, which can easily be distorted, Ni^{2+} ions exhibit preferentially quadratic planar and quadratic pyramidal coordination geometries. Because of the change from a (4,4) square grid in **3a** to a (3,4) Kagomé layer in **3b** (Supporting Information, Figure S10), ring strain is observed in the latter which could cause its structural instability. The information can also be used in the attempt to explain the formation of **3a** and **3b** under the different reaction conditions. Under conventional heating **3b** is preferentially formed at short reactions times, but we were never able to obtain a pure phase product. Only the use of microwave assisted heating as well as the optimal reaction conditions of low overall reaction mixture concentration, stirring, and excess base amounts led to single phase **3b**. By applying Ostwald's rule of stages,⁶⁹ the structure **3b** seems to be the kinetically preferred metastable product. This is also supported by the fact that **3b** has a lower framework density compared to **3a** ($\rho_{\text{framework}} = 0.735/0.861$ g cm^{-3} for **3b** and **3a** respectively). Thus, during the product formation nucleation of **3b** should occur first. Under conventional heating, nuclei of both polymorphs are formed that grow to mixtures of **3a** and **3b**. Since crystals of **3a** are present, **3b** can

undergo a solvent-mediated transformation to form the more thermodynamically stable **3a**.⁷⁰ Microwave assisted heating is known to increase the nucleation rate in crystallization processes.^{71,72} Therefore, the results can be interpreted as follows: high solvent content together with stirring and large amounts of DABCO, microwave assisted heating leads exclusively to nuclei of **3b**. Because of the high nucleation rate, the reactant concentrations drop below the critical nucleation concentration necessary for the formation of **3a** and thereby, only crystals of **3b** are formed. Under these reaction conditions, a solvent mediated transformation is not observed since no crystal seeds of **3a** are present. These findings highlight the importance of microwave assisted heating compared to conventional methods in discovering new phases, investigating selective synthesis of polymorphs and less stable structures with larger pore sizes. In addition, this also supports the fact that the new metal–organic structures can be still obtained with well established common organic linkers such as terephthalic or trimesic acid by systematically trying out new synthesis methods. Often metastable products of a reaction system are overlooked because of inadequate understanding of the kinetic and thermodynamic parameters.

Crystal structure of non paddle-wheel based compounds (**1b**, **3c**): Compound $[Ni_6(BTC)_2(DMF)_6(HCOO)_6]$ (**1b**) crystallizes in a dense layered kgd -a structure with hexanuclear Ni_6O_{32} clusters similar to the isostructural Mn^{2+} compound.^{39,63} Each Ni^{2+} ion is six-coordinated by oxygen atoms from one DMF molecule, three formate ions, and two BTC linkers to form distorted NiO_6 polyhedra. Six corner-sharing polyhedra form hexanuclear cores which are linked by BTC linkers to construct a 2D layered network along the *ab* plane (Supporting Information, Figure S11). The BTC linker molecules are all coordinated to the Ni ions in a *syn*-mode, while the sterically less hindered formate groups act as bridging ligands connecting three Ni^{2+} ions. Thus coordination in *syn*- and *anti*-mode is observed.

The structure of $[Ni(BDC)(DABCO) \cdot (DMF)_{1.5}(H_2O)_2]$ (**3c**) was solved from XRPD data. Title compound **3c** crystallizes in a layered (4,4) rectangular-grid topology containing NiO_4N_2 polyhedra.⁷³ Direct bonding of two carboxylate groups to the Ni^{2+} ion is observed (Figure 6), which leads to the formation of chains of alternating Ni^{2+} and BDC^{2-} ions along the *a* axis (Figure 8). These chains are connected along the *b* axis by the DABCO molecules to form layers. DMF and water molecules are located between these layers.

Sorption Measurements. Nitrogen sorption measurements were performed at 77 K on the title compounds with paddle-wheel building units (**1a**, **2**, **3a**, **3b**) to examine their porosity (Figure 9). The samples were first activated at 150 °C under vacuum for 12 h to remove the guest molecules in the pores. The experimental apparent specific surface area (Brunauer–Emmett–Teller (BET) method) and micropore volume of **1a** were determined to be 920 m^2/g and 0.35 cm^3/g respectively (Table 3). These values are smaller than expected probably because of partial decomposition of the structure or the incomplete activation. Different synthesis methods and improved activation procedures could yield higher porosity values. Isostructural copper-based HKUST-1 has been reported with surface areas and micropore volumes of 692–1820 m^2/g and 0.33–0.74 cm^3/g , respectively (Supporting Information, Table S21).

Compound **2** does not exhibit any porosity for nitrogen as anticipated because of the restricted pore window size of 3×4 Å (without the axial water ligands). On the other hand, the isostructural copper-based MOF-14 shows surface area of

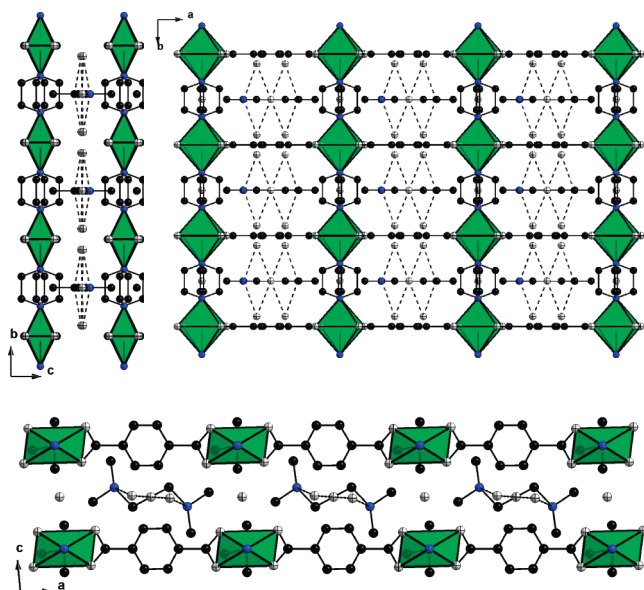


Figure 8. Sections of the crystal structure of the layered compound **3c**. Alternating BDC linkers and *direct*-bonded Ni²⁺ ions form chains along the *a* axis (bottom). Top left diagram showing DABCO molecules connecting the chains along the *b* axis. The hydrogen bonding (broken lines) between DMF and H₂O molecules are shown in the top right diagram in the *ab* plane.

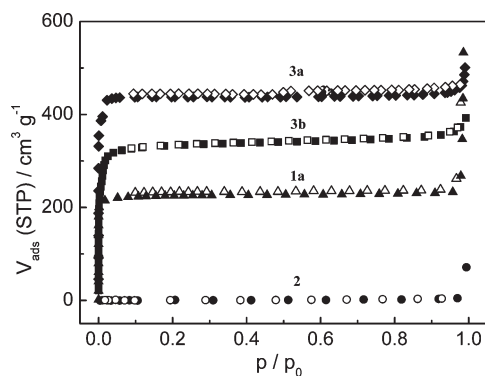


Figure 9. Nitrogen sorption isotherms measured at 77 K for the four paddle-wheel based Ni²⁺ compounds **1**, **2**, **3a**, and **3b**. All compounds with the exception of **2** exhibit microporous type I behavior. Solid symbols denote adsorption, hollow symbols denote desorption.

1502 m²/g and a micropore volume of 0.53 cm³/g (Supporting Information, Table S21).⁴² Nevertheless, sorption experiments of **2** using other adsorbate molecules with smaller kinetic diameters⁷⁴ have shown increasing adsorption in the following order: N₂ < Ar < H₂ (77 K) and CO₂ < H₂O (298 K) (Figure 10). Substantial hysteresis was observed in the H₂ and the H₂O sorption measurement. While for water as the adsorbent this is often observed, hysteresis in H₂ sorption measurements is rather rare. Interestingly, almost no H₂ molecules were liberated during the desorption process indicating a kinetic trapping of the adsorbates in the pores (Figure 10 inset graph).⁷⁵ The highest specific surface area was achieved with compound **3a**, and the experimental micropore volume is in good agreement with calculated values (Table 3, Figure 9). This proves the robustness and high stability of **3a**. In comparison to the lower micropore

Table 3. Specific Surface Areas and Micropore Volumes of the Paddle-Wheel Based Ni(II) Compounds^a

compound	specific surface area S_{BET} (obs.)/m ² g ⁻¹	micropore volume/cm ³ g ⁻¹	
		obs. at $p/p_0 = 0.5$	calcd (PLATON) ²⁹
1a	920	0.35	0.83
2	0	0	0.68
3a	1807	0.66	0.66
3b	1231	0.53	0.84

^aTheoretical micropore volumes are calculated without the axial ligands.

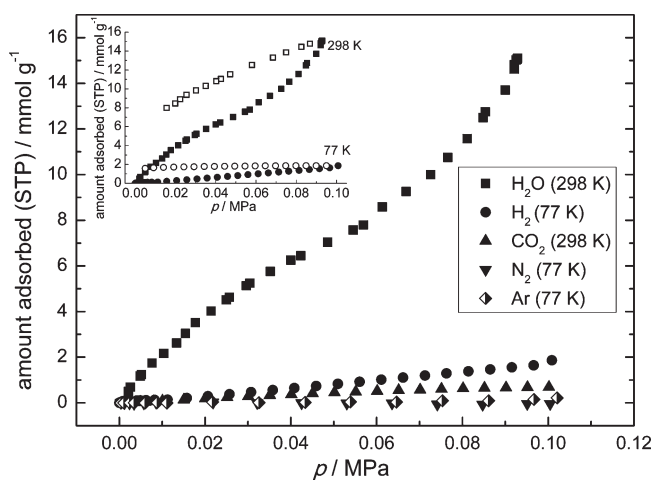


Figure 10. Increasing adsorption of molecules with decreasing kinetic diameters in compound **2**. Measurements using H₂, Ar, and N₂ were conducted at 77 K; H₂O and CO₂ at 298 K. The uptake depends strongly on the kinetic diameter of the guest molecules employed. The inset graph shows the hysteresis occurring during the desorption of H₂O and H₂ (solid symbols: adsorption, hollow: desorption).

volume of the polymorph **3b** with trigonal frameworks with the theoretical value indicates the decomposition of the structure which was confirmed via XRPD measurement. The comparison of values obtained with isostructural compounds with other transition metal ions are given in Supporting Information, Table S21.

Chemical and Thermal Stability. High thermal stability and inertness to air as well as moisture are some of the essential requirements for the application of porous MOFs. For these reasons, thermogravimetric (TG) analyses and XRPD measurements of samples exposed to air as well as solvent-exchanged samples were performed. The weight losses observed in the TG experiments deviate in some cases from the results of the elemental analyses. Slightly lower values in TG experiments are found since the content of the pores and cages can vary because of the gas flow at the beginning of the experiments. TG analysis of **1a** in nitrogen, [Ni₃(BTC)₂(Me₂NH)₃]·(DMF)₄(H₂O)₄, revealed a gradual weight loss up to 320 °C which corresponds to the removal of four H₂O and three DMF molecules (obs. 26.9%, calcd 26.7%). The next significant weight loss up to 600 °C yielded elemental nickel (Supporting Information, Figure S12). The temperature-dependent XRPD measurements in a capillary (Supporting Information, Figure S12) confirm the

thermal stability of **1a** up to 300 °C. Upon exposure to ambient conditions **1a** decomposes rapidly at room temperature to form a green X-ray amorphous product (Supporting Information, Figure S2). Solvent-exchange experiments with diverse organic solvents such as ethanol, dichloromethane, and acetonitrile have shown a rapid disintegration of the crystal structure which indicates the instability of compound **1a**. The TG curve of $[\text{Ni}_6(\text{BTC})_2(\text{HCOO})_6(\text{DMF})_6]$ **1b** shows three weight losses. The first weight loss (14.5%, calcd 14.9%) up to 250 °C could be due to the loss of three coordinated DMF molecules. Between 250 and 350 °C a loss of 24.9% (calcd 24.0%) is observed which is in accordance with the removal of the other three coordinated DMF molecules and three formate ions (Supporting Information, Figure S12). The solid residue after the third weight loss was determined to be NiO.

Compound **2**, $[\text{Ni}_3(\text{BTB})_2(2\text{-MeIm})_{1.5}(\text{H}_2\text{O})_{1.5}] \cdot (\text{DMF})_9 \cdot (\text{H}_2\text{O})_{6.5}$, with the BTB linker is stable in air after the thermal activation, and its crystallinity even increases (Supporting Information, Figure S5). Unlike compound **1a**, the crystal structure of **2** remains intact even after 72 h of stirring in pure dichloromethane at room temperature. Upon heating during TG analysis, compound **2** loses a considerable amount of guest molecules until the first plateau at 300 °C is reached (Supporting Information, Figure S12). The observed weight loss of 33.4% corresponds to eight H₂O and seven DMF molecules (calcd 33.2%). Above 350 °C the organic units decompose and NiO is formed. The XRPD measurement of the sample treated at 250 °C confirms the stability of the framework and the structural transformation to the isomorphous subgroup with an enlarged unit cell of 3 · (a, b, c).

During the thermal decomposition of **3a**, $[\text{Ni}_2(\text{BDC})_2(\text{DABCO})] \cdot (\text{DMF})_4(\text{H}_2\text{O})_{1.5}$ (Supporting Information, Figure S12), all guest molecules are liberated from the pores up to 290 °C in a two step process (obs. 36.6%, calcd 36.4%). The substantial weight loss from 290 to 800 °C can be attributed to the decomposition of two BDC and one DABCO linker molecules (obs. 48.6%, calcd 50.2%). The residual powder was determined to be NiO by XRPD. Compound **3a** is also stable against moisture since after treatment with water, the crystallinity was preserved. **3a** has also been found to be tolerant against solvents such as ethanol, dichloromethane, and acetonitrile in solvent exchange experiments at room temperature. TG analysis of the compound **3b**, $[\text{Ni}_2(\text{BDC})_2(\text{DABCO})] \cdot (\text{DMF})_4(\text{H}_2\text{O})_4$, which has a polymorphic framework, two weight loss steps because of the removal of the guest molecules are observed (Supporting Information, Figure S12). The first weight loss between 40–120 °C corresponds to the removal of four H₂O molecules (obs. 7.4%, calcd 7.8%), while the second weight loss (120–300 °C) can be attributed to the removal of the four DMF molecules (obs. 29.6%, calcd 31.7%). Further heating up to 800 °C led to NiO. Unlike **3a**, **3b** with the trigonal framework is moisture sensitive and gradual decomposition upon storage at ambient conditions is observed. This gradual decomposition of the **3b** crystal structure was also observed after solvent exchange experiments. The TG analysis of **3c**, $[\text{Ni}(\text{BDC})(\text{DABCO})] \cdot (\text{DMF})_{1.5}(\text{H}_2\text{O})_2$, shows that the guest molecules are removed in two steps up to 350 °C (obs. 29.2%, calcd 30.3%). Above 350 °C the oxidation of the organic linker molecules takes place, and NiO is formed.

IR Spectroscopy. All compounds were characterized by IR spectroscopy (Supporting Information, Figure S13, S14). Their IR spectra exhibit broad bands in the region between 3600 and 3100 cm⁻¹, which are due to $\nu(\text{O}-\text{H})$ vibrations of the uncoordinated water molecules involved in weak hydrogen bonds. Weak

aliphatic $\nu(\text{C}-\text{H})$ bands are observed in the 2950–2850 cm⁻¹. For all compounds the aromatic C–H stretching bands could not be seen because of overlap with the broad O–H bands. Two sharp aromatic $\gamma(\text{C}-\text{H})$ bands of 1,3,5-BTC linker are observed at $770 \pm 5 \text{ cm}^{-1}$ and $725 \pm 5 \text{ cm}^{-1}$ in **1a**, and **1b**.⁷⁶ Three sharp aromatic $\gamma(\text{C}-\text{H})$ deformation bands of BTB linker of **2** were seen at 857, 783, and 705 cm⁻¹.⁷⁷ For compounds **3a**, **3b**, and **3c**, the bands observed at $810 \pm 5 \text{ cm}^{-1}$ and $750 \pm 5 \text{ cm}^{-1}$ are characteristic and correspond to the $\gamma(\text{C}-\text{H})$ and the $\delta(\text{C}-\text{C})$ vibration of the 1,4-BDC linker, respectively.⁷⁸ The bands at 1090 ± 5 and $1055 \pm 5 \text{ cm}^{-1}$ could be due to the $\nu_{\text{as}}(\text{C}-\text{N})$ and $\nu_{\text{s}}(\text{C}-\text{N})$ vibrations of DABCO.⁷⁹ In all spectra, strong bands at 1670–1600 cm⁻¹ and 1400–1350 cm⁻¹ are observed which can be assigned to the $\nu_{\text{as}}(\text{C}-\text{O})$ and $\nu_{\text{s}}(\text{C}-\text{O})$ vibrations of the $-\text{COO}^-$ groups. Around 1680 cm⁻¹ the band of the $\nu(\text{C}=\text{O})$ vibration of DMF molecules is detected.

CONCLUSION

With the aid of high-throughput (HT) methods we have identified the fields of formation of six new compounds. In addition to four porous Ni based MOFs with paddle-wheel building units, two compounds with dense layered structures (**1b**, **3c**) were also discovered. All compounds were fully characterized. In the system containing H₃BTC as starting material, a comprehensive screening of compositional and process parameters allowed to establish the reaction conditions for the Ni paddle-wheel unit. Application of these reaction conditions and replacing H₃BTC with the extended tritopic linker molecule H₃BTB, the paddle-wheel containing compound **2** was discovered. Changing the tritopic to a ditopic linker molecule (H₂BDC) and adding DABCO as the base, the formation of two pillared layered structures with the composition $[\text{Ni}_2(\text{BDC})_2(\text{DABCO})]$ was accomplished. The synthesis condition for each polymorph was scrutinized by employing HT-methods under conventional and microwave assisted heating. Rapid nucleation via microwave assisted heating coupled with the systematic investigation has been proven valuable for selectively obtaining the MOF **3b**. On the basis of the results of this study, the synthesis of other Ni containing MOFs with paddle-wheel units should be feasible, which have been described previously mainly with Cu²⁺ and Zn²⁺ ions.

ASSOCIATED CONTENT

S Supporting Information. Exact amounts used for the high-throughput synthesis, SEM and optical images, Rietveld refinement results, XRPD patterns, TGA analyses and IR spectra are available. This material is available free of charge via the Internet at <http://pubs.acs.org>. The Cambridge Crystallographic Data Center (CCDC) 802889–802894 contains the supplementary crystallographic data for this paper. These data can be obtained free of charge via the Internet at www.ccdc.cam.ac.uk/conts/retrieving.html (or from the CCDC, 12 Union Road, Cambridge CB2 1EZ, U.K; fax, +44 1223 360333; e-mail, deposit@ccdc.ac.uk).

AUTHOR INFORMATION

Corresponding Author

*E-mail: stock@ac.uni-kiel.de. Phone: (+49)431-880-1675. Fax: (+49)431-880-1775.

ACKNOWLEDGMENT

The authors thank Inke Jess (Christian-Albrechts-Universität zu Kiel) and Dr. Alexandra Lieb (Otto-von-Guericke-Universität Magdeburg) for the acquisition of single crystal data, Adam Wutkowski (Christian-Albrechts-Universität zu Kiel) for TG measurements, Steffen Schmidt (Ludwig-Maximilians-Universität München) for high-resolution SEM images, Prof. Michael Fröba, Ute Sazama, and Sandra Maracke (Universität Hamburg) for H₂-sorption measurements. The work has been supported by the State of Schleswig-Holstein and the Deutsche Forschungsgemeinschaft (DFG) through the priority program SPP 1362 "Porous Metal–Organic Frameworks" under Grant STO 643/5-1.

REFERENCES

- (1) Koinuma, H.; Takeuchi, I. *Nat. Mater.* **2004**, *3*, 429–438.
- (2) Maier, W. F.; Stöwe, K.; Sieg, S. *Angew. Chem., Int. Ed.* **2007**, *46*, 6016. *Angew. Chem.* **2007**, *119*, 6122–6179.
- (3) Stock, N. *Microporous Mesoporous Mater.* **2010**, *129*, 287–295.
- (4) Stock, N.; Bein, T. *Solid State Sci.* **2003**, *5*, 1207–1210.
- (5) Akporiaye, D. E.; Dahl, I. M.; Karlsson, A.; Wendelbo, R. *Angew. Chem., Int. Ed.* **1998**, *37*, 609–611. *Angew. Chem.* **1998**, *110*, 629–631.
- (6) Stock, N.; Bein, T. *Angew. Chem., Int. Ed.* **2004**, *43*, 749–752. *Angew. Chem.* **2004**, *116*, 767–770.
- (7) Forster, P. M.; Burbank, A. R.; O'Sullivan, M. C.; Guillou, N.; Livage, C.; Férey, G.; Stock, N.; Cheetham, A. K. *Solid State Sci.* **2005**, *7*, 1549–1555.
- (8) Banerjee, R.; Phan, A.; Wang, B.; Knobler, C.; Furukawa, H.; O'Keeffe, M.; Yaghi, O. M. *Science* **2008**, *319*, 939–943.
- (9) Bauer, S.; Stock, N. *Chem. Unserer Zeit* **2007**, *41*, 390–398.
- (10) Mueller, U.; Schubert, M.; Teich, F.; Puetter, H.; Schierle-Arndt, K.; Pastré, J. J. *Mater. Chem.* **2006**, *16*, 626–636.
- (11) Horcajada, P.; Serre, C.; Vallet-Regi, M.; Sebban, M.; Taulelle, F.; Férey, G. *Angew. Chem., Int. Ed.* **2006**, *45*, 5974–5978. *Angew. Chem.* **2006**, *118*, 6120–6124.
- (12) Sonnauer, A.; Hoffmann, F.; Fröba, M.; Kienle, L.; Duppel, V.; Thommes, M.; Serre, C.; Férey, G.; Stock, N. *Angew. Chem., Int. Ed.* **2009**, *48*, 3791–3794. *Angew. Chem.* **2009**, *121*, 3849–3852.
- (13) Bauer, S.; Serre, C.; Devic, T.; Horcajada, P.; Marrot, J.; Férey, G.; Stock, N. *Inorg. Chem.* **2008**, *47*, 7568–7576.
- (14) Ahnfeldt, T.; Gunzelmann, D.; Loiseau, T.; Hirsemann, D.; Senker, J.; Férey, G.; Stock, N. *Inorg. Chem.* **2009**, *48*, 3057–3064.
- (15) Chui, S. S.-Y.; Lo, S. M.-F.; Charmant, J. P. H.; Guy Orpen, A.; Williams, I. D. *Science* **1999**, *283*, 1148–1150.
- (16) Allen, F. H. *Acta Crystallogr.* **2002**, *B58*, 380–388. Databank search in CSD Conquest version 5.31 with Feb 2010 update.
- (17) Lee, S. W.; Kim, H. J.; Lee, Y. K.; Park, K.; Son, J.-H.; Kwon, Y.-U. *Inorg. Chim. Acta* **2003**, *353*, 151–158.
- (18) Yuen, T.; Danilovic, D.; Li, K.; Li, J. *J. Appl. Phys.* **2008**, *103*, 07B725.
- (19) Shi, Q.; Sun, Y.; Sheng, L.; Ma, K.; Cai, X.; Liu, D. *Inorg. Chim. Acta* **2009**, *362*, 4167–4173.
- (20) Zhu, L.; Chen, X.; Zhao, Q.; Li, Z.; Zhang, X.; Sun, B. *Z. Anorg. Allg. Chem.* **2010**, *636*, 1441–1443.
- (21) Arstad, B.; Fjellvåg, H.; Kongshaug, K. O.; Swang, O.; Blom, R. *Adsorption* **2008**, *14*, 755–762.
- (22) Klein, N.; Herzog, C.; Sabo, M.; Senkovska, I.; Getzschmann, J.; Paasch, S.; Lohe, M. R.; Brunner, E.; Kaskel, S. *Phys. Chem. Chem. Phys.* **2010**, *12*, 11778–11784.
- (23) Guillou, N.; Gao, Q.; Forster, P. M.; Chang, J.-S.; Noguès, M.; Park, S.-E.; Férey, G.; Cheetham, A. K. *Angew. Chem., Int. Ed.* **2001**, *40*, 2831–2834. *Angew. Chem.* **2001**, *113*, 2913–2916.
- (24) Zou, R.-Q.; Sakurai, H.; Xu, Q. *Angew. Chem., Int. Ed.* **2006**, *45*, 2542–2546. *Angew. Chem.* **2006**, *118*, 2604–2608.
- (25) Forster, P. M.; Eckert, J.; Heiken, B. D.; Parise, J. B.; Yoon, J. W.; Jhung, S. H.; Chang, J.-S.; Cheetham, A. K. *J. Am. Chem. Soc.* **2006**, *128*, 16846–16850.
- (26) Lamberti, C.; Zecchina, A.; Groppo, E.; Bordiga, S. *Chem. Soc. Rev.* **2010**, *39*, 4951–5001.
- (27) Maniam, P.; Näther, C.; Stock, N. *Eur. J. Inorg. Chem.* **2010**, 3866–3874.
- (28) *XRED version 1.19, XSHAPE version 1.06*; Stoe & Cie GmbH: Darmstadt, Germany, 1999.
- (29) Spek, A. L. *PLATON; a multipurpose crystallographic tool*; Utrecht University: Utrecht, The Netherlands, 2001.
- (30) Sheldrick, G. M. *SADABS version*; Bruker AXS Inc., Madison, WI, 2007.
- (31) Sheldrick, G. M. *Acta Crystallogr.* **2008**, *A64*, 112–122.
- (32) Altomare, A.; Camalli, M.; Cuocci, C.; Giacovazzo, C.; Moliterni, A.; Rizzi, R. *J. Appl. Crystallogr.* **2009**, *42*, 1197–1202.
- (33) *Materials Studio, v5.0*; Accelrys Software Inc.: San Diego, CA, 2009.
- (34) Favre-Nicolin, V.; Cerny, R. *J. Appl. Crystallogr.* **2002**, *35*, 734–743.
- (35) Coelho, A. A. *TOPAS-Academic; Program for indexing, structure resolution and Rietveld refinement on powder data, V4.1*; Bruker AXS Inc., Madison, WI, 2007.
- (36) Bauer, S.; Bein, T.; Stock, N. *Inorg. Chem.* **2005**, *44*, 5882–5889.
- (37) Biemmi, E.; Christian, S.; Stock, N.; Bein, T. *Microporous Mesoporous Mater.* **2009**, *117*, 111–117.
- (38) Sonnauer, A.; Stock, N. *Eur. J. Inorg. Chem.* **2008**, 5038–5045.
- (39) Chen, J.; Ohba, M.; Kitagawa, S. *Chem. Lett.* **2006**, *35*, 526–527.
- (40) Biemmi, E.; Bein, T.; Stock, N. *Solid State Sci.* **2006**, *8*, 363–370.
- (41) Forster, P. M.; Burbank, A. R.; Livage, C.; Férey, G.; Cheetham, A. K. *Chem. Commun.* **2004**, 368–369.
- (42) Chen, B.; Eddaoudi, M.; Hyde, S. T.; O'Keeffe, M.; Yaghi, O. M. *Science* **2001**, *291*, 1021–1023.
- (43) Takei, T.; Ii, T.; Kawashima, J.; Ohmura, T.; Ichikawa, M.; Hosoe, M.; Shinya, Y.; Kanoya, I.; Mori, W. *Chem. Lett.* **2007**, *36*, 1136–1137.
- (44) Seki, K.; Takamizawa, S.; Mori, W. *Chem. Lett.* **2001**, *30*, 332–333.
- (45) Dybtsev, D. N.; Chun, H.; Kim, K. *Angew. Chem., Int. Ed.* **2004**, *43*, 5033–5036. *Angew. Chem.* **2004**, *116*, 5143–5146.
- (46) Chun, H.; Dybtsev, D. N.; Kim, H.; Kim, K. *Chem.—Eur. J.* **2005**, *11*, 3521–3529.
- (47) Szyozi, I. *Prog. Theor. Phys.* **1951**, *6*, 306–308.
- (48) Chun, H.; Moon, J. *Inorg. Chem.* **2007**, *46*, 4371–4373.
- (49) Kondo, M.; Takashima, Y.; Seo, J.; Kitagawa, S.; Furukawa, S. *CrystEngComm* **2010**, *12*, 2350–2353.
- (50) Friscic, T.; Reid, D. G.; Halasz, I.; Stein, R. S.; Dinnebier, R. E.; Duer, M. J. *Angew. Chem., Int. Ed.* **2010**, *49*, 712–715. *Angew. Chem.* **2010**, *122*, 724–727.
- (51) Dunitz, J. D.; Bernstein, J. *Acc. Chem. Res.* **1995**, *28*, 193–200.
- (52) Herrero, M. A.; Kremsner, J. M.; Kappe, C. O. *J. Org. Chem.* **2008**, *73*, 36–47.
- (53) Sonnauer, A.; Stock, N. *J. Solid State Chem.* **2008**, *181*, 3065–3070.
- (54) Jhung, S. H.; Chang, J.-S.; Hwang, J. S.; Park, S.-E. *Microporous Mesoporous Mater.* **2003**, *64*, 33–39.
- (55) Jhung, S. H.; Lee, J. H.; Forster, P. M.; Férey, G.; Cheetham, A. K.; Chang, J.-S. *Chem.—Eur. J.* **2006**, *12*, 7899–7905.
- (56) Kondepudi, D. K.; Kaufman, R. J.; Singh, N. *Science* **1990**, *250*, 975–976.
- (57) McBride, J. M.; Carter, R. L. *Angew. Chem., Int. Ed. Engl.* **1991**, *30*, 293–295. *Angew. Chem.* **1991**, *103*, 298–300.
- (58) Hanif, N.; Anderson, M. W.; Alfredsson, V.; Terasaki, O. *Phys. Chem. Phys.* **2000**, *2*, 3349–3357.
- (59) Yang, E.; Song, X.-C.; Zhu, J.-W. *Acta Crystallogr., Sect. E* **2008**, *64*, o1764.
- (60) Ahnfeldt, T.; Guillou, N.; Gunzelmann, D.; Margiolaki, I.; Loiseau, T.; Férey, G.; Senker, J.; Stock, N. *Angew. Chem., Int. Ed.* **2009**, *48*, 5163–5166. *Angew. Chem.* **2009**, *121*, 5265–5268.
- (61) Khan, N. A.; Jun, J. W.; Jhung, S. H. *Eur. J. Inorg. Chem.* **2010**, 1043–1048.

- (62) Carrell, C. J.; Carrell, H. L.; Erlebacher, J.; Glusker, J. P. *J. Am. Chem. Soc.* **1988**, *110*, 8651–8656.
- (63) O’Keeffe, M.; Peskov, M. A.; Ramsden, S. J.; Yaghi, O. M. *Acc. Chem. Res.* **2008**, *41*, 1782–1789.
- (64) Xie, L.; Liu, S.; Gao, C.; Cao, R.; Cao, J.; Sun, C.; Su, Z. *Inorg. Chem.* **2007**, *46*, 7782–7788.
- (65) Kramer, M.; Schwarz, U.; Kaskel, S. *J. Mater. Chem.* **2006**, *16*, 2245–2248.
- (66) Murray, L. J.; Dinca, M.; Yano, J.; Chavan, S.; Bordiga, S.; Brown, C. M.; Long, J. R. *J. Am. Chem. Soc.* **2010**, *132*, 7856–7857.
- (67) Ma, S.; Sun, D.; Ambrogio, M.; Fillinger, J. A.; Parkin, S.; Zhou, H.-C. *J. Am. Chem. Soc.* **2007**, *129*, 1858–1859.
- (68) Wondratschek, H.; Müller, U. *International Tables for Crystallography*; Kluwer Academic Publishers: Dordrecht, The Netherlands, 2006, Vol. A1, p 689.
- (69) Ostwald, W. Z. *Phys. Chem.* **1897**, *22*, 289–330.
- (70) Davey, R. J.; Blagden, N.; Potts, G. D.; Docherty, R. *J. Am. Chem. Soc.* **1997**, *119*, 1767–1772.
- (71) Gharibeh, M.; Tompssett, G. A.; Conner, W. C.; Yngvesson, K. S. *ChemPhysChem* **2008**, *9*, 2580–2591.
- (72) Khan, N. A.; Haque, E.; Hwa Jhung, S. *Phys. Chem. Chem. Phys.* **2010**, *12*, 2625–2631.
- (73) Natarajan, S.; Mahata, P. *Chem. Soc. Rev.* **2009**, *38*, 2304–2318.
- (74) Li, J.-R.; Kuppler, R. J.; Zhou, H.-C. *Chem. Soc. Rev.* **2009**, *38*, 1477–1504.
- (75) Zhao, X.; Xiao, B.; Fletcher, A. J.; Thomas, K. M.; Bradshaw, D.; Rosseinsky, M. J. *Science* **2004**, *306*, 1012–1015.
- (76) Green, J. H. S.; Harrison, D. J.; Kynaston, W. *Spectrochim. Acta, Part A* **1971**, *27*, 793–806.
- (77) Jutand, A.; Negri, S. *Eur. J. Inorg. Chem.* **1998**, *9*, 1811–1821.
- (78) Arenas, J. F.; Marcos, J. I. *Spectrochim. Acta, Part A* **1980**, *36*, 1075–1081.
- (79) McDivitt, J. R.; Humphrey, G. L. *Spectrochim. Acta, Part A* **1974**, *30*, 1021–1033.

4.4.4 Poly[(μ_3 -benzene-1,3,5-tricarboxylato- $\kappa^3 O^1:O^3:O^5$)(μ_2 -2-methylimidazolato- $\kappa^2 N:N'$)tris(2-methylimidazole- κN)dizinc(II)]

This article has been published in its final form in "Acta Crystallographica Section E": DOI: 10.1107/S1600536811015844. Copyright © 2011 International Union of Crystallography, Weinheim. The supporting information of this article is placed in the Appendices section (Appendix 5).

This article reports the crystal structure of the compound $[Zn_2(C_9H_3O_6)(C_4H_5N_2)(C_4H_6N_2)_3]$ which was obtained during the high-throughput metal ion screening experiments with the reactants, sodium 1,3,5-benzenetricarboxylate (Na_3BTC) and 2-methylimidazole (2-MelmH) in aqueous solution. Several attempts were made to reproduce the pure-phase compound, but this has proven to be not possible up to now. The structure determination of the compound was performed via single crystal X-ray diffraction. The asymmetric unit of the structure consists of two crystallographic independent Zn^{2+} ions, one fully deprotonated $(BTC)^{3-}$ ion, one 2-methylimidazolate $(2-Melm)^-$ ion and three 2-MelmH ligands. Tetrahedrally coordinated Zn^{2+} ions form ZnN_3O and ZnO_2N_2 polyhedra. Each $(BTC)^{3-}$ ion is connected to two ZnN_2O_2 and one ZnN_3O polyhedra. The interconnection of polyhedra by $(BTC)^{3-}$ and N:N'-bridging $(2-Melm)^-$ ions leads to the creation of a layered structure. The remaining uncoordinated oxygen atoms from carboxyl groups act as proton acceptor for H-atoms from 2-MelmH ligands and thus, weak hydrogen bonds are formed. These hydrogen bonds link the layers to a three-dimensional network.

Acta Crystallographica Section E

Structure Reports

Online

ISSN 1600-5368

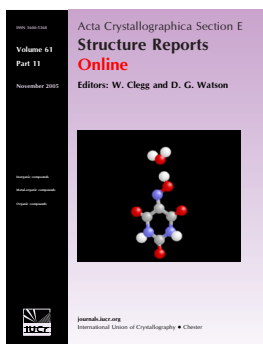
Editors: W.T.A. Harrison, J. Simpson and M. Weil

Poly[(μ_3 -benzene-1,3,5-tricarboxylato- $\kappa^3 O^1:O^3:O^5$)(μ_2 -2-methylimidazolato- $\kappa^2 N:N'$)tris(2-methylimidazole- κN)dizinc(II)]

Palanikumar Maniam and Norbert Stock

Acta Cryst. (2011). E67, m669–m670

This open-access article is distributed under the terms of the Creative Commons Attribution Licence <http://creativecommons.org/licenses/by/2.0/uk/legalcode>, which permits unrestricted use, distribution, and reproduction in any medium, provided the original authors and source are cited.



Acta Crystallographica Section E: Structure Reports Online is the IUCr's highly popular open-access structural journal. It provides a simple and easily accessible publication mechanism for the growing number of inorganic, metal-organic and organic crystal structure determinations. The electronic submission, validation, refereeing and publication facilities of the journal ensure very rapid and high-quality publication, whilst key indicators and validation reports provide measures of structural reliability. The journal publishes over 4000 structures per year. The average publication time is less than one month.

Crystallography Journals **Online** is available from journals.iucr.org

Poly[(μ_3 -benzene-1,3,5-tricarboxylato- κ^3 O¹:O³:O⁵)(μ_2 -2-methylimidazolato- κ^2 N:N')tris(2-methylimidazole- κ N)-dizinc(II)]

Palanikumar Maniam and Norbert Stock*

Institut für Anorganische Chemie, Christian-Albrechts-Universität zu Kiel, Max-Eyth-Strasse 2, 24118 Kiel, Germany

Correspondence e-mail: stock@ac.uni-kiel.de

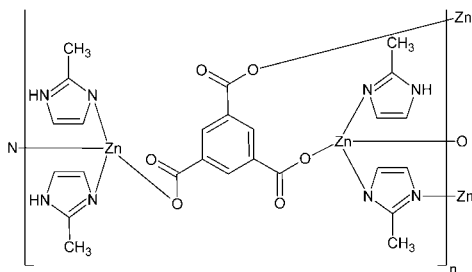
Received 21 April 2011; accepted 26 April 2011

Key indicators: single-crystal X-ray study; $T = 293$ K; mean $\sigma(\text{C}-\text{C}) = 0.006$ Å; R factor = 0.061; wR factor = 0.143; data-to-parameter ratio = 20.9.

Hydrothermal reaction involving zinc nitrate hexahydrate, trisodium benzene-1,3,5-tricarboxylate (Na_3BTC) and 2-methylimidazole (2-MeImH) yielded the title compound, $[\text{Zn}_2(\text{C}_9\text{H}_3\text{O}_6)(\text{C}_4\text{H}_5\text{N}_2)(\text{C}_4\text{H}_6\text{N}_2)_3]$. In this mixed-ligand metal-organic compound, Zn^{2+} ions are coordinated by N atoms from 2-MeImH molecules and $(2\text{-MeIm})^-$ ions, as well as by O atoms from $(\text{BTC})^{3-}$ ions. This results in two different distorted tetrahedra, *viz.* ZnN_3O and ZnN_2O_2 . These tetrahedra are interconnected *via* $(\text{BTC})^{3-}$ ions and $N:N'$ -bridging $(2\text{-MeIm})^-$ ions, thus forming a layered structure in the *bc* plane. Hydrogen bonds between the O atoms of carboxylate ions and NH groups of 2-MeImH ligands link the layers into a three-dimensional structure.

Related literature

For metal-organic frameworks, see: Li *et al.* (1999); Kitagawa *et al.* (2004); Stock (2010); Maniam *et al.* (2010). For related structures, see: Cheng *et al.* (2001); Zheng *et al.* (2010); Huang *et al.* (2006); Martins *et al.* (2010); Park *et al.* (2006).



Experimental

Crystal data

$[\text{Zn}_2(\text{C}_9\text{H}_3\text{O}_6)(\text{C}_4\text{H}_5\text{N}_2)(\text{C}_4\text{H}_6\text{N}_2)_3]$	$V = 5725.3$ (3) Å ³
$M_r = 665.28$	$Z = 8$
Orthorhombic, $Pbcn$	Mo $K\alpha$ radiation
$a = 18.9722$ (6) Å	$\mu = 1.73$ mm ⁻¹
$b = 18.2247$ (4) Å	$T = 293$ K
$c = 16.5585$ (4) Å	$0.16 \times 0.09 \times 0.07$ mm

Data collection

Stoe IPDS-1 diffractometer	38494 measured reflections
Absorption correction: numerical (<i>X-RED</i> and <i>X-SHAPE</i> ; Stoe & Cie, 2008)	7732 independent reflections
$T_{\min} = 0.684$, $T_{\max} = 0.814$	6222 reflections with $I > 2\sigma(I)$
	$R_{\text{int}} = 0.050$

Refinement

$R[F^2 > 2\sigma(F^2)] = 0.061$	370 parameters
$wR(F^2) = 0.143$	H-atom parameters constrained
$S = 1.13$	$\Delta\rho_{\text{max}} = 0.47$ e Å ⁻³
7732 reflections	$\Delta\rho_{\text{min}} = -0.54$ e Å ⁻³

Table 1

Selected geometric parameters (Å, °).

Zn1—O4	1.942 (3)	Zn1—N1F	1.998 (3)
Zn2—O6	1.968 (3)	Zn1—N1G	2.015 (4)
Zn2—O1 ⁱ	1.976 (2)	Zn2—N1H	1.992 (3)
Zn1—N2H ⁱⁱ	1.971 (3)	Zn2—N1E	2.027 (3)

Symmetry codes: (i) $x, -y, z + \frac{1}{2}$; (ii) $-x + \frac{3}{2}, y + \frac{1}{2}, z$.

Table 2

Hydrogen-bond geometry (Å, °).

$D-H\cdots A$	$D-H$	$H\cdots A$	$D\cdots A$	$D-H\cdots A$
$\text{N2E}-\text{H2EN}\cdots\text{O3}^{\text{iii}}$	0.86	2.06	2.912 (5)	169
$\text{N2F}-\text{H2FN}\cdots\text{O2}^{\text{iv}}$	0.86	1.84	2.693 (5)	172
$\text{N2G}-\text{H2GN}\cdots\text{O5}^{\text{v}}$	0.86	1.94	2.798 (5)	175

Symmetry codes: (iii) $x + \frac{1}{2}, -y + \frac{1}{2}, -z$; (iv) $-x + 1, y, -z - \frac{1}{2}$; (v) $-x + 1, y, -z + \frac{1}{2}$.

Data collection: *X-AREA* (Stoe & Cie, 2008); cell refinement: *X-AREA*; data reduction: *X-AREA*; program(s) used to solve structure: *SHELXS97* (Sheldrick, 2008); program(s) used to refine structure: *SHELXL97* (Sheldrick, 2008); molecular graphics: *DIAMOND* (Brandenburg, 2010); software used to prepare material for publication: *XCIF* in *SHELXTL* (Sheldrick, 2008).

The authors thank Dr Christian Näther and Inke Jess (University of Kiel) for the acquisition of the single-crystal data. This work was supported by the State of Schleswig-Holstein, Germany and the German Research Foundation (DFG; SPP-1362).

Supplementary data and figures for this paper are available from the IUCr electronic archives (Reference: BT5531).

References

- Brandenburg, K. (2010). *DIAMOND*. Crystal Impact GbR, Bonn, Germany.
- Cheng, D., Khan, M. A. & Houser, R. P. (2001). *Inorg. Chem.* **40**, 6858–6859.
- Huang, X. C., Lin, Y. Y., Zhang, J. P. & Chen, X. M. (2006). *Angew. Chem. Int. Ed.* **45**, 1557–1559.
- Kitagawa, S., Kitaura, R. & Noro, S. (2004). *Angew. Chem. Int. Ed.* **43**, 2334–2375.
- Li, H., Eddadoudi, M., O’Keeffe, M. & Yaghi, O. M. (1999). *Nature (London)*, **402**, 276–279.
- Maniam, P., Näther, C. & Stock, N. (2010). *Eur. J. Inorg. Chem.* pp. 3866–3874.
- Martins, G. A. V., Byrne, P. J., Allan, P., Tea, S. J., Slawin, A. M. Z., Li, Y. & Morris, R. E. (2010). *Dalton Trans.* **39**, 1758–1762.
- Park, K. S., Ni, Z., Coté, A. P., Choi, J. Y., Huang, R., Uribe-Romo, F. J., Chae, H. K., O’Keeffe, M. & Yaghi, O. M. (2006). *Proc. Natl Acad. Sci. USA*, **103**, 10186–10191.
- Sheldrick, G. M. (2008). *Acta Cryst.* **A64**, 112–122.
- Stock, N. (2010). *Microporous Mesoporous Mater.* **129**, 287–295.
- Stoe & Cie (2008). *X-AREA, X-RED* and *X-SHAPE*. Stoe & Cie, Darmstadt, Germany.
- Zheng, S., Wu, T., Zhang, J., Chow, M., Nieto, R. A., Feng, P. & Bu, X. (2010). *Angew. Chem. Int. Ed.* **49**, 5362–5366.

5 Conclusion

The first part of the cumulative section covers the synthesis of 4-phosphonobenzenesulfonic acid and the resulting metal phosphonosulfonates yielded from the system $M^{2+} / H_2O_3PC_6H_4SO_3H / NaOH / H_2O$ under hydrothermal reaction conditions. Various divalent metal ions were screened ($M = Ni, Mg, Cu, Zn, Co, Fe, Mn, Sn, Cd, Sr, Pb$ and Ba) using high-throughput (HT) synthesis and XRPD characterization. Single crystals of lead(II), copper(II) and tin(II) phosphonatobenzenesulfonates were obtained and the crystal structures were determined via single crystal X-ray diffraction. Systematic investigation with HT methods has enabled the rapid screening of counter ions and molar ratios of reactants which has helped to determine the optimal synthesis conditions of the Pb^{2+} - and Cu^{2+} -based compounds. In addition, the employment of discovery and focused array set-ups was essential in the study of reaction systems with several co-crystallizing phases and narrow formation fields, especially with the Cu(II) phosphonosulfonate structures. By using 4,4'-bipyridine (*bipy*), the study of metal phosphonosulfonates was expanded to mixed-linker systems. A new structure incorporating copper(II) ions, $HO_3PC_6H_4SO_3$ ions, *bipy* ligands and hydrogen bonded water molecules was synthesized which exhibits structural transformation upon dehydration. A closer look in the Jahn-Teller distorted copper(II) octahedra has revealed a directional switching of the elongated axial bonds which is reversible upon rehydration.

High-throughput methods were also employed in the investigation of porous metal-organic frameworks (MOF). The second part of the dissertation deals with the systematic investigation of Ni(II) based MOFs with paddle-wheel building units. Four paddle-wheel containing nickel compounds were discovered via solvothermal synthesis with dimethylformamide as the solvent. In the first system involving 1,3,5-benzenetricarboxylic acid as the linker, the presence of 2-methylimidazole as an additive was important to obtain the porous paddle-wheel based structure. Using these results, the study was expanded to a reaction system with the larger tripodal linker 4,4',4''-benzene-1,3,5-triyl-tris(benzoic acid). In this case, 2-methylimidazole is not only an additive which regulates the basicity of the reaction mixture, but also a coordinating axial ligand. The sorption experiments using different gases/vapors have shown that large cavities in the structure only allow adsorbates with small kinetic diameters to pass through the narrow pore windows. In the reaction system involving terephthalic acid (H_2BDC) and 1,4-diazabicyclo[2.2.2]octane (DABCO), pseudo-polymorphic mixed-ligand nickel(II) compounds were obtained. Although the paddle-wheel clusters are the same, different connectivities by the BDC linkers lead to two pillared-layered structures with different layer topologies. Phase selective synthesis of both pseudo-polymorphs was

accomplished by employing microwave-assisted heating, varying DABCO and overall concentration as well as stirring.

Table 5.1 Inorganic-organic hybrid compounds synthesized in this work.

Chapter	No.	Compound	CCDC no.	Structural characterization
4.3.1	1	Pb ₂ [(O ₃ PC ₆ H ₄ SO ₃)(OH)]	772438	SC
	2	Cu _{1.5} [(O ₃ PC ₆ H ₄ SO ₃)(H ₂ O)]	772439	SC
	3	NaCu(O ₃ PC ₆ H ₄ SO ₃)(H ₂ O) ₃	-	Elem. / Ind.
	4	Cu ₂ [(O ₃ PC ₆ H ₄ SO ₃)(OH)(H ₂ O)]	772440	SC
	5	Cu ₃ [(O ₃ PC ₆ H ₄ SO ₃) ₂ (H ₂ O) ₂]	772441	SC
4.3.2	6	[Sn ₂ (O ₃ PC ₆ H ₄ SO ₃)(OH)]	819291	SC
4.3.3	7	[Cu(HO ₃ PC ₆ H ₄ SO ₃)(C ₁₀ N ₂ H ₈)]·H ₂ O	822923	SC
	8	[Cu(HO ₃ PC ₆ H ₄ SO ₃)(C ₁₀ N ₂ H ₈)]	823351	RR
4.4.3	9	[Ni ₃ (BTC) ₂ (Me ₂ NH) ₃]·(DMF) ₄ (H ₂ O) ₄	802889	SC
	10	[Ni ₆ (BTC) ₂ (DMF) ₆ (HCOO) ₆]	802890	SC
	11	[Ni ₃ (BTB) ₂ (2-MelmH) _{1.5} (H ₂ O) _{1.5}]·(DMF) ₉ (H ₂ O) _{6.5}	802891	SC
	12	[Ni ₂ (BDC) ₂ (DABCO)]·(DMF) ₄ (H ₂ O) _{1.5}	802892	RR
	13	[Ni ₂ (BDC) ₂ (DABCO)]·(DMF) ₄ (H ₂ O) ₄	802893	RR
	14	[Ni(BDC)(DABCO)]·(DMF) _{1.5} (H ₂ O) ₂	802894	RR
4.4.4	15	[Zn ₂ (BTC)(2-Melm)(2-MelmH) ₃]	829949	SC

Abbreviations: SC = single crystal X-ray diffraction; RR = Rietveld refinement; Elem. = CHNS and EDX elemental analysis; Ind. = indexing of X-ray powder diffraction pattern; BTC = 1,3,5-benzenetricarboxylate; Me₂NH = dimethylamine; DMF = dimethylformamide; 2-MelmH = 2-methylimidazole; DABCO = 1,4-diazabicyclo[2.2.2]-octane.

5.1 Metal phosphonatobenzenesulfonates

Eight new crystalline compounds were synthesized which incorporate the 4-phosphonobenzenesulfonic acid linker. High-throughput studies have shown that numerous new compounds can be obtained with only a single linker (Table 5.1). This is mainly achieved by systematic screening of different metal ions in the reaction system M²⁺ / linker / NaOH / H₂O. Most profound influence on the product formations are exerted by molar ratios of the reactants. The type of counter-ions in the metal salts and the amount of NaOH influence the

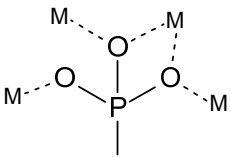
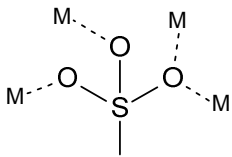
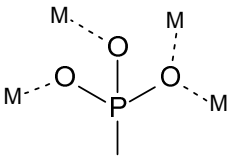
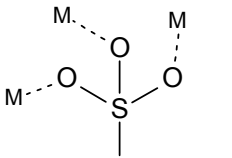
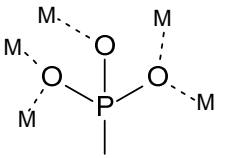
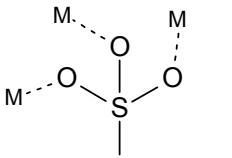
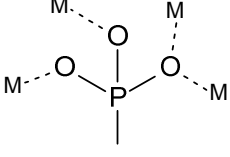
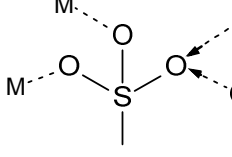
pH values of the reaction mixtures. Only high molar ratios of Pb^{2+} : linker and NaOH : linker lead to the formation of $\text{Pb}_2[(\text{O}_3\text{PC}_6\text{H}_4\text{SO}_3)(\text{OH})]$. The effect of large amounts of NaOH can also be seen by the incorporation of hydroxide ions in the structure. On the other hand, copper(II) ions yielded diverse crystal structures, many of which crystallize in very narrow formation fields. The consequent use of discovery and focused arrays has made the rapid determination of the specific formation areas possible.

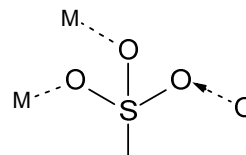
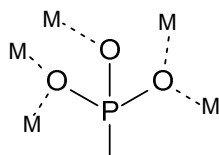
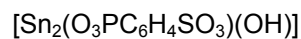
The structure of $\text{Pb}_2[(\text{O}_3\text{PC}_6\text{H}_4\text{SO}_3)(\text{OH})]$ is composed of Pb-O-Pb chains which are formed via edge-sharing of Pb_2O_{10} clusters (Table 5.2). These chains are densely connected to each other by phosphonate and sulfonate groups creating layers that are pillared by phenyl rings to construct the three-dimensional framework. In the copper(II)-based compounds, various Cu-O-Cu connectivities are observed which range from isolated CuO_6 , dinuclear Cu_2O_8 , hexanuclear Cu_6O_{24} clusters to Cu-O-Cu chains. In general, the Cu-O-Cu clusters or chains are cross-linked to each other by phosphonate and sulfonate groups forming layers. The remaining pillaring phenyl rings or hydrogen bonding interconnect such layers. Interestingly, although the coordination number of Cu^{2+} ions is lower than of Pb^{2+} ions, the Cu-O-Cu chains in $\text{Cu}_2[(\text{O}_3\text{PC}_6\text{H}_4\text{SO}_3)(\text{OH})(\text{H}_2\text{O})]$ is built up of similar edge-sharing M_2O_{10} clusters as observed in $\text{Pb}_2[(\text{O}_3\text{PC}_6\text{H}_4\text{SO}_3)(\text{OH})]$. The steric effect of lone pairs was found to be more striking in tin(II) compound than in the lead(II) based structure. In $[\text{Sn}_2(\text{O}_3\text{PC}_6\text{H}_4\text{SO}_3)(\text{OH})]$, narrow voids are observed between Sn_4O_{12} clusters that indicate the position of lone pairs. The lone pairs in $\text{Pb}_2[(\text{O}_3\text{PC}_6\text{H}_4\text{SO}_3)(\text{OH})]$ point in the direction of the organic part of the crystal structure.

The use of the auxiliary *para*-bridging 4,4'-bipyridine ligand has produced a mixed-linker structure containing isolated Jahn-Teller distorted CuO_6 octahedra. These octahedra are interconnected by phosphonate and sulfonate groups forming chains which cross-linked to each other by phenyl rings and bipyridine fragments. The resulting 3D framework contains non-coordinating water molecules involved in hydrogen bonding with the oxygen atoms of protonated phosphonate and deprotonated sulfonate groups. The presence of these water molecules is determined to be very essential for the structural transformation as the elongated axial Cu-O bonds switch their direction upon dehydration. In the dehydrated structure, the elongation of the bonds is between the oxygen atoms of the phosphonate groups while in the hydrated structure, the oxygen atoms of the sulfonate groups show the large Cu-O distances. Such reversible "Jahn-Teller switching" is rarely observed which also contradicts the general trend seen in the M-O bonds lengths in the metal 4-phosphonatobenzenesulfonates. The comparison of coordination modes of sulfonate groups of the compounds obtained in this work (Table 5.2) demonstrates that sulfonate groups are

always fully deprotonated and the M-O bonds originating from sulfonate groups are usually longer than of the ones originating from the phosphonate groups. The longer M-O bonds and lower coordination to the metal ion indicates that these bonds are much weaker which is typical for sulfonates. In addition, only in the mixed-linker compound, a non-fully deprotonated 4-phosphonobenzenesulfonate linker is observed. In all single linker systems, all phosphonate and sulfonate groups are fully deprotonated irrespective of the added base amount.

Table 5.2 Coordination modes and the dimensionality observed in metal 4-phosphonatobenzene-sulfonates. * = formation of a 3D network via extensive hydrogen bonding.

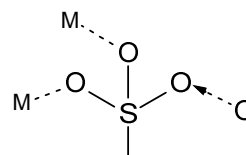
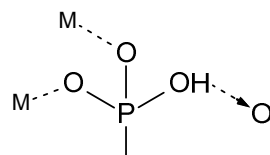
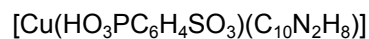
Compound	M...O bond lengths & coordination modes		Network / nuclearity
$\text{Pb}_2[(\text{O}_3\text{PC}_6\text{H}_4\text{SO}_3)(\text{OH})]$	 $5 \cdot (\text{M} \cdots \text{O}) = 2.317(14) - 2.858(10) \text{ \AA}$	 $4 \cdot (\text{M} \cdots \text{O}) = 2.731(14) - 2.875(14) \text{ \AA}$	3D / $(\text{Pb}_2\text{O}_{10})_\infty$ chains via edge- sharing
$\text{Cu}_{1.5}[(\text{O}_3\text{PC}_6\text{H}_4\text{SO}_3)(\text{H}_2\text{O})]$	 $4 \cdot (\text{M} \cdots \text{O}) = 1.945(3) - 2.039(3) \text{ \AA}$	 $3 \cdot (\text{M} \cdots \text{O}) = 1.948(3) - 2.428(3) \text{ \AA}$	3D / Cu_6 , Cu_2O_8
$\text{Cu}_2[(\text{O}_3\text{PC}_6\text{H}_4\text{SO}_3)(\text{OH})(\text{H}_2\text{O})]$	 $5 \cdot (\text{M} \cdots \text{O}) = 1.927(4) - 2.402(3) \text{ \AA}$	 $3 \cdot (\text{M} \cdots \text{O}) = 2.019(4) - 2.526(4) \text{ \AA}$	3D / $(\text{Cu}_2\text{O}_{10})_\infty$ chains via edge- sharing
$\text{Cu}_3[(\text{O}_3\text{PC}_6\text{H}_4\text{SO}_3)_2(\text{H}_2\text{O})_2]$	 $4 \cdot (\text{M} \cdots \text{O}) = 1.900(4) - 2.008(5) \text{ \AA}$	 $2 \cdot (\text{M} \cdots \text{O}) = 1.996(5) - 2.244(5) \text{ \AA}$	2D * / Cu_6O_{24}



3D /
Sn₄O₁₂

$$5 \cdot (\text{M} \cdots \text{O}) = 2.124(2) - 2.726(3) \text{ \AA}$$

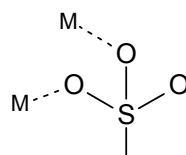
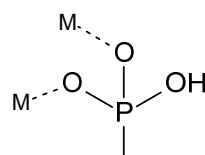
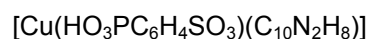
$$2 \cdot (\text{M} \cdots \text{O}) = 2.412(3) - 2.587(3) \text{ \AA}$$



3D /
CuO₆

$$2 \cdot (\text{M} \cdots \text{O}) = 1.930(2) - 1.942(2) \text{ \AA}$$

$$2 \cdot (\text{M} \cdots \text{O}) = 2.556(2) - 2.620(3) \text{ \AA}$$



3D /
CuO₆

$$2 \cdot (\text{M} \cdots \text{O}) = 2.549(17) - 2.776(11) \text{ \AA}$$

$$2 \cdot (\text{M} \cdots \text{O}) = 1.934(19) - 2.136(23) \text{ \AA}$$

5.2 Nickel-based metal-organic frameworks (MOF) with paddle-wheel building units

Porous MOFs containing nickel(II) paddle-wheel units were discovered via high-throughput synthesis. Solvothermal synthesis with dimethylformamide (DMF) as the solvent was one of the key factors in obtaining the paddle-wheel based structures. In the reaction system involving tripodal linkers, 1,3,5-benzenetricarboxylic acid (H₃BTC) and 4,4',4''-benzene-1,3,5-triyl-tris-benzoic acid (H₃BTB), the addition of 2-methylimidazole (2-MelmH) as an organic base was essential in setting up the optimal synthesis conditions. Although the role of the additive cannot be explained in detail, it may certainly influence the basicity of the reaction mixture and thus, support the selective crystallization of the targeted [Ni₃(BTC)₂(Me₂NH)₃] framework with paddle-wheel units. Besides the presence of 2-methylimidazole, the specific molar ratio Ni²⁺ : H₃BTC : 2-MelmH is very important in suppressing the co-crystallization of the dense phase [Ni₆(BTC)₂(DMF)₆(HCOO)₆]. An optimal reaction temperature of 170 °C was determined via high-throughput screening of reaction temperatures from 150-180 °C. As the scale-up of [Ni₃(BTC)₂(Me₂NH)₃] was not possible in glass tubes reactions, a separate HT experiment containing multiple identical reaction mixtures was performed to procure enough

substance for further characterization. The ineffectiveness of scale-up in glass tubes may well be due to the fact that some compounds are preferentially formed in the presence of Teflon surfaces. Strong *in situ* hydrolysis of DMF solvent was evident in the solvothermal reaction as dimethylamine molecules were determined to be the terminal axial ligands in the paddle-wheel clusters. The microporosity of the compound was confirmed via nitrogen sorption isotherm that resulted in a specific surface area (BET) of 920 m² g⁻¹.

For the synthesis of [Ni₃(BTB)₂(2-MelmH)_{1.5}(H₂O)_{1.5}] which contains the larger BTB linker, an excess of the 2-MelmH base is required or else only X-ray amorphous product are yielded. Similar to the synthesis of [Ni₃(BTC)₂(Me₂NH)₃], a relatively high reaction temperature of 170 °C is needed for the optimal yield and product purity. The axial positions of the nickel ions in the paddle-wheel unit are occupied by water and 2-MelmH molecules. The pore windows in [Ni₃(BTB)₂(2-MelmH)_{1.5}(H₂O)_{1.5}] are blocked by the axial ligands and thereby, the access to large 16 Å cavities is hindered. The subsequent removal of water ligands by thermal activation allows the selective uptake of small molecules such H₂O and H₂. Interestingly, no H₂ gas is released during desorption which indicates a form of kinetic trapping in the pores. Microwave-assisted (MW) heating was also tested for the synthesis of [Ni₃(BTC)₂(Me₂NH)₃] and [Ni₃(BTB)₂(2-MelmH)_{1.5}(H₂O)_{1.5}] but it turns out that these compounds can only be produced applying conventional heating.

On the other hand, MW-assisted heating was important in the selective synthesis of the pseudo-polymorphic [Ni₂(BDC)₂(DABCO)] pillared-layered frameworks. Conventional heating has only led to pure-phase of the tetragonal framework. The other pseudo-polymorph of this structure has a trigonal framework which can only be obtained pure-phase via MW-assisted heating. The latter structure possesses larger pores and should exhibit larger micropore volumes and specific surfaces. The influence of the molar ratio Ni²⁺ : H₂BDC : DABCO, stirring and overall concentration were investigated with high-throughput MW-assisted heating. The results of the systematic HT studies have enabled the phase selective synthesis of each pseudo-polymorph. Excess DABCO, continuous stirring and low overall concentration of reaction mixtures result in the crystallization of the trigonal framework. The reverse conditions lead to the formation of the tetragonal frameworks. According to the nitrogen sorption experiments, both pseudo-polymorphs have very high specific surface areas. Although the porosity of the trigonal framework should be higher than the tetragonal frameworks, a lower surface area was obtained due to gradual structural decomposition. A dense layered compound of [Ni(BDC)(DABCO)] was also discovered in the Ni²⁺ / H₂BDC / DABCO reaction system. This phase is dominant when the overall concentration of the stirred reaction mixture is very high and a large excess of DABCO is present.

The thermal stability of all four nickel based compounds with paddle-wheel building units was studied with thermogravimetric analysis. In general, frameworks of all these polycarboxylate-based compounds start to decompose at approximately 300 °C. The chemical stability tests to air, moisture and several organic solvents have been performed for these compounds as well. The tests show that between the structures with tripodal linkers BTC and BTB, the compound $[\text{Ni}_3(\text{BTB})_2(2\text{-MeImH})_{1.5}(\text{H}_2\text{O})_{1.5}]$ is more stable. The comparison of bond lengths in the paddle-wheel dimers indicates a slightly longer separation of Ni-Ni ions in the compound containing BTB linker (Table 5.3). The Ni-Ni internuclear distance is also determined to be longer for the tetragonal framework structure of $[\text{Ni}_2(\text{BDC})_2(\text{DABCO})]$. Consequently, the tetragonal framework is also found to be chemically more stable than the trigonal framework pseudo-polymorph. A further inspection of the dimeric nickel paddle-wheel units in all four compounds (Table 5.3) has revealed that the N-ligands are preferably coordinated to the nickel ions in the axial positions, although O-ligands such as water is present in the reaction mixtures. Nevertheless, the affinity of N-ligands cannot be correlated to Ni-O or Ni-N bond distances as no clear trend is observed.

Table 5.3 Bonds lengths of Ni-Ni, Ni-O and Ni-N in the dimeric nickel paddle-wheel building units.

Compound	Bond lengths in paddle-wheel dimers
$[\text{Ni}_3(\text{BTC})_2(\text{Me}_2\text{NH})_3] \cdot (\text{DMF})_4(\text{H}_2\text{O})_4$	$\text{N} \cdots \cdots \text{Ni} \xleftrightarrow{2.713(1) \text{ \AA}} \text{Ni} \cdots \cdots \text{N}$ (Ni-N) _{axial} : 1.979(5) Å (Ni-O) _{equatorial} : 2.010(3)
$[\text{Ni}_3(\text{BTB})_2(2\text{-MeImH})_{1.5}(\text{H}_2\text{O})_{1.5}] \cdot (\text{DMF})_9(\text{H}_2\text{O})_{6.5}$	$\text{O} \cdots \cdots \text{Ni} \xleftrightarrow{2.846(1) \text{ \AA}} \text{Ni} \cdots \cdots \text{N}$ (Ni-O) _{axial} : 1.981(8) Å (Ni-N) _{axial} : 2.000(8) Å (Ni-O) _{equatorial} : 1.954(5) - 2.050(3) Å
$[\text{Ni}_2(\text{BDC})_2(\text{DABCO})] \cdot (\text{DMF})_4(\text{H}_2\text{O})_{1.5}$ (tetragonal framework)	$\text{N} \cdots \cdots \text{Ni} \xleftrightarrow{2.683(8) \text{ \AA}} \text{Ni} \cdots \cdots \text{N}$ (Ni-N) _{axial} : 2.053(14) Å (Ni-O) _{equatorial} : 1.966(10) Å
$[\text{Ni}_2(\text{BDC})_2(\text{DABCO})] \cdot (\text{DMF})_4(\text{H}_2\text{O})_4$ (trigonal framework)	$\text{N} \cdots \cdots \text{Ni} \xleftrightarrow{2.589(3) \text{ \AA}} \text{Ni} \cdots \cdots \text{N}$ (Ni-N) _{axial} : 2.041(5) Å (Ni-O) _{equatorial} : 1.974(4) – 1.993(3) Å

6 Outlook

The metal 4-phosphonatobenzenesulfonates which are documented in this work exhibit various M-O-M connectivities and the crystal structures are mostly comprised of pillared-layered frameworks. Many divalent metal ions were screened with the 4-phosphonobenzenesulfonic acid linker which led to the determination of crystal structures with Cu^{2+} , Pb^{2+} and Sn^{2+} ions. Copper(II) ions have exhibited the unusual ability to form different Cu-O polyhedra as well as clusters and hence result in several structurally distinct compounds. The structural diversity is also due to the fact that the sulfonate group is weakly coordinating compared to the phosphonate group. Further study with trivalent and tetravalent ions such as rare earth ions and Zr^{4+} with this linker may possibly generate novel structures which deviate from the pillared-layered structural trend observed with divalent ions.

The mixed-linker copper compound containing the phosphonosulfonate and 4,4'-bipyridine linker has demonstrated an interesting structural transition upon dehydration. In general, the field of mixed-linker compounds is still in its early stages and the investigations should not be limited to this amine ligand. There is the opportunity to use other co-ligands to discover new structures. Besides amine ligands such as 1,10-phenanthroline, 4-phenylenediamine, piperazine, auxiliary ligands with other functional groups, for example carboxylic acid have yet to be thoroughly investigated.

Large linkers often produce highly porous structures which until now only have been reported with polycarboxylic linkers. Porous metal phosphonosulfonates are yet to be discovered and one restraining factor is the unavailability of large or longer polyfunctional acid linkers. The preparation of simple phosphonosulfonic acids already involves multiple reaction steps and at the end, the product yield is often low. In addition, the solubility of the linker in water also decreases when the fraction of the organic group increases. The use of mixed-solvent reaction system could alleviate this problem by using aqueous solution for metal salts and organic solution for the linker. Nevertheless, several potential phosphonosulfonic linkers can be envisioned for future studies. Figure 6.1 illustrates the structure of some of possible linkers.

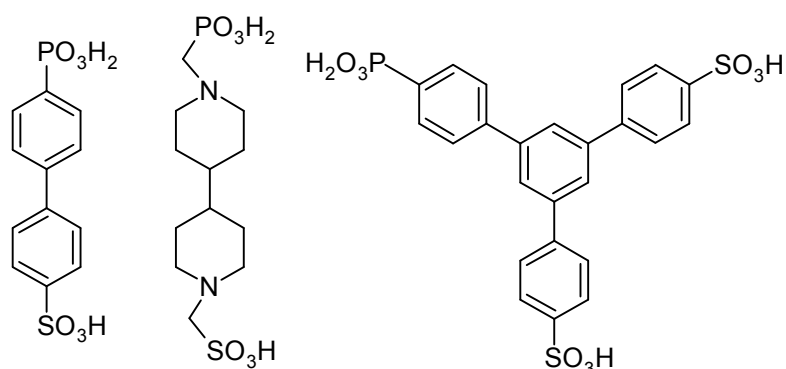


Figure 6.1 Potential phosphonosulfonic acid linkers for the synthesis of porous structures.

The synthesis of porous nickel(II) based MOFs with paddle-wheel units has proven to be not trivial. Compositional parameters such as nickel(II) salts, organic base additives, solvents had to be screened in order to obtain the right reactants. With the help of high-throughput methods, systematic investigations were performed which determined nickel(II) nitrate, dimethylformamide and most importantly, 2-methylimidazole as the optimal starting materials. High reaction temperature up to 170 °C is also necessary for the best yield and purity. With these results, two paddle-wheel based nickel compounds were obtained with tripodal linkers, namely $[\text{Ni}_3(\text{BTC})_2(\text{Me}_2\text{NH})_3]$ and $[\text{Ni}_3(\text{BTB})_2(2\text{-MeImH})_{1.5}(\text{H}_2\text{O})_{1.5}]$. Using this knowledge, new nickel(II) structures can be investigated with other tripodal tricarboxylic acid linkers. For example, in order to obtain a structure that is isorecticular to $[\text{Ni}_3(\text{BTC})_2(\text{Me}_2\text{NH})_3]$, the linker 4,4',4''-s-triazine-2,4,6-triyl-tribenzoic acid (H_3TATB) can be employed (Figure 6.2). Although H_3TATB is structurally similar to H_3BTB , H_3TATB is planar and therefore, a non-interwoven framework can be expected.

Although the synthesis of mixed-linker system $[\text{Ni}_2(\text{BDC})_2(\text{DABCO})_2]$ does not involve any additive, it required extensive investigation of reaction parameters for the phase selective synthesis of each pseudo-polymorph. The pure-phase formation of the pseudo-polymorphs is highly dependent on the amount of DABCO, stirring and overall concentration as well as the type of heating. Microwave-assisted heating provides more rapid nucleation rates compared to conventional heating and thus, enabled the crystallization of metastable trigonal framework structure. Nevertheless, the kinetics behind the phase selective crystallization of the pseudo-polymorphs could be further scrutinized in real time with methods such as *in situ* EDXRD or EXAFS. These results could be exploited and applied for the synthesis of new porous pillared-layered structures with paddle-wheel units. Nickel(II) ions could be reacted with extended linkers such as 4,4'-biphenyldicarboxylic acid (H_2BPDC) and 4,4'-bipyridine (*bipy*) which again could require the mixed-solvent approach due to solubility problems (Figure 6.2).

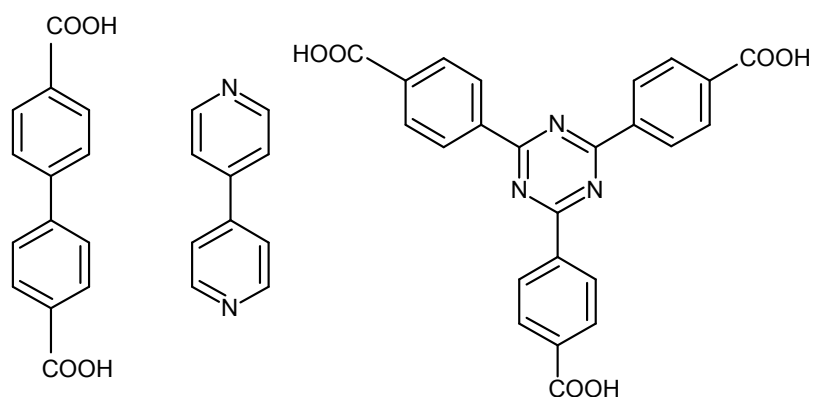


Figure 6.2 Potential linkers for the isorecticular synthesis of porous nickel(II) compounds (*from left*: H_2BPDC , *bipy*, H_3TATB).

Appendix 1

Supporting Information

P. Maniam, C. Näther, N. Stock, *Eur. J. Inorg. Chem.* **2010**, 3866-3874.

Systematic Hydrothermal Investigation of Metal Phosphonatobenzenesulfonates via High-Throughput Methods

Palanikumar Maniam, Christian Näther and Norbert Stock*

Institute of Inorganic Chemistry,
Christian-Albrechts-University Kiel, Max-Eyth-Straße 2, D-24118 Kiel,

* Prof. Dr. Norbert Stock, Tel.: +49-431-880-1675, Fax: +49-431-880-1775.

e-mail: stock@ac.uni-kiel.de

(1) Tables of high-throughput experiment	page 2 - 7
(2) Bond lengths and angles	page 8
(3) IR-spectra	page 9
(4) Comparison of simulated and measured XRD patterns	page 9
(5) Lattice parameter refinement of compound 3	page 10
(6) Thermal analysis	page 11
(7) SEM micrographs of compounds 1, 4, and 5	page 12
(8) Magnetic susceptibility measurements of compounds 4 and 5	page 13

Table S1. Exact amounts of reactants for the high throughput metal-screening investigation of the system M^{2+} : H_3L : $NaOH$: H_2O .

Nr.	molar ratios			Salt (molar mass)	M^{2+} mg	H_3L^a μL	$NaOH^b$ μl	H_2O μl	Reaction result/ substance appearance	PXRD
	M^{2+}	H_3L	$NaOH$							
1	1.5	1	3	Ni ($NiCl_2$) 129.60	3.8	50	50	100	yellow brown powder	X-ray amorphous
2	2	1	3		5.2	50	50	100	yellow brown powder	X-ray amorphous
3	3	1	3		7.8	50	50	100	yellow brown powder	product of low crystallinity
4	4	1	3		10.6	50	50	100	yellow brown powder	X-ray amorphous
5	1.5	1	3	Mg ($Mg(NO_3)_2 \cdot 6H_2O$) 256.41	8.5	50	50	100	white powder	X-ray amorphous
6	2	1	3		11.4	50	50	100	white powder	X-ray amorphous
7	3	1	3		15.4	50	50	100	white powder	product of low crystallinity
8	4	1	3		20.3	50	50	100	white powder	X-ray amorphous
9	1.5	1	3	Cu ($Cu(NO_3)_2 \cdot 3H_2O$) 241.60	7.3	50	50	100	clear solution	-
10	2	1	3		10.0	50	50	100	white powder + green crystals	4 + crystalline impurities
11	3	1	3		14.6	50	50	100	blue + green crystals	4 + 5 + crystalline impurities
12	4	1	3		19.7	50	50	100	blue powder	X-ray amorphous
13	1.5	1	3	Zn ($Zn(NO_3)_2 \cdot 6H_2O$) 297.49	9.7	50	50	100	white powder	X-ray amorphous
14	2	1	3		11.9	50	50	100	white powder	X-ray amorphous
15	3	1	3		17.8	50	50	100	white powder	product of low crystallinity
16	4	1	3		23.3	50	50	100	white powder	X-ray amorphous
17	1.5	1	3	Co ($Co(NO_3)_2 \cdot 6H_2O$) 291.03	8.7	50	50	100	purple and green powder	X-ray amorphous
18	2	1	3		12.0	50	50	100	purple and green powder	X-ray amorphous
19	3	1	3		17.5	50	50	100	purple and green powder	X-ray amorphous
20	4	1	3		23.1	50	50	100	purple and green powder	X-ray amorphous
21	1.5	1	3	Fe ($FeCl_2 \cdot 4H_2O$) 198.91	6.0	50	50	100	dark brown powder	X-ray amorphous
22	2	1	3		8.3	50	50	100	dark brown powder	X-ray amorphous
23	3	1	3		11.6	50	50	100	dark brown powder	X-ray amorphous
24	4	1	3		16.3	50	50	100	dark brown powder	X-ray amorphous
25	1.5	1	3	Mn ($MnCl_2 \cdot 4H_2O$) 197.91	5.9	50	50	100	beige powder	X-ray amorphous
26	2	1	3		7.8	50	50	100	beige powder	X-ray amorphous
27	3	1	3		11.9	50	50	100	beige powder	product of low crystallinity
28	4	1	3		15.9	50	50	100	beige powder	X-ray amorphous
29	1.5	1	3	Sn ($SnCl_2 \cdot 2H_2O$) 225.65	6.8	50	50	100	white powder	product of low crystallinity
30	2	1	3		8.8	50	50	100	metallic powder	Sn
31	3	1	3		13.5	50	50	100	metallic powder	Sn
32	4	1	3		17.9	50	50	100	metallic powder	Sn
33	1.5	1	3	Cd ($CdCl_2 \cdot 1H_2O$) 201.32	6.2	50	50	100	white powder	product of low crystallinity
34	2	1	3		8.4	50	50	100	white powder	X-ray amorphous
35	3	1	3		12.5	50	50	100	white powder	X-ray amorphous
36	4	1	3		16.4	50	50	100	white powder	X-ray amorphous
37	1.5	1	3	Sr ($SrCl_2 \cdot 6H_2O$) 266.62	7.4	50	50	100	clear solution	-
38	2	1	3		10.8	50	50	100	clear solution	-
39	3	1	3		16.8	50	50	100	clear solution	-
40	4	1	3		21.3	50	50	100	clear solution	-
41	1.5	1	3	Pb ($Pb(NO_3)_2$) 331.21	9.0	50	50	100	white powder	X-ray amorphous
42	2	1	3		13.1	50	50	100	white powder	X-ray amorphous
43	3	1	3		20.1	50	50	100	white powder	X-ray amorphous
44	4	1	3		26.5	50	50	100	white powder + colorless crystals	1
45	1.5	1	3	Ba ($BaCl_2 \cdot 2H_2O$) 244.26	7.7	50	50	100	clear solution	-
46	2	1	3		10.1	50	50	100	clear solution	-
47	3	1	3		14.7	50	50	100	clear solution	-
48	4	1	3		19.5	50	50	100	clear solution	-

^a 0.4 M $H_2O_3P-C_6H_4-SO_3H \cdot 2H_2O$ ^b 1.2 M NaOHreactor fill volume: 200 μL Temperature profile: heat-up phase = 2.2 $^{\circ}C/min$ to 150 $^{\circ}C$ residence time = 36 h at 150 $^{\circ}C$ cool down phase = 0.27 $^{\circ}C/min$ to room temperature(1) : $Pb_2[(O_3P-C_6H_4-SO_3)(OH)]$ (4) : $Cu_2[(O_3P-C_6H_4-SO_3)(OH)(H_2O)]$ (5) : $Cu_3[(O_3P-C_6H_4-SO_3)_2(H_2O)_2]$

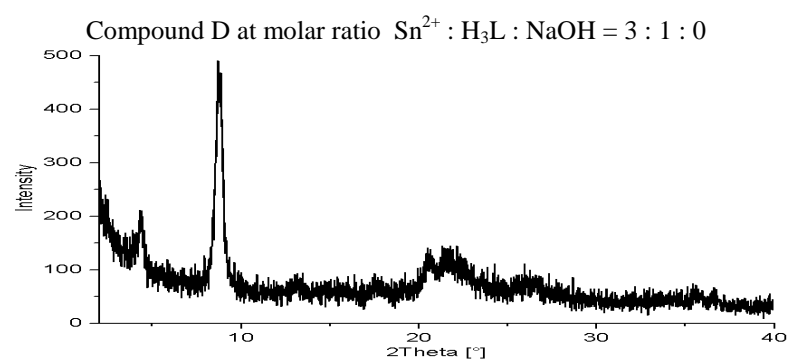
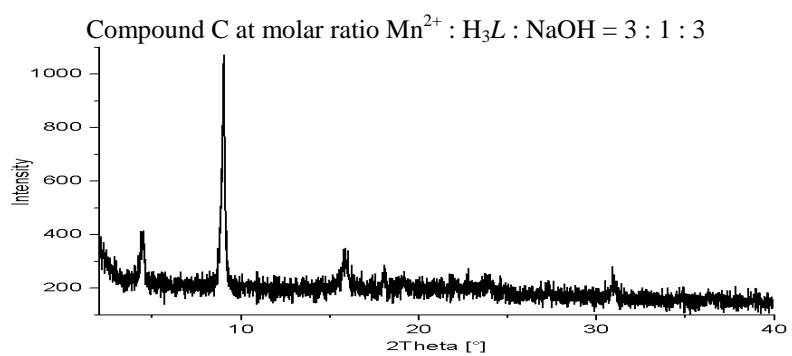
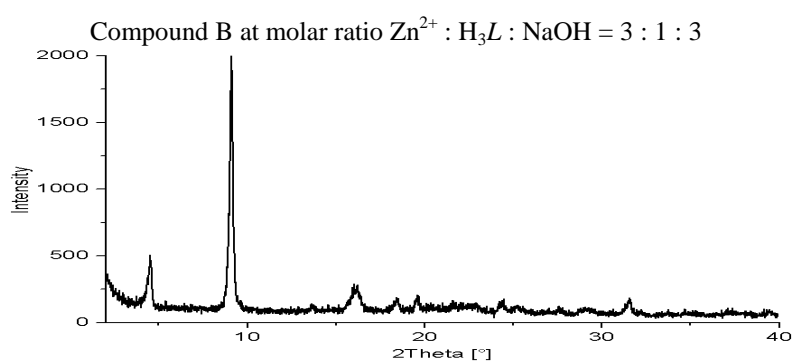
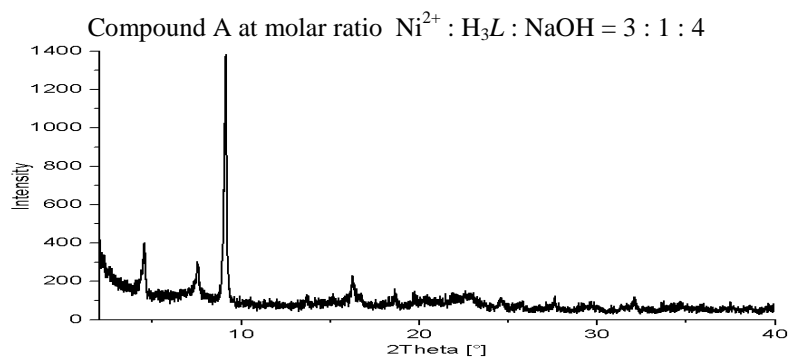
Table S2. Exact amounts of reactants for the focused high throughput metal-screening investigation of the system $M^{2+}:H_3L:NaOH:H_2O$.

Nr.	molar ratios			Salt (molar mass)	M^{2+} mg	H_3L^a μL	$NaOH^b$ μL	H_2O μL	pH	Reaction result/ substance appearance	PXRD
	M^{2+}	H_3L	NaOH								
1	3	1	0	Ni (NiCl ₂) 129.60	14.3	25	0	175	1	clear solution	-
2	3	1	1		14.3	25	20	155	2	clear solution	-
3	3	1	2		14.3	25	40	135	4	clear solution	-
4	3	1	3		14.3	25	60	115	5	yellow brown powder	A
5	3	1	4		14.3	25	80	95	7	yellow brown powder	A
6	3	1	5		14.3	25	100	75	7	yellow brown powder	A
7	3	1	0	Mg (Mg(NO ₃) ₂ ·6H ₂ O) 256.41	15.4	25	0	175	1	clear solution	-
8	3	1	1		15.4	25	20	155	2	clear solution	-
9	3	1	2		15.4	25	40	135	5	clear solution	-
10	3	1	3		15.4	25	60	115	8	clear solution	-
11	3	1	4		15.4	25	80	95	9	white powder	X-ray amorphous
12	3	1	5		15.4	25	100	75	10	white powder	X-ray amorphous
13	3	1	0	Cu (Cu(NO ₃) ₂ ·3H ₂ O) 241.60	14.5	25	0	175	1	light blue powder	X-ray amorphous
14	3	1	1		14.5	25	20	155	3	green crystals	X-ray amorphous
15	3	1	1.5		14.5	25	30	145	4	green crystals	(4) + (5)
16	3	1	2		14.5	25	40	135	4	green powder	X-ray amorphous
17	3	1	2.5		14.5	25	50	125	4	turquoise crystals	(4) + (5)
18	3	1	3		14.5	25	60	115	5	green powder	(4) + (5)
19	3	1	0	Zn (Zn(NO ₃) ₂ ·6H ₂ O) 297.49	17.8	25	0	175	1	clear solution	-
20	3	1	1		17.8	25	20	155	2	clear solution	-
21	3	1	2		17.8	25	40	135	5	white powder	B
22	3	1	3		17.8	25	60	115	6	white powder	B
23	3	1	4		17.8	25	80	95	6	white powder	B
24	3	1	5		17.8	25	100	75	6	white powder	B
25	3	1	0	Mn (MnCl ₂ ·4H ₂ O) 197.91	11.9	25	0	175	1	clear solution	-
26	3	1	1		11.9	25	20	155	2	clear solution	-
27	3	1	2		11.9	25	40	135	4	clear solution	-
28	3	1	3		11.9	25	60	115	5	grey powder	C
29	3	1	4		11.9	25	80	95	6	beige powder	C
30	3	1	5		11.9	25	100	75	6	beige powder	C
31	3	1	0	Sn (SnCl ₂ ·2H ₂ O) 225.65	13.5	25	0	175	1	white powder	D
32	3	1	1		13.5	25	20	155	2	white powder	D
33	3	1	2		13.5	25	40	135	2	white powder	D
34	3	1	3		13.5	25	60	115	3	metallic + white powder	X-ray amorphous
35	3	1	4		13.5	25	80	95	3	white powder	SnO ₂
36	3	1	5		13.5	25	100	75	3	metallic powder	Sn
37	1.5	1	0	Cd (CdCl ₂ ·1H ₂ O) 201.32	4.03	25	0	175	1	clear solution	-
38	1.5	1	1		4.03	25	20	155	2	clear solution	-
39	1.5	1	2		4.03	25	40	135	4	clear solution	-
40	1.5	1	3		4.03	25	60	115	8	white powder	E
41	1.5	1	4		4.03	25	80	95	8	white powder	E
42	1.5	1	5		4.03	25	100	75	11	white powder	Cd(OH) ₂
43	4	1	0	Pb (Pb(NO ₃) ₂) 331.21	26.5	25	0	175	2	yellow powder	PbO
44	4	1	1		26.5	25	20	155	2	white powder	X-ray amorphous
45	4	1	2		26.5	25	40	135	3	white powder	(1) + impurities
46	4	1	3		26.5	25	60	115	5	colorless crystals + white powder	(1) + impurities
47	4	1	4		26.5	25	80	95	6	colorless crystals + white powder	(1) + impurities
48	4	1	5		26.5	25	100	75	6	colorless crystals + white powder	(1) + impurities

^a 0.8 M H₂O₃P-C₆H₄-SO₃H·2H₂O^b 1.0 M NaOHreactor fill volume: 200 μL Temperature profile: heat-up phase = 2.2 °C/min to 150 °C
residence time = 36 h at 150 °C
cool down phase = 0.27 °C/min to room temperature.(1) : Pb₂[(O₃P-C₆H₄-SO₃)(OH)]
(4) : Cu₂[(O₃P-C₆H₄-SO₃)(OH)(H₂O)]
(5) : Cu₃[(O₃P-C₆H₄-SO₃)₂(H₂O)₂]

PXRD patterns of compound A to E are displayed in the next page.

XRPD patterns of crystalline compounds observed during the metal screening experiment (Table S2).



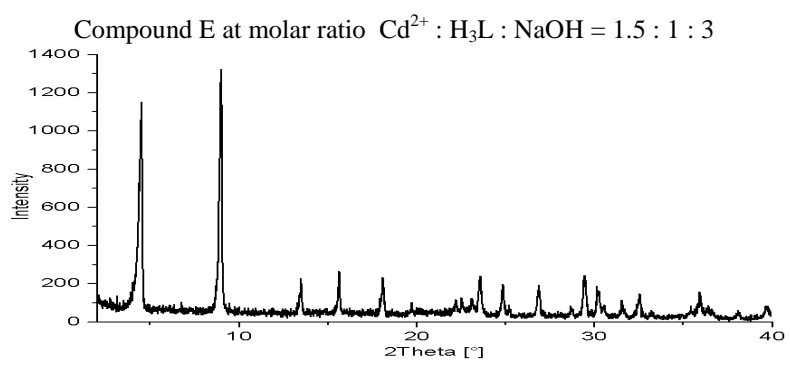


Table S3. Exact amounts of reactants for the high throughput investigation of the system $\text{Pb}(\text{NO}_3)_2:\text{H}_3\text{L}:\text{NaOH}:\text{H}_2\text{O}$ (ternary diagram in Figure 1).

Nr.	molar ratios			Salt (molar mass)	Pb^{2+} mg	$\text{H}_3\text{L}^{\text{a}}$ μL	NaOH^{b} μL	H_2O μL	pH	Reaction result/ substance appearance	PXRD
	Pb^{2+}	H_3L	NaOH								
1	1	2	0	Pb [$\text{Pb}(\text{NO}_3)_2$] 331.21	6.6	20	0	180	1	white powder	$\text{Pb}(\text{NO}_3)_2$
2	1	2	1		6.6	20	20	160	1	white powder	$\text{Pb}(\text{NO}_3)_2$
3	1	2	2		6.6	20	40	140	2	white powder	$\text{Pb}(\text{NO}_3)_2$
4	1	2	3		6.6	20	60	120	2	white powder	$\text{Pb}(\text{NO}_3)_2$
5	1	2	4		6.6	20	80	100	3	white powder	$\text{Pb}(\text{NO}_3)_2$
6	1	2	5		6.6	20	100	80	6	white powder	$\text{Pb}(\text{NO}_3)_2$
7	1	1	0		6.6	20	0	180	1	white powder	$\text{Pb}(\text{NO}_3)_2$
8	1	1	1		6.6	20	20	160	2	white powder	$\text{Pb}(\text{NO}_3)_2$
9	1	1	2		6.6	20	40	140	2	white powder	$\text{Pb}(\text{NO}_3)_2$
10	1	1	3		6.6	20	60	120	3	white powder	$\text{Pb}(\text{NO}_3)_2$
11	1	1	4		6.6	20	80	100	4	white powder	$\text{Pb}(\text{OH})_2$
12	1	1	5		6.6	20	100	80	8	white powder	$\text{Pb}(\text{OH})_2$
13	2	1	0		13.2	20	0	180	1	white powder	$\text{Pb}(\text{NO}_3)_2$
14	2	1	1		13.2	20	20	160	1	yellow powder	$\text{Pb}(\text{NO}_3)_2 + \text{PbO}$
15	2	1	2		13.2	20	30	150	1	colorless needles + yellow powder	(1) + PbO + impurities
16	2	1	3		13.2	20	40	140	3	colorless needles + white powder	(1) + impurities
17	2	1	4		13.2	20	50	130	4	colorless needles + white powder	(1) + impurities
18	2	1	5		13.2	20	60	120	5	colorless needles + white powder	(1) + impurities
19	3	1	0		19.9	20	0	180	1	white powder	$\text{Pb}(\text{NO}_3)_2$
20	3	1	1		19.9	20	20	160	1	colorless needles + white powder	(1) + $\text{Pb}(\text{NO}_3)_2$ + impurities
21	3	1	2		19.9	20	40	140	1	colorless needles + white powder	(1) + $\text{Pb}(\text{NO}_3)_2$
22	3	1	3		19.9	20	60	120	2	colorless needles + white powder	(1) + $\text{Pb}(\text{NO}_3)_2$
23	3	1	4		19.9	20	80	100	4	colorless needles + white powder	(1) + $\text{Pb}(\text{NO}_3)_2$
24	3	1	5		19.9	20	100	80	4	colorless needles + white powder	(1) + impurities
25	4	1	0		26.5	20	0	180	1	white powder	$\text{Pb}(\text{NO}_3)_2$
26	4	1	0.5		26.5	20	10	170	1	colorless needles + white powder	(1) + impurities
27	4	1	1		26.5	20	20	160	1	colorless needles + white powder	(1) + impurities
28	4	1	1.5		26.5	20	30	150	1	colorless needles + yellow powder	(1) + impurities
29	4	1	2		26.5	20	40	140	1	colorless needles + yellow powder	(1) + impurities
30	4	1	2.5		26.5	20	50	130	3	colorless needles + white powder	(1) + impurities
31	4	1	3		26.5	20	60	120	3	colorless needles + white powder	(1) + impurities
32	4	1	3.5		26.5	20	70	110	5	colorless needles + white powder	(1) + impurities
33	4	1	4		26.5	20	80	100	5	colorless needles	(1)
34	4	1	4.5		26.5	20	90	90	5	colorless needles	(1)
35	4	1	5		26.5	20	100	80	5	colorless needles	(1)
36	4	1	5.5		26.5	20	110	70	5	colorless needles + white powder	(1) + impurities

^a 1.0 M $\text{H}_2\text{O}_3\text{P}-\text{C}_6\text{H}_4-\text{SO}_3\text{H}\cdot 2\text{H}_2\text{O}$ ^b 1.0 M NaOHreactor fill volume: 200 μL Temperature profile: heat-up phase = 1.1 $^\circ\text{C}/\text{min}$ to 150 $^\circ\text{C}$ residence time = 48 h at 150 $^\circ\text{C}$ cool down phase = 10.8 $^\circ\text{C}/\text{h}$ to room temperature(1): $\text{Pb}_2[(\text{O}_3\text{P}-\text{C}_6\text{H}_4-\text{SO}_3)(\text{OH})]$

Table S4. Exact amounts of reactants for the focused array high throughput investigation of the system $\text{CuCl}_2 \cdot 2\text{H}_2\text{O}:\text{H}_3\text{L}:\text{NaOH}:\text{H}_2\text{O}$ (ternary diagram in Figure 2C).

Nr.	molar ratios			Salt (molar mass)	CuCl_2^{a} μL	$\text{H}_3\text{L}^{\text{b}}$ μL	NaOH^{c} μL	H_2O μL	pH	Reaction result/ substance appearance	PXRD
	Cu^{2+}	H_3L	NaOH								
1	2.70	1	4.65	Cu ($\text{CuCl}_2 \cdot 2\text{H}_2\text{O}$) 170.48	54	20	93	33	4	green platelet crystals	(4)
2	2.70	1	4.75		54	20	95	31	5	green platelet crystals	(4)
3	2.70	1	4.85		54	20	97	29	4	light blue powder	(3)
4	2.75	1	4.65		55	20	93	32	4	light blue powder	(3)
5	2.75	1	4.75		55	20	95	30	4	light blue powder	(3)
6	2.75	1	4.85		55	20	97	28	4	light blue powder	(3)
7	2.80	1	4.65		56	20	93	31	4	light blue powder	(3)
8	2.80	1	4.75		56	20	95	29	4	light blue powder	(3)
9	2.80	1	4.85		56	20	97	27	5	green platelet crystals	(4)
10	2.85	1	4.65		57	20	93	30	4	light blue powder	(3)
11	2.85	1	4.75		57	20	95	28	4	light blue powder	(3)
12	2.85	1	4.85		57	20	97	26	4	light blue powder	(3)
13	2.90	1	4.65		58	20	93	29	4	light blue powder	(3)
14	2.90	1	4.75		58	20	95	27	4	light blue powder	(3)
15	2.90	1	4.85		58	20	97	25	4	green platelet crystals	(4)
16	2.95	1	4.65		59	20	93	28	4	light blue powder	(3)
17	2.95	1	4.75		59	20	95	26	4	light blue powder	(3)
18	2.95	1	4.85		59	20	97	24	5	light blue powder	(3)
19	3.00	1	4.65		60	20	93	27	4	light blue powder	(3)
20	3.00	1	4.75		60	20	95	25	5	green platelet crystals	(4)
21	3.00	1	4.85		60	20	97	23	4	light blue powder	(3)
22	3.00	1	4.65		60	20	93	27	4	light blue powder	(3)
23	3.00	1	4.75		60	20	95	25	4	green platelet crystals	(4)
24	3.00	1	4.85		60	20	97	23	3	green platelet crystals	(4)
25	2.90	1	2.55		58	20	51	71	4	blue needlelike crystals	(5)
26	2.90	1	2.65		58	20	53	69	3	clear solution	-
27	2.90	1	2.75		58	20	55	67	3	clear solution	-
28	2.90	1	2.85		58	20	57	65	4	blue needlelike crystals	(5)
29	2.90	1	2.95		58	20	59	63	4	blue needlelike crystals	(5)
30	2.90	1	3.05		58	20	61	61	4	blue needlelike crystals	(5)
31	3.00	1	2.55		60	20	51	69	2	clear solution	-
32	3.00	1	2.65		60	20	53	67	4	blue needlelike crystals	(5)
33	3.00	1	2.75		60	20	55	65	3	clear solution	-
34	3.00	1	2.85		60	20	57	63	3	clear solution	-
35	3.00	1	2.95		60	20	59	61	4	blue needlelike crystals	(5)
36	3.00	1	3.05		60	20	61	59	4	blue needlelike crystals	(5)
37	3.10	1	2.55		62	20	51	67	2	clear solution	-
38	3.10	1	2.65		62	20	53	65	2	clear solution	-
39	3.10	1	2.75		62	20	55	63	4	blue needlelike crystals	(5)
40	3.10	1	2.85		62	20	57	61	4	blue needlelike crystals	(5)
41	3.10	1	2.95		62	20	59	59	4	blue needlelike crystals	(5)
42	3.10	1	3.05		62	20	61	57	4	blue needlelike crystals	(5)
43	3.20	1	2.55		64	20	51	65	4	blue needlelike crystals	(5)
44	3.20	1	2.65		64	20	53	63	4	blue needlelike crystals	(5)
45	3.20	1	2.75		64	20	55	61	3	blue needlelike crystals	(5)
46	3.20	1	2.85		64	20	57	59	4	blue needlelike crystals	(5)
47	3.20	1	2.95		64	20	59	57	4	blue needlelike crystals	(5)
48	3.20	1	3.05		64	20	61	55	2	clear solution	-

^a 1.0 M $\text{CuCl}_2 \cdot 2\text{H}_2\text{O}$ ^b 1.0 M $\text{H}_2\text{O}_3\text{P}-\text{C}_6\text{H}_4-\text{SO}_3\text{H} \cdot 2\text{H}_2\text{O}$ ^c 1.0 M NaOHreactor fill volume: 200 μL Temperature profile: heat-up phase = 1.1 $^\circ\text{C}/\text{min}$ to 150 $^\circ\text{C}$ residence time = 48 h at 150 $^\circ\text{C}$ cool down phase = 10.8 $^\circ\text{C}/\text{h}$ to room temperature(3) : $\text{NaCu}(\text{O}_3\text{P}-\text{C}_6\text{H}_4-\text{SO}_3)(\text{H}_2\text{O})_3$ (4) : $\text{Cu}_2[(\text{O}_3\text{P}-\text{C}_6\text{H}_4-\text{SO}_3)(\text{OH})(\text{H}_2\text{O})]$ (5) : $\text{Cu}_3[(\text{O}_3\text{P}-\text{C}_6\text{H}_4-\text{SO}_3)_2(\text{H}_2\text{O})_2]$

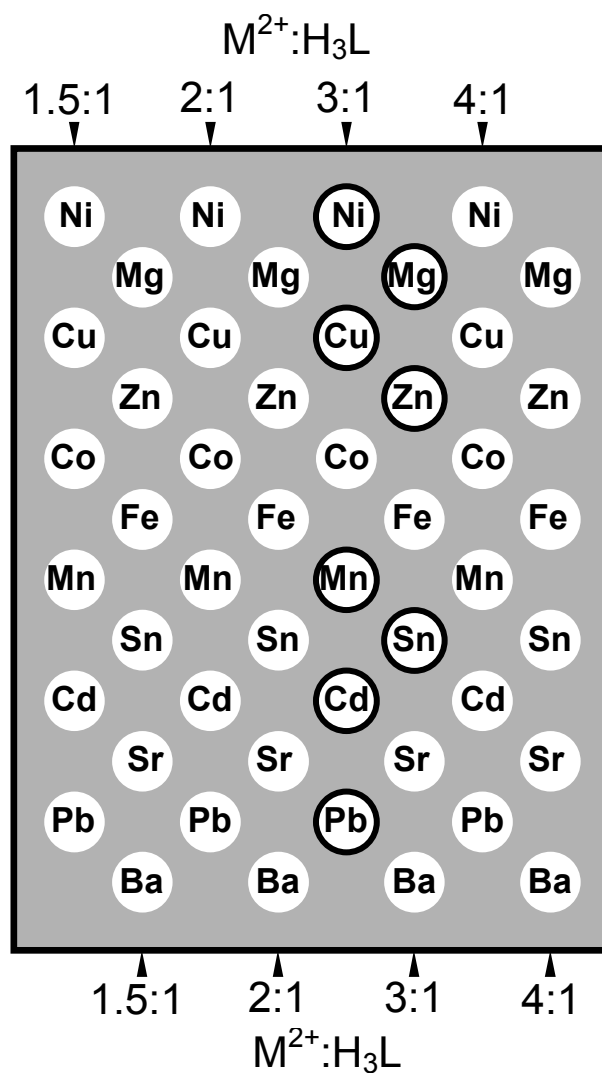


Figure S1. Metal-screening set-up containing twelve M^{2+} ions and four different metal-to-linker ratios (molar ratio $M^{2+}:H_3L:NaOH:H_2O = 1.5-4:1:3:556$) resulting in 48 individual reactions (see Table S1 for compositional and process parameters). Products were analyzed with automated powder X-ray diffraction. Bold circles indicate crystalline PXRD products. Circles without bold lines signify X-ray amorphous products.

Table S5. Hydrogen bond distances (pm) for compound $\text{Cu}_3[(\text{O}_3\text{P}-\text{C}_6\text{H}_4-\text{SO}_3)_2(\text{H}_2\text{O})_2]$ (**5**).

D-H...A	Bond distances (pm)			Bond angle (deg)
	D-H	H...A	D...A	D-H...A
O7-H1O7...O4B	83.9(6)	191.2(6)	272.2(8)	161.7(4)
O7-H2O7...O5	84.0(4)	232.1(5)	314.0(6)	164.8(4)
O8-H1O8...O4B	84.0(4)	208.1(5)	291.6(6)	172.8(4)
O8-H2O8...O5	83.9(6)	193.2(6)	276.0(8)	168.8(4)

Table S6. Selected bond distances (pm) for compounds **1**, **2**, **4** and **5**.

1: Pb₂[(O₃P-C₆H₄-SO₃)(OH)]					
P1 – O1	151.3(12)	P1 – C1	183.7(19)	Pb1 – O6	278.2(15)
P1 – O2	151.4(12)	S1 – C4	174.3(20)	Pb1 – O7	272.3(12)
P1 – O3	153.2(12)	Pb1 – O1	231.7(14)	Pb2 – O2	237.8(11)
S1 – O4	146.1(17)	Pb1 – O2	285.8(10)	Pb2 – O4	287.5(14)
S1 – O5	145.4(14)	Pb1 – O3	245.0(12)	Pb2 – O5	273.1(14)
S1 – O6	144.5(16)	Pb1 – O4	282.2(15)	Pb2 – O7	232.3(12)
2: Cu_{1.5}[(O₃P-C₆H₄-SO₃)(H₂O)]					
S1 – O1	145.8(4)	P1 – O6	151.1(4)	Cu1 – O7	201.0(4)
S1 – O2	145.2(3)	P1 – C4	180.6(4)	Cu2 – O1	194.8(3)
S1 – O3	148.4(3)	S1 – C1	178.1(4)	Cu2 – O3	242.8(3)
P1 – O4	155.8(3)	Cu1 – O2	240.8(3)	Cu2 – O4	194.8(3)
P1 – O5	152.2(3)	Cu1 – O5	194.5(3)	Cu2 – O6	194.1(3)
4: Cu₂[(O₃P-C₆H₄-SO₃)(OH)(H₂O)]					
P1 – O4	153.3(3)	P1 – C4	181.4(5)	Cu2 – O2	201.9(4)
P1 – O5	152.1(3)	S1 – C1	176.3(5)	Cu2 – O4	233.6(3)
P1 – O6	152.9(3)	Cu1 – O1	248.6(4)	Cu2 – O7	199.0(3)
S1 – O1	146.5(3)	Cu1 – O3	252.6(4)	Cu2 – O5	192.7(4)
S1 – O2	146.3(3)	Cu1 – O6	196.5(2)	Cu2 – O6	240.2(3)
S1 – O3	146.3(4)	Cu1 – O7	196.8(2)	Cu2 – O8	197.6(4)
5: Cu₃[(O₃P-C₆H₄-SO₃)₂(H₂O)₂]					
P1B – O1B	151.4(6)	S1 – O5	144.6(5)	Cu2 – O1B	287.5(5)
P1B – O2B	152.1(5)	S1 – O6	146.2(5)	Cu2 – O2B	191.3(3)
P1B – O3B	156.6(5)	P1B – C1B	179.3(5)	Cu2 – O3B	199.4(5)
P1 – O1	156.4(5)	P1 – C1	179.9(5)	Cu2 – O4	200.1(5)
P1 – O2	152.2(5)	S1B – C4B	175.8(5)	Cu2 – O5B	224.4(5)
P1 – O3	152.2(5)	S1 – C4	178.1(6)	Cu2 – O8	196.1(4)
S1B – O4B	146.5(5)	Cu1 – O1B	190.0(4)	Cu3 – O1	198.4(5)
S1B – O5B	144.6(5)	Cu1 – O2	191.0(3)	Cu3 – O3	190.4(4)
S1B – O6B	148.0(6)	Cu1 – O3B	199.7(6)	Cu3 – O6	220.7(5)
S1 – O4	148.3(5)	Cu1 – O1	200.8(5)	Cu3 – O7	195.9(4)

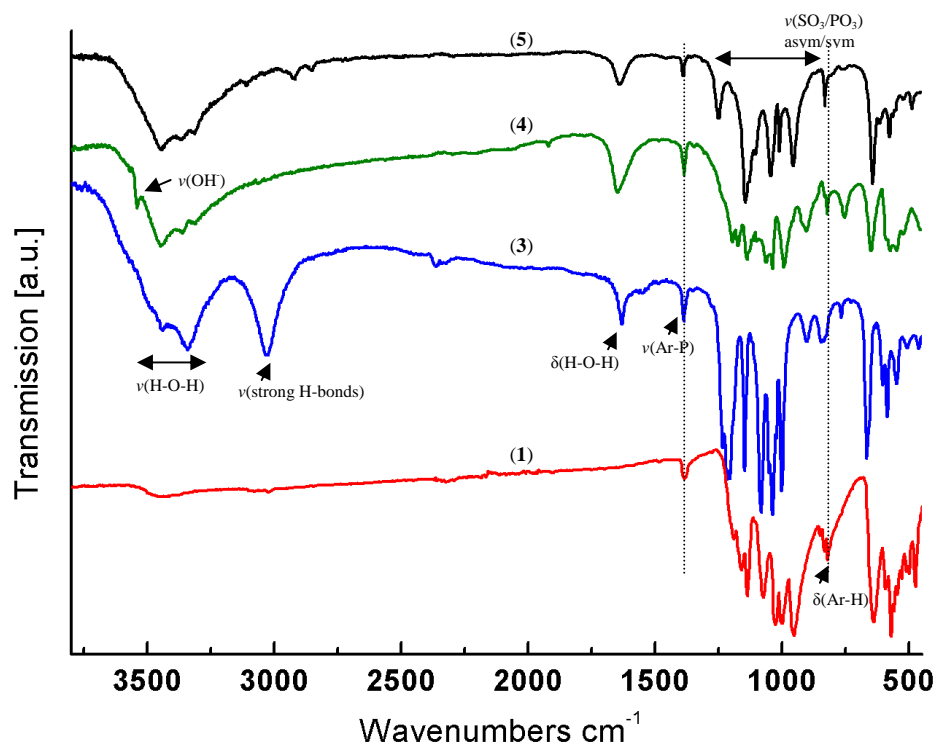


Figure S2. IR spectra of $\text{Pb}_2[(\text{O}_3\text{P}-\text{C}_6\text{H}_4-\text{SO}_3)(\text{OH})]$ (1), $\text{NaCu}(\text{O}_3\text{P}-\text{C}_6\text{H}_4-\text{SO}_3)(\text{H}_2\text{O})_3$ (3), $\text{Cu}_2[(\text{O}_3\text{P}-\text{C}_6\text{H}_4-\text{SO}_3)(\text{OH})(\text{H}_2\text{O})]$ (4) and $\text{Cu}_3[(\text{O}_3\text{P}-\text{C}_6\text{H}_4-\text{SO}_3)_2(\text{H}_2\text{O})_2]$ (5). (ν = stretching, δ = deformation)

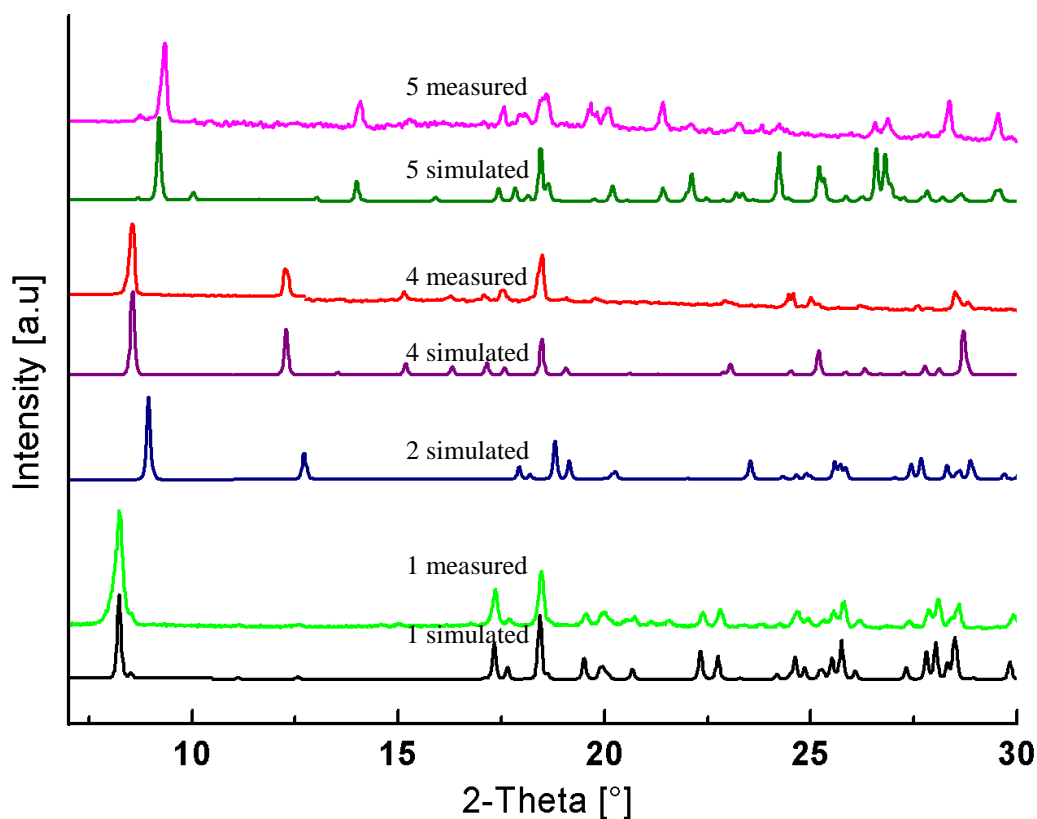
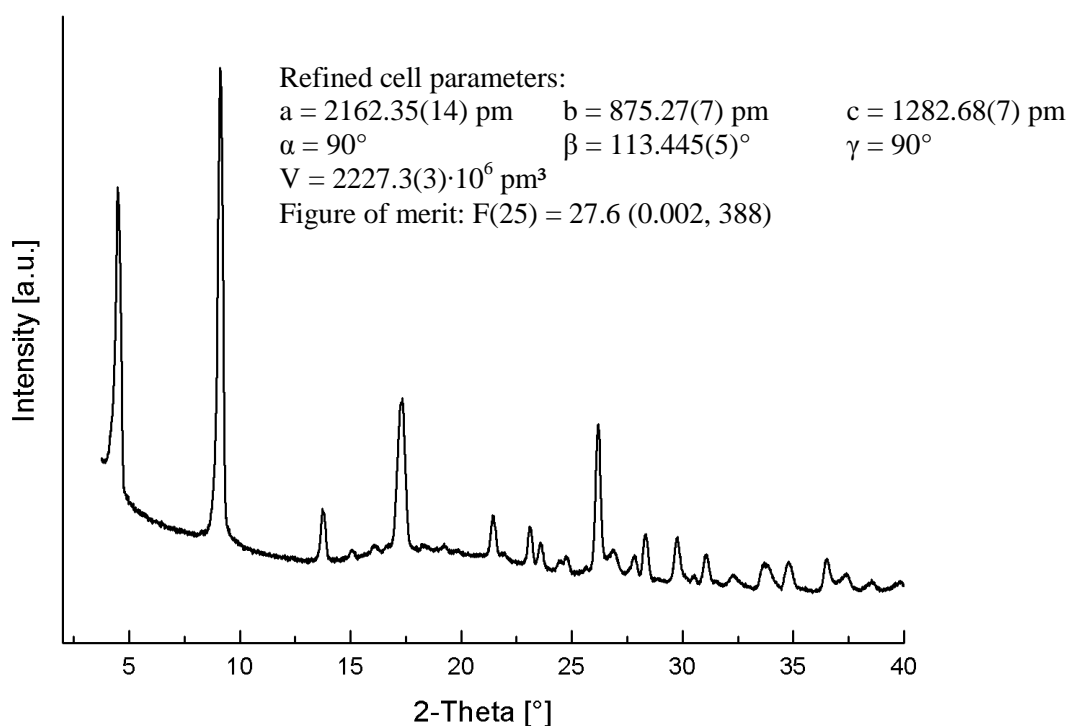


Figure S3. Measured and simulated powder XRD patterns for compounds $\text{Pb}_2[(\text{O}_3\text{P}-\text{C}_6\text{H}_4-\text{SO}_3)(\text{OH})]$ (1), $\text{Cu}_{1.5}(\text{O}_3\text{P}-\text{C}_6\text{H}_4-\text{SO}_3)(\text{H}_2\text{O})$ (2), $\text{Cu}_2[(\text{O}_3\text{P}-\text{C}_6\text{H}_4-\text{SO}_3)(\text{OH})(\text{H}_2\text{O})]$ (4) and $\text{Cu}_3[(\text{O}_3\text{P}-\text{C}_6\text{H}_4-\text{SO}_3)_2(\text{H}_2\text{O})_2]$ (5) ($\text{Cu K}\alpha_1$ radiation).

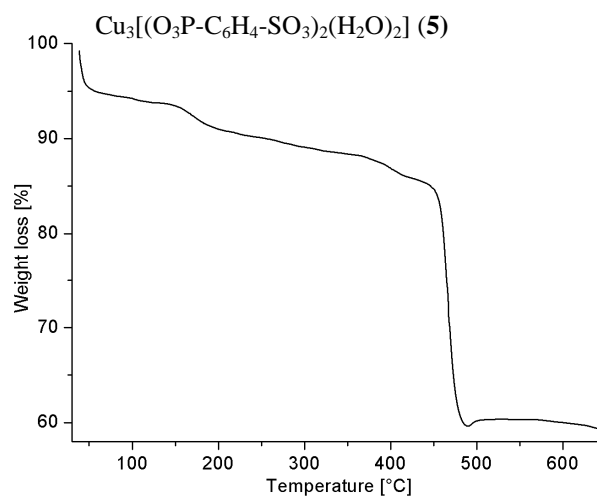
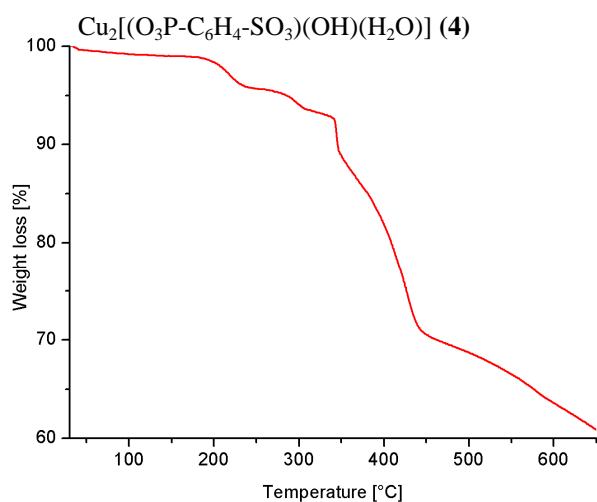
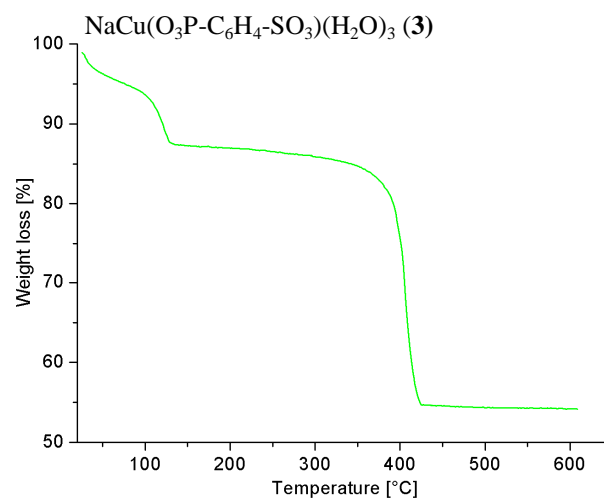
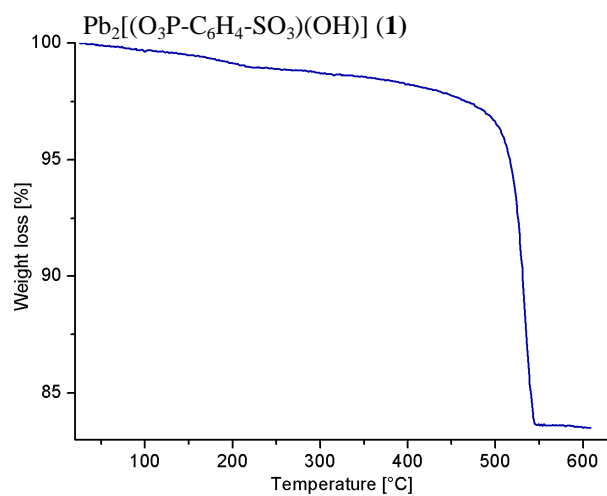
Figure S4. Powder X-ray diffraction pattern of $\text{NaCu}(\text{O}_3\text{P}-\text{C}_6\text{H}_4-\text{SO}_3)(\text{H}_2\text{O})_3$ (**3**).Table S7: Results of the cell parameter refinement of the PXRD pattern of title compound **3**.

Wavelength : 1.540598 Number of accepted peaks : 25
 2Theta window : 0.050 2Theta zeropoint : 0.0000 (refineable)
 Symmetry : Monoclinic_P

Initial cell parameters :				Refined cell parameters :					
Cell_A	: 2162.18 pm	Cell_A	: 2162.35(14) pm						
Cell_B	: 875.28 pm	Cell_B	: 875.27(7) pm						
Cell_C	: 1282.62 pm	Cell_C	: 1282.68(7) pm						
Cell_Beta	: 113.445 °	Cell_Beta	: 113.445(5) pm						
				Cell_Volume: 2227.2(3) · 10 ⁶ pm ³					
Number of single indexed lines : 23				Number of unindexed lines : 0					
2Theta zeropoint : 0.0018(15)				Final 2Theta window : 0.0200					
N	2Th[obs]	H	K	L	2Th[calc]	obs-calc	Int.	d[obs]	d[calc]
1	4.451	1	0	0	4.451	0.0007	79.6	19.8353	19.8384
2	9.082	-2	0	1	9.084	-0.0016	100	9.7293	9.7277
3	13.766	2	0	1	13.765	0.0007	23.3	6.4277	6.428
4	15.044	0	0	2	15.045	-0.0009	16.7	5.8843	5.884
5	16.067	-3	1	1	16.067	-0.0005	17.8	5.5119	5.5118
6	17.326	1	0	2	17.328	-0.0013	44.4	5.114	5.1136
7	21.444	-5	0	2	21.442	0.0021	22.3	4.1404	4.1408
8	23.136	-2	1	3	23.133	0.0031	20.7	3.8412	3.8417
9	23.584	-1	1	3	23.58	0.0047	18.2	3.7693	3.77
10	24.745	-5	0	3	24.747	-0.0015	15.2	3.595	3.5948
11	26.18	-4	2	1	26.181	-0.0016	39.6	3.4012	3.401
12	26.915	-6	1	1	26.918	-0.0028	16.9	3.3099	3.3096
13	27.836	-3	0	4	27.836	0.0005	15.5	3.2024	3.2025
14	28.318	5	1	1	28.317	0.0007	19.2	3.149	3.1491
15	31.072	-7	1	1	31.074	-0.0014	15.9	2.8759	2.8758
16	32.307	-6	2	1	32.308	-0.0015	12.1	2.7688	2.7687
17	33.761	-1	3	2	33.759	0.0016	13.9	2.6528	2.6529
18	34.792	-2	2	4	34.792	-0.0006	14.8	2.5765	2.5764
19	36.499	-3	1	5	36.505	-0.0053	15.1	2.4598	2.4594
20	37.415	-9	0	2	37.412	0.0029	12.4	2.4017	2.4018
21	38.582	1	2	4	38.58	0.0014	10.8	2.3317	2.3317
22	39.81	1	3	3	39.797	0.0126	10.8	2.2625	2.2632
		-9	1	1	39.816	-0.0062			2.2622
23	40.863	-4	2	5	40.847	0.0158	11.2	2.2066	2.2074
		5	3	1	40.851	0.0117			2.2072
24	44.471	-7	0	6	44.469	0.002	12.1	2.0356	2.0357
25	47.282	-4	2	6	47.283	-0.001	10	1.9209	1.9209

Average delta(2Theta) = 0.002
 Maximum delta(2Theta) = 0.012 (peak 23) = 5.0 * average
 Figure of Merit F(25) = 27.6 (0.002, 388)
 Durbin-Watson serial correlation = 2.388 (not significant)
 Sqrt[sum(w * delta(q)^2) / (Nobs - Nvar)] = 1.8958e-005

Figure S5. Results of thermogravimetric investigations of compounds $\text{Pb}_2[(\text{O}_3\text{P}-\text{C}_6\text{H}_4-\text{SO}_3)(\text{OH})]$ (**1**), $\text{NaCu}(\text{O}_3\text{P}-\text{C}_6\text{H}_4-\text{SO}_3)(\text{H}_2\text{O})_3$ (**3**), $\text{Cu}_2[(\text{O}_3\text{P}-\text{C}_6\text{H}_4-\text{SO}_3)(\text{OH})(\text{H}_2\text{O})]$ (**4**) and $\text{Cu}_3[(\text{O}_3\text{P}-\text{C}_6\text{H}_4-\text{SO}_3)_2(\text{H}_2\text{O})_2]$ (**5**) (all measured under nitrogen atmosphere).



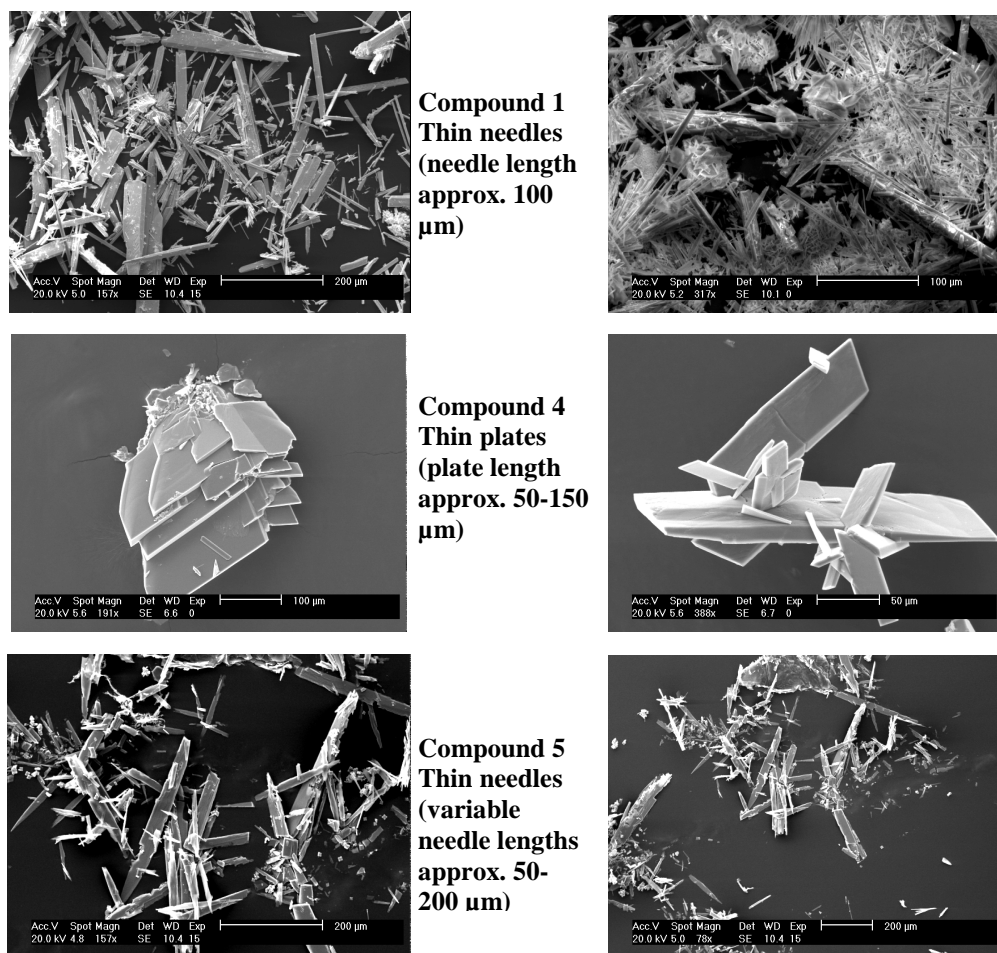


Figure S6. SEM micrographs of the single crystals of compound $\text{Pb}_2[(\text{O}_3\text{P}-\text{C}_6\text{H}_4-\text{SO}_3)(\text{OH})]$ (**1**), $\text{Cu}_2[(\text{O}_3\text{P}-\text{C}_6\text{H}_4-\text{SO}_3)(\text{OH})(\text{H}_2\text{O})]$ (**4**) and $\text{Cu}_3[(\text{O}_3\text{P}-\text{C}_6\text{H}_4-\text{SO}_3)_2(\text{H}_2\text{O})_2]$ (**5**).

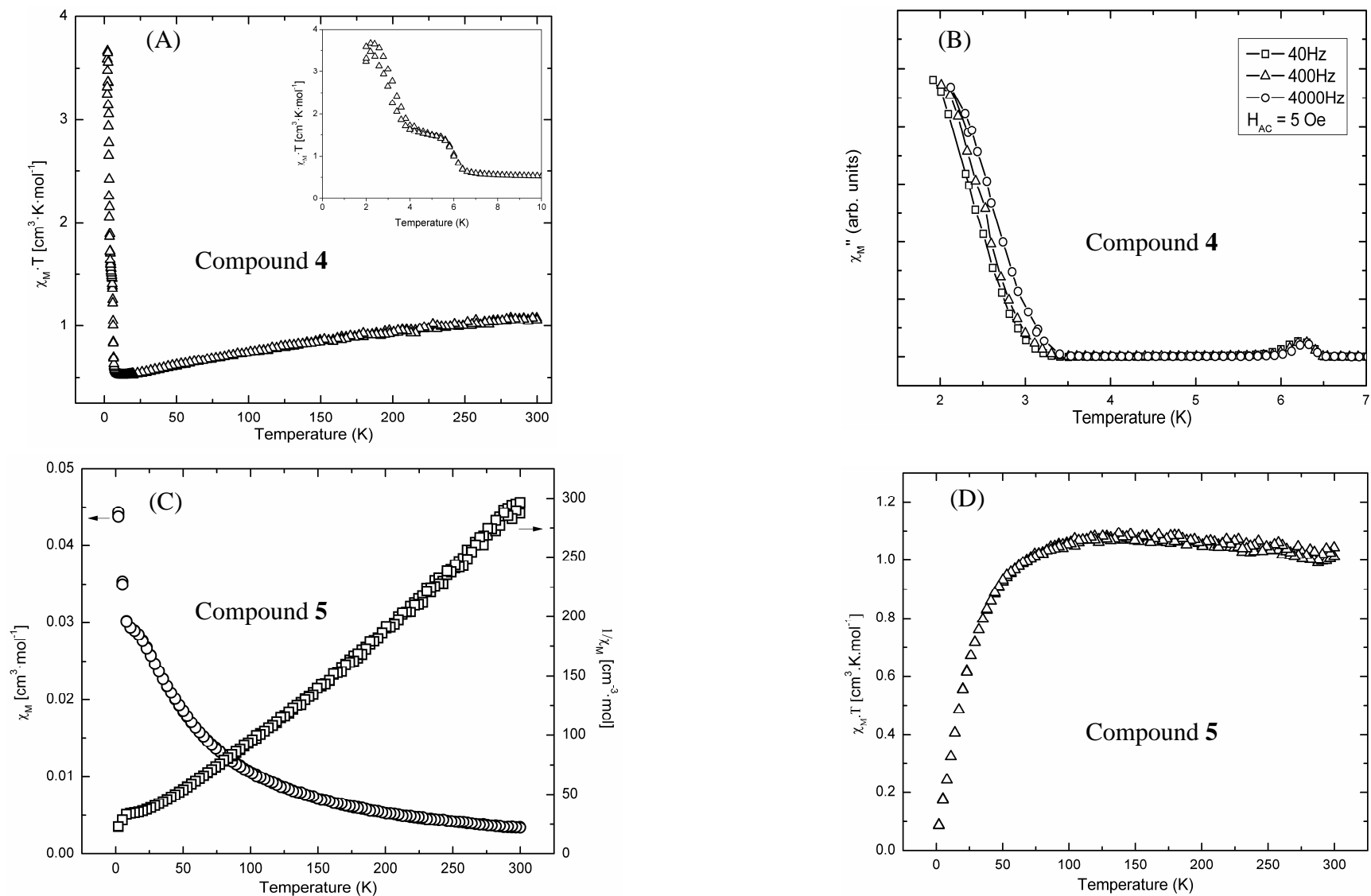


Figure S7. Results of the magnetic susceptibility investigations of $\text{Cu}_2[(\text{O}_3\text{P}-\text{C}_6\text{H}_4-\text{SO}_3)(\text{OH})(\text{H}_2\text{O})]$ (**4**) with plots of $\chi_M \cdot T$ (dc-field, ZFC, at $H = 1 \text{ kOe}$) (A) and frequency dependent out-of-phase χ_M'' (ac-field, $H = 5 \text{ Oe}$) (B) as function of temperature. For $\text{Cu}_3[(\text{O}_3\text{P}-\text{C}_6\text{H}_4-\text{SO}_3)_2(\text{H}_2\text{O})_2]$ (**5**), the plots $\chi_M + \text{reciprocal } \chi_M$ (C) and $\chi_M \cdot T$ (D) (dc-field, ZFC, at $H = 10 \text{ kOe}$) as function of temperature are shown.

Appendix 2

Supporting Information

P. Maniam, N. Stock, *Acta Cryst.* **2011**, C67, m73-m76.

A three-dimensional tin(II) phosphonatobenzenesulfonate with Sn₄O₁₂ clusters

Palanikumar Maniam and Norbert Stock*

Institute of Inorganic Chemistry,
Christian-Albrechts-University Kiel, Max-Eyth-Straße 2, D-24118 Kiel,

* Prof. Dr. Norbert Stock, Tel.: +49-431-880-1675, Fax: +49-431-880-1775.

e-mail: stock@ac.uni-kiel.de

A three-dimensional tin(II) phosphonatobenzenesulfonate with (Sn₄O₁₂) clusters

Palanikumar Maniam and Norbert Stock*

Related literature

For related literature, see: Adair *et al.* (1998); Adani *et al.* (1998); Alberti & Casciola (2003); Alberti *et al.* (1978, 1992, 1996); Clearfield (1998); Clearfield & Stynes (1964); Du *et al.* (2006); Holt *et al.* (1987); Kawamura *et al.* (1999); Lansky *et al.* (2001); Levi (1924); Libowitzky (1999); Maniam *et al.* (2010); McDonald & Eriks (1980); Montoneri & Ricca (1991*a*, 1991*b*); Montoneri *et al.* (2007); Poojary *et al.* (1996*a*, 1996*b*); Ramaswamy *et al.* (2008); Sonnauer & Stock (2008*b*); Sonnauer *et al.* (2007, 2008*a*, 2009); Stein *et al.* (1996); Stock (2010); Stock *et al.* (2000); Yang & Clearfield (1987); Zhang *et al.* (2008).

Poly[μ -hydroxido-(μ 7-4-phosphonatobenzenesulfonato)ditin(II)]

Crystal data

C ₆ H ₅ O ₇ PSSn ₂	Z = 2
<i>M_r</i> = 489.56	<i>F</i> (000) = 456
Triclinic, <i>P</i> $\bar{1}$	<i>D_x</i> = 2.847 Mg m ⁻³
Hall symbol: -P 1	Mo <i>K</i> α radiation, λ = 0.71073 Å
<i>a</i> = 7.0045 (14) Å	Cell parameters from 1556 reflections
<i>b</i> = 8.487 (2) Å	θ = 1.9–28.2°
<i>c</i> = 10.0570 (17) Å	μ = 4.72 mm ⁻¹
α = 81.10 (2)°	<i>T</i> = 293 K
β = 86.17 (2)°	Plate, Colourless
γ = 75.25 (3)°	0.14 × 0.10 × 0.07 mm
<i>V</i> = 571.0 (2) Å ³	

Data collection

STOE IPDS-1 diffractometer	2550 independent reflections
Radiation source: fine-focus sealed tube graphite	2146 reflections with <i>I</i> > 2σ(<i>I</i>)
Phi scans	<i>R</i> _{int} = 0.048
Absorption correction: Numerical STOE <i>X-RED</i> rev 1.19 and <i>X-SHAPE</i> rev 1.06	θ_{\max} = 28.1°, θ_{\min} = 2.5°
<i>T</i> _{min} = 0.380, <i>T</i> _{max} = 0.581	<i>h</i> = -9→9
6691 measured reflections	<i>k</i> = -11→11
	<i>l</i> = -13→13

Refinement

Refinement on <i>F</i> ²	Secondary atom site location: Difference Fourier map
Least-squares matrix: Full	Hydrogen site location: Inferred from neighbouring sites
$R[F^2 > 2\sigma(F^2)] = 0.025$	H-atom parameters constrained
$wR(F^2) = 0.066$	$w = 1/[\sigma^2(F_o^2) + (0.0397P)^2]$
	where $P = (F_o^2 + 2F_c^2)/3$

$S = 1.02$	$(\Delta/\sigma)_{\max} = 0.001$
2550 reflections	$\Delta\rho_{\max} = 0.79 \text{ e } \text{\AA}^{-3}$
155 parameters	$\Delta\rho_{\min} = -1.08 \text{ e } \text{\AA}^{-3}$
0 restraints	Extinction correction: <i>SHELXL</i> , $\text{Fc}^* = k\text{Fc}[1 + 0.001x\text{Fc}^2\lambda^3/\sin(2\theta)]^{-1/4}$
Primary atom site location: Structure-invariant direct methods	Extinction coefficient: 0.0121 (9)

Special details

Geometry. All e.s.d.'s (except the e.s.d. in the dihedral angle between two l.s. planes) are estimated using the full covariance matrix. The cell e.s.d.'s are taken into account individually in the estimation of e.s.d.'s in distances, angles and torsion angles; correlations between e.s.d.'s in cell parameters are only used when they are defined by crystal symmetry. An approximate (isotropic) treatment of cell e.s.d.'s is used for estimating e.s.d.'s involving l.s. planes.

Refinement. Refinement of F^2 against ALL reflections. The weighted R -factor wR and goodness of fit S are based on F^2 , conventional R -factors R are based on F , with F set to zero for negative F^2 . The threshold expression of $F^2 > \sigma(F^2)$ is used only for calculating R -factors(gt) *etc.* and is not relevant to the choice of reflections for refinement. R -factors based on F^2 are statistically about twice as large as those based on F , and R -factors based on ALL data will be even larger.

Fractional atomic coordinates and isotropic or equivalent isotropic displacement parameters (\AA^2)

	x	y	z	$U_{\text{iso}}^*/U_{\text{eq}}$
Sn1	-0.18614 (4)	0.83666 (3)	0.57934 (2)	0.01832 (10)
Sn2	-0.35359 (4)	0.61742 (3)	0.35282 (2)	0.01956 (10)
P1	0.12971 (14)	0.57551 (11)	0.34654 (8)	0.01184 (19)
S1	0.37171 (15)	0.93625 (12)	-0.21627 (8)	0.0192 (2)
O1	-0.0710 (4)	0.6751 (3)	0.3976 (2)	0.0150 (5)
O2	0.1080 (4)	0.4085 (3)	0.3189 (2)	0.0178 (5)
O3	0.2898 (4)	0.5661 (3)	0.4465 (2)	0.0173 (5)
O4	0.2573 (5)	0.9067 (4)	-0.3215 (3)	0.0323 (7)
O5	0.5823 (5)	0.8540 (4)	-0.2319 (3)	0.0270 (7)
O6	0.3415 (5)	1.1096 (4)	-0.2013 (3)	0.0290 (7)
O7	-0.4330 (4)	0.7917 (3)	0.4877 (2)	0.0164 (5)
H7	-0.5508	0.8395	0.5044	0.025*
C1	0.1893 (6)	0.6797 (4)	0.1859 (3)	0.0158 (7)
C2	0.2372 (10)	0.5963 (6)	0.0754 (4)	0.0482 (16)
H2	0.2351	0.4861	0.0837	0.058*
C3	0.2879 (12)	0.6763 (6)	-0.0469 (5)	0.057 (2)
H3	0.3180	0.6203	-0.1211	0.069*
C4	0.2942 (6)	0.8397 (5)	-0.0594 (3)	0.0213 (8)
C5	0.2430 (7)	0.9258 (5)	0.0479 (4)	0.0253 (9)
H5	0.2455	1.0359	0.0389	0.030*
C6	0.1875 (7)	0.8459 (5)	0.1701 (4)	0.0260 (9)
H6	0.1487	0.9044	0.2423	0.031*

Atomic displacement parameters (\AA^2)

	U^{11}	U^{22}	U^{33}	U^{12}	U^{13}	U^{23}
Sn1	0.02088 (18)	0.01538 (14)	0.01944 (15)	-0.00646 (11)	-0.00125 (10)	-0.00118 (9)
Sn2	0.01846 (18)	0.02484 (16)	0.01551 (14)	-0.00269 (12)	-0.00038 (9)	-0.00787 (10)
P1	0.0122 (5)	0.0145 (4)	0.0075 (4)	-0.0030 (4)	0.0025 (3)	0.0007 (3)
S1	0.0209 (5)	0.0235 (5)	0.0096 (4)	-0.0031 (4)	0.0045 (3)	0.0022 (3)
O1	0.0129 (14)	0.0192 (12)	0.0121 (11)	-0.0036 (11)	0.0035 (9)	-0.0019 (9)
O2	0.0247 (17)	0.0140 (12)	0.0138 (11)	-0.0049 (11)	-0.0020 (10)	0.0012 (9)
O3	0.0147 (15)	0.0226 (13)	0.0135 (11)	-0.0051 (11)	-0.0016 (9)	0.0020 (10)
O4	0.032 (2)	0.050 (2)	0.0148 (13)	-0.0133 (16)	-0.0001 (11)	0.0001 (13)
O5	0.0213 (18)	0.0370 (17)	0.0170 (13)	0.0009 (14)	0.0059 (11)	-0.0030 (12)
O6	0.039 (2)	0.0227 (15)	0.0184 (13)	-0.0017 (14)	0.0080 (12)	0.0043 (11)
O7	0.0104 (15)	0.0216 (13)	0.0161 (11)	-0.0012 (11)	0.0031 (9)	-0.0049 (9)
C1	0.017 (2)	0.0190 (17)	0.0106 (14)	-0.0047 (15)	0.0027 (12)	0.0000 (13)
C2	0.103 (5)	0.022 (2)	0.021 (2)	-0.023 (3)	0.026 (2)	-0.0072 (17)
C3	0.126 (6)	0.027 (2)	0.020 (2)	-0.025 (3)	0.032 (3)	-0.0093 (18)
C4	0.024 (2)	0.0267 (19)	0.0105 (15)	-0.0062 (17)	0.0060 (14)	0.0015 (14)
C5	0.041 (3)	0.0223 (19)	0.0143 (17)	-0.0131 (19)	0.0088 (16)	-0.0033 (14)
C6	0.046 (3)	0.0216 (19)	0.0125 (16)	-0.0136 (19)	0.0103 (16)	-0.0051 (14)

Geometric parameters (\AA , $^\circ$)

Sn1—O1	2.427 (3)	S1—C4	1.780 (3)
Sn1—O2 ⁱ	2.124 (2)	O2—Sn1 ⁱ	2.124 (2)
Sn1—O5 ⁱⁱ	2.410 (3)	O3—Sn2 ⁱ	2.344 (2)
Sn1—O7	2.155 (3)	O5—Sn1 ^v	2.410 (3)
Sn2—O1	2.246 (3)	O7—H7	0.8400
Sn2—O3 ⁱ	2.344 (2)	C1—C2	1.386 (5)
Sn2—O3 ⁱⁱⁱ	2.726 (3)	C1—C6	1.391 (5)
Sn2—O6 ^{iv}	2.586 (3)	C2—C3	1.381 (6)
Sn2—O7	2.108 (3)	C2—H2	0.9300
P1—O1	1.545 (3)	C3—C4	1.384 (6)
P1—O2	1.532 (3)	C3—H3	0.9300
P1—O3	1.535 (3)	C4—C5	1.373 (6)
P1—C1	1.795 (3)	C5—C6	1.391 (5)
S1—O4	1.460 (4)	C5—H5	0.9300
S1—O5	1.472 (3)	C6—H6	0.9300
S1—O6	1.462 (4)		
O2 ⁱ —Sn1—O7	91.85 (10)	P1—O1—Sn1	136.42 (15)
O2 ⁱ —Sn1—O5 ⁱⁱ	78.75 (11)	Sn2—O1—Sn1	99.92 (10)
O7—Sn1—O5 ⁱⁱ	80.68 (10)	P1—O2—Sn1 ⁱ	135.22 (15)
O2 ⁱ —Sn1—O1	76.93 (9)	P1—O3—Sn2 ⁱ	126.01 (14)
O7—Sn1—O1	69.83 (10)	S1—O5—Sn1 ^v	133.80 (16)
O5 ⁱⁱ —Sn1—O1	140.72 (10)	Sn2—O7—Sn1	114.23 (12)
O1—Sn2—O3 ⁱ	83.17 (9)	Sn2—O7—H7	122.9
O3 ⁱ —Sn2—O3 ⁱⁱⁱ	74.26 (8)	Sn1—O7—H7	122.9
O3 ⁱⁱⁱ —Sn2—O6 ^{iv}	119.16 (10)	C2—C1—C6	118.8 (3)
O6 ^{iv} —Sn2—O1	73.59 (10)	C2—C1—P1	120.6 (3)
O7—Sn2—O1	74.32 (9)	C6—C1—P1	120.5 (3)

O6 ^{iv} —Sn2—O3 ⁱ	152.18 (9)	C3—C2—C1	120.2 (4)
O1—Sn2—O3 ⁱⁱⁱ	147.71 (10)	C3—C2—H2	119.9
O2—P1—O3	114.80 (16)	C1—C2—H2	119.9
O2—P1—O1	109.26 (16)	C2—C3—C4	120.2 (4)
O3—P1—O1	109.44 (15)	C2—C3—H3	119.9
O2—P1—C1	105.37 (16)	C4—C3—H3	119.9
O3—P1—C1	109.46 (16)	C5—C4—C3	120.6 (3)
O1—P1—C1	108.27 (16)	C5—C4—S1	120.4 (3)
O4—S1—O6	114.6 (2)	C3—C4—S1	119.1 (3)
O4—S1—O5	110.96 (19)	C4—C5—C6	119.1 (4)
O6—S1—O5	112.1 (2)	C4—C5—H5	120.5
O4—S1—C4	107.95 (19)	C6—C5—H5	120.5
O6—S1—C4	105.61 (18)	C1—C6—C5	121.0 (4)
O5—S1—C4	104.99 (19)	C1—C6—H6	119.5
P1—O1—Sn2	120.56 (15)	C5—C6—H6	119.5
O2—P1—O1—Sn2	-22.08 (19)	O3 ⁱ —Sn2—O7—Sn1	73.83 (12)
O3—P1—O1—Sn2	-148.56 (14)	O2 ⁱ —Sn1—O7—Sn2	-64.68 (13)
C1—P1—O1—Sn2	92.19 (18)	O5 ⁱⁱ —Sn1—O7—Sn2	-142.96 (13)
O2—P1—O1—Sn1	133.51 (19)	O1—Sn1—O7—Sn2	10.67 (10)
O3—P1—O1—Sn1	7.0 (2)	O2—P1—C1—C2	-10.4 (5)
C1—P1—O1—Sn1	-112.2 (2)	O3—P1—C1—C2	113.5 (4)
O7—Sn2—O1—P1	172.42 (17)	O1—P1—C1—C2	-127.2 (4)
O3 ⁱ —Sn2—O1—P1	88.70 (16)	O2—P1—C1—C6	169.4 (4)
O7—Sn2—O1—Sn1	9.22 (9)	O3—P1—C1—C6	-66.7 (4)
O3 ⁱ —Sn2—O1—Sn1	-74.49 (10)	O1—P1—C1—C6	52.6 (4)
O2 ⁱ —Sn1—O1—P1	-71.2 (2)	C6—C1—C2—C3	1.9 (9)
O7—Sn1—O1—P1	-168.1 (2)	P1—C1—C2—C3	-178.3 (5)
O5 ⁱⁱ —Sn1—O1—P1	-124.3 (2)	C1—C2—C3—C4	1.0 (11)
O2 ⁱ —Sn1—O1—Sn2	87.68 (11)	C2—C3—C4—C5	-2.5 (10)
O7—Sn1—O1—Sn2	-9.25 (9)	C2—C3—C4—S1	177.0 (5)
O5 ⁱⁱ —Sn1—O1—Sn2	34.56 (19)	O4—S1—C4—C5	-129.6 (4)
O3—P1—O2—Sn1 ⁱ	20.6 (3)	O6—S1—C4—C5	-6.6 (4)
O1—P1—O2—Sn1 ⁱ	-102.7 (2)	O5—S1—C4—C5	112.0 (4)
C1—P1—O2—Sn1 ⁱ	141.1 (2)	O4—S1—C4—C3	51.0 (5)
O2—P1—O3—Sn2 ⁱ	-42.0 (2)	O6—S1—C4—C3	174.0 (5)
O1—P1—O3—Sn2 ⁱ	81.3 (2)	O5—S1—C4—C3	-67.4 (5)
C1—P1—O3—Sn2 ⁱ	-160.22 (18)	C3—C4—C5—C6	0.9 (8)
O4—S1—O5—Sn1 ^v	46.6 (3)	S1—C4—C5—C6	-178.5 (4)
O6—S1—O5—Sn1 ^v	-82.9 (3)	C2—C1—C6—C5	-3.5 (7)
C4—S1—O5—Sn1 ^v	163.0 (2)	P1—C1—C6—C5	176.7 (4)
O1—Sn2—O7—Sn1	-11.25 (10)	C4—C5—C6—C1	2.0 (7)

Symmetry codes: (i) $-x, -y+1, -z+1$; (ii) $x-1, y, z+1$; (iii) $x-1, y, z$; (iv) $-x, -y+2, -z$; (v) $x+1, y, z-1$.

Hydrogen-bond geometry (Å, °)

<i>D</i> —H \cdots <i>A</i>	<i>D</i> —H	H \cdots <i>A</i>	<i>D</i> \cdots <i>A</i>	<i>D</i> —H \cdots <i>A</i>
O7—H7 \cdots O4 ⁱⁱ	0.84	2.19	2.878 (4)	139

Symmetry code: (ii) $x-1, y, z+1$.

Appendix 3

Supporting Information

P. Maniam, N. Stock, *Z. Anorg. Allg. Chem.* **2011**, DOI: 10.1002/zaac.201100202.

Synthesis and characterization of the mixed-linker copper(II) coordination polymer [Cu(HO₃PC₆H₄SO₃)(C₁₀N₂H₈)]·H₂O

Palanikumar Maniam and Norbert Stock*

Institute of Inorganic Chemistry,
Christian-Albrechts-University Kiel, Max-Eyth-Straße 2, D-24118 Kiel,

* Prof. Dr. Norbert Stock, Tel.: +49-431-880-1675, Fax: +49-431-880-1775.

e-mail: stock@ac.uni-kiel.de

- (1) Table S1-S2: Details of each high-throughput experiment
- (2) Table S3. Selected bond lengths / Å and angles / ° for **1** and **1-h**.
- (3) Figure S1. XRPD patterns of the dehydrated compound **1-h** measured at 290 °C, **1-h** upon cooling to 25 °C, hydrated compound **1** at 25 °C as well as the simulated XRPD pattern of **1**.
- (4) Figure S2: IR spectra of compound **1** and **1-h**.
- (5) Figure S3: TG / DTA analysis of compound **1**.

Table S1: Exact amounts of reactants for the HT solvent screening of the system
 $\text{Cu}(\text{NO}_3)_2 \cdot 3\text{H}_2\text{O}/\text{H}_3\text{L}/4,4'$ -bipy/solvent at 130 °C.

Nr.	molar ratios			$\text{Cu}(\text{NO}_3)_2 \cdot 3\text{H}_2\text{O}^{\text{a}}$ μL	$\text{H}_3\text{L}^{\text{b}}$ μL	$4,4'$ - <i>bipy</i> ^c μL	excess solvent μL		Reaction result/ substance appearance	PXRD
	$\text{Cu}(\text{NO}_3)_2 \cdot 3\text{H}_2\text{O}$	H_3L	$4,4'$ - <i>bipy</i>							
1	1	1	0	40	20	0	140		no precipitate	X-ray amorphous
2	1	0	1	40	0	20	140		blue powder	unknown crystalline phase
3	1	1	1	40	20	20	120		light blue powder	1
4	2	1	1	80	20	20	80		light blue + dark blue powder	1 + impurities
5	3	1	1	120	20	20	40		light blue + dark blue powder	1 + impurities
6	1	1	2	40	20	40	100		light blue + dark blue powder	1 + impurities
7	1	1	3	40	20	60	80	H ₂ O	light blue + dark blue powder	1 + impurities
8	2	1	2	80	20	40	60		light blue + dark blue powder	1 + impurities
9	2	2	1	80	40	20	60		light blue powder	1
10	3	1	2	120	20	40	20		light blue + dark blue powder	1 + impurities
11	3	2	1	120	40	20	20		light blue + dark blue powder	1 + impurities
12	3	2	2	120	40	40	0		light blue powder	1
13	1	1	0	40	20	0	140	isopropanol	mixed phases	unknown crystalline phase
14	1	0	1	40	0	20	140		mixed phases	unknown crystalline phase
15	1	1	1	40	20	20	120		mixed phases	1 + unknown crystalline phase
16	2	1	1	80	20	20	80		mixed phases	1 + unknown crystalline phase
17	3	1	1	120	20	20	40		mixed phases	1 + unknown crystalline phase
18	1	1	2	40	20	40	100		mixed phases	1 + unknown crystalline phase
19	1	1	3	40	20	60	80		mixed phases	1 + unknown crystalline phase
20	2	1	2	80	20	40	60		mixed phases	1 + unknown crystalline phase
21	2	2	1	80	40	20	60	mixed phases	1 + unknown crystalline phase	
22	3	1	2	120	20	40	20	mixed phases	1 + unknown crystalline phase	
23	3	2	1	120	40	20	20	mixed phases	1 + unknown crystalline phase	
24	3	2	2	120	40	40	0	mixed phases	1 + unknown crystalline phase	
25	1	1	0	40	20	0	140	Dimethylformamide	no precipitate	X-ray amorphous
26	1	0	1	40	0	20	140		red brown powder	Cu_2O + other phases ^d
27	1	1	1	40	20	20	120		green powder	unknown crystalline phase
28	2	1	1	80	20	20	80		mixed phases	unknown crystalline phase
29	3	1	1	120	20	20	40		mixed phases	1 + impurities
30	1	1	2	40	20	40	100		mixed phases	1 + impurities
31	1	1	3	40	20	60	80		mixed phases	1 + impurities
32	2	1	2	80	20	40	60		mixed phases	$\text{Cu} + \text{Cu}_2\text{O}$ + other phases
33	2	2	1	80	40	20	60		mixed phases	$\text{Cu} + \text{Cu}_2\text{O}$ + other phases
34	3	1	2	120	20	40	20		mixed phases	$\text{Cu} + \text{Cu}_2\text{O}$ + other phases
35	3	2	1	120	40	20	20	mixed phases	$\text{Cu} + \text{Cu}_2\text{O}$ + other phases	
36	3	2	2	120	40	40	0	mixed phases	$\text{Cu} + \text{Cu}_2\text{O}$ + other phases	
37	1	1	0	40	20	0	140	Acetonitrile	green powder	unknown crystalline phase
38	1	0	1	40	0	20	140		mixed phases	X-ray amorphous
39	1	1	1	40	20	20	120		mixed phases	X-ray amorphous
40	2	1	1	80	20	20	80		mixed phases	X-ray amorphous
41	3	1	1	120	20	20	40		mixed phases	unknown crystalline phase ^e
42	1	1	2	40	20	40	100		mixed phases	unknown crystalline phase
43	1	1	3	40	20	60	80		mixed phases	unknown crystalline phase
44	2	1	2	80	20	40	60		mixed phases	unknown crystalline phase
45	2	2	1	80	40	20	60	mixed phases	unknown crystalline phase	
46	3	1	2	120	20	40	20	mixed phases	unknown crystalline phase	
47	3	2	1	120	40	20	20	mixed phases	unknown crystalline phase	
48	3	2	2	120	40	40	0	mixed phases	unknown crystalline phase	

^a 0.5 M $\text{Cu}(\text{NO}_3)_2 \cdot 3\text{H}_2\text{O}$ in respective solvent

^b 1.0 M $\text{H}_3\text{L} \cdot 2\text{H}_2\text{O}$ in respective solvent

^c 0.5 M 4,4'-bipyridine in respective solvent

Reactor fill volume: 200 μL (48-er HT-reactor)

Temperature profile:

heat-up phase = 0.92 °C/min from 20 ° to 130 °C

heating period = 48 h at 130 °C (conventional heating)

cooling phase = 0.15 °C/min to 20 °C

1: $[\text{Cu}(\text{HL})(4,4'\text{-bipy})] \cdot \text{H}_2\text{O}$

d : red crystals of $[\text{Cu}(4,4'\text{-bipy})(\text{OH})]^{[\text{S1}]}$ were obtained & identified via unit cell indexing.

e : green crystals of $[\text{Cu}_2(\text{CH}_3\text{COO})_4(4,4'\text{-bipy})] \cdot \text{CH}_3\text{CN}^{[\text{S2}]}$ were obtained & identified via unit cell indexing.

[S1] S. P. Chen, G. Fan, S. L. Gao, *Acta Chimica Sinica*, **2007**, *65*, 1385-1388.

[S2] Y. H. Wen, Y. H. He, Y. L. Feng, *Chin. J. Struct. Chem.* **2007**, *26*, 29-32.

Table S2: Exact amounts of reactants for the HT Cu(II)-salt screening of the system $\text{Cu}^{2+}/\text{H}_3\text{L}/4,4'\text{-bipy}/\text{H}_2\text{O}$ at 130 °C.

Nr.	molar ratios			Cu(II) ^a μL	H ₃ L ^b μL	4,4'- bipy ^c μL	excess solvent μL		pH ^e	Reaction result/ substance appearance	PXRD
	Cu ²⁺	H ₃ L	2- Melm								
1	1	1	1	27	20	100	53		1	blue powder	1 + impurities
2	1	1	1	27	20	100	53	CuSO ₄ ·5H ₂ O	1	blue powder	1 + impurities
3	2	1	1	53	20	100	27		1	blue powder	1 + impurities
4	2	1	1	53	20	100	27		1	blue powder	1 + impurities
5	3	1	1	80	20	100	0		1	blue powder	1 + impurities
6	3	1	1	80	20	100	0		1	blue + green powder	1 + impurities
7	1	1	1	4.0 ^d	20	100	80		Cu(CH ₃ COO) ₂ ·H ₂ O	3	blue powder
8	1	1	1	4.0 ^d	20	100	80	4		blue powder	1 + impurities
9	2	1	1	8.0 ^d	20	100	80	5		blue powder	1 + Cu ₂ O + impurities
10	2	1	1	8.0 ^d	20	100	80	5		red + blue powder	1 + Cu ₂ O + impurities
11	3	1	1	12.0 ^d	20	100	80	6		red + blue powder	1 + Cu ₂ O + impurities
12	3	1	1	12.0 ^d	20	100	80	7		red + blue powder	1 + Cu ₂ O + impurities
13	1	1	1	27	20	100	53	Cu(NO ₃) ₂ ·3H ₂ O	1	blue powder	1
314	1	1	1	27	20	100	53		1	blue powder	1
15	2	1	1	53	20	100	27		1	blue + green powder	1 + impurities
16	2	1	1	53	20	100	27		1	blue + green powder	1 + impurities
17	3	1	1	80	20	100	0		1	blue + green powder	1 + impurities
18	3	1	1	80	20	100	0		1	blue powder	1 + impurities
19	1	1	1	27	20	100	53	CuCl ₂ ·2H ₂ O	1	light blue powder	α-[Cu(4,4'-bipy)Cl ₂] ^[S3]
20	1	1	1	27	20	100	53		1	light blue powder	α-[Cu(4,4'-bipy)Cl ₂] ^[S3]
21	2	1	1	53	20	100	27		1	light blue powder	α-[Cu(4,4'-bipy)Cl ₂] ^[S3]
22	2	1	1	53	20	100	27		1	light blue powder	α-[Cu(4,4'-bipy)Cl ₂] ^[S3]
23	3	1	1	80	20	100	0		1	light blue powder	α-[Cu(4,4'-bipy)Cl ₂] ^[S3]
24	3	1	1	80	20	100	0		1	light blue powder	α-[Cu(4,4'-bipy)Cl ₂] ^[S3]

^a 0.75 M Cu(SO₄)₂·5H₂O in H₂O, 0.75 M Cu(NO₃)₂·3H₂O in H₂O, 0.75 M Cu(Cl)₂·2H₂O in H₂O

^b 1.0 M H₃L·2H₂O in H₂O

^c 0.2 M 4,4'-bipyridine in H₂O

^d The water-insoluble Cu(CH₃COO)₂·H₂O was weighed in directly into the Teflon reactor inserts.

^e The pH value of the reaction solution was determined after the synthesis.

Reactor fill volume: 200 μL (48-er HT-reactor)

Temperature profile:

heat-up phase = 0.92 °C/min from 20 ° to 130 °C
 heating period = 48 h at 130 °C (conventional heating)
 cooling phase = 0.15 °C/min to 20 °C

1: [Cu(HL)(4,4'-bipy)]·H₂O

[S3] N. Masciocchi, P. Cairati, L. Carlucci, G. Mezza, G. Ciani, A. Sironi, *J. Chem. Soc., Dalton Trans.* **1996**, 2739-2746.

Table S3. Selected bond lengths / Å and angles / ° for **1** and **1-h**.

Bond	1	1-h
Cu1-N1	2.008(3)	2.285(35)
Cu1-N2	2.024(3)	1.916(45)
Cu1-O1	2.556(2)	1.934(19)
Cu2-O2	2.621(3)	2.136(23)
Cu1-O6	1.942(2)	2.776(11)
Cu2-O5	1.930(2)	2.549(17)
Cu2-N3	2.007(3)	2.045(37)
Cu2-N4	2.025(3)	2.174(46)
S1-O1	1.438(2)	1.543(23)
S1-O2	1.456(2)	1.466(25)
S1-O3	1.452(2)	1.471(27)
S1-C1	1.773(3)	1.821(28)
P1-O4	1.571(2)	1.544(13)
P1-O5	1.489(2)	1.553(13)
P1-O6	1.491(2)	1.530(14)
P1-C4	1.807(3)	1.735(25)
C1-C2	1.380(4)	1.396(28)
C1-C6	1.379(4)	1.396(37)
C2-C3	1.381(4)	1.442(29)
N1-C7	1.332(3)	1.359(26)
C7-C8	1.383(4)	1.341(37)
C8-C9	1.396(4)	1.335(25)
C9-C10	1.474(5)	1.362(52)
C10-11	1.390(3)	1.352(34)
C11-C12	1.386(4)	1.411(15)
C12-N2	1.333(3)	1.403(35)
C13-C14	1.374(4)	1.395(14)
C14-C15	1.384(4)	1.440(20)
C16-C17	1.380(4)	1.365(31)
O6-Cu1-N1	86.46(6)	86.84(37)
O6-Cu1-N2	93.54(6)	93.17(37)
N1-Cu1-O1	91.96(5)	92.44(72)
N3-Cu2-O2	97.12(4)	96.48(74)
N3-Cu2-O5	90.77(6)	87.20(52)
N4-Cu2-O5	89.23(6)	92.80(52)
N4-Cu2-O2	82.88(4)	83.52(74)
O1-S1-C1	107.10(13)	102.3(12)
O4-P1-C4	104.93(12)	112.9(9)
C2-C1-C6	120.17(27)	126.4(18)
N1-C7-C8	122.83(20)	121.8(20)
N3-C13-C14	123.06(28)	119.5(9)

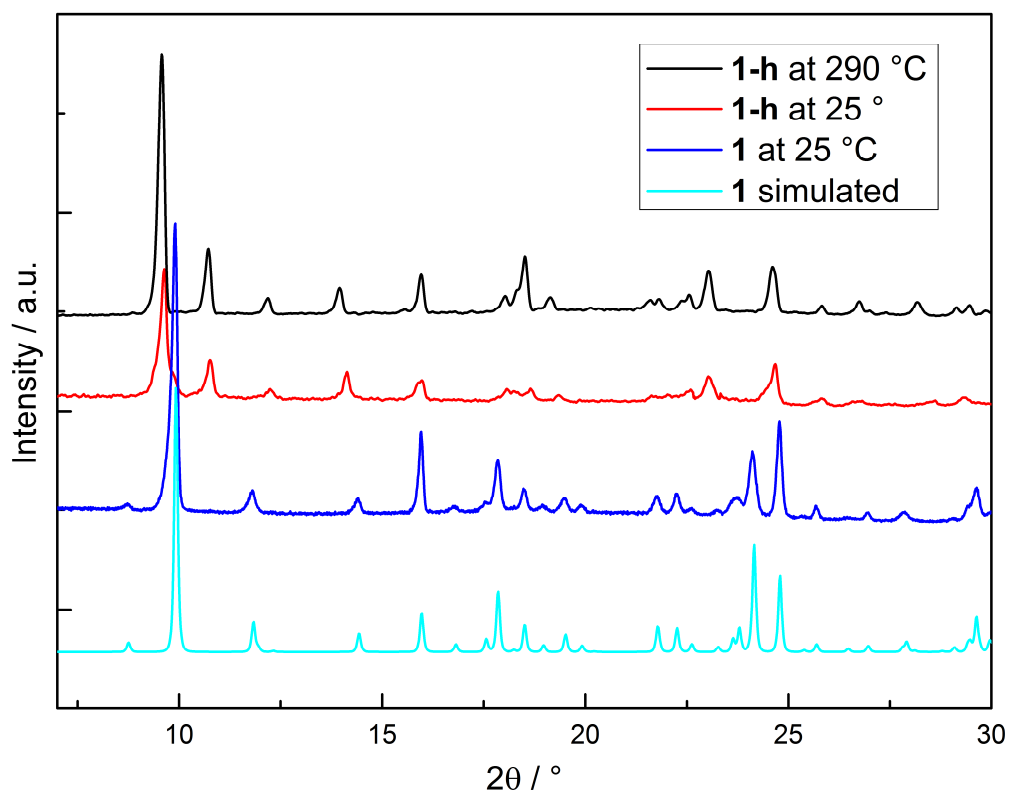


Figure S1. XRPD patterns of the dehydrated compound **1-h** measured at 290 °C and upon cooling to 25 °C. Upon hydration at ambient conditions, **1-h** transforms to compound **1**. For comparison, the simulated pattern of **1** is included.

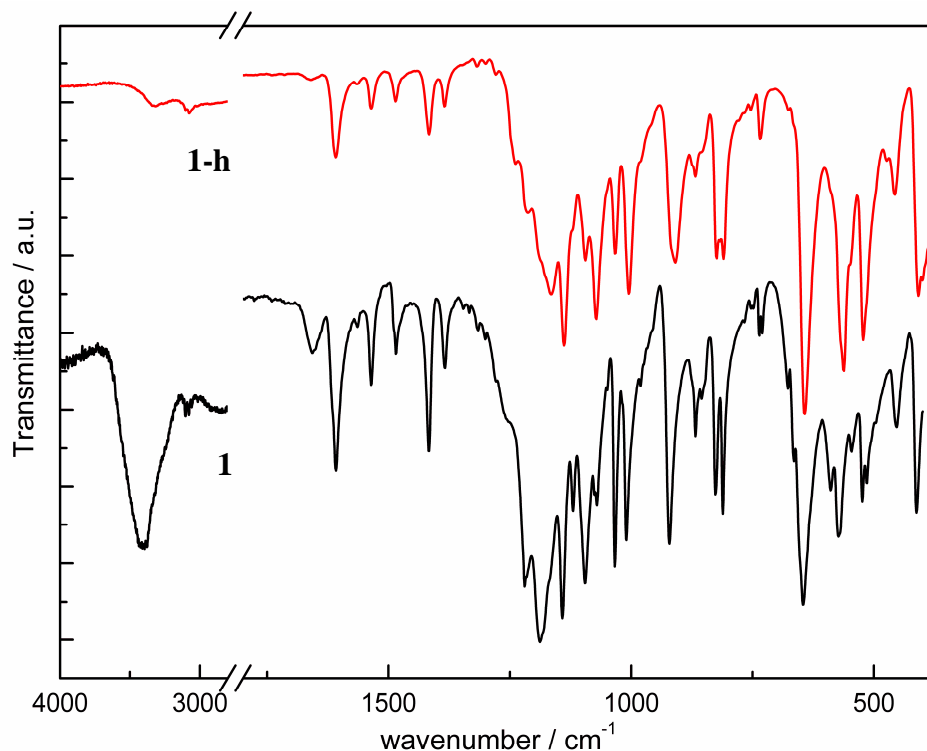


Figure S2. IR spectra of compounds **1** and **1-h**. A break is inserted in the x-axis to increase the clarity of the bands in the fingerprint region. No significant bands were observed in the excluded range.

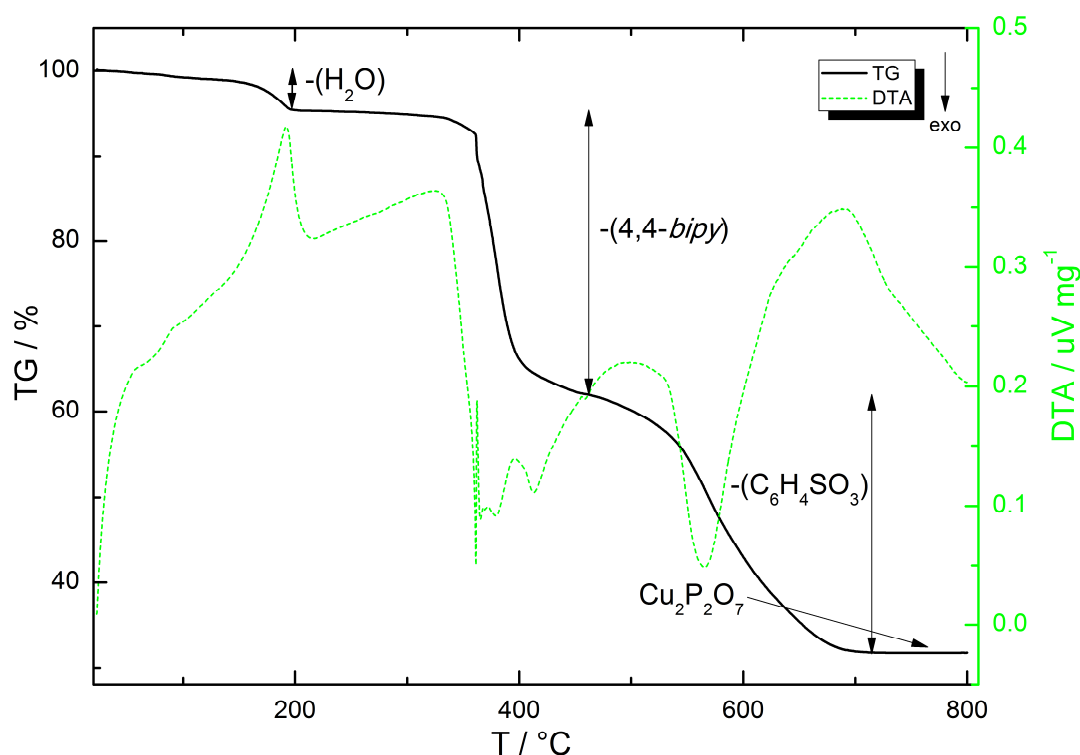


Figure S3. Results of TG/DTA analyses of compound **1**. The fragments in brackets are assumed to be released during the respective disintegration stages based on mass difference comparison. The solid residue was determined to be $\text{Cu}_2\text{P}_2\text{O}_7$ per XRPD analysis. The TG measurement was conducted under air atmosphere.

Appendix 4

Supporting Information

P. Maniam, N. Stock, *Inorg. Chem.* **2011**, 50, 5085-5097.

Investigation of Porous Ni-Based Metal Organic Frameworks Containing Paddle-Wheel Type Inorganic Building Units via High-Throughput Methods

Palanikumar Maniam and Norbert Stock*

Institute of Inorganic Chemistry,
Christian-Albrechts-University Kiel, Max-Eyth-Straße 2, D-24118 Kiel,

* Prof. Dr. Norbert Stock, Tel.: +49-431-880-1675, Fax: +49-431-880-1775.

e-mail: stock@ac.uni-kiel.de

Table of contents:

- (1) Table S1-S19: details of each high-throughput experiment
- (2) Figure S1: SEM and optical images
- (3) Figure S2: Color changes of compounds **1a** and **2** during activation
- (4) Figure S3: Results of HT reaction temperature investigation of the system Ni(NO₃)₂·6H₂O/H₂BDC/DABCO/DMF.
- (5) Figure S4: XRPD patterns of **1a**, **1b** & **1c**.
- (6) Figure S5: XRPD patterns of **2** and **2-ht**.
- (7) Figure S6: XRPD patterns of **3a**, **3b** & **3c**.
- (8) Figure S7: Final Rietveld plot of **3a**.
- (9) Figure S8: Final Rietveld plot of **3b**.
- (10) Figure S9: Final Rietveld plot of **3c**.
- (11) Figure S10: Angles in the paddle-wheel units of **3a** & **3b**.
- (12) Figure S11: Crystal structure of **1b**.
- (13) Table S20: Selected bond lengths in Ni(II) paddle-wheel units.
- (13) Figure S12: TG analysis of compounds **1a**, **1b**, **2**, **3a**, **3b** & **3c**.
- (14) Figure S13: IR spectra of Ni(II) compounds with paddle-wheel units.
- (15) Figure S14: IR spectra of Ni(II) compounds with non paddle-wheel units.
- (16) Table S21: Comparison of synthesis conditions and N₂-sorption properties of isostructural compounds.

Table S1: Exact amounts of reactants for the HT-base screening investigation of the system NiCl₂·6H₂O/H₃BTC/base/DMF.

Nr.	molar ratios			Ni(II)-salt (M g/mol)	base	Ni ²⁺ mg	H ₃ BTC ^a μL	base mg	DMF μL	Reaction result/ substance appearance	XRPD
	Ni ²⁺	H ₃ BTC	Base								
1	1	3	1	NiCl ₂ ·6H ₂ O (237.69)	2-Methylimidazole	17.8	1000	6.2	500	dark & light green powder	1a + crystalline impurities
2	2	3	1			35.7	1000	6.2	500	dark & light green powder	1a + crystalline impurities
3	3	3	1			53.5	1000	6.2	500	dark & light green powder	1a + crystalline impurities
4	3	1	1			53.5	333	6.2	1167	dark & light green powder	1a + crystalline impurities
5	3	2	1			53.5	667	6.2	833	dark & light green powder	1a + crystalline impurities
6	3	3	2			53.5	1000	12.3	500	dark & light green powder	1a + crystalline impurities
7	1	3	1		Imidazole	17.8	1000	5.1	500	dark & light green powder	low-crystalline 1a + impurities
8	2	3	1			35.7	1000	5.1	500	dark & light green powder	low-crystalline 1a + impurities
9	3	3	1			53.5	1000	5.1	500	dark & light green powder	low-crystalline 1a + impurities
10	3	1	1			53.5	333	5.1	1167	dark & light green powder	low-crystalline 1a + impurities
11	3	2	1			53.5	667	5.1	833	dark & light green powder	low-crystalline 1a + impurities
12	3	3	2			53.5	1000	10.2	500	dark & light green powder	low-crystalline 1a + impurities
13	1	3	1		DABCO	17.8	1000	8.4	500	red powder	unknown phase ^b
14	2	3	1			35.7	1000	8.4	500	red powder	unknown phase ^b
15	3	3	1			53.5	1000	8.4	500	red powder	unknown phase ^b
16	3	1	1			53.5	333	8.4	1167	red powder	unknown phase ^b
17	3	2	1			53.5	667	8.4	833	red powder	unknown phase ^b
18	3	3	2			53.5	1000	16.8	500	red powder	unknown phase ^b
19	1	3	1		4,4'-Bipyridine	17.8	1000	11.7	500	green & blue powder	(ADOLOV) ^c + cryst. impurities
20	2	3	1			35.7	1000	11.7	500	green & blue powder	(ADOLOV) ^c + cryst. impurities
21	3	3	1			53.5	1000	11.7	500	green & blue powder	(ADOLOV) ^c + cryst. impurities
22	3	1	1			53.5	333	11.7	1167	green & blue powder	(ADOLOV) ^c + cryst. impurities
23	3	2	1			53.5	667	11.7	833	green & blue powder	(ADOLOV) ^c + cryst. impurities
24	3	3	2			53.5	1000	23.4	500	green & blue powder	(ADOLOV) ^c + cryst. impurities

^a 0.225 M H₃BTC in DMF

^b Powder diffraction could not be indexed.

^c Indexing of the XRPD pattern matches the simulated pattern of a known structure: [Ni(HBTC)(4,4'-Bipy)]·(DMF)₃ CCDC code: ADOLOV. ^[S1]

Reactor fill volume: 1500 μL (24-er HT-reactor)

Temperature profile:

heat-up phase = 1.1 °C/min to 150 °C

heating period = 48 h at 150 °C (conventional heating)

cooling phase = 0.18 °C/min to room temperature

1a : [Ni₃(BTC)₂(Me₂NH)₃]·(DMF)₄(H₂O)₄

[S1] Gao, C.; Liu, S.; Xie, L.; Ren, Y.; Cao, J.; Sun, C. *CrystEngComm*. **2007**, *9*, 545-547.

Table S2: Exact amounts of reactants for the HT Ni(II) salt screening investigation of the system Ni-salt/H₃BTC/2-MeIm/DMF.

Nr.	molar ratios			Ni(II) -salt	Ni ²⁺ mg	H ₃ BTC ^a μL	2- MeIm ^b μL	DMF μL	Reaction result/ substance appearance	XRPD
	Ni ²⁺	H ₃ BTC	2-MeIm							
1	1	3	1	NiSO ₄ ·6H ₂ O	19.7	900	200	400	green powder	X-ray amorphous
2	2	3	1		39.4	900	200	400	green powder	X-ray amorphous
3	3	3	1		59.1	900	200	400	green powder	X-ray amorphous
4	3	1	1		59.1	300	200	1000	green powder	X-ray amorphous
5	3	2	1		59.1	600	200	700	green powder	X-ray amorphous
6	3	3	2		59.1	900	400	200	green powder	X-ray amorphous
7	1	3	1	Ni(CH ₃ COO) ₂ ·4H ₂ O	18.7	900	200	400	green powder	X-ray amorphous
8	2	3	1		37.3	900	200	400	green powder	X-ray amorphous
9	3	3	1		56.0	900	200	400	green powder	X-ray amorphous
10	3	1	1		56.0	300	200	1000	green powder	X-ray amorphous
11	3	2	1		56.0	600	200	700	green powder	X-ray amorphous
12	3	3	2		56.0	900	400	200	green powder	low-crystalline 1a + impurities
13	1	3	1	Ni(NO ₃) ₂ ·6H ₂ O	21.8	900	200	400	dark green crystals + green powder	1a + cryst. impurities
14	2	3	1		43.6	900	200	400	dark green crystals + green powder	1a + 1b
15	3	3	1		65.4	900	200	400	dark green crystals + green powder	1a + cryst. impurities
16	3	1	1		65.4	300	200	1000	dark green crystals + green powder	1a + cryst. impurities
17	3	2	1		65.4	600	200	700	dark green crystals + green powder	1a + 1b
18	3	3	2		65.4	900	400	200	dark green crystals + green powder	1a + 1b
19	1	3	1	Ni(ClO ₄) ₂ ·6H ₂ O	27.4	900	200	400	light green powder	1b + cryst. impurities
20	2	3	1		54.9	900	200	400	light green powder	1b + cryst. impurities
21	3	3	1		82.3	900	200	400	light green powder	1b + cryst. impurities
22	3	1	1		82.3	300	200	1000	light green powder	1b
23	3	2	1		82.3	600	200	700	light green powder	1b + cryst. impurities
24	3	3	2		82.3	900	400	200	light green powder	1b + cryst. impurities

^a 0.25 M H₃BTC in DMF^b 0.375 M 2-MeIm in DMF^c For the reactant amounts and the results involving NiCl₂·6H₂O, refer to Tab. S1.

Reactor fill volume: 1500 μL (24-er HT-reactor)

Temperature profile:

..heat-up phase = 1.1 °C/min to 150 °C

heating period = 48 h at 150 °C (conventional heating)

cooling phase = 0.18 °C/min to room temperature

1a : [Ni₃(BTC)₂(Me₂NH)₃]·(DMF)₄(H₂O)₄**1b** : [Ni₆(BTC)₂(DMF)₆(HCOO)₆]

Table S3: Exact amounts of reactants for the HT solvent screening investigation of the system Ni-salt/H₃BTC/2-MeIm/solvent.

Nr.	molar ratios			solvent type	Ni(NO ₃) ₂ ·6H ₂ O ^a μL	H ₃ BTC ^b μL	2-MeIm ^c μL	excess solvent μL	Reaction result/ substance appearance	XRPD
	Ni(NO ₃) ₂ ·6H ₂ O	H ₃ BTC	2-MeIm							
1	2.5	2	1	DMF	50	80	20	50	dark green crystals + green powder	1a + crystalline impurities
2	2	2.5	1		40	100	20	40	dark green crystals + green powder	1a + 1b
3	3	2	0.5		60	80	10	50	dark green crystals + green powder	1a + crystalline impurities
4	3	2	1		60	80	20	40	dark green crystals + green powder	1a + 1b
5	3	2	1.5		60	80	30	30	dark green crystals + green powder	1a + 1b
6	3	2	2		60	80	40	20	dark green crystals + green powder	1a + crystalline impurities
7	2.5	2	1	DMA	50	80	20	50	light brown powder	X-ray amorphous
8	2	2.5	1		40	100	20	40	light brown powder	X-ray amorphous
9	3	2	0.5		60	80	10	50	light brown powder	X-ray amorphous
10	3	2	1		60	80	20	40	light brown powder	X-ray amorphous
11	3	2	1.5		60	80	30	30	light brown powder	X-ray amorphous
12	3	2	2		60	80	40	20	light brown powder	X-ray amorphous
13	2.5	2	1	DEF	50	80	20	50	light brown powder	X-ray amorphous
14	2	2.5	1		40	100	20	40	light brown powder	X-ray amorphous
15	3	2	0.5		60	80	10	50	light brown powder	X-ray amorphous
16	3	2	1		60	80	20	40	light brown powder	X-ray amorphous
17	3	2	1.5		60	80	30	30	light brown powder	X-ray amorphous
18	3	2	2		60	80	40	20	light brown powder	X-ray amorphous
19	2.5	2	1	DMF + H ₂ O + Ethanol (Vol.: 2:1:1)	50	80	20	50	yellow-green powder	X-ray amorphous
20	2	2.5	1		40	100	20	40	yellow-green powder	X-ray amorphous
21	3	2	0.5		60	80	10	50	yellow-green powder	X-ray amorphous
22	3	2	1		60	80	20	40	yellow-green powder	X-ray amorphous
23	3	2	1.5		60	80	30	30	yellow-green powder	X-ray amorphous
24	3	2	2		60	80	40	20	yellow-green powder	X-ray amorphous

^a 0.5 M Ni(NO₃)₂·6H₂O in DMF^b 0.25 M H₃BTC in DMF^c 0.5 M 2-MeIm in DMF

Reactor fill volume: 200 μL (48-er HT-reactor)

Temperature profile: heat-up phase = 1.1 °C/min to 150 °C
 heating period = 48 h at 150 °C (conventional heating)
 cooling phase = 0.18 °C/min to room temperature

1a : [Ni₃(BTC)₂(Me₂NH)₃]·(DMF)₄(H₂O)₄**1b** : [Ni₆(BTC)₂(DMF)₆(HCOO)₆]

Table S4: Exact amounts of reactants for the HT reaction temperature investigation of the system Ni(NO₃)₂·6H₂O/H₃BTC/2-MeIm/DMF at 140 °C with discover array set-up.

Nr.	molar ratios			Ni(NO ₃) ₂ ·6H ₂ O ^a H ₃ BTC ^b 2-MeIm ^c excess solvent				Reaction result/ substance appearance	XRPD
	Ni(NO ₃) ₂ ·6H ₂ O	H ₃ BTC	2-MeIm	μL	μL	μL	μL		
1	1	1	0	10	30	0	160	-	-
2	0	1	1	0	30	10	160	-	-
3	1	0	1	10	0	10	180	-	-
4	1	1	6	10	30	60	100	green powder	X-ray amorphous
5	2	1	5	20	30	50	100	green powder	1b
6	3	1	4	30	30	40	100	green powder	1b
7	4	1	3	40	30	30	100	green powder	1b
8	5	1	2	50	30	20	100	green powder	1b
9	6	1	1	60	30	10	100	green powder	X-ray amorphous
10	1	2	5	10	60	50	80	green powder	X-ray amorphous
11	1	1	2	10	30	20	140	green powder	X-ray amorphous
12	1.5	1	1.5	15	30	15	140	green powder	1b
13	2	1	1	20	30	10	140	green powder	X-ray amorphous
14	5	2	1	50	60	10	80	green powder	X-ray amorphous
15	1	3	4	10	90	40	60	green powder	1b
16	1	1.5	1.5	10	45	15	130	green powder	X-ray amorphous
17	1.5	1.5	1	15	45	10	130	green powder	1b
18	4	3	1	40	90	10	60	green powder	1b
19	1	4	3	10	120	30	40	green powder	X-ray amorphous
20	1	2	1	10	60	10	120	green powder	1b
21	3	4	1	30	120	10	40	green powder	1b
22	1	5	2	10	150	20	20	green powder	1b
23	2	5	1	20	150	10	20	green powder	1b
24	1	6	1	10	180	10	0	green powder	X-ray amorphous
25	1	1	3.5	10	30	35	125	green powder	1b
26	1.5	1	2.5	15	30	25	130	green powder	1b
27	2.5	1	2	25	30	20	125	green powder	1b
28	3	1	1.5	30	30	15	125	green powder	X-ray amorphous
29	5.5	1.5	1	55	45	10	90	green powder	X-ray amorphous
30	1	1.5	2.5	10	45	25	120	green powder	1b
31	1	1	1.5	10	30	15	145	green powder	1b
32	2	1.5	1	20	45	10	125	green powder	1b
33	4.5	2.5	1	45	75	10	70	green powder	1b
34	1	2.5	2	10	75	20	95	green powder	X-ray amorphous
35	1.5	2	1	15	60	10	115	green powder	X-ray amorphous
36	3.5	3.5	1	35	105	10	50	green powder	X-ray amorphous
37	1	3	1.5	10	90	15	85	green powder	X-ray amorphous
38	2.5	4.5	1	25	135	10	30	green powder	X-ray amorphous
39	1.5	5.5	1	15	165	10	10	green powder	1b
40	1	1.5	5.5	10	45	55	90	green powder	1b
41	1	2.5	4.5	10	75	45	70	green powder	1b
42	1	3.5	3.5	10	105	35	50	green powder	X-ray amorphous
43	1	4.5	2.5	10	136	25	29	green powder	1b
44	1	5.5	1.5	10	165	15	10	green powder	X-ray amorphous
45	2.5	2.6	1	25	79	10	86	green powder	X-ray amorphous
46	3.5	2	1	35	60	10	95	green powder	X-ray amorphous
47	2	3	1	20	90	10	80	green powder	X-ray amorphous
48	1	1	1	10	30	10	150	green powder	X-ray amorphous

^a 1.0 M Ni(NO₃)₂·6H₂O in DMF^b 0.33 M H₃BTC in DMF^c 1.0 M 2-MeIm in DMF

Reactor fill volume: 200 μL (48-er HT-reactor)

Temperature profile:

heat-up phase = 1.0 °C/min to 140 °C

heating period = 48 h at 140 °C (conventional heating)

cooling phase = 0.167 °C/min to room temperature

1b : [Ni₆(BTC)₂(DMF)₆(HCOO)₆]

Table S5: Exact amounts of reactants for the HT reaction temperature investigation of the system Ni(NO₃)₂·6H₂O/H₃BTC/2-MeIm/DMF at 150 °C with discover array set-up.

Nr.	molar ratios			Ni(NO ₃) ₂ ·6H ₂ O ^a μL	H ₃ BTC ^b μL	2-MeIm ^c μL	excess solvent μL	Reaction result/ substance appearance	XRPD
	Ni(NO ₃) ₂ ·6H ₂ O	H ₃ BTC	2-MeIm						
1	1	1	0	10	30	0	160	-	-
2	0	1	1	0	30	10	160	-	-
3	1	0	1	10	0	10	180	-	-
4	1	1	6	10	30	60	100	green powder	X-ray amorphous
5	2	1	5	20	30	50	100	green powder	X-ray amorphous
6	3	1	4	30	30	40	100	brown powder	X-ray amorphous
7	4	1	3	40	30	30	100	brown powder	X-ray amorphous
8	5	1	2	50	30	20	100	brown powder	X-ray amorphous
9	6	1	1	60	30	10	100	brown powder	X-ray amorphous
10	1	2	5	10	60	50	80	green powder	X-ray amorphous
11	1	1	2	10	30	20	140	green powder	X-ray amorphous
12	1.5	1	1.5	15	30	15	140	green powder	1b
13	2	1	1	20	30	10	140	green powder	X-ray amorphous
14	5	2	1	50	60	10	80	brown powder	X-ray amorphous
15	1	3	4	10	90	40	60	green powder	X-ray amorphous
16	1	1.5	1.5	10	45	15	130	green powder	1a + 1b
17	1.5	1.5	1	15	45	10	130	green powder	1b
18	4	3	1	40	90	10	60	green powder	1b
19	1	4	3	10	120	30	40	green powder	X-ray amorphous
20	1	2	1	10	60	10	120	green powder	X-ray amorphous
21	3	4	1	30	120	10	40	green powder	1b
22	1	5	2	10	150	20	20	green powder	X-ray amorphous
23	2	5	1	20	150	10	20	green powder	1b
24	1	6	1	10	180	10	0	green powder	X-ray amorphous
25	1	1	3.5	10	30	35	125	green powder	X-ray amorphous
26	1.5	1	2.5	15	30	25	130	green powder	1a + 1b
27	2.5	1	2	25	30	20	125	brown powder	X-ray amorphous
28	3	1	1.5	30	30	15	125	brown powder	X-ray amorphous
29	5.5	1.5	1	55	45	10	90	brown powder	X-ray amorphous
30	1	1.5	2.5	10	45	25	120	brown powder	X-ray amorphous
31	1	1	1.5	10	30	15	145	green powder	X-ray amorphous
32	2	1.5	1	20	45	10	125	green powder	1a
33	4.5	2.5	1	45	75	10	70	green powder	1b
34	1	2.5	2	10	75	20	95	green powder	X-ray amorphous
35	1.5	2	1	15	60	10	115	green powder	X-ray amorphous
36	3.5	3.5	1	35	105	10	50	green powder	1b
37	1	3	1.5	10	90	15	85	green powder	1b
38	2.5	4.5	1	25	135	10	30	green powder	1b
39	1.5	5.5	1	15	165	10	10	green powder	1b
40	1	1.5	5.5	10	45	55	90	green powder	1c
41	1	2.5	4.5	10	75	45	70	green powder	1c
42	1	3.5	3.5	10	105	35	50	green powder	X-ray amorphous
43	1	4.5	2.5	10	136	25	29	green powder	X-ray amorphous
44	1	5.5	1.5	10	165	15	10	green powder	X-ray amorphous
45	2.5	2.6	1	25	79	10	86	green powder	1b
46	3.5	2	1	35	60	10	95	green powder	1b
47	2	3	1	20	90	10	80	green powder	1b
48	1	1	1	10	30	10	150	green powder	1b

^a 1.0 M Ni(NO₃)₂·6H₂O in DMF^b 0.33 M H₃BTC in DMF^c 1.0 M 2-MeIm in DMF

Reactor fill volume: 200 μL (48-er HT-reactor)

Temperature profile:

heat-up phase = 1.08 °C/min to 150 °C

heating period = 48 h at 150 °C (conventional heating)

cooling phase = 0.18 °C/min to room temperature

1a : [Ni₃(BTC)₂(Me₂NH)₃]·(DMF)₄(H₂O)₄**1b** : [Ni₆(BTC)₂(DMF)₆(HCOO)₆]**1c** : Structure cannot be determined.

Table S6: Exact amounts of reactants for the HT reaction temperature investigation of the system Ni(NO₃)₂·6H₂O/H₃BTC/2-MeIm/DMF at 160 °C with discover array set-up.

Nr.	molar ratios			Ni(NO ₃) ₂ ·6H ₂ O ^a μL	H ₃ BTC ^b μL	2-MeIm ^c μL	excess solvent μL	Reaction result/ substance appearance	XRPD
	Ni(NO ₃) ₂ ·6H ₂ O	H ₃ BTC	2-MeIm						
1	1	1	0	10	30	0	160	-	-
2	0	1	1	0	30	10	160	-	-
3	1	0	1	10	0	10	180	-	-
4	1	1	6	10	30	60	100	green powder	X-ray amorphous
5	2	1	5	20	30	50	100	green powder	1a
6	3	1	4	30	30	40	100	brown powder	X-ray amorphous
7	4	1	3	40	30	30	100	brown powder	X-ray amorphous
8	5	1	2	50	30	20	100	brown powder	X-ray amorphous
9	6	1	1	60	30	10	100	brown powder	X-ray amorphous
10	1	2	5	10	60	50	80	green powder	X-ray amorphous
11	1	1	2	10	30	20	140	green powder	1a
12	1.5	1	1.5	15	30	15	140	green powder	X-ray amorphous
13	2	1	1	20	30	10	140	brown powder	X-ray amorphous
14	5	2	1	50	60	10	80	brown powder	X-ray amorphous
15	1	3	4	10	90	40	60	green powder	1c
16	1	1.5	1.5	10	45	15	130	green powder	1a
17	1.5	1.5	1	15	45	10	130	green powder	1a
18	4	3	1	40	90	10	60	green powder	1b
19	1	4	3	10	120	30	40	green powder	X-ray amorphous
20	1	2	1	10	60	10	120	green powder	X-ray amorphous
21	3	4	1	30	120	10	40	green powder	1b
22	1	5	2	10	150	20	20	green powder	X-ray amorphous
23	2	5	1	20	150	10	20	green powder	X-ray amorphous
24	1	6	1	10	180	10	0	green powder	X-ray amorphous
25	1	1	3.5	10	30	35	125	green powder	X-ray amorphous
26	1.5	1	2.5	15	30	25	130	green powder	1b
27	2.5	1	2	25	30	20	125	brown powder	X-ray amorphous
28	3	1	1.5	30	30	15	125	brown powder	X-ray amorphous
29	5.5	1.5	1	55	45	10	90	brown powder	X-ray amorphous
30	1	1.5	2.5	10	45	25	120	green powder	X-ray amorphous
31	1	1	1.5	10	30	15	145	green powder	X-ray amorphous
32	2	1.5	1	20	45	10	125	green powder	1a
33	4.5	2.5	1	45	75	10	70	brown powder	X-ray amorphous
34	1	2.5	2	10	75	20	95	green powder	1a
35	1.5	2	1	15	60	10	115	green powder	X-ray amorphous
36	3.5	3.5	1	35	105	10	50	green powder	1b
37	1	3	1.5	10	90	15	85	green powder	1a
38	2.5	4.5	1	25	135	10	30	green powder	1b
39	1.5	5.5	1	15	165	10	10	green powder	X-ray amorphous
40	1	1.5	5.5	10	45	55	90	green powder	1c
41	1	2.5	4.5	10	75	45	70	green powder	1c
42	1	3.5	3.5	10	105	35	50	green powder	1c
43	1	4.5	2.5	10	136	25	29	green powder	X-ray amorphous
44	1	5.5	1.5	10	165	15	10	green powder	X-ray amorphous
45	2.5	2.6	1	25	79	10	86	green powder	1b
46	3.5	2	1	35	60	10	95	green powder	1a + 1b
47	2	3	1	20	90	10	80	green powder	1b
48	1	1	1	10	30	10	150	green powder	1a

^a 1.0 M Ni(NO₃)₂·6H₂O in DMF^b 0.33 M H₃BTC in DMF^c 1.0 M 2-MeIm in DMF

Reactor fill volume: 200 μL (48-er HT-reactor)

Temperature profile:

heat-up phase = 1.17 °C/min to 160 °C

heating period = 48 h at 160 °C (conventional heating)

cooling phase = 0.19 °C/min to room temperature

1a : [Ni₃(BTC)₂(Me₂NH)₃]·(DMF)₄(H₂O)₄**1b** : [Ni₆(BTC)₂(DMF)₆(HCOO)₆]**1c** : Structure cannot be determined.

Table S7: Exact amounts of reactants for the HT reaction temperature investigation of the system Ni(NO₃)₂·6H₂O/H₃BTC/2-MeIm/DMF at 170 °C with discover array set-up.

Nr.	molar ratios			Ni(NO ₃) ₂ ·6H ₂ O ^a μL	H ₃ BTC ^b μL	2-MeIm ^c μL	excess solvent μL	Reaction result/ substance appearance	XRPD
	Ni(NO ₃) ₂ ·6H ₂ O	H ₃ BTC	2-MeIm						
1	1	1	0	10	30	0	160	-	-
2	0	1	1	0	30	10	160	-	-
3	1	0	1	10	0	10	180	-	-
4	1	1	6	10	30	60	100	green powder	X-ray amorphous
5	2	1	5	20	30	50	100	green powder	1a
6	3	1	4	30	30	40	100	brown powder	X-ray amorphous
7	4	1	3	40	30	30	100	brown powder	X-ray amorphous
8	5	1	2	50	30	20	100	brown powder	X-ray amorphous
9	6	1	1	60	30	10	100	brown powder	X-ray amorphous
10	1	2	5	10	60	50	80	green powder	X-ray amorphous
11	1	1	2	10	30	20	140	green powder	1a
12	1.5	1	1.5	15	30	15	140	brown powder	1a
13	2	1	1	20	30	10	140	brown powder	1a
14	5	2	1	50	60	10	80	brown powder	X-ray amorphous
15	1	3	4	10	90	40	60	green powder	1c
16	1	1.5	1.5	10	45	15	130	green powder	1a
17	1.5	1.5	1	15	45	10	130	green powder	1a
18	4	3	1	40	90	10	60	green powder	1a
19	1	4	3	10	120	30	40	green powder	1c
20	1	2	1	10	60	10	120	green powder	1c
21	3	4	1	30	120	10	40	green powder	1b
22	1	5	2	10	150	20	20	green powder	1a
23	2	5	1	20	150	10	20	green powder	1b + H ₃ BTC
24	1	6	1	10	180	10	0	green powder	H ₃ BTC
25	1	1	3.5	10	30	35	125	green powder	X-ray amorphous
26	1.5	1	2.5	15	30	25	130	brown powder	1a
27	2.5	1	2	25	30	20	125	brown powder	X-ray amorphous
28	3	1	1.5	30	30	15	125	brown powder	X-ray amorphous
29	5.5	1.5	1	55	45	10	90	brown powder	X-ray amorphous
30	1	1.5	2.5	10	45	25	120	green powder	1a
31	1	1	1.5	10	30	15	145	green powder	1a
32	2	1.5	1	20	45	10	125	brown powder	1a
33	4.5	2.5	1	45	75	10	70	green powder	X-ray amorphous
34	1	2.5	2	10	75	20	95	green powder	X-ray amorphous
35	1.5	2	1	15	60	10	115	green powder	1a + 1b
36	3.5	3.5	1	35	105	10	50	green powder	1b
37	1	3	1.5	10	90	15	85	green powder	X-ray amorphous
38	2.5	4.5	1	25	135	10	30	green powder	1b + 1c
39	1.5	5.5	1	15	165	10	10	green powder	H ₃ BTC
40	1	1.5	5.5	10	45	55	90	green powder	X-ray amorphous
41	1	2.5	4.5	10	75	45	70	green powder	1c
42	1	3.5	3.5	10	105	35	50	green powder	1c
43	1	4.5	2.5	10	136	25	29	green powder	1a
44	1	5.5	1.5	10	165	15	10	green powder	1a
45	2.5	2.6	1	25	79	10	86	green powder	1b
46	3.5	2	1	35	60	10	95	green powder	1a
47	2	3	1	20	90	10	80	green powder	1b
48	1	1	1	10	30	10	150	green powder	1a

^a 1.0 M Ni(NO₃)₂·6H₂O in DMF^b 0.33 M H₃BTC in DMF^c 1.0 M 2-MeIm in DMF

Reactor fill volume: 200 μL (48-er HT-reactor)

Temperature profile:

heat-up phase = 1.25 °C/min to 170 °C

heating period = 48 h at 170 °C (conventional heating)

cooling phase = 0.21 °C/min to room temperature

1a : [Ni₃(BTC)₂(Me₂NH)₃]·(DMF)₄(H₂O)₄**1b** : [Ni₆(BTC)₂(DMF)₆(HCOO)₆]**1c** : Structure cannot be determined.

Table S8: Exact amounts of reactants for the HT reaction temperature investigation of the system $\text{Ni}(\text{NO}_3)_2 \cdot 6\text{H}_2\text{O}/\text{H}_3\text{BTC}/2\text{-MeIm}/\text{DMF}$ at 180 °C with discover array set-up.

Nr.	molar ratios			$\text{Ni}(\text{NO}_3)_2 \cdot 6\text{H}_2\text{O}^a$	H_3BTC^b	2-MeIm ^c	excess solvent	Reaction result/ substance appearance	XRPD
	$\text{Ni}(\text{NO}_3)_2 \cdot 6\text{H}_2\text{O}$	H_3BTC	2-MeIm						
1	1	1	0	10	30	0	160	-	-
2	0	1	1	0	30	10	160	-	-
3	1	0	1	10	0	10	180	-	-
4	1	1	6	10	30	60	100	green powder	X-ray amorphous
5	2	1	5	20	30	50	100	green powder	X-ray amorphous
6	3	1	4	30	30	40	100	brown powder	X-ray amorphous
7	4	1	3	40	30	30	100	brown powder	X-ray amorphous
8	5	1	2	50	30	20	100	brown powder	X-ray amorphous
9	6	1	1	60	30	10	100	brown powder	X-ray amorphous
10	1	2	5	10	60	50	80	green powder	X-ray amorphous
11	1	1	2	10	30	20	140	green powder	1a
12	1.5	1	1.5	15	30	15	140	green powder	1a
13	2	1	1	20	30	10	140	green powder	1a
14	5	2	1	50	60	10	80	brown powder	1a
15	1	3	4	10	90	40	60	green powder	X-ray amorphous
16	1	1.5	1.5	10	45	15	130	green powder	1a
17	1.5	1.5	1	15	45	10	130	green powder	1a
18	4	3	1	40	90	10	60	green powder	1a + 1b
19	1	4	3	10	120	30	40	green powder	1a
20	1	2	1	10	60	10	120	green powder	1a + H₃BTC
21	3	4	1	30	120	10	40	green powder	1a + 1b
22	1	5	2	10	150	20	20	green powder	1a
23	2	5	1	20	150	10	20	green powder	H_3BTC
24	1	6	1	10	180	10	0	green powder	X-ray amorphous
25	1	1	3.5	10	30	35	125	green powder	X-ray amorphous
26	1.5	1	2.5	15	30	25	130	green powder	1a
27	2.5	1	2	25	30	20	125	brown powder	X-ray amorphous
28	3	1	1.5	30	30	15	125	brown powder	X-ray amorphous
29	5.5	1.5	1	55	45	10	90	brown powder	X-ray amorphous
30	1	1.5	2.5	10	45	25	120	green powder	1a + 1b
31	1	1	1.5	10	30	15	145	green powder	X-ray amorphous
32	2	1.5	1	20	45	10	125	green powder	1a
33	4.5	2.5	1	45	75	10	70	green powder	1a
34	1	2.5	2	10	75	20	95	green powder	1a
35	1.5	2	1	15	60	10	115	green powder	1a
36	3.5	3.5	1	35	105	10	50	green powder	1a + 1b
37	1	3	1.5	10	90	15	85	green powder	X-ray amorphous
38	2.5	4.5	1	25	135	10	30	green powder	X-ray amorphous
39	1.5	5.5	1	15	165	10	10	green powder	X-ray amorphous
40	1	1.5	5.5	10	45	55	90	green powder	X-ray amorphous
41	1	2.5	4.5	10	75	45	70	-	X-ray amorphous
42	1	3.5	3.5	10	105	35	50	green powder	X-ray amorphous
43	1	4.5	2.5	10	136	25	29	green powder	1a
44	1	5.5	1.5	10	165	15	10	green powder	1a
45	2.5	2.6	1	25	79	10	86	green powder	1a + 1b
46	3.5	2	1	35	60	10	95	green powder	1a
47	2	3	1	20	90	10	80	green powder	1a
48	1	1	1	10	30	10	150	green powder	1a

^a 1.0 M $\text{Ni}(\text{NO}_3)_2 \cdot 6\text{H}_2\text{O}$ in DMF^b 0.33 M H_3BTC in DMF^c 1.0 M 2-MeIm in DMFReactor fill volume: 200 μL (48-er HT-reactor)

Temperature profile:

heat-up phase = 1.33 °C/min to 180 °C

heating period = 48 h at 180 °C (conventional heating)

cooling phase = 0.22 °C/min to room temperature

1a : $[\text{Ni}_3(\text{BTC})_2(\text{Me}_2\text{NH})_3] \cdot (\text{DMF})_4(\text{H}_2\text{O})_4$ **1b** : $[\text{Ni}_6(\text{BTC})_2(\text{DMF})_6(\text{HCOO})_6]$ **1c** : Structure cannot be determined.

Table S9: Exact amounts of reactants for the HT reaction temperature investigation of the system $\text{Ni}(\text{NO}_3)_2 \cdot 6\text{H}_2\text{O}/\text{H}_3\text{BTB}/2\text{-MeIm}/\text{DMF}$ at 150 °C with discover array set-up.

Nr.	molar ratios			$\text{Ni}(\text{NO}_3)_2 \cdot 6\text{H}_2\text{O}^a$ μL	H_3BTB^b μL	2- MeIm ^c μL	excess solvent μL	Reaction result/ substance appearance	XRPD
	$\text{Ni}(\text{NO}_3)_2 \cdot 6\text{H}_2\text{O}$	H_3BTB	2- MeIm						
1	1	1	0	10	30	0	160	green powder	X-ray amorphous
2	0	1	1	0	30	10	160	-	-
3	1	0	1	10	0	10	180	-	-
4	1	1	6	10	30	60	100	-	-
5	2	1	5	20	30	50	100	dark brown cubes	2
6	3	1	4	30	30	40	100	green powder	X-ray amorphous
7	4	1	3	40	30	30	100	green powder	X-ray amorphous
8	5	1	2	50	30	20	100	green powder	X-ray amorphous
9	6	1	1	60	30	10	100	green powder	X-ray amorphous
10	1	2	5	10	60	50	80	dark brown cubes	2
11	1	1	2	10	30	20	140	dark brown cubes	2
12	1.5	1	1.5	15	30	15	140	green powder	X-ray amorphous
13	2	1	1	20	30	10	140	green powder	X-ray amorphous
14	5	2	1	50	60	10	80	green powder	X-ray amorphous
15	1	3	4	10	90	40	60	dark brown cubes	2
16	1	1.5	1.5	10	45	15	130	green powder	X-ray amorphous
17	1.5	1.5	1	15	45	10	130	green powder	X-ray amorphous
18	4	3	1	40	90	10	60	green powder	X-ray amorphous
19	1	4	3	10	120	30	40	green powder	X-ray amorphous
20	1	2	1	10	60	10	120	green powder	X-ray amorphous
21	3	4	1	30	120	10	40	green powder	X-ray amorphous
22	1	5	2	10	150	20	20	green powder	X-ray amorphous
23	2	5	1	20	150	10	20	green powder	X-ray amorphous
24	1	6	1	10	180	10	0	-	-
25	1	1	3.5	10	30	35	125	dark brown cubes	2
26	1.5	1	2.5	15	30	25	130	green powder	X-ray amorphous
27	2.5	1	2	25	30	20	125	green powder	X-ray amorphous
28	3	1	1.5	30	30	15	125	green powder	X-ray amorphous
29	5.5	1.5	1	55	45	10	90	green powder	X-ray amorphous
30	1	1.5	2.5	10	45	25	120	dark brown cubes	2
31	1	1	1.5	10	30	15	145	green powder	X-ray amorphous
32	2	1.5	1	20	45	10	125	green powder	X-ray amorphous
33	4.5	2.5	1	45	75	10	70	green powder	X-ray amorphous
34	1	2.5	2	10	75	20	95	dark brown cubes	2
35	1.5	2	1	15	60	10	115	green powder	X-ray amorphous
36	3.5	3.5	1	35	105	10	50	green powder	X-ray amorphous
37	1	3	1.5	10	90	15	85	green powder	X-ray amorphous
38	2.5	4.5	1	25	135	10	30	green powder	X-ray amorphous
39	1.5	5.5	1	15	165	10	10	green powder	X-ray amorphous
40	1	1.5	5.5	10	45	55	90	dark brown cubes	2
41	1	2.5	4.5	10	75	45	70	dark brown cubes	2
42	1	3.5	3.5	10	105	35	50	dark brown cubes	2
43	1	4.5	2.5	10	136	25	29	dark brown cubes	2
44	1	5.5	1.5	10	165	15	10	green powder	X-ray amorphous
45	2.5	2.6	1	25	79	10	86	green powder	X-ray amorphous
46	3.5	2	1	35	60	10	95	green powder	X-ray amorphous
47	2	3	1	20	90	10	80	green powder	X-ray amorphous
48	1	1	1	10	30	10	150	green powder	X-ray amorphous

^a 1.0 M $\text{Ni}(\text{NO}_3)_2 \cdot 6\text{H}_2\text{O}$ in DMF^b 0.33 M H_3BTB in DMF^c 1.0 M 2-MeIm in DMF

Reactor fill volume: 200 μL (48-er HT-reactor)

Temperature profile:

heat-up phase = 1.08 °C/min to 150 °C

heating period = 72 h at 150 °C (conventional heating)

cooling phase = 0.18 °C/min to room temperature

2 : $[\text{Ni}_3(\text{BTB})_2(2\text{-MeIm})_{1.5}(\text{H}_2\text{O})_{1.5}] \cdot (\text{DMF})_9(\text{H}_2\text{O})_{6.5}$

Table S10: Exact amounts of reactants for the HT reaction temperature investigation of the system $\text{Ni}(\text{NO}_3)_2 \cdot 6\text{H}_2\text{O}/\text{H}_3\text{BTB}/2\text{-MeIm}/\text{DMF}$ at 150 °C with **focused** array set-up.

Nr.	molar ratios			$\text{Ni}(\text{NO}_3)_2 \cdot 6\text{H}_2\text{O}^a$	H_3BTB^b	2-MeIm ^c	excess solvent	Reaction result/ substance appearance	XRPD
	$\text{Ni}(\text{NO}_3)_2 \cdot 6\text{H}_2\text{O}$	H_3BTB	2-MeIm						
1	1	1	6	10	35	60	95	dark brown cubes	2
2	1	1.25	5.75	10	44	58	89	green powder	X-ray amorphous
3	1	1.5	5.5	10	53	55	83	dark brown cubes	2
4	1	1.75	5.25	10	61	53	76	-	-
5	1	2	5	10	70	50	70	dark brown cubes + green powder	2 + impurities
6	1	2.25	4.75	10	79	48	64	green powder	X-ray amorphous
7	1	2.5	4.5	10	88	45	58	dark brown cubes	2
8	1	2.75	4.25	10	96	43	51	dark brown cubes	2
9	1	3	4	10	105	40	45	dark brown cubes	2
10	1	3.25	3.75	10	114	38	39	-	-
11	1	3.5	3.5	10	123	35	33	-	-
12	1	3.75	3.25	10	131	33	26	-	-
13	1.25	1	5.75	13	35	58	95	dark brown cubes	2
14	1.25	1.25	5.5	13	44	55	89	dark brown cubes	2
15	1.25	1.5	5.25	13	53	53	83	dark brown cubes	2
16	1.25	1.75	5	13	61	50	76	dark brown cubes	2
17	1.25	2	4.75	13	70	48	70	dark brown cubes	2
18	1.25	2.25	4.5	13	79	45	64	dark brown cubes	2
19	1.25	2.5	4.25	13	88	43	58	dark brown cubes	2
20	1.25	2.75	4	13	96	40	51	dark brown cubes	2
21	1.25	3	3.75	13	105	38	45	dark brown cubes	2
22	1.25	3.25	3.5	13	114	35	39	dark brown cubes	2
23	1.25	3.5	3.25	13	123	33	33	dark brown cubes	2
24	1.25	3.75	3	13	131	30	26	dark brown cubes	2
25	1.5	1	5.5	15	35	55	95	green powder	X-ray amorphous
26	1.5	1.25	5.25	15	44	53	89	dark brown cubes	2
27	1.5	1.5	5	15	53	50	83	dark brown cubes	2
28	1.5	1.75	4.75	15	61	48	76	dark brown cubes	2
29	1.5	2	4.5	15	70	45	70	dark brown cubes	2
30	1.5	2.25	4.25	15	79	43	64	dark brown cubes	2
31	1.5	2.5	4	15	88	40	58	dark brown cubes	2
32	1.5	2.75	3.75	15	96	38	51	dark brown cubes	2
33	1.5	3	3.5	15	105	35	45	dark brown cubes	2
34	1.5	3.25	3.25	15	114	33	39	dark brown cubes	2
35	1.5	3.5	3	15	123	30	33	dark brown cubes	2
36	1.5	3.75	2.75	15	131	28	26	dark brown cubes	2
37	2	1	5	20	35	50	95	green powder	X-ray amorphous
38	2	1.25	4.75	20	44	48	89	green powder	X-ray amorphous
39	2	1.5	4.5	20	53	45	83	green powder	X-ray amorphous
40	2	1.75	4.25	20	61	43	76	dark brown cubes	2
41	2	2	4.0	20	70	40	70	dark brown cubes	2
42	2	2.25	3.75	20	79	38	64	dark brown cubes	2
43	2	2.5	3.5	20	88	35	58	dark brown cubes	2
44	2	2.75	3.25	20	96	33	51	dark brown cubes	2
45	2.0	3.0	3	20	105	30	45	dark brown cubes	2
46	2	3.25	2.75	20	114	28	39	green powder	X-ray amorphous
47	2	3.5	2.5	20	123	25	33	dark brown cubes + green powder	2 + impurities
48	2	3.75	2.25	20	131	23	26	green powder	X-ray amorphous

^a 1.0 M $\text{Ni}(\text{NO}_3)_2 \cdot 6\text{H}_2\text{O}$ in DMF^b 0.29 M H_3BTB in DMF^c 1.0 M 2-MeIm in DMFReactor fill volume: 200 μL (48-er HT-reactor)

Temperature profile:

heat-up phase = 1.08 °C/min to 150 °C

heating period = 72 h at 150 °C (conventional heating)

cooling phase = 0.18 °C/min to room temperature

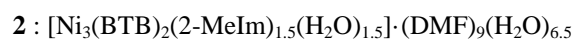


Table S11: Exact amounts of reactants for the HT reaction temperature investigation of the system $\text{Ni}(\text{NO}_3)_2 \cdot 6\text{H}_2\text{O}/\text{H}_2\text{BDC}/\text{DABCO}/\text{DMF}$ at 90 °C with discover array set-up.

Nr.	molar ratios			$\text{Ni}(\text{NO}_3)_2 \cdot 6\text{H}_2\text{O}^a$	H_2BDC^b	DABCO^c	excess solvent	Reaction result/ substance appearance	XRPD
	$\text{Ni}(\text{NO}_3)_2 \cdot 6\text{H}_2\text{O}$	H_2BDC	DABCO						
1	1	1	1	10	30	10	150	green powder	3a
2	1	1	0	10	30	0	160	-	-
3	1.5	1.5	1	15	45	10	130	green powder	3a
4	1.5	1	1	15	30	10	145	green powder	3a
5	1	1.5	1	10	45	10	135	green powder	3a
6	1	2	1	10	60	10	120	green powder	3a
7	2	1	1	20	30	10	140	green powder	3a
8	1	5	1	10	150	10	30	green powder	3a
9	5	1	1	50	30	10	110	green powder	3a
10	1	4	1	10	120	10	60	green powder	3a
11	4	1	1	40	30	10	120	green powder	3a
12	1	3	1	10	90	10	90	green powder	3a
13	3	1	1	30	30	10	130	green powder	3a
14	1.5	2	1	15	60	10	115	green powder	3a
15	2	1.5	1	20	45	10	125	green powder	3a
16	2.5	1.5	1	25	45	10	120	green powder	3a
17	2.5	2.5	1	25	75	10	90	green powder	3a
18	1.5	2.5	1	15	75	10	100	green powder	3a
19	2	3.5	1	20	105	10	65	green powder	3a
20	3.5	1.5	1	35	45	10	110	green powder	3a
21	2	2	1	20	60	10	110	green powder	3a
22	1.2	1	1	12	30	10	148	green powder	3a
23	1	1.2	1	10	36	10	144	green powder	3a
24	1	1	1.2	10	30	12	148	green powder	3a
25	1	1.5	1.5	10	45	15	130	green powder	3a
26	1.5	1	1.5	15	30	15	140	green powder	3a
27	1	1	1.5	10	30	15	145	green powder	3a
28	1	2	1.5	10	60	15	115	green powder	3a
29	2.5	1	1.5	25	30	15	130	green powder	3a + 3c
30	1	2.5	1.5	10	75	15	100	green powder	3a
31	3.5	1	1.5	35	30	15	120	green powder	3a
32	1	1	2	10	30	20	140	green powder	3a + 3c
33	1.5	1	2	15	30	20	135	green powder	3a + 3c
34	1	1.5	2	10	45	20	125	green powder	3a
35	1	3.5	2	10	105	20	65	green powder	3a
36	3.5	1	2	35	30	20	115	pale green powder	3c
37	1.5	1	2.5	15	30	25	130	green powder	3a + 3c
38	1	1.5	2.5	10	45	25	120	green powder	3a
39	1	2.5	2.5	10	75	25	90	green powder	3a
40	2.5	1	2.5	25	30	25	120	pale green powder	3c
41	1	1	3.0	10	30	30	130	pale green powder	3c
42	4	1	3	40	30	30	100	pale green powder	3c
43	2	1.0	3.5	20	30	35	115	pale green powder	3c
44	1	1.5	3.5	10	45	35	110	pale green powder	3c
45	1.5	1.0	3.5	15	30	35	120	green powder	3b + 3c
46	1	1	4	10	30	40	120	pale green powder	3c
47	3	1	4	30	30	40	100	pale green powder	3c
48	1	1	5	10	30	50	110	pale green powder	3c

^a 1.0 M $\text{Ni}(\text{NO}_3)_2 \cdot 6\text{H}_2\text{O}$ in DMF^b 0.33 M H_2BDC in DMF^c 1.0 M DABCO in DMFReactor fill volume: 200 μL (48-er HT-reactor)

Temperature profile:

heat-up phase = 0.58 °C/min to 90 °C

heating period = 48 h at 90 °C (conventional heating)

cooling phase = 0.1 °C/min to room temperature

3a : $[\text{Ni}_2(\text{BDC})_2(\text{DABCO})] \cdot (\text{DMF})_4(\text{H}_2\text{O})_{1.5}$ **3b** : $[\text{Ni}_2(\text{BDC})_2(\text{DABCO})] \cdot (\text{DMF})_4(\text{H}_2\text{O})_4$ **3c** : $[\text{Ni}(\text{BDC})(\text{DABCO})] \cdot (\text{DMF})_{1.5}(\text{H}_2\text{O})_2$

Table S12: Exact amounts of reactants for the HT reaction temperature investigation of the system $\text{Ni}(\text{NO}_3)_2 \cdot 6\text{H}_2\text{O}/\text{H}_2\text{BDC}/\text{DABCO}/\text{DMF}$ at 110 °C with discover array set-up.

Nr.	molar ratios			$\text{Ni}(\text{NO}_3)_2 \cdot 6\text{H}_2\text{O}^a$	H_2BDC^b	DABCO^c	excess solvent	Reaction result/ substance appearance	XRPD
	$\text{Ni}(\text{NO}_3)_2 \cdot 6\text{H}_2\text{O}$	H_2BDC	DABCO						
1	1	1	1	10	30	10	150	green powder	3a
2	1	1.5	1.5	10	45	15	130	green powder	3a
3	1.5	1.5	1	15	45	10	130	green powder	3a
4	1.5	1	1.5	15	30	15	140	green powder	3a + 3b
5	1	1	1.5	10	30	15	145	green powder	3a
6	1.5	1	1	15	30	10	145	green powder	3a
7	1	1.5	1	10	45	10	135	green powder	3a
8	1	1	2	10	30	20	140	green powder	3a + 3c
9	1	2	1	10	60	10	120	green powder	3a
10	2	1	1	20	30	10	140	green powder	3a + 3b
11	1	1	5	10	30	50	110	pale green powder	3c
12	1	5	1	10	150	10	30	green powder	3a
13	5	1	1	50	30	10	110	green powder	3a + 3c
14	1	1	4	10	30	40	120	pale green powder	3c
15	1	4	1	10	120	10	60	green powder	3a
16	4	1	1	40	30	10	120	green powder	3a + 3b
17	1	1	3	10	30	30	130	pale green powder	3c
18	1	3	1	10	90	10	90	green powder	3a
19	3	1	1	30	30	10	130	green powder	3a + 3b
20	1.5	1	2	15	30	20	135	green powder	3a + 3b
21	1.5	2	1	15	60	10	115	green powder	3a
22	2	1.5	1	20	45	10	125	green powder	3a
23	1	2	1.5	10	60	15	115	green powder	3a
24	1.5	1	2.5	15	30	25	130	pale green powder	3c
25	2.5	1	1.5	25	30	15	130	green powder	3a + 3b
26	1	2.5	1.5	10	75	15	100	green powder	3a
27	1	1.5	2.5	10	45	25	120	green powder	3a + 3c
28	2.5	1.5	1	25	45	10	120	green powder	3a
29	2.5	2.5	1	25	75	10	90	green powder	3a
30	1	2.5	2.5	10	75	25	90	green powder	3a + 3c
31	2.5	1	2.5	25	30	25	120	green powder	3a + 3b + 3c
32	1	1.5	2	10	45	20	125	green powder	3a
33	1.5	2.5	1	15	75	10	100	green powder	3a
34	1	3.5	2	10	105	20	65	green powder	3a
35	2	1	3.5	20	30	35	115	pale green powder	3c
36	3.5	1	2	35	30	20	115	green powder	3a + 3b + 3c
37	2	3.5	1	20	105	10	65	green powder	3a
38	1	1.5	3.5	10	45	35	110	pale green powder	3c
39	3.5	1	1.5	35	30	15	120	green powder	3a
40	3.5	1.5	1	35	45	10	110	green powder	3a
41	1.5	1	3.5	15	30	35	120	green powder	3b + 3c
42	4	3	1	40	90	10	60	green powder	3a
43	4	1.0	3	40	30	30	100	pale green powder	3c
44	3	1	4	30	30	40	100	pale green powder	3c
45	1.0	1.0	1.2	10	30	12	148	green powder	3a
46	1.2	1	1	12	30	10	148	green powder	3a
47	1	1.2	1	10	36	10	144	green powder	3a
48	1	1	0	10	30	0	160	-	X-ray amorphous

^a 1.0 M $\text{Ni}(\text{NO}_3)_2 \cdot 6\text{H}_2\text{O}$ in DMF^b 0.33 M H_2BDC in DMF^c 1.0 M DABCO in DMFReactor fill volume: 200 μL (48-er HT-reactor)

Temperature profile:

heat-up phase = 0.75 °C/min to 110 °C

heating period = 48 h at 110 °C (conventional heating)

cooling phase = 0.125 °C/min to room temperature

3a : $[\text{Ni}_2(\text{BDC})_2(\text{DABCO})] \cdot (\text{DMF})_4(\text{H}_2\text{O})_{1.5}$ **3b** : $[\text{Ni}_2(\text{BDC})_2(\text{DABCO})] \cdot (\text{DMF})_4(\text{H}_2\text{O})_4$ **3c** : $[\text{Ni}(\text{BDC})(\text{DABCO})] \cdot (\text{DMF})_{1.5}(\text{H}_2\text{O})_2$

Table S13: Exact amounts of reactants for the HT reaction temperature investigation of the system Ni(NO₃)₂·6H₂O/H₂BDC/DABCO/DMF at 130 °C with discover array set-up.

Nr.	molar ratios			Ni(NO ₃) ₂ ·6H ₂ O ^a μL	H ₂ BDC ^b μL	DABCO ^c μL	excess solvent μL	Reaction result/ substance appearance	XRPD
	Ni(NO ₃) ₂ ·6H ₂ O	H ₂ BDC	DABCO						
1	1	1	1	10	30	10	150	green powder	3a
2	1	1.5	1.5	10	45	15	130	green powder	3a
3	1.5	1.5	1	15	45	10	130	green powder	3a
4	1.5	1	1.5	15	30	15	140	green powder	3a
5	1	1	1.5	10	30	15	145	green powder	3a
6	1.5	1	1	15	30	10	145	green powder	3a
7	1	1.5	1	10	45	10	135	green powder	3a
8	1	1	2	10	30	20	140	green powder	3a
9	1	2	1	10	60	10	120	green powder	3a
10	2	1	1	20	30	10	140	green powder	3a
11	1	1	5	10	30	50	110	pale green powder	3c
12	1	5	1	10	150	10	30	green powder	3a
13	5	1	1	50	30	10	110	-	X-ray amorphous
14	1	1	4	10	30	40	120	pale green powder	3c
15	1	4	1	10	120	10	60	green powder	3a
16	4	1	1	40	30	10	120	green powder	3a
17	1	1	3	10	30	30	130	green powder	3a + 3c
18	1	3	1	10	90	10	90	green powder	3a
19	3	1	1	30	30	10	130	green powder	3a
20	1.5	1	2	15	30	20	135	green powder	3a + 3b
21	1.5	2	1	15	60	10	115	green powder	3a
22	2	1.5	1	20	45	10	125	green powder	3a
23	1	2	1.5	10	60	15	115	green powder	3a
24	1.5	1	2.5	15	30	25	130	green powder	3a + 3b
25	2.5	1	1.5	25	30	15	130	green powder	3a
26	1	2.5	1.5	10	75	15	100	green powder	3a
27	1	1.5	2.5	10	45	25	120	green powder	3a + 3c
28	2.5	1.5	1	25	45	10	120	green powder	3a
29	2.5	2.5	1	25	75	10	90	green powder	3a
30	1	2.5	2.5	10	75	25	90	green powder	3a
31	2.5	1	2.5	25	30	25	120	green powder	3a + 3b + 3c
32	1	1.5	2	10	45	20	125	green powder	3a
33	1.5	2.5	1	15	75	10	100	green powder	3a
34	1	3.5	2	10	105	20	65	green powder	3a
35	2	1	3.5	20	30	35	115	pale green powder	3c
36	3.5	1	2	35	30	20	115	green powder	3a + 3b
37	2	3.5	1	20	105	10	65	green powder	3a
38	1	1.5	3.5	10	45	35	110	green powder	3a + 3c
39	3.5	1	1.5	35	30	15	120	green powder	3a
40	3.5	1.5	1	35	45	10	110	green powder	3a
41	1.5	1	3.5	15	30	35	120	pale green powder	3c
42	4	3	1	40	90	10	60	green powder	3a
43	4	1.0	3	40	30	30	100	pale green powder	3c
44	3	1	4	30	30	40	100	pale green powder	3c
45	1.0	1.0	1.2	10	30	12	148	green powder	3a
46	1.2	1	1	12	30	10	148	green powder	3a
47	1	1.2	1	10	36	10	144	green powder	3a
48	1	1	0	10	30	0	160	-	X-ray amorphous

^a 1.0 M Ni(NO₃)₂·6H₂O in DMF^b 0.33 M H₂BDC in DMF^c 1.0 M DABCO in DMF

Reactor fill volume: 200 μL (48-er HT-reactor)

Temperature profile:

heat-up phase = 0.92 °C/min to 130 °C

heating period = 48 h at 130 °C (conventional heating)

cooling phase = 0.15 °C/min to room temperature

3a : [Ni₂(BDC)₂(DABCO)]·(DMF)₄(H₂O)_{1.5}**3b** : [Ni₂(BDC)₂(DABCO)]·(DMF)₄(H₂O)₄**3c** : [Ni(BDC)(DABCO)]·(DMF)_{1.5}(H₂O)₂

Table S14: Exact amounts of reactants for the HT reaction temperature investigation of the system $\text{Ni}(\text{NO}_3)_2 \cdot 6\text{H}_2\text{O}/\text{H}_2\text{BDC}/\text{DABCO}/\text{DMF}$ at 150 °C with discover array set-up.

Nr.	molar ratios			$\text{Ni}(\text{NO}_3)_2 \cdot 6\text{H}_2\text{O}^a$	H_2BDC^b	DABCO^c	excess solvent	Reaction result/ substance appearance	XRPD
	$\text{Ni}(\text{NO}_3)_2 \cdot 6\text{H}_2\text{O}$	H_2BDC	DABCO						
1	1	1	1	10	30	10	150	green powder	3a
2	1	1.5	1.5	10	45	15	130	green powder	3a
3	1.5	1.5	1	15	45	10	130	green powder	3a
4	1.5	1	1.5	15	30	15	140	green powder	3a
5	1	1	1.5	10	30	15	145	green powder	3a
6	1.5	1	1	15	30	10	145	green powder	3a
7	1	1.5	1	10	45	10	135	green powder	3a
8	1	1	2	10	30	20	140	green powder	3a
9	1	2	1	10	60	10	120	green powder	3a
10	2	1	1	20	30	10	140	green powder	3a
11	1	1	5	10	30	50	110	pale green powder	3c
12	1	5	1	10	150	10	30	green powder	3a
13	5	1	1	50	30	10	110	green powder	3a + 3b
14	1	1	4	10	30	40	120	pale green powder	3c
15	1	4	1	10	120	10	60	green powder	3a
16	4	1	1	40	30	10	120	green powder	3a
17	1	1	3	10	30	30	130	green powder	3a + 3c
18	1	3	1	10	90	10	90	green powder	3a
19	3	1	1	30	30	10	130	green powder	3a
20	1.5	1	2	15	30	20	135	green powder	3a
21	1.5	2	1	15	60	10	115	green powder	3a
22	2	1.5	1	20	45	10	125	green powder	3a
23	1	2	1.5	10	60	15	115	green powder	3a
24	1.5	1	2.5	15	30	25	130	green powder	3a + 3b
25	2.5	1	1.5	25	30	15	130	green powder	3a
26	1	2.5	1.5	10	75	15	100	green powder	3a
27	1	1.5	2.5	10	45	25	120	green powder	3b + 3c
28	2.5	1.5	1	25	45	10	120	green powder	3a
29	2.5	2.5	1	25	75	10	90	green powder	3a
30	1	2.5	2.5	10	75	25	90	green powder	3a
31	2.5	1	2.5	25	30	25	120	green powder	3a + 3c
32	1	1.5	2	10	45	20	125	green powder	3a
33	1.5	2.5	1	15	75	10	100	green powder	3a
34	1	3.5	2	10	105	20	65	green powder	3a
35	2	1	3.5	20	30	35	115	pale green powder	3c
36	3.5	1	2	35	30	20	115	green powder	3a
37	2	3.5	1	20	105	10	65	green powder	3a
38	1	1.5	3.5	10	45	35	110	green powder	3a + 3c
39	3.5	1	1.5	35	30	15	120	green powder	3a
40	3.5	1.5	1	35	45	10	110	green powder	3a
41	1.5	1	3.5	15	30	35	120	green powder	3c
42	2	2	1	20	60	10	110	green powder	3a
43	4	1.0	3	40	30	30	100	pale green powder	3c
44	3	1	4	30	30	40	100	pale green powder	3c
45	1.0	1.0	1.2	10	30	12	148	green powder	3a
46	1.2	1	1	12	30	10	148	green powder	3a
47	1	1.2	1	10	36	10	144	green powder	3a
48	1	1	0	10	30	0	160	-	X-ray amorphous

^a 1.0 M $\text{Ni}(\text{NO}_3)_2 \cdot 6\text{H}_2\text{O}$ in DMF^b 0.33 M H_2BDC in DMF^c 1.0 M DABCO in DMFReactor fill volume: 200 μL (48-er HT-reactor)

Temperature profile:

heat-up phase = 1.08 °C/min to 130 °C

heating period = 48 h at 130 °C (conventional heating)

cooling phase = 0.18 °C/min to room temperature

3a : $[\text{Ni}_2(\text{BDC})_2(\text{DABCO})] \cdot (\text{DMF})_4(\text{H}_2\text{O})_{1.5}$ **3b** : $[\text{Ni}_2(\text{BDC})_2(\text{DABCO})] \cdot (\text{DMF})_4(\text{H}_2\text{O})_4$ **3c** : $[\text{Ni}(\text{BDC})(\text{DABCO})] \cdot (\text{DMF})_{1.5}(\text{H}_2\text{O})_2$

Table S15: Exact amounts of reactants for the HT reaction time (1 h) investigation of the system Ni(NO₃)₂·6H₂O/H₂BDC/DABCO/DMF at 110 °C with discover array set-up.

Nr.	molar ratios			Ni(NO ₃) ₂ ·6H ₂ O ^a μL	H ₂ BDC ^b μL	DABCO ^c μL	excess solvent μL	Reaction result/ substance appearance	XRPD
	Ni(NO ₃) ₂ ·6H ₂ O	H ₂ BDC	DABCO						
1	1	1	0	10	30	0	160	-	X-ray amorphous
2	1	1	1	10	30	10	150	green powder	3a + 3c
3	1.5	1.5	1	15	45	10	130	green powder	3a + 3c
4	1.5	1	1	15	30	10	145	green powder	3a + 3c
5	1	1.5	1	10	45	10	135	green powder	3a
6	1	2	1	10	60	10	120	green powder	3a
7	2	1	1	20	30	10	140	green powder	3a + 3b
8	1	5	1	10	150	10	30	green powder	3a
9	5	1	1	50	30	10	110	-	X-ray amorphous
10	1	4	1	10	120	10	60	green powder	3a
11	4	1	1	40	30	10	120	-	X-ray amorphous
12	1	3	1	10	90	10	90	green powder	3a
13	3	1	1	30	30	10	130	-	X-ray amorphous
14	1.5	2	1	15	60	10	115	green powder	3a
15	2	1.5	1	20	45	10	125	green powder	3a
16	2.5	1.5	1	25	45	10	120	-	X-ray amorphous
17	2.5	2.5	1	25	75	10	90	green powder	3a
18	1.5	2.5	1	15	75	10	100	green powder	3a
19	2	3.5	1	20	105	10	65	-	X-ray amorphous
20	3.5	1.5	1	35	45	10	110	-	X-ray amorphous
21	4	3	1	40	90	10	60	-	X-ray amorphous
22	1.2	1	1	12	30	10	148	green powder	3a
23	1	1.2	1	10	36	10	144	green powder	3a
24	1	1	1.2	10	30	12	148	green powder	3a + 3c
25	1	1.5	1.5	10	45	15	130	green powder	3a
26	1.5	1	1.5	15	30	15	140	green powder	3a + 3c
27	1	1	1.5	10	30	15	145	green powder	3b + 3c
28	1	2	1.5	10	60	15	115	green powder	3a
29	2.5	1	1.5	25	30	15	130	green powder	3a + 3c
30	1	2.5	1.5	10	75	15	100	green powder	3a
31	3.5	1	1.5	35	30	15	120	pale green powder	3c
32	1	1	2	10	30	20	140	green powder	3a + 3c
33	1.5	1	2	15	30	20	135	green powder	3a + 3b + 3c
34	1	1.5	2	10	45	20	125	green powder	3a + 3c
35	1	3.5	2	10	105	20	65	green powder	3a
36	3.5	1	2	35	30	20	115	pale green powder	3c
37	1.5	1	2.5	15	30	25	130	green powder	3a + 3b + 3c
38	1	1.5	2.5	10	45	25	120	green powder	3a + 3c
39	1	2.5	2.5	10	75	25	90	green powder	3a
40	2.5	1	2.5	25	30	25	120	pale green powder	3c
41	1	1	3.0	10	30	30	130	green powder	3b + 3c
42	4	1	3	40	30	30	100	pale green powder	3c
43	2	1.0	3.5	20	30	35	115	pale green powder	3c
44	1	1.5	3.5	10	45	35	110	pale green powder	3c
45	1.5	1.0	3.5	15	30	35	120	pale green powder	3c
46	1	1	4	10	30	40	120	green powder	3b + 3c
47	3	1	4	30	30	40	100	pale green powder	3c
48	1	1	5	10	30	50	110	green powder	3b + 3c

^a 1.0 M Ni(NO₃)₂·6H₂O in DMF^b 0.33 M H₂BDC in DMF^c 1.0 M DABCO in DMF

Reactor fill volume: 200 μL (48-er HT-reactor)

Temperature profile:

heat-up phase = 3 °C/min to 110 °C

heating period = 1 h at 110 °C (conventional heating)

cooling phase = 1.5 °C/min to room temperature

3a : [Ni₂(BDC)₂(DABCO)]·(DMF)₄(H₂O)_{1.5}**3b** : [Ni₂(BDC)₂(DABCO)]·(DMF)₄(H₂O)₄**3c** : [Ni(BDC)(DABCO)]·(DMF)_{1.5}(H₂O)₂

Table S16: Exact amounts of reactants for the HT investigation of the effects of base amount in the system $\text{Ni}(\text{NO}_3)_2 \cdot 6\text{H}_2\text{O}/\text{H}_2\text{BDC}/\text{DABCO}/\text{DMF}$ at 110 °C with microwave heating (HT-MW) set-up.

Nr.	molar ratios			$\text{Ni}(\text{NO}_3)_2 \cdot 6\text{H}_2\text{O}^{\text{a}}$ μL	$\text{H}_2\text{BDC}^{\text{b}}$ μL	DABCO^{c} μL	excess solvent μL	stirring ^d	Reaction result/ substance appearance	XRPD
	$\text{Ni}(\text{NO}_3)_2 \cdot 6\text{H}_2\text{O}$	H_2BDC	DABCO							
1	1	1	0	200	300	0	1500	All reaction mixtures are magnetically stirred	green & whitish powder	low crystalline phase
2	1	1	0.5	200	300	100	1400		green powder	3a + 3b
3	1	1	1	200	300	200	1300		green powder	3b
4	1	1	1.5	200	300	300	1200		green powder	3b
5	1	1	2	200	300	400	1100		green powder	3b
6	1	1	2.5	200	300	500	1000		green powder	3b
7	1	1	3	200	300	600	900		green powder	3b
8	1	1	4	200	300	800	700		green powder	3b
9	1.5	1	0	300	300	0	1400		green & whitish powder	low crystalline phase
10	1.5	1	0.5	300	300	100	1300		green powder	3a + 3b
11	1.5	1	1	300	300	200	1200		green powder	3a + 3b
12	1.5	1	1.5	300	300	300	1100		green powder	3b
13	1.5	1	2	300	300	400	1000		green powder	3b
14	1.5	1	2.5	300	300	500	900		green powder	3b
15	1.5	1	3	300	300	600	800		green powder	3b
16	1.5	1	4	300	300	800	600		green powder	3b
17	2	1	0	400	300	0	1300	green & whitish powder	low crystalline phase	
18	2	1	0.5	400	300	100	1200	green powder	3a + 3b	
19	2	1	1	400	300	200	1100	green powder	3a + 3b	
20	2	1	1.5	400	300	300	1000	green powder	3a + 3b	
21	2	1	2	400	300	400	900	green powder	3b	
22	2	1	2.5	400	300	500	800	green powder	3b	
23	2	1	3	400	300	600	700	green powder	3b	
24	2	1	4	400	300	800	500	green powder	3b	

^a 0.5 M $\text{Ni}(\text{NO}_3)_2 \cdot 6\text{H}_2\text{O}$ in DMF

^b 0.33 M H_2BDC in DMF

^c 0.5 M DABCO in DMF

^d highest stirring rate is used

Reactor fill volume: 2000 μL (24-er HT-MW reactor)

Temperature profile:

heat-up phase = 3 °C/min to 110 °C

heating period = 1 h at 110 °C (microwave heating)

cooling phase = 3 °C/min to room temperature

3a : $[\text{Ni}_2(\text{BDC})_2(\text{DABCO})] \cdot (\text{DMF})_4(\text{H}_2\text{O})_{1.5}$

3b : $[\text{Ni}_2(\text{BDC})_2(\text{DABCO})] \cdot (\text{DMF})_4(\text{H}_2\text{O})_4$

Table S17: Exact amounts of reactants for the HT investigation of the stirring in the system Ni(NO₃)₂·6H₂O/H₂BDC/DABCO/DMF at 110 °C with microwave heating (HT-MW) set-up.

Nr.	molar ratios			Ni(NO ₃) ₂ ·6H ₂ O ^a μL	H ₂ BDC ^b μL	DABCO ^c μL	excess solvent μL	stirring ^d	Reaction result/ substance appearance	XRPD
	Ni(NO ₃) ₂ ·6H ₂ O	H ₂ BDC	DABCO							
1	2	2	1	400	600	200	800	no	green powder	(3a) ^e
2	2	2	1	400	600	200	800		green powder	(3a) ^e
3	2	2	1	400	600	200	800		green powder	(3a) ^e
4	2	2	1	400	600	200	800		green powder	(3a) ^e
5	2	2	1	400	600	200	800		green powder	(3a) ^e
6	2	2	1	400	600	200	800		green powder	(3a) ^e
7	2	2	1	400	600	200	800	yes	green powder	(3a + 3b) ^e
8	2	2	1	400	600	200	800		green powder	(3a + 3b) ^e
9	2	2	1	400	600	200	800		green powder	(3a + 3b) ^e
10	2	2	1	400	600	200	800		green powder	(3a + 3b) ^e
11	2	2	1	400	600	200	800		green powder	(3a + 3b) ^e
12	2	2	1	400	600	200	800		green powder	(3a + 3b) ^e
13	1	1	4	200	300	800	700	no	green powder	(3a + 3b) ^f
14	1	1	4	200	300	800	700		green powder	(3a + 3b) ^f
15	1	1	4	200	300	800	700		green powder	(3a + 3b) ^f
16	1	1	4	200	300	800	700		green powder	(3a + 3b) ^f
17	1	1	4	200	300	800	700		green powder	(3a + 3b) ^f
18	1	1	4	200	300	800	700		green powder	(3a + 3b) ^f
19	1	1	4	200	300	800	700	yes	green powder	3b
20	1	1	4	200	300	800	700		green powder	3b
21	1	1	4	200	300	800	700		green powder	3b
22	1	1	4	200	300	800	700		green powder	3b
23	1	1	4	200	300	800	700		green powder	3b
24	1	1	4	200	300	800	700		green powder	3b

^a 0.5 M Ni(NO₃)₂·6H₂O in DMF^b 0.33 M H₂BDC in DMF^c 0.5 M DABCO in DMF^d highest stirring rate is used^e **3a** is the major phase, **3b** is the minor phase^f **3b** is the major phase, **3a** is the minor phase

Reactor fill volume: 2000 μL (24-er HT-MW reactor)

Temperature profile:

heat-up phase = 3 °C/min to 110 °C

heating period = 1 h at 110 °C (microwave heating)

cooling phase = 3 °C/min to room temperature

3a : [Ni₂(BDC)₂(DABCO)]·(DMF)₄(H₂O)_{1.5}**3b** : [Ni₂(BDC)₂(DABCO)]·(DMF)₄(H₂O)₄

Table S18: Exact amounts of reactants for the HT study of the overall concentration in the system $\text{Ni}(\text{NO}_3)_2 \cdot 6\text{H}_2\text{O}/\text{H}_2\text{BDC}/\text{DABCO}/\text{DMF}$ at 110 °C with microwave heating (HT-MW) set-up.

Nr	molar ratios			$\text{Ni}(\text{NO}_3)_2 \cdot 6\text{H}_2\text{O}^a$	H_2BDC^b	DABCO^c	excess solvent	stirring ^d	Reaction result/ substance appearance	PXRD
	$\text{Ni}(\text{NO}_3)_2 \cdot 6\text{H}_2\text{O}$	H_2BDC	DABCO							
1	2	2	1	20	25	5	1950	no	green powder	(3b)
2	2	2	1	40	50	10	1900		green powder	(3b)
3	2	2	1	100	125	25	1750		green powder	(3a + 3b)^f
4	2	2	1	200	250	50	1500		green powder	(3a + 3b)^e
5	2	2	1	400	500	100	1000		green powder	(3a)
6	2	2	1	800	1000	200	0		green powder	(3a)
7	2	2	1	20	25	5	1950	yes	green powder	(3b)
8	2	2	1	40	50	10	1900		green powder	(3b)
9	2	2	1	100	125	25	1750		green powder	(3a + 3b)^f
10	2	2	1	200	250	50	1500		green powder	(3a + 3b)
11	2	2	1	400	500	100	1000		green powder	(3a + 3b)^e
12	2	2	1	800	1000	200	0		green powder	(3a)
13	1	1	4	10	13	20	1958	no	green powder	(3b)
14	1	1	4	20	25	40	1915		green powder	(3b)
15	1	1	4	50	63	100	1788		green powder	(3a + 3b)^f
16	1	1	4	100	125	200	1575		green powder	(3a + 3b)^f
17	1	1	4	200	250	400	1150		green powder	(3a + 3b)
18	1	1	4	400	500	800	300		green powder	(3a + 3b)^e
19	1	1	4	10	13	20	1958	yes	green powder	3b
20	1	1	4	20	25	40	1915		green powder	3b
21	1	1	4	50	63	100	1788		green powder	3b
22	1	1	4	100	125	200	1575		green powder	3b
23	1	1	4	200	250	400	1150		green powder	(3b + 3c)^g
24	1	1	4	400	500	800	300		pale green powder	(3c)

^a 0.5 M $\text{Ni}(\text{NO}_3)_2 \cdot 6\text{H}_2\text{O}$ in DMF

^b 0.4 M H_2BDC in DMF

^c 1.0 M DABCO in DMF

^d highest stirring rate is used

^e **3a** is the major phase, **3b** is the minor phase

^f **3b** is the major phase, **3a** is the minor phase

^g **3b** is the major phase, **3c** is the minor phase

Reactor fill volume: 2000 μL (24-er HT-MW reactor)

Temperature profile:

heat-up phase = 3 °C/min to 110 °C

heating period = 1 h at 110 °C (microwave heating)

cooling phase = 3 °C/min to room temperature

3a : $[\text{Ni}_2(\text{BDC})_2(\text{DABCO})] \cdot (\text{DMF})_4(\text{H}_2\text{O})_{1.5}$

3b : $[\text{Ni}_2(\text{BDC})_2(\text{DABCO})] \cdot (\text{DMF})_4(\text{H}_2\text{O})_4$

3c : $[\text{Ni}(\text{BDC})(\text{DABCO})] \cdot (\text{DMF})_{1.5}(\text{H}_2\text{O})_2$

Table S19: Exact amounts of reactants for the HT investigation of the effects of Ni(II) salt anions in the system Ni(NO₃)₂·6H₂O/H₂BDC/DABCO/DMF at 110 °C with microwave heating (HT-MW) set-up.

Nr.	molar ratios			nickel salt type	(Ni ²⁺) ^a μL	H ₂ BDC ^b μL	DABCO ^c μL	excess solvent μL	stirring ^d	Reaction result/ substance appearance	XRPD
	Ni ²⁺	H ₂ BDC	DABCO								
1	2	2	1	Ni(NO ₃) ₂ ·6H ₂ O	400	600	200	800	no	green powder	(3a) ^e
2	2	2	1		400	600	200	800		green powder	(3a) ^e
3	2	2	1		400	600	200	800		green powder	(3a) ^e
4	2	2	1		400	600	200	800		green powder	(3a)
5	2	2	1		400	600	200	800		green powder	(3a)
6	2	2	1		400	600	200	800		green powder	(3a)
7	2	2	1	Ni(NO ₃) ₂ ·6H ₂ O	400	600	200	800	yes	green powder	(3a) ^e
8	2	2	1		400	600	200	800		green powder	(3a) ^e
9	2	2	1		400	600	200	800		green powder	(3a) ^e
10	2	2	1		400	600	200	800		green powder	(3a + 3b)
11	2	2	1		400	600	200	800		green powder	(3a + 3b)
12	2	2	1		400	600	200	800		green powder	(3a + 3b)
13	1	1	4	Ni(NO ₃) ₂ ·6H ₂ O	200	300	800	700	no	green powder	(3a + 3b) ^e
14	1	1	4		200	300	800	700		green powder	(3a + 3b) ^e
15	1	1	4		200	300	800	700		green powder	(3a + 3b) ^e
16	1	1	4		200	300	800	700		green powder	(3a + 3b)
17	1	1	4		200	300	800	700		green powder	(3a + 3b)
18	1	1	4		200	300	800	700		green powder	(3a + 3b)
19	1	1	4	Ni(NO ₃) ₂ ·6H ₂ O	200	300	800	700	yes	green powder	3b + [(H ₂ DABCO)(BDC)] ^f
20	1	1	4		200	300	800	700		green powder	3b + [(H ₂ DABCO)(BDC)] ^f
21	1	1	4		200	300	800	700		green powder	3b + [(H ₂ DABCO)(BDC)] ^f
22	1	1	4		200	300	800	700		green powder	3b
23	1	1	4		200	300	800	700		green powder	3b
24	1	1	4		200	300	800	700		green powder	3b

^a 0.5 M Ni(NO₃)₂·6H₂O in DMF, 0.5 M NiSO₄·6H₂O in DMF respectively

^b 0.33 M H₂BDC in DMF

^c 0.5 M DABCO in DMF

^d highest stirring rate is used

^e crystallinity of compounds produced with sulfate salt is generally low than ones with nitrate salt.

^f [(H₂DABCO)(BDC)] organic salt compound with the CCDC code: HOFLIY.^[S2]

Reactor fill volume: 2000 μL (24-er HT-MW reactor)

Temperature profile:

heat-up phase = 3 °C/min to 110 °C

heating period = 1 h at 110 °C (microwave heating)

cooling phase = 3 °C/min to room temperature

3a : [Ni₂(BDC)₂(DABCO)]·(DMF)₄(H₂O)_{1.5}

3b : [Ni₂(BDC)₂(DABCO)]·(DMF)₄(H₂O)₄

Figure S1: Scanning electron microscope (SEM) and optical microscope images of selected compounds.

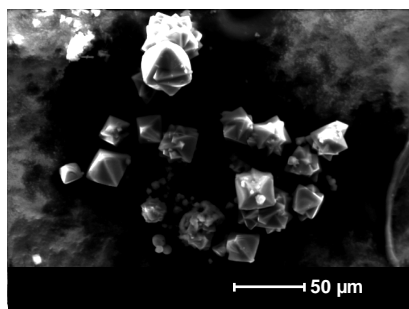
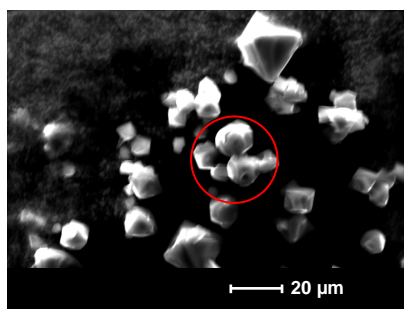
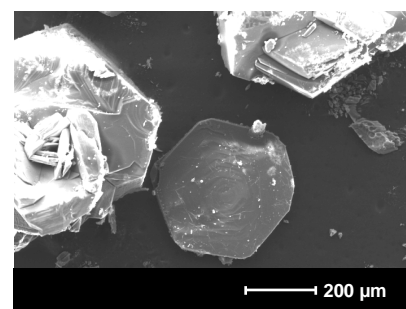
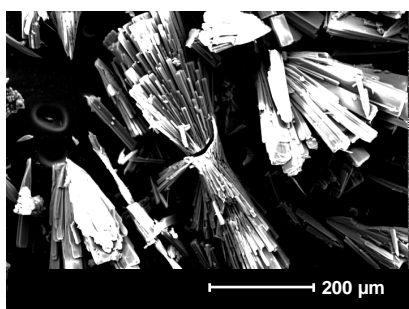
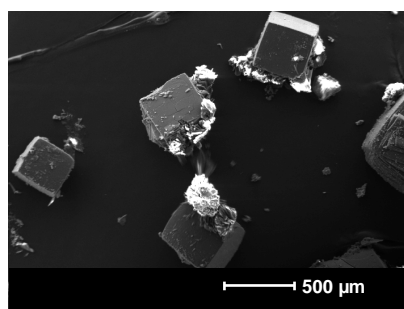
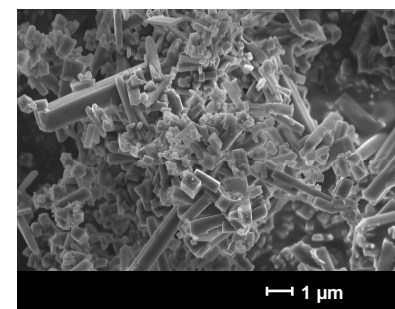
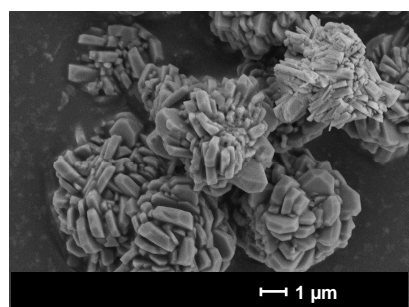
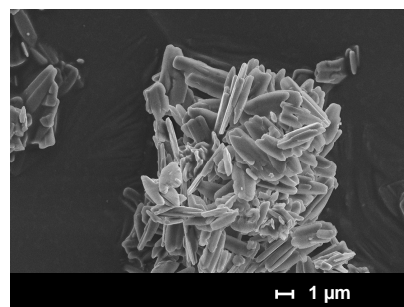
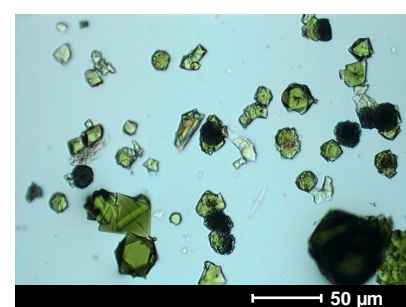
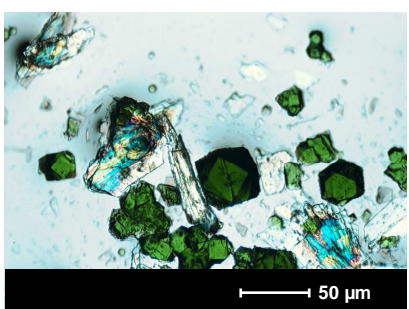
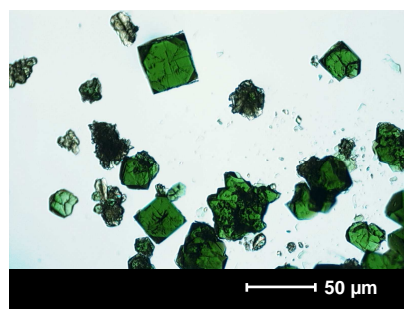
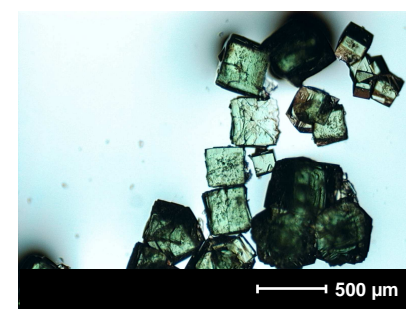
(a) : octahedral crystals of **1a**
(synthesis at 160 °C)(b) : sphere-like crystal morphology
of **1a** (synthesis at 180 °C)(c) : hexagonal plates of **1b**(d) : rod-like crystals of **1c**(e) : block crystals of **2**(f) : microcrystalline powder of **3a**(g) : microcrystalline powder of **3b**(h) : microcrystalline powder of **3c**(i) : crystals of **1a** (octahedral
morphology)(j) : crystals of **1a** (cuboctahedral
morphology)(k) : crystals of **1a** (truncated cube
morphology)(l) : crystals of **2** (cube morphology)

Figure S2: Color changes of compound **1a** and **2**.

dark green color
(as-synthesized)



dark red color
(after activation)
150 °C 12 h



light green color (after
activation and
exposure to air),
X-ray amorphous



dark brown color (as-
synthesized) changes to
green upon exposure to
air



dark red-brown
color (after
activation)
150 °C 12h



light green color
(after activation and
exposure to air),
crystalline



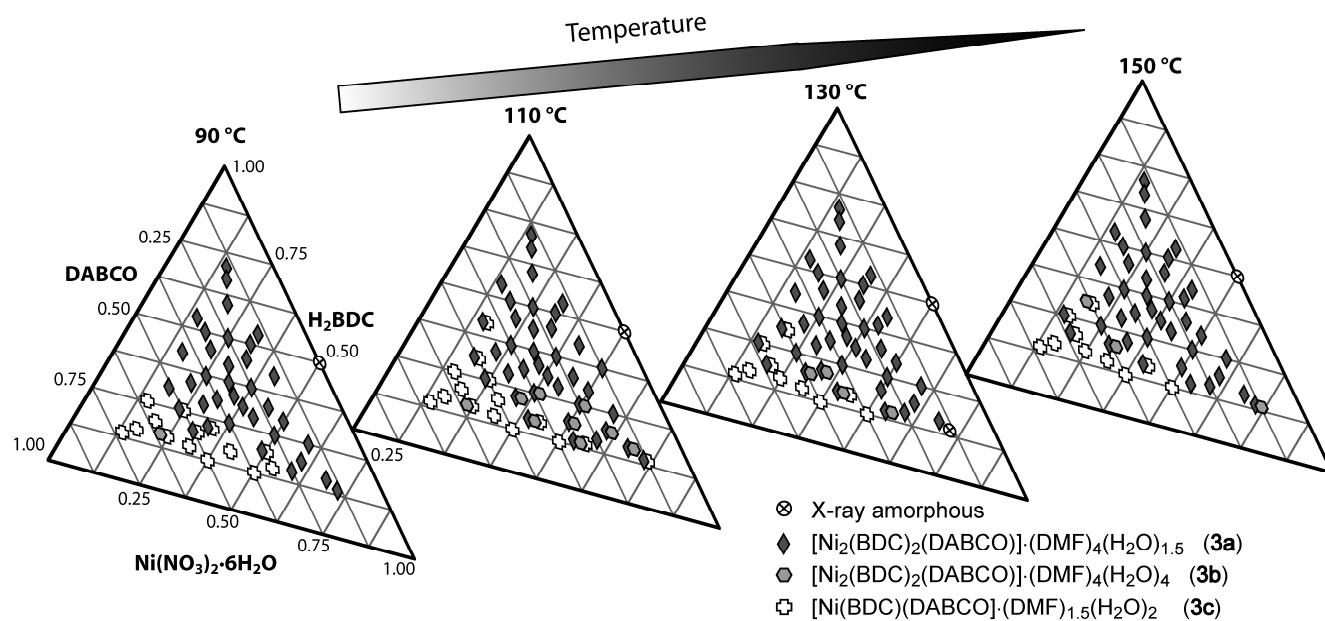


Figure S3: Crystallization diagram of the system $\text{Ni}(\text{NO}_3)_2 \cdot 6\text{H}_2\text{O}$ / H_2BDC / DABCO in the temperature range of 90° - 150 °C in steps of 20 °C. All reactions were subjected to 48 hours of constant reaction temperature and 12 hours of cooling step.

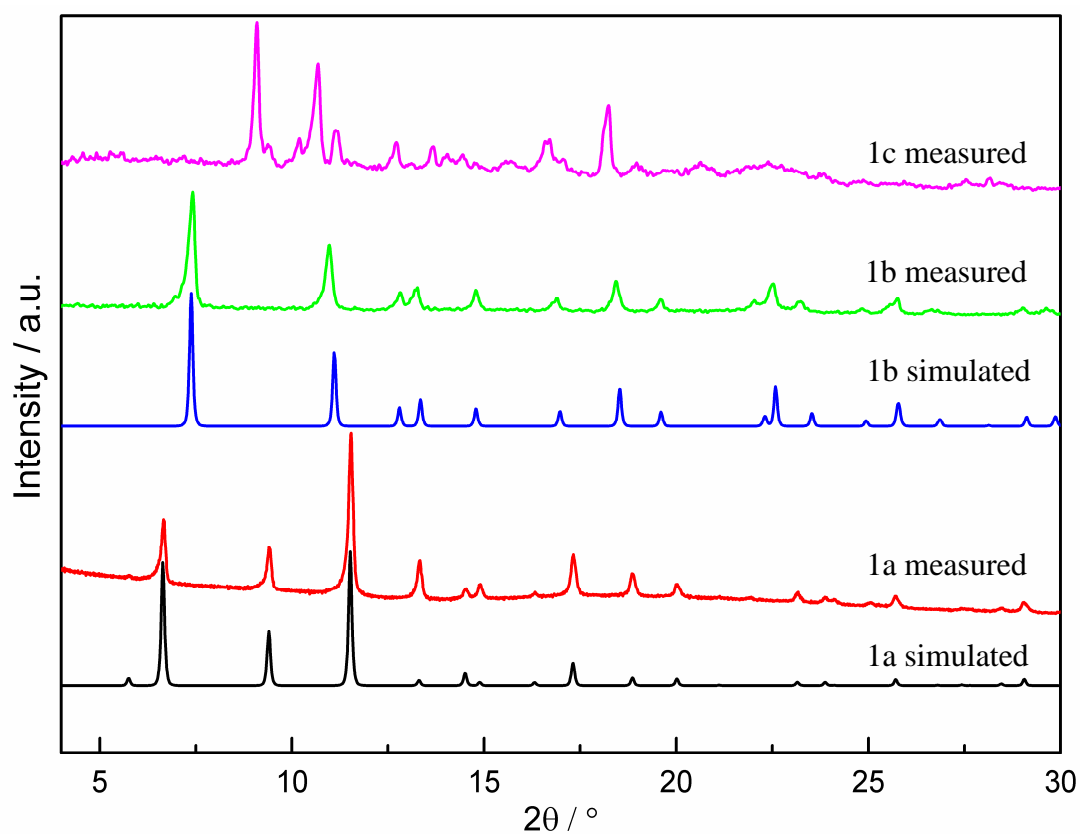


Figure S4: Measured and simulated XRPD patterns for compounds $[\text{Ni}_3(\text{BTC})_2(\text{Me}_2\text{NH})_3] \cdot (\text{DMF})_4(\text{H}_2\text{O})_4$ (**1a**) and $[\text{Ni}_6(\text{BTC})_2(\text{DMF})_6(\text{HCOO})_6]$ (**1b**). XRPD measurement of **1c** is unsatisfactory due to rapid decomposition upon exposure to air.

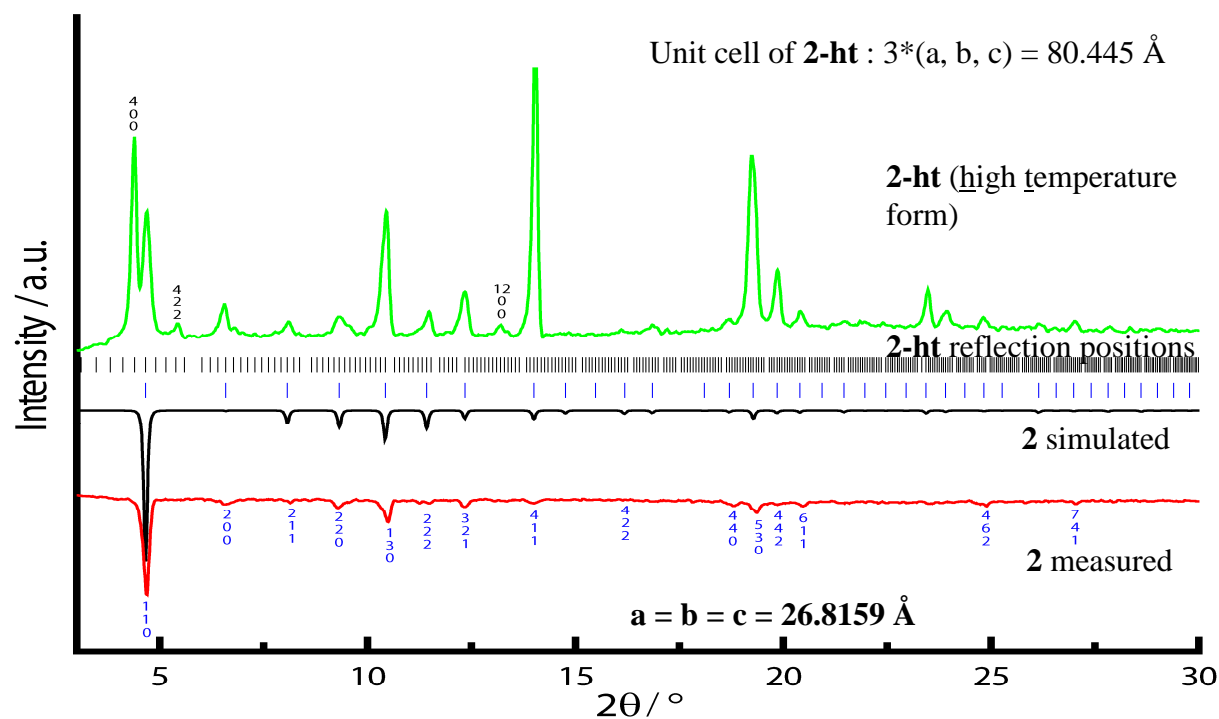


Figure S5. Measured and simulated powder XRPD patterns for **2**. New reflections observed for compound **2** activated at high temperature ($> 100 \text{ }^\circ\text{C}$) which corresponds to the reflection positions of an isomorphic enlarged unit cell (**2-ht**) in the space group $Im\bar{3}$ with cell parameters $3 \cdot (a, b, c)$ (black ticks).^[S3]

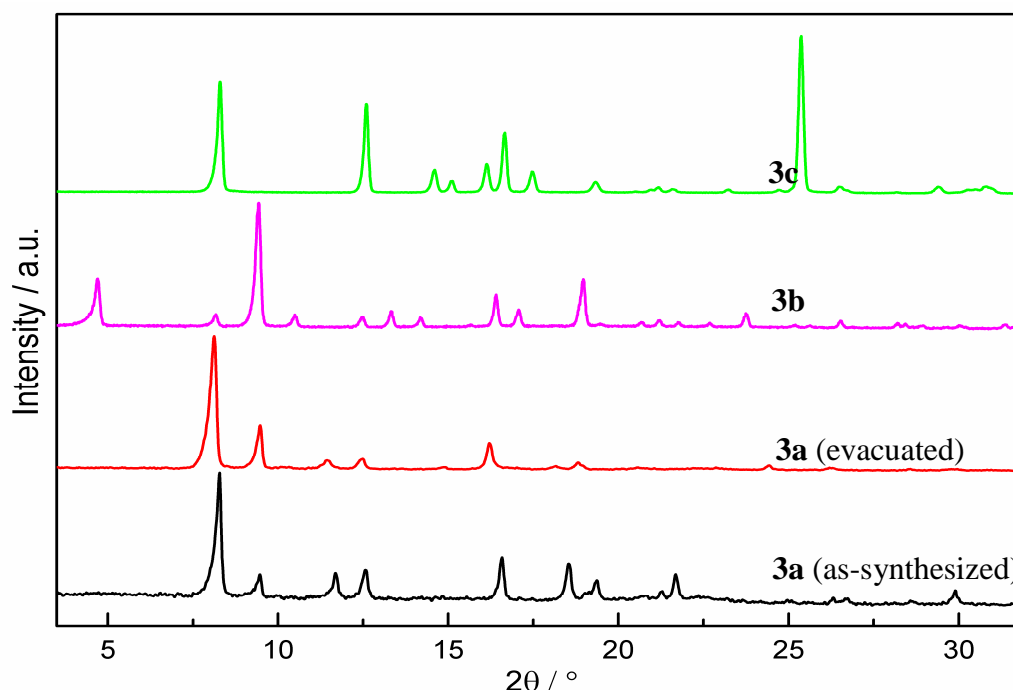


Figure S6. XRPD measurements of $[\text{Ni}_2(\text{BDC})_2(\text{DABCO})] \cdot (\text{DMF})_4(\text{H}_2\text{O})_{1.5}$ (**3a**, as-synthesized and evacuated form), $[\text{Ni}_2(\text{BDC})_2(\text{DABCO})] \cdot (\text{DMF})_4(\text{H}_2\text{O})_4$ (**3b**) and $[\text{Ni}(\text{BDC})(\text{DABCO})] \cdot (\text{DMF})_{1.5}(\text{H}_2\text{O})_2$ (**3c**).

[S3] Wondratschek, H.; Müller, U. *International Tables for Crystallography*; Vol. A1, Kluwer Academic Publishers: Dordrecht, 2006, pp. 689.

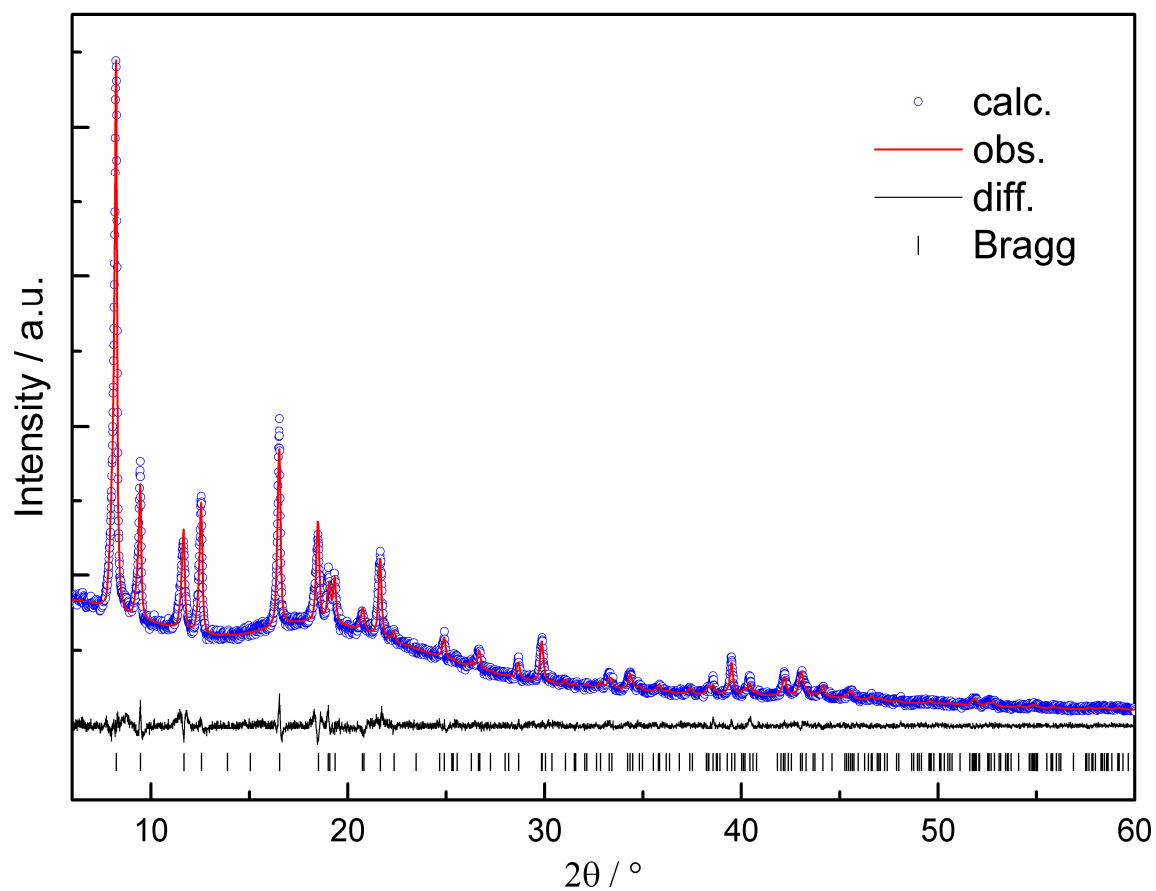


Figure S7: Final Rietveld plot of **3a**. The structure model is based on the isostructural Zn compound.^[S4]

[S4] D. N. Dybtsev, H. Chun, K. Kim, *Angew. Chem., Int. Ed.* **2004**, *43*, 5033-5036; *Angew. Chem.* **2004**, *116*, 5143-5146.

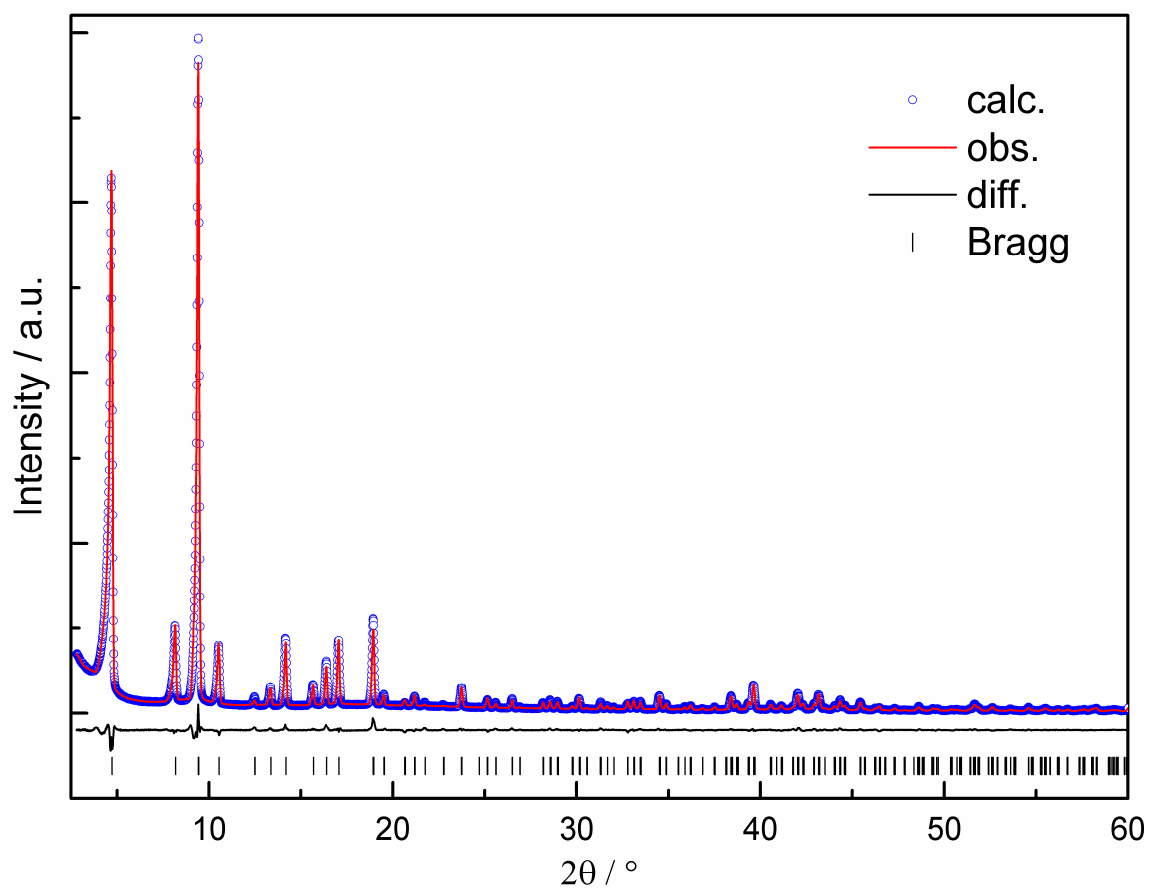
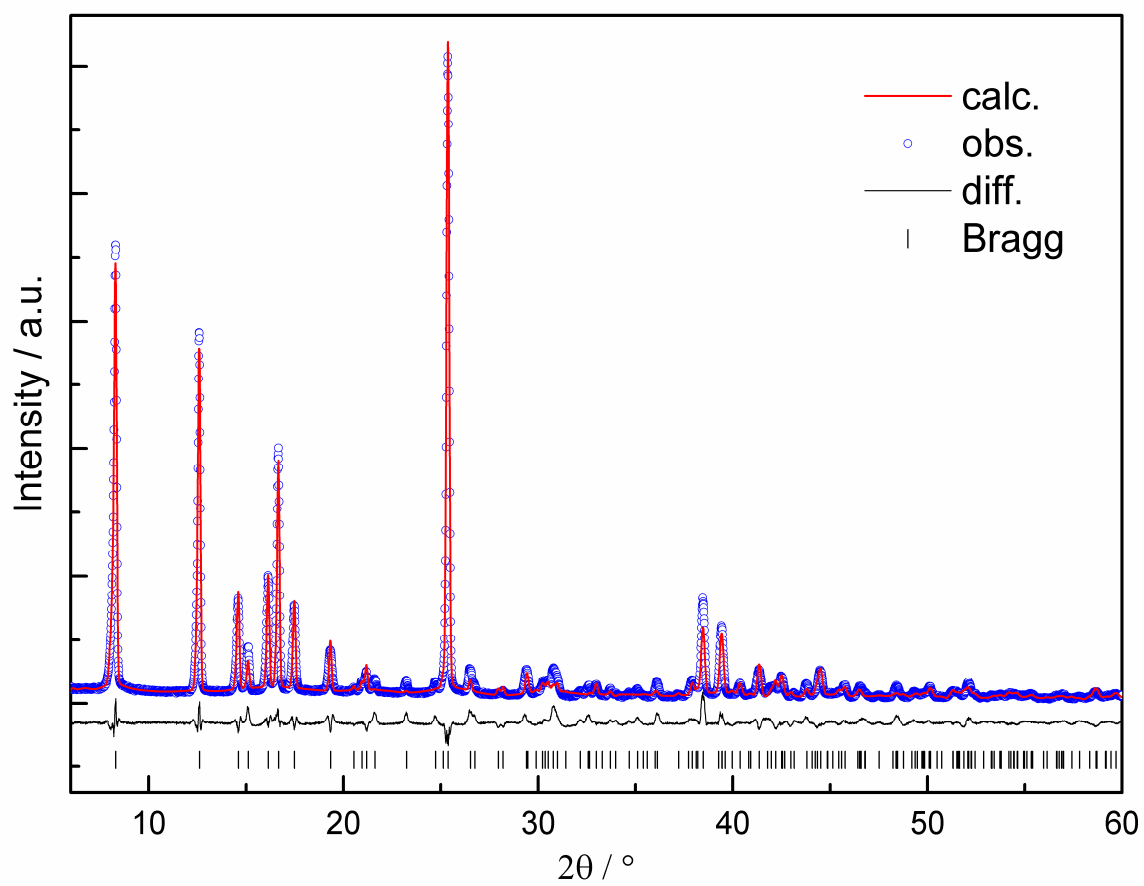


Figure S8: Final Rietveld plot of **3b**. The structure model is based on the isostructural Zn compound.^[S5]

[S5] Chun, H.; Moon, J. *Inorg. Chem.* **2007**, *46*, 4371-4373.

Figure S9: Final Rietveld plot of **3c**.

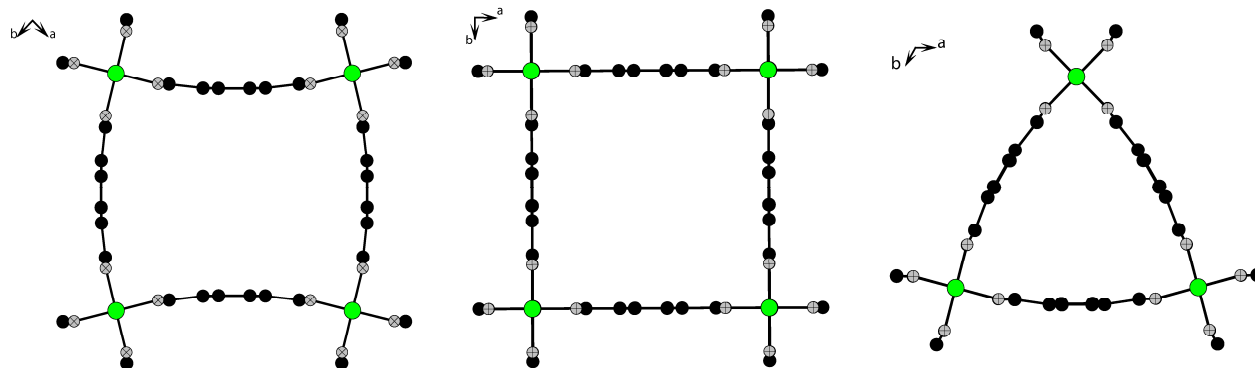


Figure S10: Cages of observed in as-synthesized **3a** (left) and evacuated **3a** (middle) with C_4 -symmetry. Trigonal cage of **3b** which exhibits C_3 -symmetry (right).

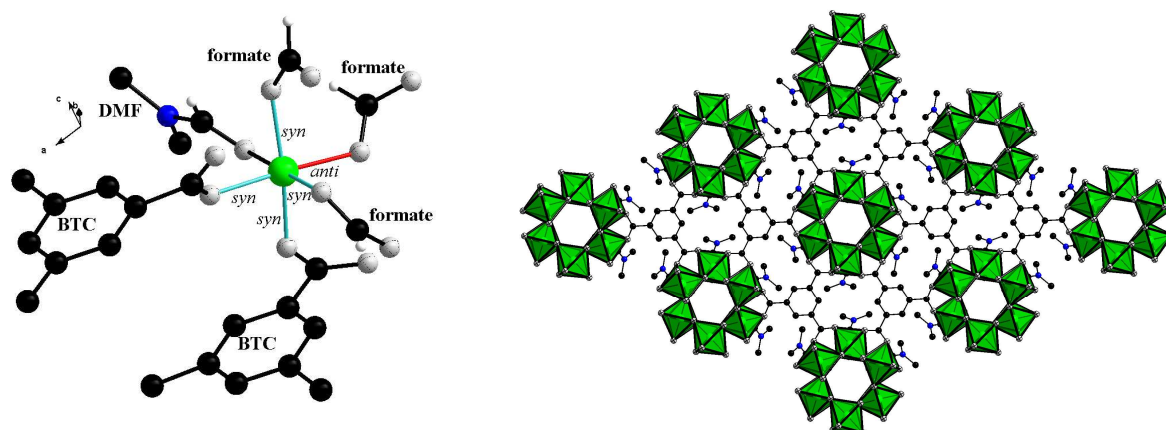


Figure S11: Left: Types of carboxylate ion bonding to Ni^{2+} ion. Right: A section of the crystal structure of $[\text{Ni}_6(\text{BTC})_2(\text{DMF})_6(\text{HCOO})_6]$ (**1b**) with 2D layered networks (view along [001]).

Table S20. Bond lengths in the Ni(II) paddle-wheel units of **1a**, **2**, **3a** and **3b**.

Bond type	1a (Å)	2 (Å)	3a (Å)	3b (Å)
Ni-Ni	2.712(1)	2.846(1)	2.683(8)	2.589(3)
Ni-O (equatorial)	2.009(3)	2.049(3)	1.966(10)	O1: 1.974(4) O2: 1.993(3)
Ni-O (axial)	-	1.982(8)	-	-
Ni-N (axial)	1.976(5)	2.005(8)	2.053(14)	2.041(5)

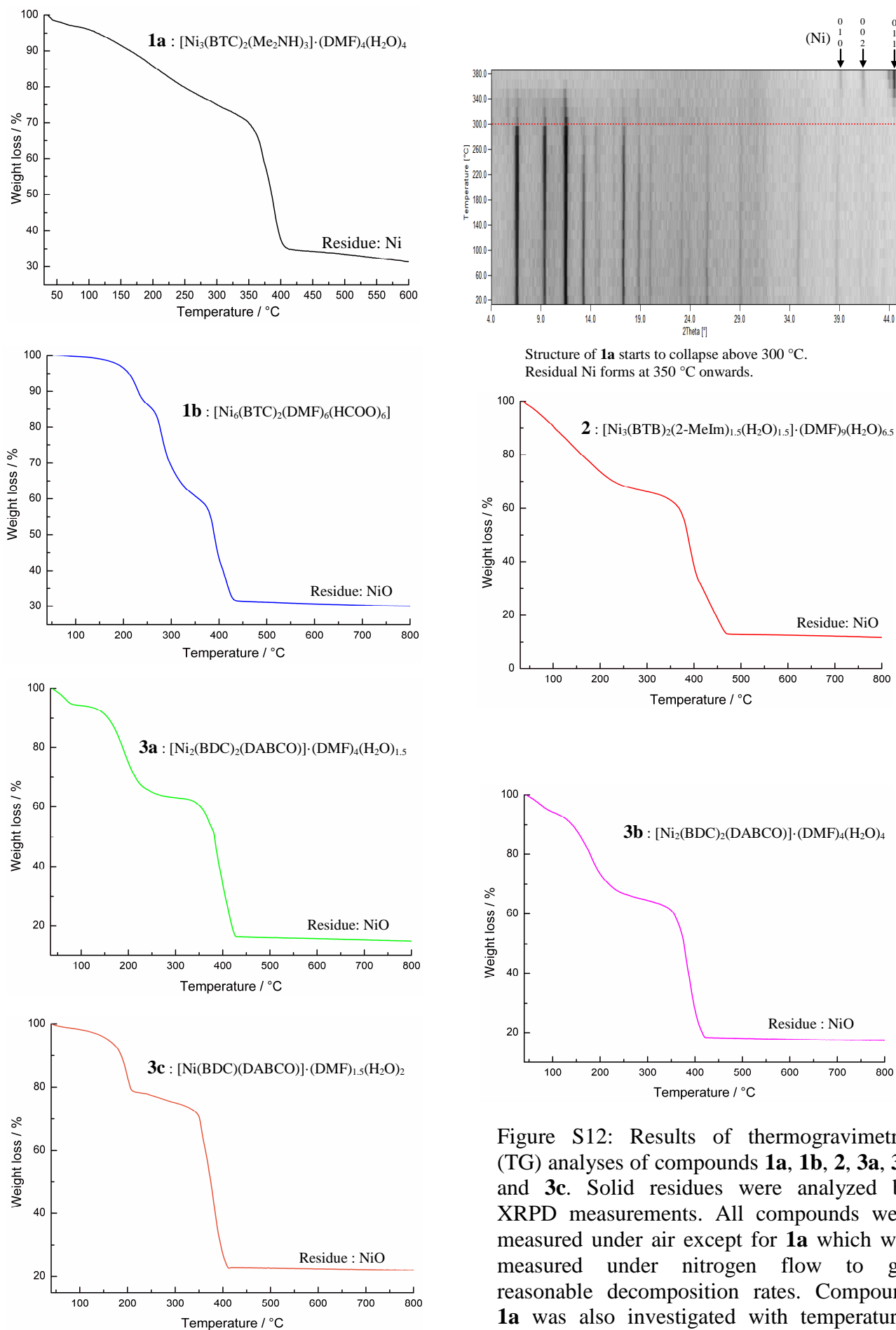


Figure S12: Results of thermogravimetric (TG) analyses of compounds **1a**, **1b**, **2**, **3a**, **3b** and **3c**. Solid residues were analyzed by XRPD measurements. All compounds were measured under air except for **1a** which was measured under nitrogen flow to get reasonable decomposition rates. Compound **1a** was also investigated with temperature-dependent XRPD analysis.

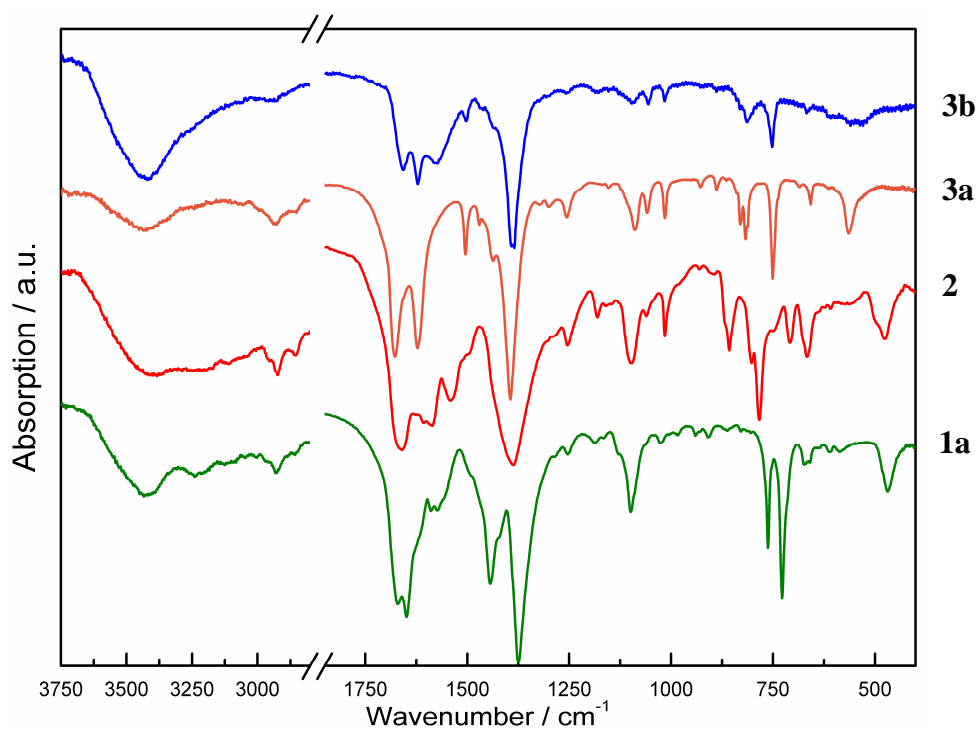
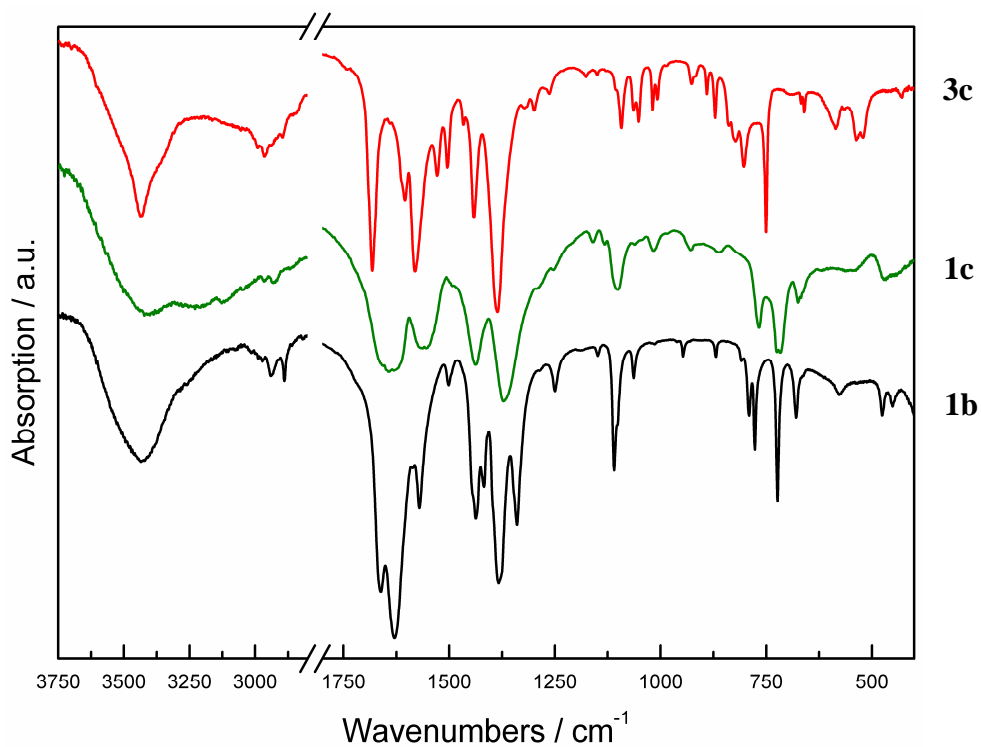
Figure S13: IR spectra of paddle-wheel based compounds **1a**, **2**, **3a** and **3b**.Figure S14: IR spectra of non paddle-wheel based compounds **1b**, **1c** and **3c**.

Table S21: Comparison of synthesis conditions and nitrogen sorption properties between porous nickel(II) MOFs from this work with isostructural compounds.

compound	synthesis method	synthesis temperature, time, solvent,	BET surface area (m ² /g), micropore volume (cm ³ /g)
1a	solvothermal, conventional heating	170 °C, 48 h, DMF	920, 0.35
1a-Cu (HKUST-1) ^[S6]	solvothermal, conventional heating	180 °C, 12 h, H ₂ O + EtOH (1:1, v:v)	692, 0.33
1a-Cu (HKUST-1) ^[S7]	electrochemical	25 °C, 2.5 h, MeOH	1820 _{Langmuir} , -
1a-Cu (HKUST-1) ^[S8]	ambient pressure at reflux	-, 6 h, DMF	1239, 0.62
1a-Cu (HKUST-1) ^[S9]	microwave assisted heating	140 °C, 1 h, H ₂ O + EtOH	1392, 0.56
1a-Cu (HKUST-1) ^[S10]	mechanochemical	-, 20 min, DMF	1421, 0.74
1a-Cu (HKUST-1) ^[S11]	sonochemical	-, 1 h, H ₂ O + EtOH	1100, 0.57
1a-Mo ^[S12]	solvothermal, conventional heating	150 °C, 200 h, DMF	1280, 0.67
1a-Fe ^[S13]	solvothermal, conventional heating	150 °C, 96 h, DMF	-, -
1a-Cr ^[S14]	solvothermal, conventional heating	~150 °C, 72 h, DMF	1810, -
2	solvothermal, conventional heating	170 °C, 48 h, DMF	0, 0
2-Cu (MOF-14) ^[S15]	conventional heating	65 °C, 24 h, DMF + EtOH + H ₂ O (3:3:2, v:v)	1502 (Langmuir), 0.53
3a	microwave assisted heating	110 °C, 1 h, DMF	1807, 0.66
3a-Cu ^[S16]	only stirring	25 °C, > 48 h, H ₂ O + MeOH + pyridine	1300, 0.63
3a-Zn ^[S16]	only stirring	25 °C, > 48 h, H ₂ O + MeOH + pyridine + benzene	1165, 0.63
3a-Co ^[S16]	conventional heating	65 °C, > 48 h, H ₂ O + MeOH + pyridine	1595, 0.77
3b	microwave assisted heating	110 °C, 1 h, DMF	1231, 0.53
3b-Zn ^[S5]	conventional heating	110 °C, 48 h, DMF + CH ₃ CN (4:1, v:v)	1603, 0.86

[S6] Chui, S. S.-Y.; Lo, S. M.-F.; Charmant, J. P. H.; Guy Orpen, A.; Williams, I. D. *Science*, **1999**, 283, 1148-1150.

[S7] Mueller, U.; Schubert, M.; Teich, F.; Puetter, H.; Schierle-Arndt, K.; Pastré, J. *J. Mater. Chem.* **2006**, 16, 626-636.

[S8] Krawiec, P.; Kramer, M.; Sabo, M.; Kunschke, R.; Fröde, H.; Kaskel, S.; *Adv. Eng. Mater.* **2006**, 8, 293-296.

[S9] Seo, Y. K.; Hundal, G.; Jang, I. T.; Hwang, Y. K.; Jun, C. H.; Chang, J. S.; *Micropor. Mesopor. Mater.* **2009**, 119, 331-336.

[S10] Schlesinger, M.; Schulze, S.; Hietschold, M.; Mehring, M.; *Micropor. Mesopor. Mater.* **2010**, 132, 121-127.

[S11] Li, Z.-Q.; Qiu, L.-G.; Xu, T.; Wu, Y.; Wang, W.; Wu, Z.-Y.; Jiang, X.; *Mater. Lett.* **2009**, 63, 78-80.

[S12] Kramer, M.; Schwarz, U.; Kaskel, S. *J. Mater. Chem.* **2006**, 16, 2245-2248.

- [S13] Xie, L.; Liu, S.; Gao, C.; Cao, R.; Cao, J.; Sun, C.; Su, Z. *Inorg. Chem.* **2007**, *46*, 7782-7788.
- [S14] Murray, L. J.; Dinca, M.; Yano, J.; Chavan, S.; Bordiga, S.; Brown, C. M.; Long, J. R. *J. Am. Chem. Soc.* **2010**, *132*, 7856-7857.
- [S15] Chen, B.; Eddaoudi, M.; Hyde, S. T.; O'Keeffe, M.; Yaghi, O. M. *Science*, **2001**, *291*, 1021-1023.
- [S16] Takei, T.; Kawashima, J.; Ii, T.; Maeda, A.; Hasegawa, M.; Kitagawa, T.; Ohmura, T.; Ichikawa, M.; Hosoe, M.; Kanoya, I.; Mori, W. *Bull. Chem. Soc. Jpn.* **2008**, *81*, 847-856.

Appendix 5

Supporting Information

P. Maniam, N. Stock, *Acta Cryst.* **2011**, *E67*, m669-m670.

Poly[(μ^3 -benzene-1,3,5-tricarboxylato- κ^3 O¹:O³:O⁵)(μ^2 -2-methylimidazolato- κ^2 N:N')tris(2-methylimidazole- κ N)dizinc(II)]

Palanikumar Maniam and Norbert Stock*

Institute of Inorganic Chemistry,
Christian-Albrechts-University Kiel, Max-Eyth-Straße 2, D-24118 Kiel,

* Prof. Dr. Norbert Stock, Tel.: +49-431-880-1675, Fax: +49-431-880-1775.

e-mail: stock@ac.uni-kiel.de

Acta Cryst. (2011). E67, m669-m670 [doi:10.1107/S1600536811015844]

Poly[(μ_3 -benzene-1,3,5-tricarboxylato- $\kappa^3 O^1:O^3:O^5$)(μ_2 -2-methylimidazolato- $\kappa^2 N:N'$)tris(2-methylimidazole- κN)dizinc(II)]

P. Maniam and N. Stock

Comment

Metal-organic frameworks (MOF) are being investigated intensively, mainly for their high specific surface areas (Li *et al.*, 1999; Kitagawa *et al.*, 2004). In our workgroup, we are interested in using organic ligands containing multiple functional groups as the linkers for the MOFs. We employ high-throughput (HT) methods, which allow the rapid and systematic investigation of compound formation fields (Stock, 2010; Maniam *et al.*, 2010). HT-screening of various first row transition metal ions with trisodium benzene-1,3,5-tricarboxylate (Na₃BTC) and 2-methylimidazole (2-MeImH) has yielded the colourless block crystals of (I). The asymmetric unit of compound (I) consists of two crystallographically independent Zn²⁺ ions, one fully deprotonated (BTC)³⁻, one 2-methylimidazolate (2-MeIm)⁻ ion and three 2-MeImH ligands (Fig. 1). The Zn²⁺ ions are tetrahedrally coordinated by oxygen atoms originating from (BTC)³⁻ and nitrogen atoms from (2-MeIm)⁻ and 2-MeImH. The Zn...O bond distances lie between 1.942 (3)–1.976 (2) Å which are slightly shorter than Zn...N bonds of 1.971 (3)–2.027 (3) Å. The bond angles in ZnN₃O tetrahedra ranges between 100.42 (14)–116.61 (16)° while in ZnN₂O₂, the bond angles of 96.73 (13)–122.12 (11)° are observed (Tab. 1 & Tab. 2). It was also observed that Zn-(2-MeIm)⁻—Zn angle lies at 146.8 (1)° which is close to 145° angles in zeolitic imidazolate frameworks and zeolite structures (Park *et al.*, 2006). The C=O and C—O bonds in the carboxylate groups can be clearly distinguished from each other by their bond lengths of 1.229 (5)–1.236 (5) Å and 1.266 (4)–1.275 (4) Å, respectively. Weak hydrogen bonds in the 2.6 < *d*(O...H—N) < 3.0 Å range are observed between the O atoms of the carboxylate ions and N—H groups of the 2-MeImH ligands (Fig. 2).

By considering the ZnN₃O and ZnN₂O₂ tetrahedra bridged by the (2-MeIm)⁻ as a Zn-(2-MeIm)-Zn dimer, this dimer is connected to three terminal 2-MeImH ligands and three (BTC)³⁻ ions. Each (BTC)³⁻ ion is then further connected to two Zn-(2-MeIm)-Zn dimers (Fig. 3) and layers in the *bc* plane are formed. Through extensive O...H—N hydrogen bonding, the layers are interconnected along the *a*-axis to form a dense three-dimensional crystal structure (Fig. 4, Tab. 2).

Experimental

All reagents were of analytical grade (Aldrich and Fluka) and were used without further purification. High-throughput (HT) experiments in 300 ml Teflon-lined reactors yielded the crystals of compound (I). The reaction mixture consisted of zinc(II) nitrate hexahydrate (5.9 mg, 0.02 mmol), Na₃(BTC) (2.76 mg, 0.01 mmol), 2-methylimidazole (4.11 mg, 0.05 mmol) and deionized water (200 ml). The mixture was heated in a 300 µl Teflon-lined high-throughput reactor at 423 K for 48 h (Stock, 2010). The mixture was cooled to room temperature over a period of 12 h and colourless plate-like crystals were obtained.

Refinement

All H atoms were located in difference Fourier maps. Idealized values for the bond lengths (C—H = 0.93 Å and N—H = 0.86 Å) and angles were used and the H-atom parameters were refined using a riding model. The highest peak of 0.47 e Å⁻³ in the residual electron density map is located 0.82 Å from N1H and the deepest hole of 0.54 e Å⁻³ is located 0.69 Å from Zn1.

Figures

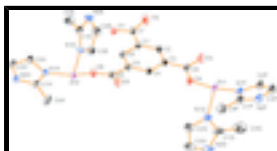


Fig. 1. The asymmetric unit of (I), showing the atom-labelling scheme. Displacement ellipsoids are drawn at the 30% probability level and H atoms are omitted for clarity.

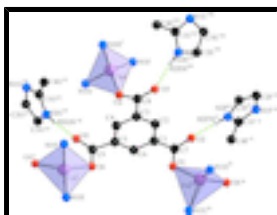


Fig. 2. The tetrahedral coordination environment of the Zn1 and Zn2 ions. Green broken lines indicate the weak hydrogen bonds between the carboxylate groups of the (BTC)³⁻ ions and H—N groups of the 2-MeImH ligands. [Symmetry codes: (i) $-x + 3/2, y + 1/2, z$; (ii) $x, -y, z + 1/2$; (iii) $x, -y, z - 1/2$; (iv) $-x + 3/2, y - 1/2, z$; (v) $x + 1/2, -y + 1/2, -z$; (vi) $-x + 1, y, -z - 1/2$; (vii) $-x + 1, y, -z + 1/2$; (viii) $x - 1/2, -y + 1/2, -z$.]

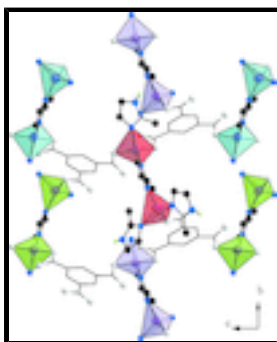


Fig. 3. Ball-and-stick representation for (I) showing the interconnection of Zn-(2-MeIm)-Zn dimers (marked as differently colored polyhedra) by (BTC)³⁻ ions and thus forming a layered arrangement in the *b,c* plane. Zn: purple, O: grey, N: blue, C: black and H: green. Hydrogen atoms of (BTC)³⁻ are omitted for clarity.

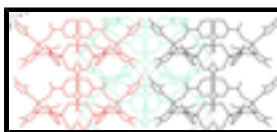


Fig. 4. Layer packing diagram of compound (I). All atoms of one layer are presented by the same colour. H-bonds (see Fig. 2) between the layers are depicted by black broken lines.

Poly[(μ_3 -benzene-1,3,5-tricarboxylato- $\kappa^3 O^1:O^3:O^5$)(μ_2 -2-methylimidazolato- $\kappa^2 N:N'$)tris(2-methylimidazole- κN)dizinc(II)]

Crystal data

[Zn₂(C₉H₃O₆)(C₄H₅N₂)(C₄H₆N₂)₃]

$M_r = 665.28$

Orthorhombic, *Pbcn*

Hall symbol: -P 2n 2ab

$a = 18.9722$ (6) Å

$b = 18.2247$ (4) Å

$F(000) = 2720$

$D_x = 1.544$ Mg m⁻³

Mo *K* α radiation, $\lambda = 0.71073$ Å

Cell parameters from 40409 reflections

$\theta = 1.6$ – 29.7°

$\mu = 1.73$ mm⁻¹

$c = 16.5585$ (4) Å
 $V = 5725.3$ (3) Å³
 $Z = 8$

$T = 293$ K
 Block, colourless
 $0.16 \times 0.09 \times 0.07$ mm

Data collection

Stoe IPDS-1 diffractometer
 Radiation source: fine-focus sealed tube
 graphite
 φ scans
 Absorption correction: numerical (*X-RED* and *X-SHAPE*; Stoe & Cie, 2008)
 $T_{\min} = 0.684$, $T_{\max} = 0.814$
 38494 measured reflections

7732 independent reflections
 6222 reflections with $I > 2\sigma(I)$
 $R_{\text{int}} = 0.050$
 $\theta_{\max} = 29.3^\circ$, $\theta_{\min} = 1.6^\circ$
 $h = -26 \rightarrow 26$
 $k = -24 \rightarrow 23$
 $l = -16 \rightarrow 22$

Refinement

Refinement on F^2
 Least-squares matrix: full
 $R[F^2 > 2\sigma(F^2)] = 0.061$
 $wR(F^2) = 0.143$
 $S = 1.13$
 7732 reflections
 370 parameters
 0 restraints

Primary atom site location: structure-invariant direct methods
 Secondary atom site location: difference Fourier map
 Hydrogen site location: inferred from neighbouring sites
 H-atom parameters constrained
 $w = 1/[\sigma^2(F_o^2) + (0.0602P)^2 + 8.9412P]$
 where $P = (F_o^2 + 2F_c^2)/3$
 $(\Delta/\sigma)_{\max} < 0.001$
 $\Delta\rho_{\max} = 0.47 \text{ e \AA}^{-3}$
 $\Delta\rho_{\min} = -0.54 \text{ e \AA}^{-3}$

Special details

Geometry. All e.s.d.'s (except the e.s.d. in the dihedral angle between two l.s. planes) are estimated using the full covariance matrix. The cell e.s.d.'s are taken into account individually in the estimation of e.s.d.'s in distances, angles and torsion angles; correlations between e.s.d.'s in cell parameters are only used when they are defined by crystal symmetry. An approximate (isotropic) treatment of cell e.s.d.'s is used for estimating e.s.d.'s involving l.s. planes.

Refinement. Refinement of F^2 against ALL reflections. The weighted R -factor wR and goodness of fit S are based on F^2 , conventional R -factors R are based on F , with F set to zero for negative F^2 . The threshold expression of $F^2 > \sigma(F^2)$ is used only for calculating R -factors(gt) etc. and is not relevant to the choice of reflections for refinement. R -factors based on F^2 are statistically about twice as large as those based on F , and R -factors based on ALL data will be even larger.

Fractional atomic coordinates and isotropic or equivalent isotropic displacement parameters (Å²)

	<i>x</i>	<i>y</i>	<i>z</i>	$U_{\text{iso}}^*/U_{\text{eq}}$
Zn1	0.45797 (2)	0.21003 (2)	0.06434 (3)	0.03012 (11)
Zn2	0.86974 (2)	-0.02837 (2)	0.16875 (2)	0.02691 (11)
O1	0.82544 (13)	0.04108 (16)	-0.22416 (15)	0.0317 (6)

supplementary materials

O2	0.75851 (19)	0.1297 (2)	-0.27156 (19)	0.0542 (9)
O3	0.54340 (16)	0.20240 (19)	-0.1090 (2)	0.0482 (8)
O4	0.53500 (14)	0.15579 (16)	0.01530 (17)	0.0372 (6)
O5	0.73489 (17)	0.0422 (2)	0.14383 (17)	0.0461 (8)
O6	0.81368 (14)	-0.01665 (16)	0.06956 (16)	0.0367 (6)
C1	0.73604 (17)	0.0869 (2)	-0.1391 (2)	0.0262 (6)
C2	0.67256 (19)	0.1251 (2)	-0.1327 (2)	0.0301 (7)
H2A	0.6548	0.1500	-0.1773	0.036*
C3	0.63563 (18)	0.1261 (2)	-0.0602 (2)	0.0299 (7)
C4	0.66398 (18)	0.0910 (2)	0.0066 (2)	0.0301 (7)
H4A	0.6397	0.0921	0.0554	0.036*
C5	0.72805 (18)	0.0544 (2)	0.0019 (2)	0.0271 (7)
C6	0.76310 (18)	0.0509 (2)	-0.0720 (2)	0.0276 (7)
H6A	0.8048	0.0243	-0.0763	0.033*
C7	0.77524 (18)	0.0865 (2)	-0.2179 (2)	0.0289 (7)
C8	0.56601 (18)	0.1652 (2)	-0.0522 (2)	0.0302 (7)
C9	0.76020 (19)	0.0245 (2)	0.0779 (2)	0.0296 (7)
C1E	0.9480 (2)	0.1157 (3)	0.1420 (3)	0.0398 (9)
C2E	0.9061 (3)	0.1880 (3)	0.2364 (3)	0.0512 (11)
H2E	0.8966	0.2290	0.2680	0.061*
C3E	0.8810 (2)	0.1201 (3)	0.2469 (3)	0.0423 (9)
H3E	0.8505	0.1058	0.2879	0.051*
C4E	0.9881 (3)	0.0916 (3)	0.0703 (3)	0.0579 (13)
H4E1	1.0137	0.1325	0.0484	0.070*
H4E2	0.9561	0.0730	0.0304	0.070*
H4E3	1.0206	0.0537	0.0856	0.070*
N1E	0.90718 (18)	0.07433 (19)	0.1879 (2)	0.0352 (7)
N2E	0.9484 (2)	0.1849 (2)	0.1696 (3)	0.0471 (9)
H2EN	0.9713	0.2210	0.1489	0.057*
C1F	0.3558 (2)	0.1785 (2)	-0.0669 (3)	0.0396 (9)
C2F	0.3373 (2)	0.2885 (3)	-0.0222 (3)	0.0427 (10)
H2F	0.3412	0.3314	0.0079	0.051*
C3F	0.2905 (2)	0.2767 (3)	-0.0822 (3)	0.0495 (11)
H3F	0.2565	0.3093	-0.1010	0.059*
C4F	0.3840 (3)	0.1032 (3)	-0.0801 (4)	0.0613 (15)
H4F1	0.3585	0.0800	-0.1232	0.074*
H4F2	0.3787	0.0749	-0.0315	0.074*
H4F3	0.4330	0.1060	-0.0941	0.074*
N1F	0.37830 (16)	0.22648 (19)	-0.0125 (2)	0.0353 (7)
N2F	0.30319 (19)	0.2075 (2)	-0.1096 (3)	0.0479 (9)
H2FN	0.2809	0.1861	-0.1482	0.057*
C1G	0.3665 (3)	0.1373 (3)	0.1915 (4)	0.0604 (14)
C2G	0.4502 (3)	0.0661 (3)	0.1528 (4)	0.0667 (16)
H2G	0.4899	0.0485	0.1260	0.080*
C3G	0.4119 (4)	0.0282 (4)	0.2072 (4)	0.0738 (17)
H3G	0.4194	-0.0198	0.2241	0.089*
C4G	0.3175 (5)	0.2000 (5)	0.1996 (7)	0.131 (4)
H4G1	0.2818	0.1883	0.2386	0.157*
H4G2	0.2958	0.2098	0.1484	0.157*

H4G3	0.3431	0.2426	0.2172	0.157*
N1G	0.4217 (2)	0.1347 (2)	0.1431 (2)	0.0444 (8)
N2G	0.3604 (3)	0.0740 (3)	0.2321 (3)	0.0631 (13)
H2GN	0.3290	0.0643	0.2680	0.076*
C1H	0.94630 (18)	-0.1645 (2)	0.1130 (2)	0.0328 (8)
C2H	1.01834 (19)	-0.0828 (2)	0.1579 (2)	0.0338 (8)
H2H	1.0369	-0.0393	0.1782	0.041*
C3H	1.05531 (18)	-0.1437 (2)	0.1393 (3)	0.0359 (8)
H3H	1.1038	-0.1493	0.1452	0.043*
C4H	0.8800 (2)	-0.2001 (3)	0.0853 (4)	0.0578 (15)
H4H1	0.8900	-0.2490	0.0671	0.069*
H4H2	0.8601	-0.1721	0.0418	0.069*
H4H3	0.8470	-0.2020	0.1293	0.069*
N1H	0.94875 (15)	-0.09609 (18)	0.14179 (19)	0.0302 (6)
N2H	1.01007 (16)	-0.19593 (18)	0.1103 (2)	0.0324 (7)

Atomic displacement parameters (\AA^2)

	U^{11}	U^{22}	U^{33}	U^{12}	U^{13}	U^{23}
Zn1	0.02406 (18)	0.0339 (2)	0.0324 (2)	-0.00044 (16)	0.00318 (16)	-0.00303 (18)
Zn2	0.02578 (18)	0.0330 (2)	0.02195 (18)	0.00254 (16)	0.00150 (15)	0.00171 (16)
O1	0.0277 (11)	0.0457 (15)	0.0218 (11)	0.0058 (10)	0.0038 (9)	-0.0020 (11)
O2	0.064 (2)	0.067 (2)	0.0317 (15)	0.0266 (17)	0.0106 (14)	0.0175 (16)
O3	0.0392 (15)	0.059 (2)	0.0460 (17)	0.0201 (14)	0.0056 (14)	0.0122 (16)
O4	0.0305 (13)	0.0449 (15)	0.0361 (15)	0.0112 (11)	0.0091 (11)	0.0009 (12)
O5	0.0490 (17)	0.066 (2)	0.0232 (12)	0.0188 (15)	0.0029 (12)	0.0022 (14)
O6	0.0354 (13)	0.0493 (17)	0.0254 (12)	0.0162 (12)	-0.0044 (10)	0.0017 (12)
C1	0.0248 (15)	0.0310 (17)	0.0228 (15)	-0.0002 (13)	0.0014 (12)	-0.0024 (13)
C2	0.0306 (16)	0.0342 (18)	0.0253 (16)	0.0060 (14)	-0.0006 (13)	0.0027 (15)
C3	0.0293 (16)	0.0323 (17)	0.0281 (17)	0.0038 (13)	0.0033 (14)	0.0000 (14)
C4	0.0268 (15)	0.0383 (19)	0.0252 (16)	0.0017 (14)	0.0035 (13)	0.0017 (15)
C5	0.0274 (15)	0.0325 (17)	0.0215 (15)	0.0023 (13)	-0.0009 (12)	-0.0003 (13)
C6	0.0255 (15)	0.0323 (17)	0.0250 (16)	0.0041 (12)	-0.0006 (12)	-0.0012 (14)
C7	0.0283 (15)	0.0357 (18)	0.0228 (15)	0.0002 (13)	0.0002 (12)	0.0002 (14)
C8	0.0256 (15)	0.0348 (18)	0.0300 (18)	0.0031 (13)	0.0010 (13)	-0.0009 (15)
C9	0.0301 (16)	0.0369 (18)	0.0217 (15)	0.0030 (14)	-0.0010 (12)	0.0014 (14)
C1E	0.037 (2)	0.044 (2)	0.038 (2)	-0.0042 (17)	0.0001 (16)	0.0052 (18)
C2E	0.058 (3)	0.041 (2)	0.054 (3)	-0.005 (2)	-0.004 (2)	-0.009 (2)
C3E	0.042 (2)	0.044 (2)	0.041 (2)	-0.0027 (17)	0.0055 (17)	-0.0072 (19)
C4E	0.061 (3)	0.065 (3)	0.048 (3)	-0.002 (3)	0.019 (2)	0.014 (3)
N1E	0.0395 (17)	0.0330 (17)	0.0330 (17)	-0.0053 (13)	0.0025 (13)	-0.0001 (13)
N2E	0.049 (2)	0.0393 (19)	0.053 (2)	-0.0128 (16)	-0.0061 (18)	0.0047 (18)
C1F	0.0324 (18)	0.042 (2)	0.045 (2)	-0.0075 (16)	-0.0023 (16)	-0.0096 (19)
C2F	0.0330 (18)	0.043 (2)	0.052 (3)	0.0046 (16)	-0.0054 (17)	-0.016 (2)
C3F	0.037 (2)	0.057 (3)	0.055 (3)	0.0069 (19)	-0.0136 (19)	-0.014 (2)
C4F	0.058 (3)	0.040 (3)	0.086 (4)	-0.003 (2)	-0.010 (3)	-0.021 (3)
N1F	0.0261 (14)	0.0379 (17)	0.0420 (18)	-0.0006 (12)	-0.0046 (13)	-0.0075 (14)
N2F	0.0368 (17)	0.057 (2)	0.049 (2)	-0.0025 (16)	-0.0129 (16)	-0.0165 (19)

supplementary materials

C1G	0.066 (3)	0.054 (3)	0.061 (3)	-0.016 (2)	0.034 (3)	-0.003 (3)
C2G	0.063 (3)	0.061 (3)	0.076 (4)	0.006 (3)	0.016 (3)	0.024 (3)
C3G	0.080 (4)	0.067 (4)	0.074 (4)	-0.005 (3)	0.008 (3)	0.028 (3)
C4G	0.130 (7)	0.093 (6)	0.169 (10)	0.021 (5)	0.116 (7)	0.016 (6)
N1G	0.0441 (19)	0.049 (2)	0.0405 (19)	-0.0053 (16)	0.0117 (16)	0.0037 (17)
N2G	0.072 (3)	0.070 (3)	0.047 (2)	-0.027 (2)	0.020 (2)	0.004 (2)
C1H	0.0244 (16)	0.039 (2)	0.0348 (19)	0.0002 (14)	0.0025 (14)	-0.0037 (16)
C2H	0.0288 (16)	0.041 (2)	0.0317 (19)	0.0012 (15)	-0.0039 (14)	-0.0053 (16)
C3H	0.0219 (15)	0.048 (2)	0.038 (2)	0.0040 (14)	-0.0044 (14)	-0.0122 (18)
C4H	0.0225 (18)	0.058 (3)	0.092 (4)	0.0010 (18)	0.000 (2)	-0.024 (3)
N1H	0.0244 (13)	0.0361 (16)	0.0302 (15)	0.0039 (12)	0.0007 (11)	-0.0044 (13)
N2H	0.0257 (14)	0.0363 (17)	0.0350 (16)	0.0034 (12)	0.0002 (12)	-0.0051 (14)

Geometric parameters (Å, °)

Zn1—O4	1.942 (3)	N2E—H2EN	0.8600
Zn2—O6	1.968 (3)	C1F—N1F	1.325 (5)
Zn2—O1 ⁱ	1.976 (2)	C1F—N2F	1.333 (6)
Zn1—N2H ⁱⁱ	1.971 (3)	C1F—C4F	1.490 (7)
Zn1—N1F	1.998 (3)	C2F—C3F	1.349 (6)
Zn1—N1G	2.015 (4)	C2F—N1F	1.381 (5)
Zn2—N1H	1.992 (3)	C2F—H2F	0.9300
Zn2—N1E	2.027 (3)	C3F—N2F	1.361 (6)
O1—C7	1.265 (4)	C3F—H3F	0.9300
O2—C7	1.228 (5)	C4F—H4F1	0.9600
O3—C8	1.236 (5)	C4F—H4F2	0.9600
O4—C8	1.274 (5)	C4F—H4F3	0.9600
O5—C9	1.236 (5)	N2F—H2FN	0.8600
O6—C9	1.269 (4)	C1G—N1G	1.319 (6)
C1—C6	1.388 (5)	C1G—N2G	1.340 (7)
C1—C2	1.395 (5)	C1G—C4G	1.480 (10)
C1—C7	1.503 (5)	C2G—C3G	1.348 (8)
C2—C3	1.390 (5)	C2G—N1G	1.372 (7)
C2—H2A	0.9300	C2G—H2G	0.9300
C3—C4	1.386 (5)	C3G—N2G	1.349 (8)
C3—C8	1.507 (5)	C3G—H3G	0.9300
C4—C5	1.389 (5)	C4G—H4G1	0.9600
C4—H4A	0.9300	C4G—H4G2	0.9600
C5—C6	1.394 (5)	C4G—H4G3	0.9600
C5—C9	1.501 (5)	N2G—H2GN	0.8600
C6—H6A	0.9300	C1H—N1H	1.336 (5)
C1E—N1E	1.321 (5)	C1H—N2H	1.339 (4)
C1E—N2E	1.340 (6)	C1H—C4H	1.488 (5)
C1E—C4E	1.477 (7)	C2H—C3H	1.348 (6)
C2E—C3E	1.338 (7)	C2H—N1H	1.369 (4)
C2E—N2E	1.368 (7)	C2H—H2H	0.9300
C2E—H2E	0.9300	C3H—N2H	1.368 (5)
C3E—N1E	1.377 (5)	C3H—H3H	0.9300
C3E—H3E	0.9300	C4H—H4H1	0.9600

C4E—H4E1	0.9600	C4H—H4H2	0.9600
C4E—H4E2	0.9600	C4H—H4H3	0.9600
C4E—H4E3	0.9600		
O4—Zn1—N2H ⁱⁱ	111.87 (13)	N1F—C1F—N2F	109.9 (4)
O4—Zn1—N1F	112.28 (13)	N1F—C1F—C4F	126.3 (4)
N2H ⁱⁱ —Zn1—N1F	110.38 (14)	N2F—C1F—C4F	123.8 (4)
O4—Zn1—N1G	100.42 (14)	C3F—C2F—N1F	109.0 (4)
N2H ⁱⁱ —Zn1—N1G	116.61 (16)	C3F—C2F—H2F	125.5
N1F—Zn1—N1G	104.81 (15)	N1F—C2F—H2F	125.5
O6—Zn2—O1 ⁱ	122.12 (11)	C2F—C3F—N2F	106.1 (4)
O6—Zn2—N1H	106.66 (12)	C2F—C3F—H3F	127.0
O1 ⁱ —Zn2—N1H	116.64 (13)	N2F—C3F—H3F	127.0
O6—Zn2—N1E	102.68 (13)	C1F—C4F—H4F1	109.5
O1 ⁱ —Zn2—N1E	96.73 (13)	C1F—C4F—H4F2	109.5
N1H—Zn2—N1E	110.08 (13)	H4F1—C4F—H4F2	109.5
C7—O1—Zn2 ⁱⁱⁱ	118.0 (2)	C1F—C4F—H4F3	109.5
C8—O4—Zn1	130.2 (3)	H4F1—C4F—H4F3	109.5
C9—O6—Zn2	113.9 (2)	H4F2—C4F—H4F3	109.5
C6—C1—C2	119.6 (3)	C1F—N1F—C2F	106.2 (3)
C6—C1—C7	120.7 (3)	C1F—N1F—Zn1	125.3 (3)
C2—C1—C7	119.7 (3)	C2F—N1F—Zn1	128.5 (3)
C3—C2—C1	120.5 (3)	C1F—N2F—C3F	108.8 (4)
C3—C2—H2A	119.8	C1F—N2F—H2FN	125.6
C1—C2—H2A	119.8	C3F—N2F—H2FN	125.6
C4—C3—C2	119.2 (3)	N1G—C1G—N2G	110.0 (5)
C4—C3—C8	119.2 (3)	N1G—C1G—C4G	125.6 (5)
C2—C3—C8	121.6 (3)	N2G—C1G—C4G	124.4 (5)
C3—C4—C5	121.1 (3)	C3G—C2G—N1G	109.4 (6)
C3—C4—H4A	119.5	C3G—C2G—H2G	125.3
C5—C4—H4A	119.5	N1G—C2G—H2G	125.3
C4—C5—C6	119.3 (3)	N2G—C3G—C2G	106.1 (6)
C4—C5—C9	118.9 (3)	N2G—C3G—H3G	126.9
C6—C5—C9	121.7 (3)	C2G—C3G—H3G	126.9
C1—C6—C5	120.3 (3)	C1G—C4G—H4G1	109.5
C1—C6—H6A	119.9	C1G—C4G—H4G2	109.5
C5—C6—H6A	119.9	H4G1—C4G—H4G2	109.5
O2—C7—O1	123.7 (3)	C1G—C4G—H4G3	109.5
O2—C7—C1	119.8 (3)	H4G1—C4G—H4G3	109.5
O1—C7—C1	116.5 (3)	H4G2—C4G—H4G3	109.5
O3—C8—O4	125.5 (3)	C1G—N1G—C2G	105.9 (4)
O3—C8—C3	119.8 (3)	C1G—N1G—Zn1	129.8 (4)
O4—C8—C3	114.7 (3)	C2G—N1G—Zn1	124.2 (3)
O5—C9—O6	124.1 (3)	C1G—N2G—C3G	108.5 (4)
O5—C9—C5	119.2 (3)	C1G—N2G—H2GN	125.8
O6—C9—C5	116.7 (3)	C3G—N2G—H2GN	125.8
N1E—C1E—N2E	110.2 (4)	N1H—C1H—N2H	112.3 (3)
N1E—C1E—C4E	126.4 (4)	N1H—C1H—C4H	123.1 (3)

supplementary materials

N2E—C1E—C4E	123.4 (4)	N2H—C1H—C4H	124.6 (4)
C3E—C2E—N2E	105.9 (4)	C3H—C2H—N1H	108.2 (3)
C3E—C2E—H2E	127.0	C3H—C2H—H2H	125.9
N2E—C2E—H2E	127.0	N1H—C2H—H2H	125.9
C2E—C3E—N1E	109.9 (4)	C2H—C3H—N2H	109.1 (3)
C2E—C3E—H3E	125.1	C2H—C3H—H3H	125.5
N1E—C3E—H3E	125.1	N2H—C3H—H3H	125.5
C1E—C4E—H4E1	109.5	C1H—C4H—H4H1	109.5
C1E—C4E—H4E2	109.5	C1H—C4H—H4H2	109.5
H4E1—C4E—H4E2	109.5	H4H1—C4H—H4H2	109.5
C1E—C4E—H4E3	109.5	C1H—C4H—H4H3	109.5
H4E1—C4E—H4E3	109.5	H4H1—C4H—H4H3	109.5
H4E2—C4E—H4E3	109.5	H4H2—C4H—H4H3	109.5
C1E—N1E—C3E	105.8 (4)	C1H—N1H—C2H	105.6 (3)
C1E—N1E—Zn2	130.0 (3)	C1H—N1H—Zn2	129.2 (2)
C3E—N1E—Zn2	122.9 (3)	C2H—N1H—Zn2	124.9 (3)
C1E—N2E—C2E	108.2 (4)	C1H—N2H—C3H	104.9 (3)
C1E—N2E—H2EN	125.9	C1H—N2H—Zn1 ^{iv}	131.5 (3)
C2E—N2E—H2EN	125.9	C3H—N2H—Zn1 ^{iv}	123.2 (2)
N2H ⁱⁱ —Zn1—O4—C8	-76.9 (4)	N1F—C2F—C3F—N2F	-0.3 (6)
N1F—Zn1—O4—C8	47.9 (4)	N2F—C1F—N1F—C2F	0.0 (5)
N1G—Zn1—O4—C8	158.8 (4)	C4F—C1F—N1F—C2F	179.9 (5)
O1 ⁱ —Zn2—O6—C9	41.1 (3)	N2F—C1F—N1F—Zn1	-178.4 (3)
N1H—Zn2—O6—C9	178.8 (3)	C4F—C1F—N1F—Zn1	1.5 (7)
N1E—Zn2—O6—C9	-65.4 (3)	C3F—C2F—N1F—C1F	0.2 (5)
C6—C1—C2—C3	-1.3 (6)	C3F—C2F—N1F—Zn1	178.5 (3)
C7—C1—C2—C3	-180.0 (3)	O4—Zn1—N1F—C1F	37.9 (4)
C1—C2—C3—C4	2.5 (6)	N2H ⁱⁱ —Zn1—N1F—C1F	163.5 (3)
C1—C2—C3—C8	-178.4 (3)	N1G—Zn1—N1F—C1F	-70.2 (4)
C2—C3—C4—C5	-0.7 (6)	O4—Zn1—N1F—C2F	-140.1 (4)
C8—C3—C4—C5	-179.9 (3)	N2H ⁱⁱ —Zn1—N1F—C2F	-14.6 (4)
C3—C4—C5—C6	-2.2 (6)	N1G—Zn1—N1F—C2F	111.8 (4)
C3—C4—C5—C9	173.4 (4)	N1F—C1F—N2F—C3F	-0.2 (6)
C2—C1—C6—C5	-1.7 (5)	C4F—C1F—N2F—C3F	179.9 (5)
C7—C1—C6—C5	177.0 (3)	C2F—C3F—N2F—C1F	0.3 (6)
C4—C5—C6—C1	3.4 (5)	N1G—C2G—C3G—N2G	-1.1 (8)
C9—C5—C6—C1	-172.1 (3)	N2G—C1G—N1G—C2G	1.3 (7)
Zn2 ⁱⁱⁱ —O1—C7—O2	-9.8 (5)	C4G—C1G—N1G—C2G	-177.9 (8)
Zn2 ⁱⁱⁱ —O1—C7—C1	171.5 (2)	N2G—C1G—N1G—Zn1	178.2 (4)
C6—C1—C7—O2	-165.6 (4)	C4G—C1G—N1G—Zn1	-1.0 (11)
C2—C1—C7—O2	13.0 (6)	C3G—C2G—N1G—C1G	-0.1 (8)
C6—C1—C7—O1	13.2 (5)	C3G—C2G—N1G—Zn1	-177.2 (5)
C2—C1—C7—O1	-168.2 (3)	O4—Zn1—N1G—C1G	-175.7 (5)
Zn1—O4—C8—O3	-16.3 (6)	N2H ⁱⁱ —Zn1—N1G—C1G	63.3 (5)
Zn1—O4—C8—C3	164.1 (3)	N1F—Zn1—N1G—C1G	-59.1 (5)
C4—C3—C8—O3	173.2 (4)	O4—Zn1—N1G—C2G	0.7 (5)
C2—C3—C8—O3	-5.9 (6)	N2H ⁱⁱ —Zn1—N1G—C2G	-120.3 (5)

C4—C3—C8—O4	-7.2 (5)	N1F—Zn1—N1G—C2G	117.3 (5)
C2—C3—C8—O4	173.7 (4)	N1G—C1G—N2G—C3G	-2.0 (7)
Zn2—O6—C9—O5	-16.2 (5)	C4G—C1G—N2G—C3G	177.2 (8)
Zn2—O6—C9—C5	161.9 (3)	C2G—C3G—N2G—C1G	1.9 (8)
C4—C5—C9—O5	-10.7 (6)	N1H—C2H—C3H—N2H	0.7 (5)
C6—C5—C9—O5	164.7 (4)	N2H—C1H—N1H—C2H	0.4 (5)
C4—C5—C9—O6	171.0 (3)	C4H—C1H—N1H—C2H	-178.0 (4)
C6—C5—C9—O6	-13.5 (5)	N2H—C1H—N1H—Zn2	-173.3 (3)
N2E—C2E—C3E—N1E	0.2 (6)	C4H—C1H—N1H—Zn2	8.2 (6)
N2E—C1E—N1E—C3E	-0.1 (5)	C3H—C2H—N1H—C1H	-0.7 (4)
C4E—C1E—N1E—C3E	-179.9 (5)	C3H—C2H—N1H—Zn2	173.4 (3)
N2E—C1E—N1E—Zn2	167.5 (3)	O6—Zn2—N1H—C1H	-57.7 (4)
C4E—C1E—N1E—Zn2	-12.4 (7)	O1 ⁱ —Zn2—N1H—C1H	82.7 (4)
C2E—C3E—N1E—C1E	-0.1 (5)	N1E—Zn2—N1H—C1H	-168.4 (3)
C2E—C3E—N1E—Zn2	-168.8 (3)	O6—Zn2—N1H—C2H	129.6 (3)
O6—Zn2—N1E—C1E	-60.7 (4)	O1 ⁱ —Zn2—N1H—C2H	-89.9 (3)
O1 ⁱ —Zn2—N1E—C1E	174.2 (4)	N1E—Zn2—N1H—C2H	18.9 (4)
N1H—Zn2—N1E—C1E	52.6 (4)	N1H—C1H—N2H—C3H	0.0 (5)
O6—Zn2—N1E—C3E	105.0 (3)	C4H—C1H—N2H—C3H	178.4 (5)
O1 ⁱ —Zn2—N1E—C3E	-20.1 (4)	N1H—C1H—N2H—Zn1 ^{iv}	-172.7 (3)
N1H—Zn2—N1E—C3E	-141.7 (3)	C4H—C1H—N2H—Zn1 ^{iv}	5.7 (7)
N1E—C1E—N2E—C2E	0.2 (5)	C2H—C3H—N2H—C1H	-0.4 (5)
C4E—C1E—N2E—C2E	-179.9 (5)	C2H—C3H—N2H—Zn1 ^{iv}	173.0 (3)
C3E—C2E—N2E—C1E	-0.2 (5)		

Symmetry codes: (i) $x, -y, z+1/2$; (ii) $-x+3/2, y+1/2, z$; (iii) $x, -y, z-1/2$; (iv) $-x+3/2, y-1/2, z$.

Hydrogen-bond geometry ($\text{\AA}, ^\circ$)

$D-H\cdots A$	$D-H$	$H\cdots A$	$D\cdots A$	$D-H\cdots A$
N2E—H2EN \cdots O3 ^v	0.86	2.06	2.912 (5)	169
N2F—H2FN \cdots O2 ^{vi}	0.86	1.84	2.693 (5)	172
N2G—H2GN \cdots O5 ^{vii}	0.86	1.94	2.798 (5)	175

Symmetry codes: (v) $x+1/2, -y+1/2, -z$; (vi) $-x+1, y, -z-1/2$; (vii) $-x+1, y, -z+1/2$.

Fig. 1

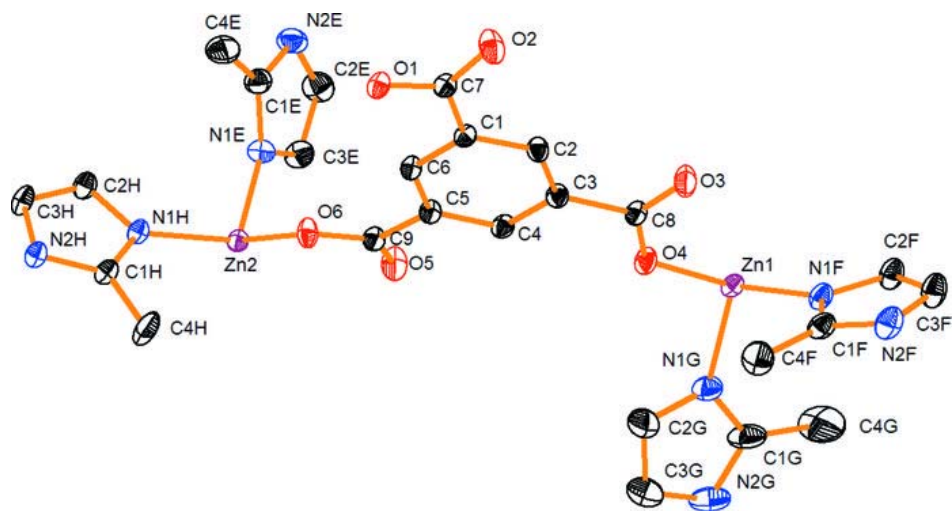


Fig. 3

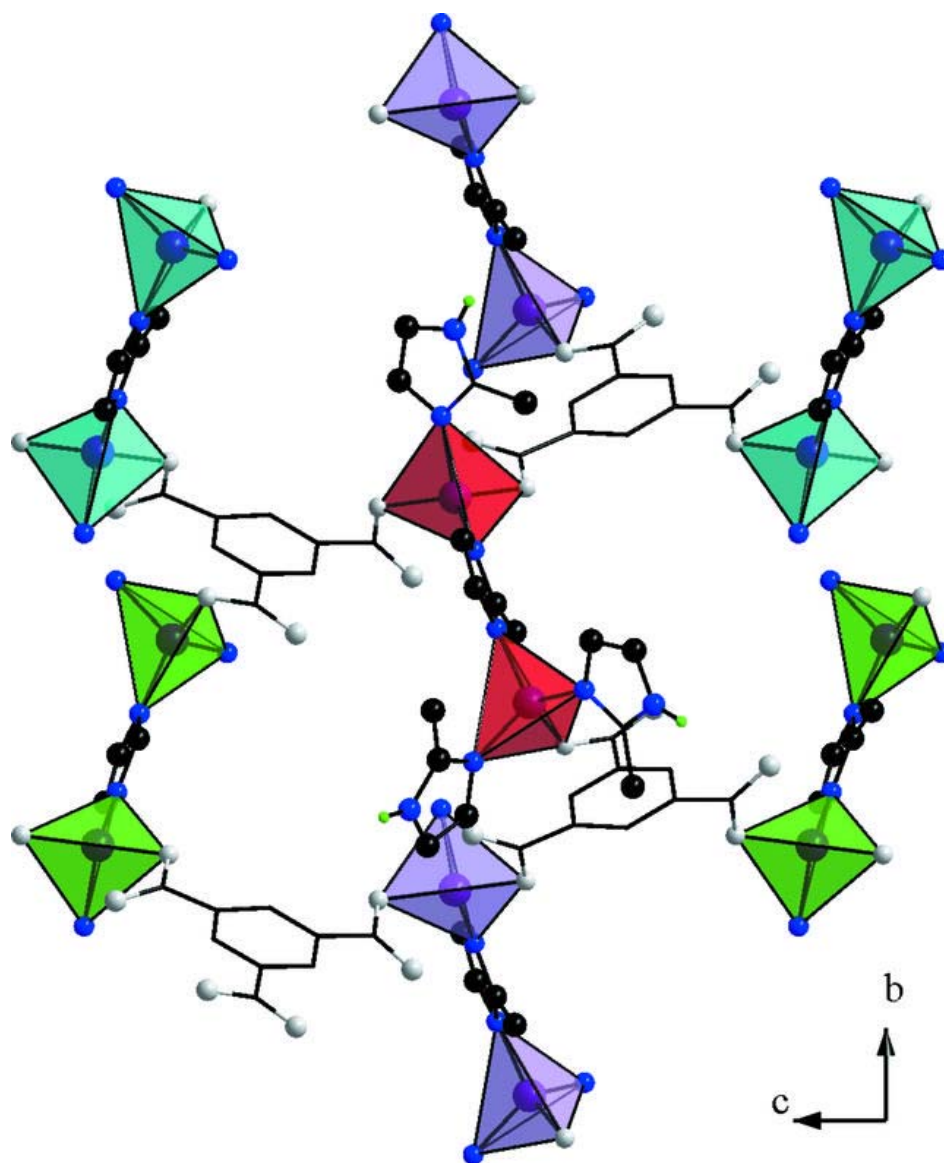
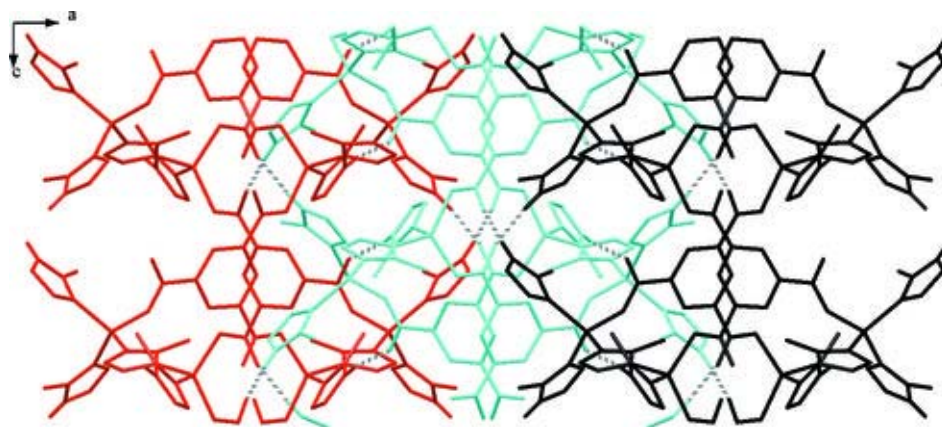


Fig. 4



8 List of publications / Contribution to conferences

Contribution to conferences

Ni(II) based MOFs with paddle-wheel building units: formation fields and polymorphism. (oral presentation)

Palanikumar Maniam and Norbert Stock.

23. *German Zeolite Conference*, 2011, Erlangen, Germany.

High-throughput investigation on the synthesis of Ni(II)-based MOFs with a paddle-wheel type inorganic building unit. (poster)

Palanikumar Maniam and Norbert Stock.

22. *German Zeolite Conference*, 2010, Munich, Germany.

High-Throughput Investigation on the Synthesis of a Nickel(II) Based MOF with Paddle-Wheel Type Inorganic Building Units. (poster)

Palanikumar Maniam and Norbert Stock.

12. *North German Doctoral-Kolloquium*, 2009, Oldenbourg, Germany.

Hot compressed water treatment of biomass. (poster)

Ali Sinag, Andrea Kruse and Palanikumar Maniam.

11. *European Meeting on Supercritical Fluids*, 2008, Barcelona, Spain.

List of publications for this Ph.D. Thesis

Synthesis and characterization of the mixed-linker copper(II) coordination polymer $[\text{Cu}(\text{HO}_3\text{PC}_6\text{H}_4\text{SO}_3)(\text{C}_{10}\text{N}_2\text{H}_8)] \cdot \text{H}_2\text{O}$.

Palanikumar Maniam and Norbert Stock. *Z. Anorg. Allg. Chem.* **2011**, *accepted*.

Investigation of porous Ni-based metal-organic frameworks containing paddle-wheel type inorganic building units via high-throughput methods.

Palanikumar Maniam and Norbert Stock. *Inorg. Chem.* **2011**, *50*, 5085-5097.

Poly $[(\mu_3\text{-benzene-1,3,5-tricarboxylato-}\kappa_3\text{O}^1:\text{O}^3:\text{O}^5)(\mu_2\text{-2-methylimidazolato-}\kappa^2\text{N:N}')\text{tris}(2\text{-methylimidazole-}\kappa\text{N})\text{dizinc(II)}]$.

Palanikumar Maniam and Norbert Stock. *Acta Cryst.* **2011**, *E67*, m669-m670.

A three-dimensional tin(II) phosphonatobenzenesulfonate with Sn₄O₁₂ clusters.

Palanikumar Maniam and Norbert Stock. *Acta Cryst.* **2011**, C67, m73-m76.

Systematic Hydrothermal Investigation of Metal Phosphonatobenzenesulfonates by High-Throughput Methods.

Palanikumar Maniam, Christian Näther and Norbert Stock. *Eur. J. Inorg. Chem.*, **2010**, 3866-3874.

Book Chapter

High-throughput methods for the systematic investigation of metal phosphonate syntheses fields, edited by A. Clearfield and K. Demadis, in *Metal phosphonates: from synthesis to applications*, Royal Society of Chemistry, Cambridge, (2011), in press.

Other publications

Hydrothermal gasification of biomass: consecutive reactions to long-living Intermediates.

Andrea Kruse, Philipp Bernolle, Nicolaus Dahmen, Eckhard Dinjus and Palanikumar Maniam. *Energy Environ. Sci.* **2010**, 3, 136-143.

Influence of Proteins on the Hydrothermal Gasification and Liquefaction of Biomass. 2. Model Compounds.

Andrea Kruse, Palanikumar Maniam and Franziska Spieler. *Ind. Eng. Chem. Res.*, **2007**, 46, 87-96.

Curriculum Vitae

PALANIKUMAR MANIAM



Personal data

Birthdate / -place: 07.03.1982 / Pahang, Malaysia
Nationality: Malaysian
Marital status: single
Academic degree: Diplom Ingenieur (FH)
Majors: Chemical technology

Work experience

03/2008 – 08/2011 **Christian-Albrechts-Universität zu Kiel, Germany**
Ph.D. thesis in the Institut of Inorganic Chemistry (Prof. Dr. Norbert Stock)
Title: *High-Throughput Investigation of Inorganic-Organic Hybrid Materials: Metal Phosphonatobenzenesulfonates and Ni-based MOFs with Paddle-Wheel Building Units*

03/2007 – 08/2007 **BASF SE, Ludwigshafen, Germany**
Diplom-Thesis in Zeolite Research Department (Prof. Dr. Jens Hagen)
Title: *Synthesis and Characterization of Metal-based Coordination Polymers and the Investigation of their Catalytic Application Potential in the Chemical Industry*

08/2005 – 02/2006 **BASF SE, Ludwigshafen, Germany**
Practical semester in Polymer Development Department (Dr. C. Krüger)
Title: *A Study on the Influences of Impact Strength Modifiers on the Gloss Levels of Hard PVC*

03/2004 – 08/2004 **Forschungszentrum Karlsruhe, Germany**
Practical semester in the Institut of Technical Chemistry (Dr. A. Kruse)
Title: *The Determination of Reaction Paths during Hydrothermal Gasification of Biomass*

Education

03/2008 – 08/2011	Christian-Albrechts-Universität zu Kiel, Germany PhD. thesis
03/2003 – 08/2007	Hochschule Mannheim, Germany Diplom Ingenieur (FH) in Chemical Technology
02/2003	Hochschule Heilbronn, Germany Technical preparatory course
07/2002 – 12/2002	German-Malaysia Institute, Malaysia Industrial Training in electronics
06/2000 – 06/2002	Universiti Teknologi Mara (INTEC), Malaysia German Language Test for University Admission (DSH) UK A-levels University Entrance Examination

Scholarship

03/2003 – 08/2007	Malaysian Government Scholarship for Engineering Course in Germany
06/2000 – 12/2002	Malaysian Government Scholarship for A-Levels and German language course in Malaysia

Languages

Tamil	mother tongue
German	fluent
English	fluent
Malay	fluent
Spanish	beginner

Hobbies

Football, Speedminton, Travel

Palanikumar Maniam